

**Charm and Beauty Production
at HERA
with D^* -Muon Events**

Charm and Beauty Production
at HERA
with D^* -Muon Events

Dissertation

zur Erlangung des Doktorgrades
des Fachbereichs Physik
der Universität Hamburg

vorgelegt von

JEANNINE WAGNER

aus Hamburg

Hamburg
2004

Gutachter/Gutachterin der Dissertation:

Prof. Dr. B. Naroska
PD. Dr. E. Elsen

Gutachter/Gutachterin der Disputation:

Prof. Dr. B. Naroska
Prof. Dr. R.-D. Heuer

Datum der Disputation:

17.06.2004

Vorsitzender des Promotionsausschusses
Dekan des Fachbereichs Physik

Prof. Dr. F.-W. Büßer
Prof. Dr. G. Huber

I would like to dedicate my thesis to my supervisor Dr. Ralf Gerhards, who died unexpectedly in December of last year.

Ralf, I am grateful for all your friendly advice and I will never forget you.

Abstract

Heavy quark production (c and b) is investigated in the H1-experiment at the ep collider HERA using events with a D^* -meson and an additional muon. Data taken during the years 1997 and 1999-2000, corresponding to an integrated luminosity of about 85 pb^{-1} , are used. Exploiting the charge and angle correlations between the D^* -meson and the muon a separation of charm and beauty production is performed. Total charm and beauty production cross sections are measured in the visible ranges of the transverse momentum $p_T(D^*) > 1.5 \text{ GeV}/c$, the pseudorapidity $|\eta(D^*)| < 1.5$, the momentum $p(\mu) > 2.0 \text{ GeV}/c$, $|\eta(\mu)| < 1.735$ and the inelasticity $0.05 < y < 0.75$ at $Q^2 < 1 \text{ GeV}^2$ and $Q^2 < 100 \text{ GeV}^2$. Also differential cross sections in various $D^*\mu$ -variables are measured and compared with the predictions of different leading order QCD Monte Carlo simulations and in the case of the $Q^2 < 1 \text{ GeV}^2$ data set also with next-to-leading order calculations. Furthermore the unintegrated gluon density is extracted.

Zusammenfassung

Die Produktion schwerer Quarks (c und b) wird beim H1 Experiment am ep Beschleuniger HERA untersucht, wobei Ereignisse mit einem D^* -Meson und einem zusätzlichen Myon verwendet werden. Die Daten der Jahre 1997 und 1999-2000, welche einer integrierten Luminosität von etwa 85 pb^{-1} entsprechen, werden verwendet. Durch Ausnutzung der Ladungs- und Winkelkorrelationen zwischen dem D^* und dem Myon wird eine Trennung von Charm- und Beauty-Produktion vorgenommen. Totale Charm- und Beauty-Produktionswirkungsquerschnitte werden in den sichtbaren Bereichen des transversalen Impulses $p_T(D^*) > 1.5 \text{ GeV}/c$, der Pseudorapidität $|\eta(D^*)| < 1.5$, des Impulses $p(\mu) > 2.0 \text{ GeV}/c$, $|\eta(\mu)| < 1.735$ und der Inelastizität $0.05 < y < 0.75$ bei $Q^2 < 1 \text{ GeV}^2$ und $Q^2 < 100 \text{ GeV}^2$ gemessen. Außerdem werden differentielle Wirkungsquerschnitte verschiedener $D^*\mu$ Größen gemessen und mit den Vorhersagen von verschiedenen QCD Monte-Carlo Simulationen in führender Ordnung verglichen, im Falle des Datensatzes mit $Q^2 < 1 \text{ GeV}^2$ auch mit NLO Rechnungen. Desweiteren wird die unintegrierte Gluondichte extrahiert.

Contents

Introduction	9
1 Theoretical Framework	3
1.1 HERA Kinematics	3
1.2 Differential Cross Sections and Structure Functions	5
1.3 QCD Framework	6
1.3.1 The Strong Coupling Constant α_s	6
1.3.2 Factorisation	8
1.3.3 Parton Densities and Evolution Models	9
1.3.4 CCFM Equation	12
1.4 Photoproduction	17
1.5 Heavy Quark Production	19
1.5.1 LO Photoproduction Cross Section	22
1.5.2 LO DIS Cross Section	23
1.5.3 NLO	24
1.5.4 Calculation Schemes	26
1.5.5 Small x Cross Sections	27
1.6 Fragmentation	28

<i>CONTENTS</i>	7
2 Reconstruction of the $Q\bar{Q}$ Final State	32
2.1 Double Tagging	32
2.1.1 Tagging of Heavy Quarks with D^* -Mesons	33
2.1.2 Tagging of Heavy Quarks via Semileptonic Decays	35
2.1.3 Branching Ratios for $D^*\mu$ Events	36
2.1.4 Charge and Angle Correlations	36
2.1.5 $D^*\mu$ -Quantities	39
2.2 Monte Carlo Simulation	41
2.3 NLO Calculations: FMNR	43
2.4 Monte Carlo Studies of $D^*\mu$ Events	48
2.5 Unintegrated Gluon Density	54
3 The H1 Experiment at HERA	58
3.1 The HERA Accelerator	58
3.2 The H1 Detector	59
3.2.1 Central Jet Chamber	62
3.2.2 Central Silicon Tracker CST	64
3.2.3 Spaghetti Calorimeter	64
3.2.4 Central Muon Detector	65
3.2.5 Trigger System	68
4 Data Selection	71
4.1 Run Selection and Detector Status	71
4.2 Level 1 Trigger Selection	73
4.2.1 L1 Prescales and Weights	75
4.3 L4 Trigger Selection and L5 Classification	76
4.4 Kinematic Selection	77
4.4.1 Selection of DIS Events	77
4.4.2 Selection of Photoproduction Events	78
4.5 Selection of D^* Events	79
4.5.1 Reconstruction of the D^*	79
4.5.2 D^* Fit Method	81
4.6 Selection of Muons in D^* Events	82
4.7 Studies to increase $N(D^*\mu)$	88

5	Comparison of Data and Simulation	91
5.1	Reweighting of the Monte Carlo Simulation	91
5.2	Description of ep Scattering	96
5.3	Description of D^* Kinematical Variables	100
5.4	Description of Muon and Combined Variables	103
5.5	Description of the Muon Background	103
6	Separation of Charm and Beauty	110
6.1	Charge and Angle Correlations	110
6.2	Determination of the Charm and Beauty Fraction	115
6.3	Control Distributions	121
6.4	Comparison with other Methods	127
7	Total Charm and Beauty Cross Sections	130
7.1	Cross Section Definitions	130
7.2	Luminosity	131
7.3	Efficiencies	132
7.4	Systematic Errors	136
7.5	Comparison to Theoretical Predictions	139
8	Differential Cross Sections	143
8.1	Differential Distributions	143
8.2	Differential Efficiencies	150
8.3	Systematic Errors	152
8.4	Normalised Differential Cross Sections	154
9	Unintegrated Gluon Density	158
9.1	Differential Distributions	159
9.2	Unfolding of Gluon Variables	160
9.3	Differential Cross Sections	163
9.4	Extraction of the Unintegrated Gluon Density	166
10	Summary and Outlook	168

A	Track Trigger for HERA II	172
A.1	The Principle of the FTT	172
A.2	Triggering Charm with D^* -Mesons	175
B	Track and Muon Selection	183
B.1	Track Selection	183
B.2	Muon Selection	184
C	Maximum Likelihood Method	185
D	Unfolding Method	187

Introduction

In particle physics the properties of the constituents of matter and their interactions are investigated. To date the microscopic world is described very successfully by the Standard Model (SM). In the SM the fundamental constituents are six quarks and six leptons. They interact via different forces, the electroweak and strong interactions. The theory of the strong force is Quantum Chromo Dynamics (QCD), which describes the interaction between quarks by the exchange of gluons.

The topic of this analysis is the production of charm and beauty quarks in ep -collisions at HERA. The dominant production mechanism of heavy quarks at HERA is photon gluon fusion (PGF). In this picture a heavy quark- antiquark pair is produced by a photon from the incoming beam electron and a gluon from the incoming proton. This process provides a good testing ground of QCD.

The calculations of cross sections in QCD are performed using perturbation theory using the strong coupling α_s as an expansion parameter. For heavy quark production in ep -collisions next-to-leading order (NLO) calculations are available. The convergence of the perturbation series is only ensured if a hard scale is present, for example the virtuality of the photon or the transverse momentum or the mass of a heavy quark. Since α_s depends on the scale, its value decreasing with increasing scale, the convergence of the perturbation series improves with increasing scale. A good convergence of the series is related to a small theoretical uncertainty of the predicted cross section. Since the beauty quark is about 3-4 times heavier than the charm quark, the theoretical uncertainties for beauty production are smaller than for charm production.

In general charm production measurements at HERA are well described by the theory, whereas the picture is somewhat unresolved in the b -sector ($p\bar{p}$: [1, 2, 3, 4], γp : [5, 6, 7, 8], $\gamma\gamma$: [9, 10], ep : [11, 12], eN : [13]). First measurements at HERA [5, 6] were about a factor 3-5 above the NLO predictions, while most recent HERA b -production cross sections [7, 8] are closer to the theory in NLO.

Most previous charm and beauty measurements at HERA were based on the measurement of one heavy quark (single tagging). In the case of charm the D^* meson is commonly used for this tag, while for beauty often the semileptonic decay into muons is taken as a signature. In the meantime, the available data samples are large especially for charm production and contain some thousands of events. More information about the heavy quark final state is accessible in events with two jets along with the D^* , as is the case in more recent charm analyses [14, 15].

In this thesis a heavy quark pair is tagged, one via a D^* -meson and the other one via a muon (double tagging). A great advantage of using D^* reconstruction is that the contributions from the light quarks u , d and s can be eliminated by a fit to a mass spectrum obtained from the D^* candidates. Double tagging provides more information about the production mechanism than single tagging. A disadvantage of double tagged samples is of course that they contain a reduced number of events.

The first analysis topic of this thesis will be the measurement of total charm and beauty cross sections. A separation of charm and beauty production is performed by exploiting the charge and angle correlations between the D^* -meson and the muon.

A double tagging analysis is highly sensitive to NLO effects, the fragmentation and the behaviour of the initial partons, which in the case of PGF are the photon emitted by the incoming electron and the gluon. The study of these effects is a second topic of this thesis. Such studies have already been carried out at fixed target experiments, e.g. at E687 [16, 17] and more recently at FOCUS [18]. Here both charm quarks were reconstructed using D mesons and the data show the expected NLO effects. These effects are even stronger than predicted. The data could be interpreted as indicating a non-zero transverse momentum of one of the initial partons.

In the third step of this analysis an attempt is made to gain further information on the structure of the proton. The structure is described by quark and gluon densities. These densities are believed to be universal and are therefore applicable in all other experiments at hadronic colliders (ep , $p\bar{p}$, pp).

Several approaches describe the evolution of such quark and gluon densities as a function of the virtuality of the photon Q^2 and the Björken variable x . In the DGLAP approximation [19] the evolution is performed using gluon emissions strongly ordered in the transverse momentum. In the more recent CCFM approach [20, 21] this ordering is no longer present. Within the CCFM approach the gluon density depends explicitly on the transverse momentum of the gluon and is called the unintegrated gluon density. Predictions of this approach have been used successfully, e.g. in forward jet production [22]. No direct measurement of the unintegrated gluon density however has been performed yet. Reconstructing the heavy quark pair the measurement of the unintegrated gluon density is possible.

This thesis is organised as follows: In the first chapter the theoretical framework is explained with emphasis on heavy quark production and on different theoretical approaches for the evolution of the parton densities. The double tagging method using a D^* -meson and a muon is described in the second chapter. The H1 detector is introduced next. Here the detector components, relevant for this analysis, are described in some detail. In the fourth chapter the selection of the $D^*\mu$ events is described. In chapter five the description of the data by the Monte-Carlo simulation is investigated, in particular studies concerning the muon background are presented. The chapter six deals with the separation of charm and beauty production. In chapter seven the total charm and beauty cross section results are presented. In chapter eight differential normalised cross sections as a function of different variables such as the azimuthal angular difference between the D^* -meson and the muon or the transverse momentum of the $D^*\mu$ -pair, are calculated and in the last chapter the extraction of the unintegrated gluon density is performed.

Chapter 1

Theoretical Framework

In this chapter the kinematical variables used to describe the ep scattering at HERA are introduced. The structure of the proton and photon structure are then considered. Evolution models which predict the structure of the proton or photon at an arbitrary scale, if the structure is known at an initial scale, are discussed in some detail and the differences between the different models are noted.

After this the heavy quark production mechanism is presented and the regimes of validity of different approximations are discussed. The special features of heavy quarks concerning the evolution models are considered. Finally hadronisation, the transition of the quarks into the observable hadrons, is explained.

1.1 HERA Kinematics

At HERA beams of electrons or positrons are collided with beams of protons. The ep scattering process can be described to leading order by the exchange of either a neutral boson - γ or Z^0 - or by a charged boson W^\pm . The case of γ or Z^0 exchange is called a neutral current exchange process. The other case, in which the incoming electron or positron transforms into an antineutrino or a neutrino respectively, is called a charged current exchange process (see figure 1.1).

The four-momenta of the incoming electron k , the outgoing electron or neutrino k' and the proton P can be used to define the following Lorentz invariant variables:

$$s = (k + P)^2 \quad (1.1)$$

$$Q^2 = -q^2 = -(k - k')^2 \quad (1.2)$$

$$x = \frac{Q^2}{2P \cdot q} \quad (1.3)$$

$$y = \frac{P \cdot q}{P \cdot k} \quad (1.4)$$

$$W_{\gamma p}^2 = (P + q)^2 \quad (1.5)$$

Here \sqrt{s} is the centre-of-mass energy of the ep system and Q^2 is the virtuality of the exchanged boson, which corresponds to the four-momentum transfer squared from the

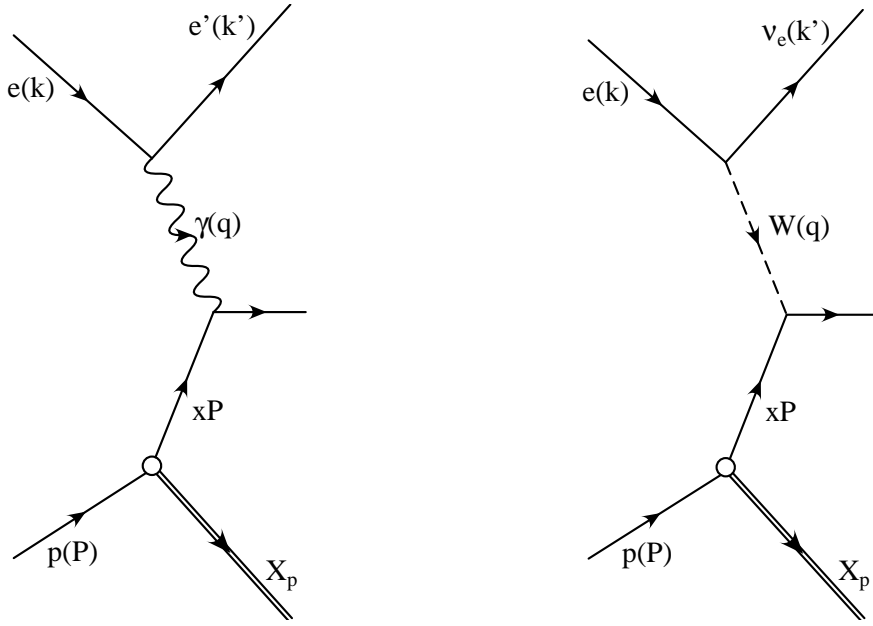


Figure 1.1: ep scattering Feynman diagrams. Left: neutral current photon exchange. Right: charged current exchange.

electron to the proton. At HERA electrons and protons are collided at a centre-of-mass energy \sqrt{s} of 300 GeV and since 1998 of 318 GeV. $W_{\gamma p}$ is the centre-of-mass energy of the γp system and x and y are Björken variables. In the Quark Parton Model (QPM) x describes the relative momentum fraction carried by the scattered parton to the total momentum of the proton. In the proton rest frame y gives the relative energy loss of the electron. x and y have values ranging between 0 and 1.

Only three of these five kinematic variables are independent and therefore three variables are enough to describe the kinematics of the process. Neglecting the masses of the electron and the proton the following relations between these quantities hold:

$$Q^2 = s \cdot x \cdot y \quad (1.6)$$

$$W_{\gamma p}^2 = y \cdot s - Q^2 \quad (1.7)$$

In analogy to optics the possible resolution to probe the internal structure of the proton in the transverse direction depends linearly on the de Broglie wave length λ . The de Broglie wave length is given via $\lambda = h/|q_t|$ where $q_t \sim \sqrt{Q^2}$ is the transverse momentum of the exchanged boson. Large Q^2 thus means high resolution. With the largest possible Q^2 at HERA structures of the size of 10^{-18} m can be investigated.

The ep scattering events are classified by the virtuality Q^2 of the exchanged boson. The regime of small Q^2 is called photoproduction and the regime of large Q^2 , Deep-Inelastic-Scattering (DIS). At the H1 experiment photoproduction events are usually selected by the cut $Q^2 < 1 \text{ GeV}^2$. Moderate DIS events are experimentally often selected by the requirement of $2 \text{ GeV} < Q^2 < 100 \text{ GeV}^2$ and DIS events at high are often selected by Q^2 via $Q^2 > 100 \text{ GeV}^2$. In this analysis events in photoproduction and at moderate Q^2 are considered.

In photoproduction and at moderate Q^2 the charged current process is strongly suppressed, due to the fact that the cross section is proportional to $(1/(Q^2 + M_W^2))^2$, which is very small due to the large mass of the W^\pm boson ($M_W = 80.4 \text{ GeV}/c^2$). The neutral current process is dominated by photon exchange and the corresponding term is proportional to $1/Q^4$. The term due to pure Z exchange is proportional to $(1/(Q^2 + M_Z^2))^2$, which is again strongly suppressed due to the large mass of the Z^0 boson ($M_Z = 91.2 \text{ GeV}/c^2$). There is also a γZ interference term proportional to $1/(Q^2 \cdot (Q^2 + M_Z^2))$. For $Q^2 < 1000 \text{ GeV}^2$ [23] the influence of the interference term can be neglected. At high Q^2 this term leads to destructive interference in the case of e^+p scattering and to a constructive interference in the case of e^-p scattering.

1.2 Differential Cross Sections and Structure Functions

The double differential neutral current cross section (QED) at moderate Q^2 is given by the following formula:

$$\frac{d^2\sigma^{e^\pm p, NC}}{dx dQ^2} = \frac{4\pi\alpha^2}{xQ^4} \cdot \left(y^2 x F_1(x, Q^2) + (1-y) F_2(x, Q^2) \right) \quad (1.8)$$

Here $F_1(x, Q^2)$ and $F_2(x, Q^2)$ indicate the proton structure functions and α is the electromagnetic coupling constant. In the QPM the structure function $F_2(x, Q^2)$ is related to the sum of the quark and antiquark densities $f_{q/p}(x, Q^2)$ and $f_{\bar{q}/p}(x, Q^2)$ according to:

$$F_2(x, Q^2) = x \sum_q e_q \cdot \left(f_{q/p}(x, Q^2) + f_{\bar{q}/p}(x, Q^2) \right) \quad (1.9)$$

e_q indicates the charge of the quark and in the sum all active flavours in the proton have to be considered. $f_{q/p}(x, Q^2)$ or $f_{\bar{q}/p}(x, Q^2)$ is the probability to find a quark (antiquark) with a momentum x at a scale Q^2 in the proton. If the strong forces between the quarks are neglected, the parton densities depend only on x (scaling behaviour), however Quantum Chromodynamics (QCD) leads to scaling violation and the quark densities depend also on Q^2 . This is discussed in detail in the next section.

A photon with a non vanishing virtuality Q^2 can be either transversely or longitudinally polarised, whereas a real photon always has a transverse polarisation. This is a consequence of the gauge invariance of electrodynamics, which is related to the zero-mass of real photons [24]. The corresponding longitudinal structure function $F_L(x, Q^2)$ is defined in the following way:

$$F_L(x, Q^2) = F_2(x, Q^2) - 2x F_1(x, Q^2) \quad (1.10)$$

The ratio of the longitudinal and transversal cross sections, σ_L and σ_T respectively, is:

$$R = \frac{\sigma_L}{\sigma_T} = \frac{F_L(x, Q^2)}{F_2(x, Q^2) - F_L(x, Q^2)} \quad (1.11)$$

and the double differential neutral current cross section can be rewritten as:

$$\frac{d^2\sigma^{e^\pm p, NC}}{dx dQ^2} = \frac{2\pi\alpha^2}{xQ^4} \cdot \left(2 \cdot (1-y) + \frac{y^2}{1+R} \right) \cdot F_2(x, Q^2) \quad (1.12)$$

Due to the y^2 dependence of the second term the longitudinal structure function can lead to sizeable effects only in the regime of large y and only in DIS. Due to angular momentum conservation the longitudinally polarised photons in DIS can interact only with quarks or gluons with a non-negligible transverse momentum. The quarks can obtain such a transverse momentum from gluon radiation or from gluon splitting, which is a consequence of QCD. In the naive QPM the proton consists only of spin 1/2 particles and F_L is zero since the Callan-Gross relation between F_1 and F_2 holds:

$$F_2(x) = 2xF_1(x) \quad (1.13)$$

F_L can be neglected in the kinematic regime important for the analysis presented here, and equation 1.12 reduces to:

$$\frac{d^2\sigma^{e^\pm p, NC}}{dx dQ^2} = \frac{2\pi\alpha^2}{xQ^4} \cdot (2 \cdot (1-y) + y^2) \cdot F_2(x, Q^2) \quad (1.14)$$

In the theory model relevant for this analysis neither the charm nor the beauty quark are active flavours in the proton. Thus the charm F_2^c or beauty contribution F_2^b to the structure function F_2 is more complicated. In particular they depend on the gluon density $f_{g/p}(x, Q^2)$ and this will be explained in section 1.5.

At high Q^2 a further structure function $F_3^{\gamma Z}(x, Q^2) = x \sum_q e_q \cdot a_q \cdot (f_{q/p}(x, Q^2) - f_{\bar{q}/p}(x, Q^2))$ due to the γZ interference term becomes important, which is related to the difference of the quark and antiquark densities. Also the structure function $F_2^Z(x, Q^2) = x \sum_q (v_q^2 + a_q^2) \cdot (f_{q/p}(x, Q^2) + f_{\bar{q}/p}(x, Q^2))$ for Z exchange has to be taken into account. v_q and a_q denote here the vector or axial-vector couplings of the quarks respectively. Since in this thesis only photoproduction or moderate DIS events are selected $F_3^{\gamma Z}$ and F_2^Z can be neglected.

1.3 QCD Framework

In QCD the strong interaction is mediated by gluons and the charge of the strong interaction is the colour (red, green, blue). Quarks carry colour and interact via the exchange of gluons (which also carry colour). In contrast to Quantum Electrodynamics (QED) the strong interaction is non-Abelian and the gluons can couple also to each other.

1.3.1 The Strong Coupling Constant α_s

In perturbative QCD (pQCD) cross sections can be computed as a power series in the strong coupling constant α_s . To leading order no internal loops contribute but at higher orders each observable receives additional contributions from loop diagrams, such as those shown in figure 1.2.

Due to the gluon self interaction in addition to the fermion loop also pure gluon loops exist. This leads to a different behaviour of the strong coupling with increasing scale Q^2 compared to QED. In QED, where only the fermion loop contributes, the charge is screened by e^-e^+ pairs at small Q^2 (low resolution). At high Q^2 (high resolution) the charge is however large and the electromagnetic coupling constant α increases slightly

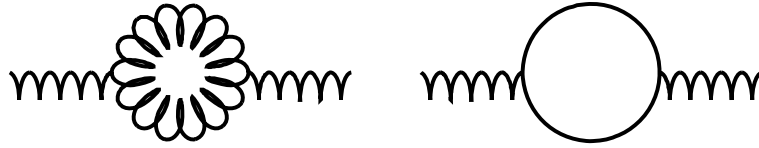


Figure 1.2: *Examples for loops in QCD. Left: gluon loop. Right: fermion loop*

with Q^2 . The fermion loop in QCD leads to the same result but the gluon loop results in an additional anti-screening. The charge is spread out by the gluons and the charge is small at large Q^2 (high resolution). For $Q^2 \rightarrow \infty$ the quarks are quasi-free, a property which is referred to as asymptotic freedom. In the other case $Q^2 \rightarrow 0$, α_s becomes large and perturbative QCD is not applicable anymore (confinement).

To calculate the contributions from a particular loop an integration over all particle momenta p in the loop has to be performed. The upper limit $p \rightarrow \infty$ leads to ultraviolet (UV) divergences, however in a renormalisation procedure these divergences are absorbed in the **running of the strong coupling constant** and an arbitrary renormalisation scale μ_R is introduced. μ_R can be regarded as the momentum at which the subtraction, which removes the divergences, is performed. The scale μ_R is arbitrary, a physical observable R (calculated to all orders of α_s) has to be independent of μ_R . Mathematically this requirement is expressed in the renormalisation group equation (RGE):

$$\mu_R^2 \frac{dR}{d\mu_R^2} = \mu_R^2 \frac{\partial R}{\partial \mu_R^2} + \mu_R^2 \frac{\partial \alpha_s}{\partial \mu_R^2} \frac{\partial R}{\partial \alpha_s} = 0 \quad (1.15)$$

The differential equation can be written as a power series in $\alpha_s(\mu_R^2)$ and so-called β functions, which can be calculated in QCD (loop corrections) as follows:

$$\mu_R^2 \frac{\partial \alpha_s}{\partial \mu_R^2} = \alpha_s \beta(\alpha_s) = -\beta_0 \alpha_s^2 - \beta_1 \alpha_s^3 - \text{higher order terms} \quad (1.16)$$

with

$$\begin{aligned} \beta_0 &= 11 - \frac{2}{3} \cdot n_f \\ \beta_1 &= 102 - \frac{38}{3} \cdot n_f \end{aligned}$$

Here n_f indicates the number of active flavours. In the one loop approximation, i.e. considering only the term β_0 , the following expression for α_s is obtained:

$$\alpha_s(\mu_R^2) = \frac{1}{b \cdot \ln\left(\frac{\mu_R^2}{\Lambda_{QCD}^2}\right)} \quad (1.17)$$

Here b is defined by $b = \beta_0/4\pi$. Λ_{QCD} is the scale where α_s gets large and the perturbative series in α_s no longer converges and thus pQCD is not applicable anymore. The value of Λ_{QCD} is determined experimentally to be about 200 MeV. It has become customary however to specify α_s at the scale of the Z^0 mass instead of using Λ_{QCD} as a reference scale. The experimental result is $\alpha_s(M_Z) = 0.119 \pm 0.004$ [25].

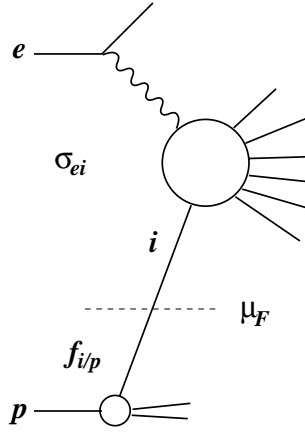


Figure 1.3: *Illustration of the factorisation principle. The factorisation scale cut μ_F distinguishes between 'short distance' ($\mu > \mu_F$) and 'long distance' ($\mu < \mu_F$) physics*

1.3.2 Factorisation

Apart from the ultra violet divergences considered above, also infrared divergences appear in QCD. They are again a consequence of the behaviour of the strong coupling constant α_s . In the soft regime, at small scales μ^2 ("long" distance physics), α_s is large (see figure 1.3). This leads to divergences i.e. for $k_T \rightarrow 0$ (almost collinear gluon radiation) due to $d\sigma/dk_T^2 \sim 1/k_T^2$. Here k_T is the transverse momentum of the emitted gluon. In the integral over k_T the introduction of an artificial regulator μ_F (a lower limit cut-off) is needed to avoid these divergences. The scale μ_F corresponds to the non-perturbative scale, where pQCD breaks down. In analogy to the ultra violet divergences, where the divergences were absorbed in the running of the charge or coupling, the singularities here are absorbed into the parton densities. This leads to a **running of the parton densities** $f_{i/p}(x, \mu_F^2)$. They are called renormalised parton densities. For all processes at a large scale $\mu^2 > \mu_F^2$ pQCD is applicable due to a small α_s and the soft processes with $\mu^2 \leq \mu_F^2$ are absorbed in the renormalised parton densities. Such separation in 'soft' and 'hard' processes is called factorisation and μ_F is therefore called factorisation scale. The principle of factorisation is sketched in figure 1.3.

Factorisation provides a rule how to treat the singularities but the treatment of the finite terms is arbitrary. The factorisation scheme, however, determines how much of these finite terms is factorised into the renormalised quark distributions. In the DIS scheme all finite contributions are absorbed in the quark distributions and F_2 is given by $F_2 = x \sum_{q, \bar{q}} e_q \cdot f_{q/p}(x, \mu^2)$ (equation 1.9). In the more common \overline{MS} scheme only one finite term is absorbed in the quark distributions in addition to the divergent part and the formula for F_2 is modified.

In general the ep cross section is the convolution of the renormalised parton density function $f_{i/p}(x, \mu_F^2)$, depending on the factorisation scale μ_F , and the hard boson parton cross section $\hat{\sigma}_i(\hat{s}, \alpha_s(\mu_R), \mu_R, \mu_F)$, which is calculable in pQCD:

$$d\sigma(ep \rightarrow e'X) = \sum_{\text{partons}} \int_0^1 dx f_{i/p}(x, \mu_F^2) \cdot d\hat{\sigma}_i(\hat{s}, \alpha_s(\mu_R), \mu_R, \mu_F) \quad (1.18)$$

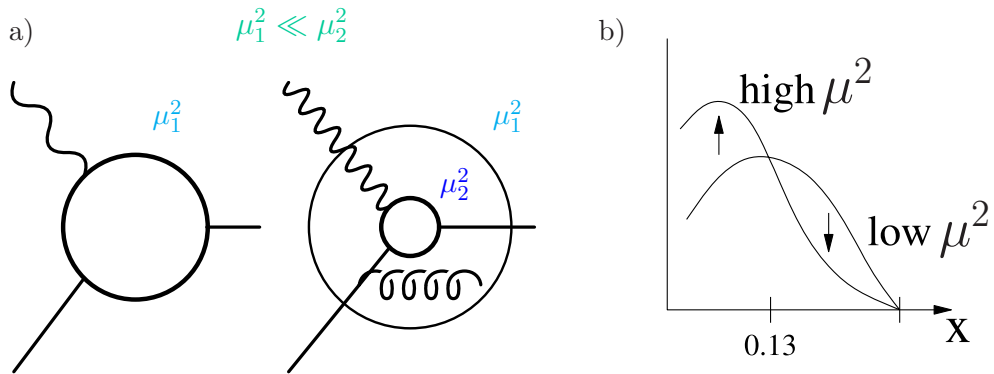


Figure 1.4: a) Resolution of the p structure at different scales μ^2 . At large scales small structures are resolved and the probability is large that the photon probes a quark, which has already emitted a gluon or which comes from gluon splitting. b) Quark density distributions at different scales.

The factorisation theorem states, that the renormalised parton density functions are universal and depend only on the hadron type. Therefore it should be possible to use the parton densities of the proton, which were determined at HERA, to study all kinds of collisions involving protons, for example at the TEVATRON or later at the LHC.

1.3.3 Parton Densities and Evolution Models

The renormalised parton densities contain the soft processes up to the factorisation scale μ_F^2 , like for example gluon radiation and gluon splitting. Therefore the parton densities depend on a scale. In DIS events a common choice for μ_F^2 is Q^2 . For events with heavy quarks this choice of μ_F^2 is modified, since the mass of the heavy quarks is also large and can act as a scale (see section 1.5). This dependence of the parton densities on a scale can be understood by considering that at large scales small structures are resolved and the probability is large that the photon probes a quark, which has already emitted a gluon or which comes from gluon splitting (see figure 1.4 a). In these cases however the momentum of the quark is smaller than the momentum of the original parton in the proton. The quark densities therefore, with increasing scale μ^2 , become progressively larger at small x and progressively smaller at small x (figure 1.4 b)).

The theory provides no fundamental prediction for the parton densities. However, if the parton densities are known at an arbitrary scale μ_0^2 it is possible to determine the parton densities at any other scale μ^2 using the QCD evolution equations. Various different evolution equations have been determined: DGLAP (**D**okshitzer, **G**ribov, **L**ipatov, **A**ltarelli **P**arisi) [19], BFKL (**B**alitsky, **F**adin, **K**uraev, **L**ipatov) [26, 27] and CCFM (**C**atani, **C**iafaloni, **F**iorani, **M**archesini) [20, 21]. The initial parton densities are provided by experimental measurements. A good introduction into the DGLAP and BFKL evolution approach can be found in [28, 29].

The evolution approaches consider all the processes shown in figure 1.5 (gluon radiation and gluon splitting). The splitting functions $P_{ij}(z)$ give the probability, that a parton j with a particular four-momentum k and a longitudinal momentum fraction x , radiates a parton of a momentum fraction $(1 - z)x$ and continues as a parton i with a momentum

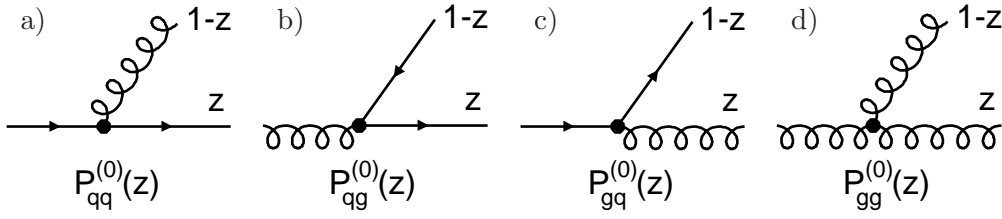


Figure 1.5: *Gluon radiation and splitting processes and definition of the Altarelli Parisi splitting functions.*

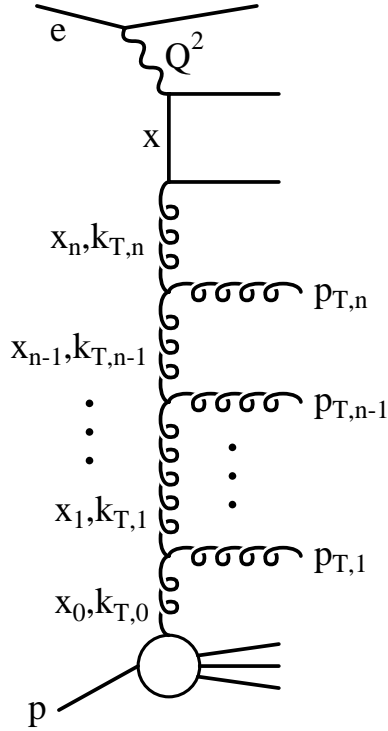
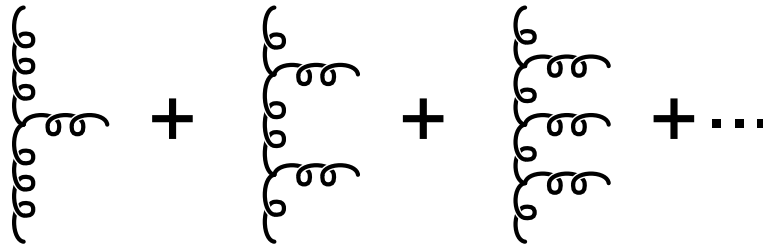


Figure 1.6: *General gluon ladder.*

fraction zx . In the case shown in figure 1.5 a) the differential cross section $d\sigma_{q \rightarrow qg}/dk^2$ for a quark radiating a gluon depends on $1/k^2$ and a singularity occurs for $k^2 \rightarrow 0$. In the case shown in figure 1.5 d), where a gluon splits into two gluons, two singularities occur, again one for $k^2 \rightarrow 0$ and another for $z \rightarrow 0$. The differential cross section here is proportional to $1/k^2 \cdot 1/z$ but has further finite terms. The three evolution approaches handle these singularities differently.

In the **DGLAP approach** the evolution of the parton densities is performed in k^2 and holds for large scales μ^2 and for moderate Bjørken x . Here the assumption is, that the emission of gluons, i.e. the parton ladder, is strongly ordered in k^2 . This implies also a strong ordering in the squared transverse momentum k_T^2 of the emitting particle or the squared transverse momentum p_T^2 of the emitted parton. The leading contribution is proportional to $1/k^2$. This is because k^2 of the parton before the emission is assumed to be much smaller than after the emission (see figure 1.6). The integration of such a term

Figure 1.7: *Summation of all considered gluon ladders.*

leads to $\ln(\mu^2)$ terms which have to be summed up to all orders giving a term of the form $\sum A_n(\ln(\mu^2))^n$. Not only the radiation of one gluon is important, but also the radiation of two or three or n gluons have to be considered (see figure 1.7). Within this approach the DGLAP evolution equations are given by:

$$\frac{\partial f_{q_j/p}(x, \mu^2)}{\partial \ln(\mu^2)} = \int_x^1 \frac{dz}{z} \frac{\alpha_s}{2\pi} \left(\hat{P}_{qq}(z) f_{q_j/p}\left(\frac{x}{z}, \mu^2\right) + \hat{P}_{qg}g\left(\frac{x}{z}, \mu^2\right) \right) \quad (1.19)$$

$$\frac{\partial g(x, \mu^2)}{\partial \ln(\mu^2)} = \sum_{q, \bar{q}} \int_x^1 \frac{dz}{z} \frac{\alpha_s}{2\pi} \left(\hat{P}_{gg}(z) g\left(\frac{x}{z}, \mu^2\right) + \hat{P}_{gq} f_{q_j/p}\left(\frac{x}{z}, \mu^2\right) \right) \quad (1.20)$$

In the **BFKL model** the evolution is performed in x and holds for moderate μ^2 and small x . In this regime the assumption is, that the momentum fraction z carried by the parton after the emission is very small. Thus the leading contribution is the $1/z$ term. This leads to a resummation of $\ln(1/x)$ terms. In contrast to the DGLAP case here the virtuality of the partons in the ladder is unordered and the virtuality k^2 of the initial parton is not negligible in comparison to the virtuality k'^2 of the parton after the emission. Thus the splitting functions in the BFKL case are more complicated. Also the factorisation theorem becomes more complicated. The hard scattering cross section has to be calculated off-shell, which means that the virtuality of the parton, which enters into the hard cross section, cannot be neglected, as done in the case for the DGLAP evolution. This is called k_T -factorisation compared to the collinear factorisation in case of the DGLAP evolution approach (hard cross section is calculated on-shell). In the BFKL model only gluons are considered initial partons, because at small x this is the dominant contribution. The gluon density depends on k_T^2 and on x . The gluon density within the BFKL approach $\mathcal{F}(x, k_T^2, \mu_0^2)$ can be related to the conventional DGLAP gluon density $g(x, \mu^2)$ as follows:

$$xg(x, \mu^2) \simeq \int_0^{\mu^2} \mathcal{F}(x, k_T^2, \mu_0^2) \frac{dk_T^2}{k_T^2} \quad (1.21)$$

The **CCFM model** can be related to both of the above approaches. In the case of large μ^2 and moderate x the CCFM model is equivalent to the DGLAP approach and in the case of small x and moderate μ^2 it is equivalent to the BFKL approach. Here a resummation of both possible singular terms in z as well as in k^2 is performed without requiring a strong ordering in k_T^2 . In analogy to the BFKL approach the omitted assumption of a strong k_T ordering leads to a hard cross section, which depends on k_T (k_T factorisation). Gluon emission is only allowed in a region of increasing emission angle (to account for colour coherence effects), thus leading to an evolution in angle. This is illustrated in figure 1.8.

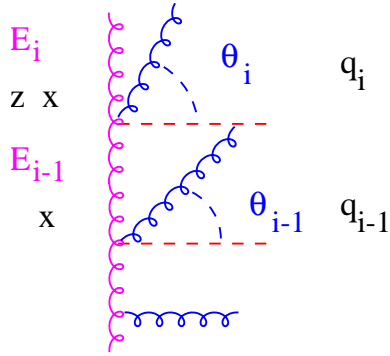


Figure 1.8: *Illustration of the angular ordering of emitted gluons in the CCFM evolution model.*

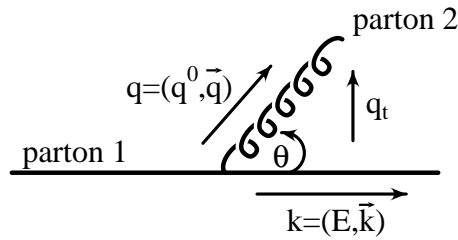


Figure 1.9: *Emission of a gluon (parton 2) from parton 1.*

In this approach the gluon density $\mathcal{A}(x_g, k_T, \vec{q}'_t)$ has apart from x_g and k_T an additional dependence on the maximum angle allowed for any emission, which corresponds to the factorisation scale μ_F^2 . The gluon density in this approach is called unintegrated gluon density.

All these approaches give a good description of the structure function F_2 at small x . However, the description of the hadronic final state is less satisfactory. For example forward jet data [22] can not be described by the DGLAP approach, whereas the BFKL and the CCFM model give a much better description. Also in the heavy quark sector there are some problems with the DGLAP formalism: In the case of charm photoproduction the Next-to-leading order (NLO) calculations do not describe all aspects observed in the D^* data [7, 30, 14, 31, 15]. The first b -measurements [5, 6] were about a factor 3-5 above the NLO calculations, while in more recent b -measurements [7, 8] in the visible range better agreement is observed.

Since in this analysis the unintegrated gluon density as used in the CCFM model will be determined, the CCFM formalism is described in more detail in the next section.

1.3.4 CCFM Equation

In this section the CCFM formalism [32, 33, 34] is treated in more detail. The CCFM model is based on the angular ordering of emitted gluons. First a simplified picture [35] to understand the angular ordering qualitatively is given using the uncertainty principle.

Consider first the evolution of a gluon ladder. First an initial parton 1 emits a gluon (parton 2), as indicated in figure 1.9. The lifetime Δt of the two parton system is given

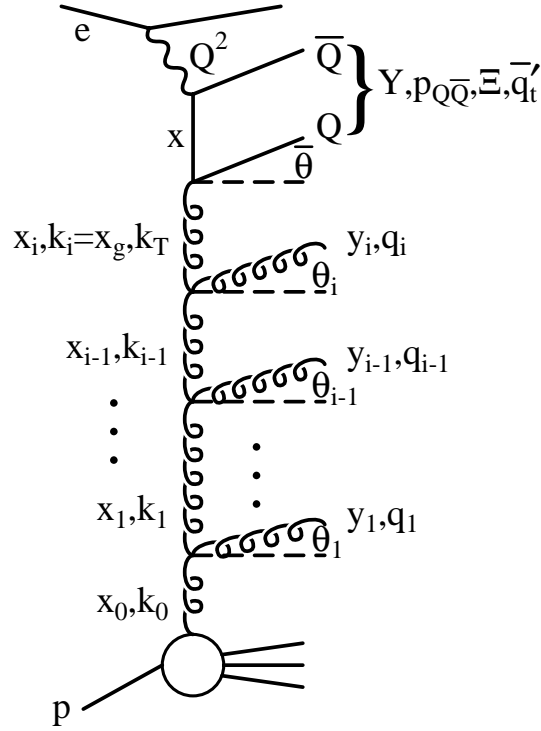


Figure 1.10: CCFM gluon ladder.

by the change of energy ΔE . For simplification a fast initial parton is considered. The initial massless system - parton 1 - has after the gluon emission acquired a mass M given by:

$$M^2 = (q + k)^2 = 2Eq^0(1 - \cos \theta) \approx 2Eq^0 \left(1 - \left(1 - \frac{\theta^2}{2} \right) \right) = Eq^0\theta^2 \quad (1.22)$$

The change of the energy of the two parton system in the rest frame ΔE^* is given by the mass M of the system. To get the change of energy in the laboratory system ΔE the time dilation factor $\gamma \approx E/M$ has to be considered, which yields the following formula for the lifetime of the two parton system in the laboratory system:

$$\Delta t = \frac{1}{\Delta E} = \gamma \cdot \frac{1}{\Delta E^*} = \frac{E}{M} \cdot \frac{1}{M} = \frac{E}{q^0 E \theta^2} = \frac{1}{q^0 \theta^2} \quad (1.23)$$

The lifetime of further gluon emissions - emission and reabsorption processes - has to be smaller than the previous lifetime of the two parton system. Otherwise no gluon ladder would arise. This leads to the following requirement for a gluon ladder:

$$\Delta t_1 > \Delta t_2 > \Delta t_3 > \dots \quad (1.24)$$

Due to equation 1.23 this is related to

$$\theta_1^2 < \theta_2^2 < \theta_3^2 < \dots \Rightarrow \theta_1 < \theta_2 < \theta_3 < \dots \quad (1.25)$$

Hence, the evolution of a gluon ladder can be related to as angular ordering.

A schematic figure of a gluon ladder in the CCFM model is shown in figure 1.10. The “internal” gluons have the four-momenta $k_i = (E_i, \vec{k}_i)$ and the emitted gluons $q_i =$

$(q_i^0, q_i^1, q_i^2, q_i^3)$. Here x_i (y_i) gives the relative momentum fraction of the initial gluon i (emitted gluon i) to the proton momentum in systems, in which the initial gluon has no transverse momentum. z_i gives the momentum reduction of the i -th initial parton for the i -th gluon emission:

$$x_i = z_i \cdot x_{i-1} \quad (1.26)$$

The four-momentum q_i of the i -th emitted gluon can be written in the following form (Sudakov decomposition):

$$q_i = (q_i^0, \vec{q}) = y_i \cdot (P + \xi_i k) + q_{t,i} \quad , \text{ where } y_i = (1 - z_i) \cdot x_{i-1} \quad (1.27)$$

Here $P = (E_p, 0, 0, E_p)$ indicates the four-momentum of the proton, $k = (E_e, 0, 0, -E_e)$ the four-momentum of the incoming electron and $q_{t,i} = (0, q_i^1, q_i^2, 0) = (0, \vec{q}_{t,i})$ is the transverse momentum of the i -th emitted gluon, which is orthogonal to P and k . The emitted gluons are assumed to be massless ($q_i^2 = 0$) and this leads to the equation ($s \approx 2Pk$):

$$\xi_i = \frac{\vec{q}_{t,i}^2}{s y_i^2} \quad (1.28)$$

The relative momentum fraction of the emitted gluon y_i can be obtained from the following consideration:

$$\begin{aligned} q_i^0 &= y_i E_p + y_i \xi_i E_e \\ q_i^3 &= y_i E_p - y_i \xi_i E_e \end{aligned}$$

which leads to

$$y_i = \frac{q_i^0 + q_i^3}{2E_p} \quad (1.29)$$

Furthermore it is possible to express the variable ξ_i in terms of the rapidity $\hat{y}_i = 1/2 \ln((q_i^0 + q_i^3)/(q_i^0 - q_i^3)) = -\ln(\tan \theta_i/2)$ of the i -th emitted gluon and thereby the angle θ_i of the i -th emitted gluon with respect to the proton flight direction. The latter equality holds because the emitted gluons are assumed to be massless:

$$\begin{aligned} q_i^0 + q_i^3 &= 2y_i E_p \\ q_i^0 - q_i^3 &= 2y_i \xi_i E_e \\ \Rightarrow \xi_i &= \frac{E_p}{E_e} \cdot \exp(-2\hat{y}_i) \end{aligned} \quad (1.30)$$

$$\xi_i = \frac{E_p}{E_e} \cdot \tan^2 \left(\frac{\theta_i}{2} \right) \quad (1.31)$$

In the ep rest frame equation 1.30 reduces to:

$$\xi_i = \exp(-2\hat{y}_i) = \tan^2 \left(\frac{\theta_i}{2} \right) \quad (1.32)$$

In the particular case of quark pair production (for example a heavy quark pair, see figure 1.10) the four-momentum of the quark pair can be written analogous to that of the emitted gluons (equation 1.27) in form of the Sudakov decomposition:

$$p_{Q\bar{Q}} = p_Q + p_{\bar{Q}} = Y(P + \Xi k) + p_{t,Q\bar{Q}} \quad (1.33)$$

Here $p_{Q\bar{Q}} = (E_{Q\bar{Q}}, p_{x,Q\bar{Q}}, p_{y,Q\bar{Q}}, p_{z,Q\bar{Q}})$ is the four-momentum of the quark pair and $p_{t,Q\bar{Q}} = (0, p_{x,Q\bar{Q}}, p_{y,Q\bar{Q}}, 0)$ the transverse momentum of the quark pair. Again the transverse momentum is orthogonal to the four-momentum of the proton and the incoming electron. With $p_{Q\bar{Q}}^2 = M_{Q\bar{Q}}^2$ the following formula is obtained for Ξ :

$$\Xi = \frac{M_{Q\bar{Q}}^2 + \vec{p}_{t,Q\bar{Q}}^2}{sY^2} \quad (1.34)$$

In analogy to y_i (equation 1.29), one obtains for Y :

$$Y = \frac{E_{Q\bar{Q}} + p_{Q\bar{Q},z}}{2E_p} \quad (1.35)$$

In a similar way as for emitted gluons, Ξ can be expressed in terms of the rapidity $\hat{y}_{Q\bar{Q}} = 1/2 \ln((E_{Q\bar{Q}} + p_{Q\bar{Q},z})/(E_{Q\bar{Q}} - p_{Q\bar{Q},z}))$ of the quark pair:

$$\Xi = \frac{E_p}{E_e} \cdot \exp(-2\hat{y}_{Q\bar{Q}}) \quad (1.36)$$

Due to colour coherence, gluon emissions are only possible in an angular ordered region of phase space, i.e. increasing angles: $\theta_i < \theta_{i+1}$. In the CCFM model this is expressed via an ordering in ξ (see equation 1.31):

$$\xi_0 < \xi_1 < \dots < \xi_i < \xi_{i+1} < \dots < \Xi \quad (1.37)$$

In the theory a so-called scaled transverse momentum often is related to the transverse momentum vector of the i -th emitted gluon:

$$q'_{t,i} = \frac{|\vec{q}_{t,i}|}{1 - z_i} \quad (1.38)$$

This scaled transverse momentum $q'_{t,i}$ can be related to x_i using equations 1.28 and 1.27:

$$q'_{t,i} = x_{i-1} \sqrt{s\xi_i} \quad (1.39)$$

Using equations 1.26 and 1.38 the angular ordering of equation 1.37 can be rewritten as:

$$q'_{t,i} > z_{i-1} q'_{t,i-1} \quad (1.40)$$

The maximal possible q'_t is therefore obtained from the maximal possible Ξ and x_{i-1} then corresponds to the x of the gluon at the quark box (top of figure 1.10), indicated here as x_g :

$$\vec{q}'_t = x_g \cdot \sqrt{s\xi} \quad (1.41)$$

In the DGLAP approach the evolution is performed for moderate z_i and with a strong k_T ordering. This is equivalent to an evolution in $|\vec{q}'_t| = p_T$. Due to equation 1.38 this implies also a q'_t ordering and thus DGLAP also implies an angular ordering. In addition the requirement given in equation 1.40 gives for small z no restriction for $|\vec{q}'_t|$ and therefore also no in k_T , equivalent to what the BFKL model requires, which holds in the limit of small z and the evolution in k_T is arbitrary. Thus the CCFM model provides a way to unify the DGLAP and BFKL evolution models.

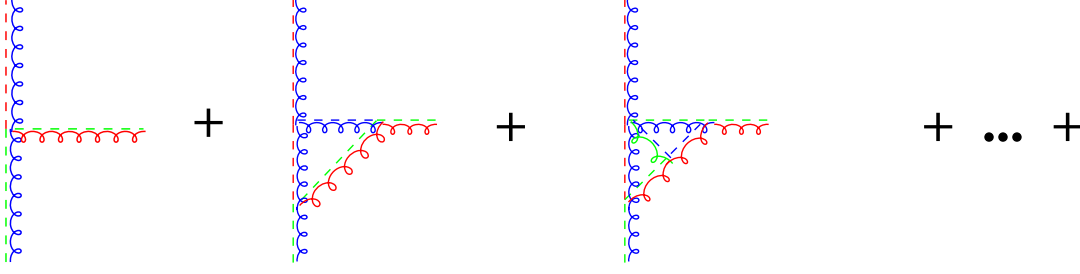


Figure 1.11: *Contributions of the non-Sudakov form factor.*

In the CCFM model the gluon density $\mathcal{A}(x_g, k_T, \bar{q}'_t)$ depends on three quantities x_g , k_T and \bar{q}'_t . In the model \bar{q}'_t serves as the factorisation scale and corresponds to the maximal allowed angle for any gluon emission.

The integral form of the CCFM evolution equation can be written as:

$$\mathcal{A}(x, k_T, \bar{q}'_t) = \mathcal{A}_0(x, k_T, \bar{q}'_t) + \int \frac{dz}{z} \int \frac{dq'_t}{q'_t} \Theta(\bar{q}'_t - zq'_t) \cdot \Delta_S(\bar{q}'_t, zq'_t) \tilde{P}(z, q'_t, k_T) \mathcal{A}\left(\frac{x}{z}, k'_T, q'_t\right) \quad (1.42)$$

Θ is the step function and is equal to one for values above zero and equal to zero for values below zero. The first term describes all paths without branching and the second considers evolution paths, which have their last branching at zq'_t . Δ_S is the Sudakov form factor:

$$\Delta_S(\mu^2) = \exp\left(-\int_{\mu_0^2}^{\mu^2} \frac{d\mu'^2}{\mu'^2} \int dz \frac{\alpha_s}{2\pi} \tilde{P}(z)\right) \quad (1.43)$$

\tilde{P} is the gluon splitting function in the CCFM model. In the evolution only gluons are considered. In the CCFM splitting function usually only the leading terms are considered, i.e.:

$$\tilde{P} = \frac{\bar{\alpha}_s(q_t^2)}{1-z} + \frac{\bar{\alpha}_s(k_T^2)}{z} \Delta_{ns}(z, q_t'^2, k_T^2) \quad (1.44)$$

Here the non-Sudakov form factor Δ_{ns} is defined by:

$$\log \Delta_{ns} = -\bar{\alpha}_s(k_T^2) \int_0^1 \frac{dz'}{z'} \int \frac{dq'_t}{q'_t} \Theta(k_T - q'_t) \Theta(q'_t - z'q_t) \quad (1.45)$$

The non-Sudakov form factor considers virtual contributions such as those shown in figure 1.11. The differential form of the CCFM evolution equation is given by [36, 34]:

$$\bar{q}'_t \frac{d}{d\bar{q}'_t{}^2} \frac{x\mathcal{A}(x, k_T, \bar{q}'_t)}{\Delta_S(\bar{q}'_t, \mu_0)} = \int dz \frac{d\phi}{2\pi} \frac{\tilde{P}(z, \bar{q}'_t/z, k_T)}{\Delta_S(\bar{q}'_t, \mu_0)} x' \mathcal{A}(x', k'_T, \frac{\bar{q}'_t}{z}) \quad (1.46)$$

The x' and k'_T are the momentum fraction and the transverse momentum before the last gluon emission.

Due to the absence of a strong k_T ordering in the CCFM model and also in the BFKL model, the k_T of the gluon can have values, which belong in the soft physics regime (the value can be lower than the k_T of the initial parton, see figure 1.12). This leads to the important consideration of when the gluon splitting is considered as hard and when it is a soft physics process. The choice of the a k_T -cut has a strong influence on the unintegrated

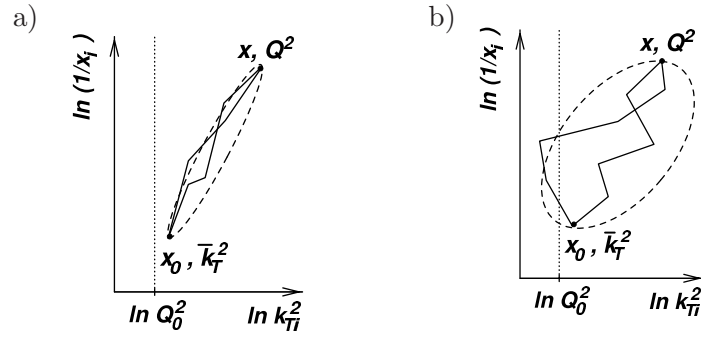


Figure 1.12: Comparison of evolution paths in the DGLAP a) and CCFM approach b).

gluon density. The largest differences between the different k_T -cut choices occur for small k_T up to 1 or 2 GeV². A factor 2-3 at low x_g is obtained [37].

Further changes to the gluon density arise when the non-singular terms in the splitting functions are included and when $\bar{\alpha}_s(q_t^2)$ instead of $\bar{\alpha}_s(k_T^2)$ is used in the second term of the splitting function equation (equation 1.44) and in the non-Sudakov form factor equation (equation 1.45).

Until now the unintegrated gluon density has only implicit experimental constraints in k_T and \bar{q}_t' from F_2 data [38, 39, 37]. By using $D^*\mu$ correlations to tag both heavy quarks it is possible to reconstruct $\bar{q}_t'(D^*\mu)$, $x_g(D^*\mu)$ and $k_T(D^*\mu)$ from the four-momenta of the two identified particles. An *extraction* of the unintegrated gluon density becomes possible. The detailed procedure will be described in chapter 2.

1.4 Photoproduction

The region of small Q^2 ($Q^2 \rightarrow 0$) is called photoproduction. Here the description of ep scattering events can be simplified by factorising the emission of quasi real photons by the electron from the subsequent interaction of the photon with the proton. In this analysis the photoproduction regime is considered alone and together with moderate DIS events. A flux of photons with an energy distribution $n(y)$ can be calculated, where in this regime the Björken variable y can be interpreted as the energy fraction of the photon relative to the energy of the incoming electron. The ep cross section can be reduced to the γp cross section in the following way:

$$d\sigma_{ep}(y) = \sigma_{\gamma p}(y) \cdot dn(y) \quad (1.47)$$

The photon spectrum $dn(y)$ is obtained using the Weizäcker Williams Approximation (WWA), which neglects the photon virtuality and terms involving the longitudinal photon polarisation. The spectrum of quasi-real photons is integrated over the whole Q^2 range - [Q_{min}^2, Q_{max}^2]:

$$dn(y, Q_{max}^2) = f_{\gamma/e}(y, Q_{max}^2) dy \quad (1.48)$$

Here $f_{\gamma/e}$ is the photon flux, which can be written as:

$$f_{\gamma/e} = \frac{\alpha_{EM}}{2\pi} \left[\frac{1 + (1-y)^2}{y} \log \left(\frac{Q_{max}^2}{Q_{min}^2} \right) - 2m_e^2 y \left(\frac{1}{Q_{min}^2} - \frac{1}{Q_{max}^2} \right) \right] \quad (1.49)$$

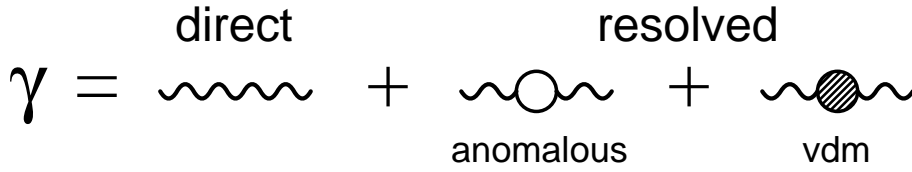


Figure 1.13: *Different states of a quasi real photon [41].*

α_{EM} denotes the fine structure constant and $Q_{min}^2 = \frac{m_e^2 y}{1-y}$ the kinematic lower limit.

Photoproduction events can be experimentally selected by requiring a scattered electron with a small scattering angle. The electrons can also be found in the electron taggers. In this analysis a photoproduction event is defined with an appropriate anti-tag condition, i.e. outgoing electrons above a given scattering angle θ_c cut are vetoed. For small angles Q_{max}^2 is given by:

$$Q_{max}^2 = Q_{min}^2 + E_e^2(1-y)\theta_c^2 \quad (1.50)$$

For heavy quark production and untagged electrons with $\theta_c < 2.5^\circ$, corrections to the WWA with respect to the exact calculation are at the two percent level for charm production and about 0.25% for beauty production [40]. For tagged photoproduction with $\theta_c < 0.3^\circ$ this approximation is even better.

In addition to DIS events with a large photon virtuality Q^2 , in which the structure of the proton is probed, the structure of the quasi-real photon itself is probed in ep scattering events with $Q^2 \approx 0$. Here the photon can interact directly with the proton as a bare photon: direct photoproduction. But it is also possible that the photon fluctuates into a $q\bar{q}$ state before interacting with the proton (resolved photoproduction). In resolved photoproduction two different cases are often distinguished. In the first case the photon fluctuates into a $q\bar{q}$ without forming a bound hadronic state (anomalous resolved) and in the second case (vdm contribution) the $q\bar{q}$ forms a vector meson with the quantum numbers of the photon, e.g. ρ, ω, ϕ with $J^{PC} = 1^{--}$. The latter case is addressed by the Vector Meson Dominance Model (VDM) [42]. In figure 1.13 the different possible states of the photon are summarised. In this analysis the vdm contribution is irrelevant. As from now only the anomalous resolved contribution is considered.

In case of heavy flavour physics the case where the photon fluctuates into a heavy quark pair ($c\bar{c}$ or $b\bar{b}$), so-called charm or beauty excitation, is important. The other possibility, which leads to contributions in heavy flavour production, is the process, where the photon fluctuates first in a light quark pair and where then one of the quarks emits a gluon. This contribution will be referred to as normal resolved contribution in this analysis. However this contribution is small in the kinematic region of this analysis as will be shown in section 2.4.

In a similar way to the parton densities on the proton side, the probability $f_{q/\gamma}$ of finding a parton within the photon can be defined within the QPM as (only the QED contributions are considered):

$$f_{q/\gamma}(x_\gamma, \mu^2) = e_q^2 \cdot \frac{\alpha_{EM}}{\pi} \left(x_\gamma^2 + (1-x_\gamma)^2 \right) \ln\left(\frac{\mu^2}{m_q^2}\right) \quad (1.51)$$

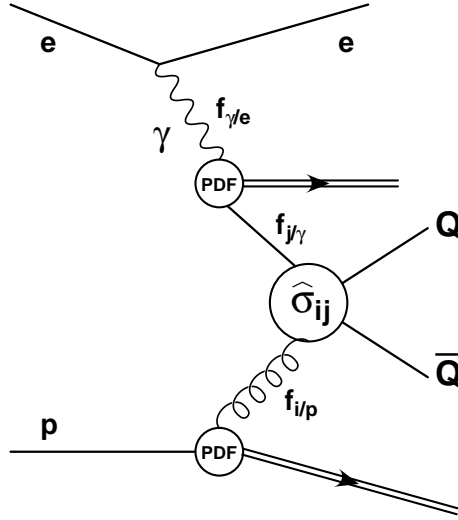


Figure 1.14: *Illustration of the factorisation for heavy quark production in case of photo-production.*

Here x_γ denotes the energy fraction which is carried by the quark relative to the energy of the photon E_γ and m_q is the mass of the free quarks. Summing over all colours n_c and flavours n_f results in the photon structure function F_2^γ :

$$\begin{aligned}
 F_2^\gamma(x_\gamma, \mu^2) &= 2x_\gamma \sum_{n_c, n_f} e_q^2 f_{q/\gamma}(x_\gamma, \mu^2) \\
 &= 3 \sum_{n_f} e_q^4 \frac{\alpha_{EM}}{\pi} x_\gamma (x_\gamma^2 + (1-x_\gamma)^2) \cdot \ln\left(\frac{\mu^2}{m_q^2}\right) \quad (1.52)
 \end{aligned}$$

The quark charge e_q contributes to the fourth power in F_2^γ in contrast to the quadratic contribution to the hadronic structure functions of the proton in F_2^p . Furthermore F_2^γ increases with increasing energy fraction x_γ of the quark in the photon. F_2^γ depends directly on a scale μ^2 at which it is probed. In F_2^p the scale enters only via the QCD evolution equations. Due to the $\ln(1/m_q^2)$ dependence of F_2^γ the heavy quark contributions (corresponding to charm or beauty resolved excitation) are suppressed compared to the contributions from light quarks.

QCD corrections to the simple QPM photon structure function can be calculated using the DGLAP evolution equations. These equations have a similar form as for the proton parton densities (see equations 1.19 and 1.20). The differ is that an additional term is included to account for the point-like (direct) coupling.

1.5 Heavy Quark Production

At HERA the basic process for producing heavy quarks is boson gluon fusion (figure 1.14). The normal top quark production is not possible due to the large mass of the top quark. Thus heavy quark production in the context of this thesis means always charm and beauty production.

To calculate the heavy quark cross section, the parton distributions of the proton and in case of photoproduction also the photon flux and the parton distributions of the photon have to be known at a scale at which the proton or photon is probed. In the case of photoproduction (γp) the heavy quark production cross section can be written as (see figure 1.14):

$$\sigma^{\gamma p}(ep \rightarrow e'QX) = \sum_{\text{partons}} \int dy \int dx_j \int dx_i f_{\gamma/e}(y, \mu^2) f_{j/\gamma}(x_j, \mu^2) f_{i/p}(x_i, \mu^2) \hat{\sigma}_{ij}(\hat{s}, m_Q, \mu^2) \quad (1.53)$$

Here the capital Q refers to the heavy quarks c or b , $\hat{\sigma}_{ij}$ indicates the hard parton cross section and \hat{s} is the centre-of-mass energy of the two interacting partons i and j . The parton i from the proton p , mainly a gluon, and parton j (in the case of direct photoproduction this is replaced by a photon) from the photon, interact and heavy quarks are produced.

In the case of DIS the ep cross section is related either to the charm or beauty contributions F_2^c and F_2^b respectively of the structure function F_2 . The structure functions are connected to the convolution of the partonic hard cross section $\hat{\sigma}_{\gamma^*i}$ and the parton distribution $f_{i/p}$ of the proton at the probing scale, e.g. $\mu_F^2 = Q^2 + m_Q^2$ (for more details see [43, 44]). Here i indicates a parton out of the proton, which is usually a gluon:

$$\frac{d^2\sigma(ep \rightarrow e'QX)}{dx dQ^2} = \frac{2\pi\alpha^2}{xQ^4} \cdot (2 \cdot (1-y) + y^2) \cdot F_2^Q(x, Q^2, m_Q^2) \quad (1.54)$$

$$F_2^Q(x, Q^2, m_Q^2) = \sum_{\text{parton}} \int_x^{z_{max}} \frac{dz}{z} f_{i/p}\left(\frac{x}{z}, m_Q^2, Q^2\right) \tilde{F}_i(z, Q^2, m_Q^2) \quad \text{with}$$

$$\tilde{F}_i(z, Q^2, m_Q^2) = \frac{Q^2}{4\pi^2\alpha} \left(\hat{\sigma}_{\gamma^*i}^T(\hat{s}, Q^2, m_Q^2) + \hat{\sigma}_{\gamma^*i}^L(\hat{s}, Q^2, m_Q^2) \right) \quad (1.55)$$

Here z denotes the momentum fraction of a gluon after emitting a gluon and z_{max} is given by $z_{max} = Q^2/(\hat{s} + Q^2)$. In Deep-Inelastic-Scattering in addition to the contribution of transversely (T) polarised photons also a contribution from longitudinally (L) polarised photons is present.

In contrast to the light quarks u , d , s , which have masses of the order of Λ_{QCD} , the heavy quarks c , b with masses much larger than Λ_{QCD} cannot be treated for all energies in the same way. In figure 1.15 different regimes for heavy quark production mechanism [45] are shown depending on the scale μ and on the Björken variable x . Heavy quark production at HERA covers mainly the regime with $\mu \approx m_Q$ but the small x regime as well as the high energy regime can be reached. If the total energy of the partonic collision is near threshold and x is moderate, the heavy quarks are treated as heavy objects which do not occur within the proton. The dominant production mechanism in this regime is the so-called flavour creation or boson gluon fusion. At high centre-of-mass energies of the initial colliding particles and moderate x (and thus high energy scales $\mu^2 \gg m_Q^2$) the mass of the heavy quarks c and b are negligible compared to μ^2 and the quarks can be treated in a similar way to the light quarks with zero mass. Therefore the dominant production mechanism in this regime is flavour excitation, where the heavy quark is an active flavour in the proton. At small x the logarithmic terms $\ln(1/x)$ become large and a small x resummation is needed, which is performed for example in the BFKL and CCFM evolution equations but not in the DGLAP approximation. In this regime the heavy

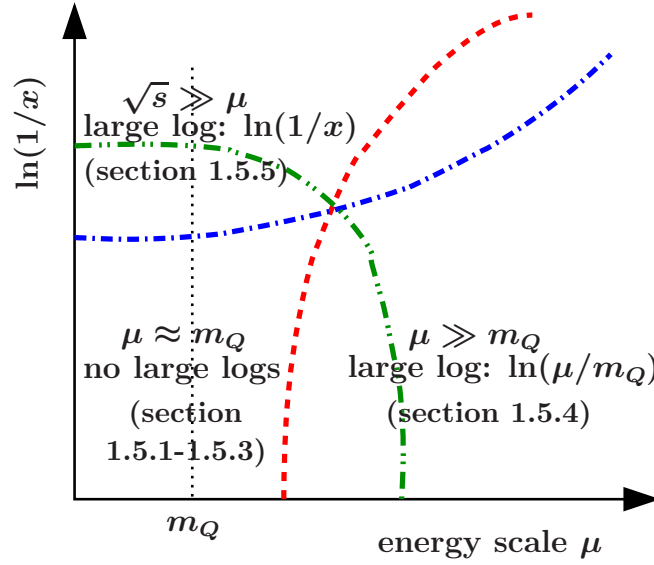


Figure 1.15: Illustration of different regimes of the heavy flavour production depending on the scale μ and the Bjorken variable x . Adopted from [45]

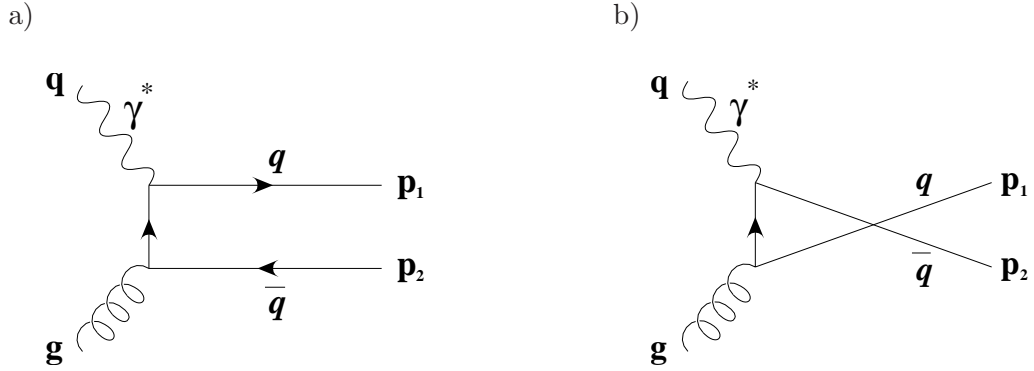


Figure 1.16: Leading order boson gluon fusion Feynman diagrams. Right side: crossed Feynman diagram.

quarks are treated as heavy objects similar to the regime with $\mu \approx m_Q$ and moderate x . The hard cross section depends on k_T in this regime.

At HERA most heavy quarks are produced near the threshold. In this regime the boson gluon fusion (BGF) process is the dominant production mechanism. The leading order diagram is shown in figure 1.16. Here a photon emitted from the incoming electron interacts with a gluon from the proton and a heavy quark pair is produced. The c and b quarks are treated as heavy particles and the calculations are done in the massive scheme.

In the next two sections the LO cross sections are introduced for heavy quark production in photoproduction and DIS within the massive scheme. The NLO calculation within this scheme is introduced in section 1.5.3. In section 1.5.4 the high energy regime is discussed and in section 1.5.5 the small x regime is explained for heavy quarks.

The pair production of charm and beauty in the fragmentation via gluon splitting $g \rightarrow Q\bar{Q}$ is in principle also a possible mechanism. At HERA this production mechanism is

suppressed, because it is in all regimes not the LO contribution but one order higher in α_s than the dominating photon gluon fusion process. This production mechanism is therefore not discussed. At the hadron collider TEVATRON the situation is different. Here the process $gg \rightarrow gQ\bar{Q}$ gives a sizeable contribution to the process $gg \rightarrow Q\bar{Q}$, since the cross section of $gg \rightarrow gg$ is about a factor 100 higher than the cross section $gg \rightarrow Q\bar{Q}$ [46].

1.5.1 LO Photoproduction Cross Section

The differential light flavour creation cross section via boson gluon fusion is given by [47]:

$$\frac{d^2\sigma}{d\hat{t}d\hat{u}} = \frac{\alpha\alpha_S\pi e_q^2}{s^2} \left(\frac{\hat{u}}{\hat{t}} + \frac{\hat{t}}{\hat{u}} \right) \delta(\hat{s} + \hat{t} + \hat{u}) \quad (1.56)$$

Here \hat{s} , \hat{t} and \hat{u} are Mandelstam variables, which are defined for a 2-body $A + B \rightarrow C + D$ reaction as follows:

$$\hat{s} = (p_A + p_B)^2 = (p_C + p_D)^2 \quad (1.57)$$

$$\hat{t} = (p_A - p_C)^2 = (p_B - p_D)^2$$

$$\hat{u} = (p_A - p_D)^2 = (p_B - p_C)^2$$

$$\hat{s} + \hat{t} + \hat{u} + Q^2 = 0 \quad (1.58)$$

In the case of heavy quark production the mass of the quarks is not negligible anymore and equation 1.56 modifies to [45, 47]:

$$\frac{d^2\sigma}{dt_1 du_1} = \frac{\alpha\alpha_S\pi e_q^2}{s^2} \left(\frac{u_1}{t_1} + \frac{t_1}{u_1} + \frac{4m_Q^2\hat{s}}{t_1 u_1} \left(1 - \frac{m_Q^2\hat{s}}{t_1 u_1} \right) \right) \delta(\hat{s} + t_1 + u_1) \quad (1.59)$$

with $t_1 = \hat{t} - m_Q^2$ and $u_1 = \hat{u} - m_Q^2$. After integrating over u_1 and t_1 the total BGF heavy quark production cross section in LO can be written as [45, 47]:

$$\sigma_{\gamma g \rightarrow Q\bar{Q}}(\hat{s}, m_Q^2) = \frac{2\pi\alpha_S(\mu^2)e_q^2}{\hat{s}} \cdot \left(\left(1 + \frac{4m_Q^2}{\hat{s}} - \frac{8m_Q^4}{\hat{s}^2} \right) \cdot \ln \left(\frac{1+\beta}{1-\beta} \right) - \left(1 + \frac{4m_Q^2}{\hat{s}} \right) \cdot \beta \right) \quad (1.60)$$

with $\beta = (1 - 4m_Q^2/\hat{s})^{1/2}$.

In figure 1.17 the total LO order heavy flavour production cross section is shown for c and b production as a function of $\sqrt{\hat{s}}$. The 1-loop values for c and b are chosen for the strong coupling constant: $\alpha_S(m_c^2) = 0.303$ and $\alpha_S(m_b^2) = 0.22$. At threshold there is a strong increase in the cross section but at $\sqrt{\hat{s}} \approx 4$ GeV in case of charm or $\sqrt{\hat{s}} \approx 12$ GeV in case of beauty it falls with increasing $\sqrt{\hat{s}}$. The β -terms in equation 1.60 lead to this threshold behaviour. Due to the smaller quark charge e_q of beauty and the larger quark mass the beauty cross section is about a factor 200 smaller than the charm cross section.

For photoproduction in addition to the direct process discussed above the resolved component also gives a sizeable contribution. The Feynman diagrams of the so called ‘‘normal resolved’’ contribution are shown in figure 1.18 a). Here a gluon or a light quark out of the photon interacts with a parton of the proton. In the resolved component referred to as ‘‘charm or beauty excitation’’ a heavy quark out of the photon takes part in the hard interaction. The different excitation diagrams are shown in figure 1.18 b) and c).

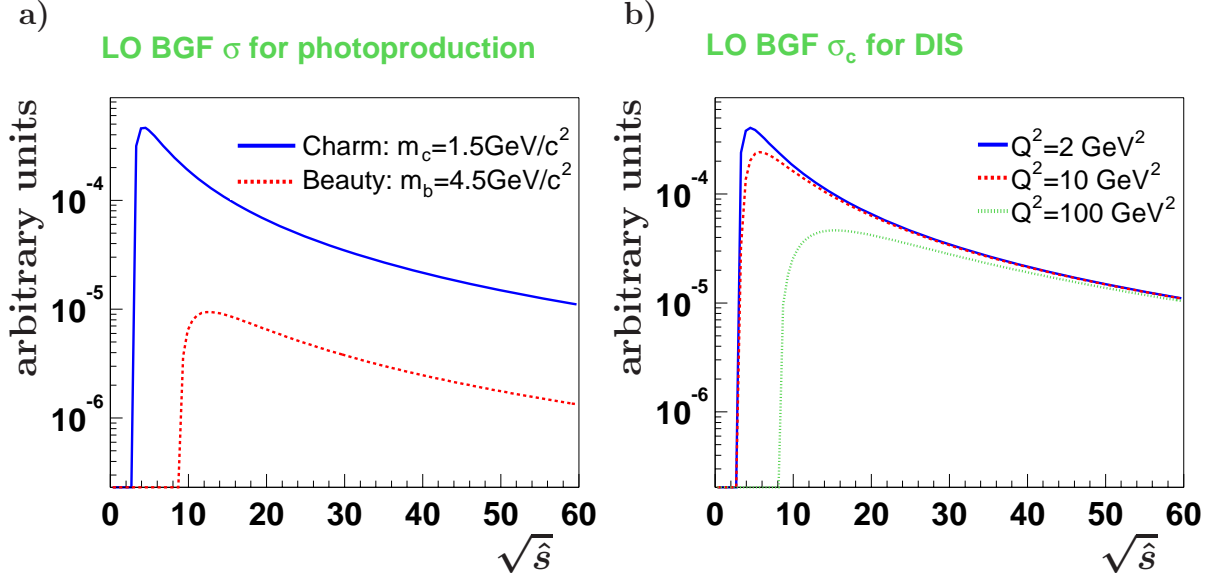


Figure 1.17: LO boson gluon fusion ($\gamma g \rightarrow Q\bar{Q}$) cross section of heavy quarks. The dependence on $\sqrt{\hat{s}}$ ($\hat{s} = x_g x_\gamma y s$) is shown. a) Photoproduction, b) DIS

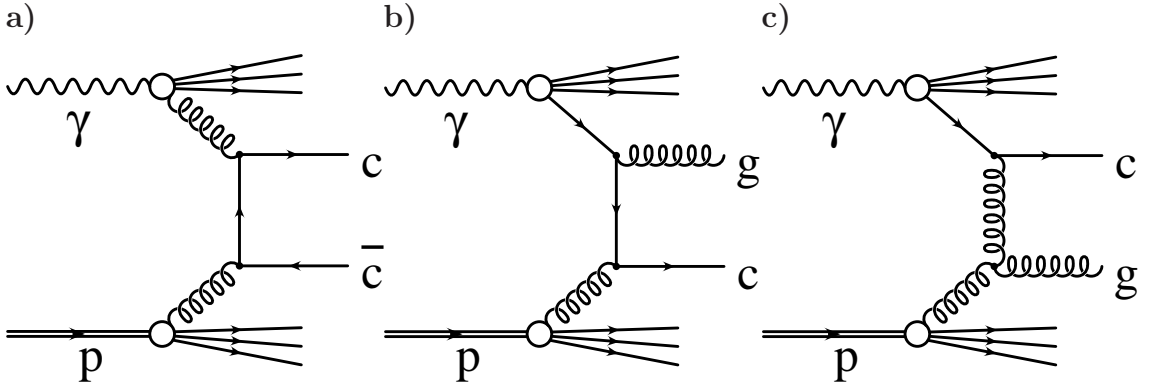


Figure 1.18: Feynman diagrams for the heavy quark production via a resolved photon. a) Normal resolved process. b,c) Charm excitation. Here the photon fluctuates into a $c\bar{c}$ pair, but only one quark takes part in the hard interaction process. Charm excitation via a quark propagator is strongly suppressed compared to the diagram with a gluon propagator.

1.5.2 LO DIS Cross Section

In the case of Deep-Inelastic-Scattering (DIS) events the partonic cross section is characterised by the reaction $\gamma^* g \rightarrow Q\bar{Q}$ and the virtuality of the photon therefore has to be considered. In addition to transversely polarised photons (T) also longitudinally polarised photons (L) could in principle take part in the hard interaction. In DIS the total heavy quark cross sections can be written as [43, 44]:

$$\sigma(\gamma^* g \rightarrow Q\bar{Q})_T = \frac{2\pi\alpha\alpha_s(\mu^2)e_q^2}{\hat{s} + Q^2} \left(\left(\frac{\hat{s}^2 - Q^4}{(\hat{s} + Q^2)^2} + \frac{4m_Q^2\hat{s}}{(\hat{s} + Q^2)^2} - \frac{8m_Q^4}{(\hat{s} + Q^2)^2} \right) \ln\left(\frac{1+\beta}{1-\beta}\right) - \left(\frac{(\hat{s} - Q^2)^2}{(\hat{s} + Q^2)^2} + \frac{4m_Q^2\hat{s}}{(\hat{s} + Q^2)^2} \right) \beta \right) \quad (1.61)$$

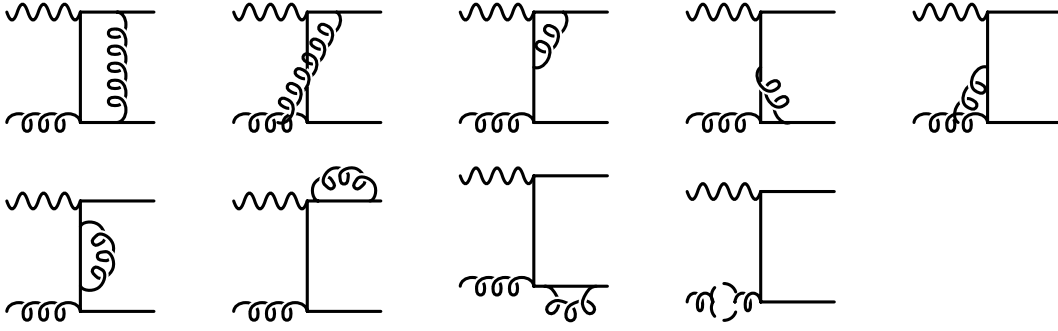


Figure 1.19: *Feynman diagrams of the virtual corrections considered in NLO calculations.*

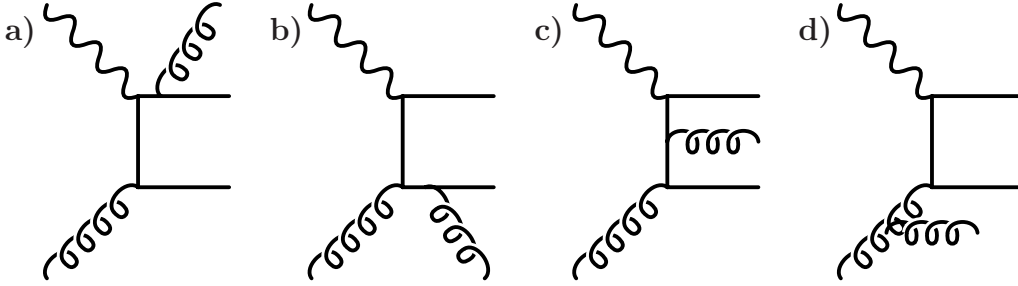


Figure 1.20: *Feynman diagrams of the gluon radiation corrections considered in NLO calculations.*

$$\sigma(\gamma^* g \rightarrow Q\bar{Q})_L = 8\pi\alpha\alpha_s(\mu^2)e_q^2 \cdot \frac{Q^2\hat{s}}{(\hat{s}+Q^2)^3} \left(\beta - \frac{2m_Q^2}{\hat{s}} \ln\left(\frac{1+\beta}{1-\beta}\right) \right)$$

In figure 1.17 b) the total LO BGF cross section is shown for charm production as a function of \hat{s} and for three different values of Q^2 . The cross section decreases strongly towards larger Q^2 . Furthermore the production threshold and the maximum is moved toward larger $\sqrt{\hat{s}}$

1.5.3 NLO

The leading order partonic cross sections have to be convoluted with the appropriate LO parton densities to calculate the hadronic cross sections and inclusive distributions. At LO the scale μ^2 appears only in the lowest order α_S (equation 1.17) and there is no real physical criteria for choosing any particular scale. Large variations in the cross section are obtained when μ^2 is varied.

In Next-to-leading order (NLO) calculations [48, 45] the partonic cross sections have to be convoluted with the appropriate NLO parton densities to calculate the hadronic cross sections. NLO calculations reduce the sensitivity to the scale μ^2 by also taking diagrams of order α_s^2 into account. Especially in the case of charm, which provides at threshold and for low Q^2 only a relatively small scale, α_s is relatively large and the convergence of the perturbation series is not as good as for beauty, which has a large mass. The charm cross section in photoproduction is thus much more sensitive to the mass and the scales than the beauty cross section. In [49] the dependence of the total heavy quark photoproduction

cross section on the mass and the scales, the renormalisation scale (default value $\mu_R^2 = m_Q^2$) as well as the factorisation scale (default values: $\mu_F = 2\mu_R$ for charm and $\mu_F = \mu_R$ for beauty), is investigated in detail. Large deviations between the upper ($m_c = 1.8 \text{ GeV}/c^2$) or lower ($m_c = 1.2 \text{ GeV}/c^2$) mass choice and the central value ($m_c = 1.5 \text{ GeV}/c^2$) of the order of a factor 2 are obtained for the total charm cross section. For beauty production deviations of only the order 20% are obtained for the analogous study, where the central beauty mass of $m_b = 4.75 \text{ GeV}/c^2$ is varied by $\pm 0.25 \text{ GeV}/c^2$. A variation of the renormalisation scale by a factor two in both directions leads for charm to deviations between 60% and 100%. For beauty these deviations are smaller, about 20%. Varying also the factorisation scale by a factor two in both directions an additional uncertainty of about 30% to 40% for charm and about 6% for beauty is obtained. A further uncertainty in the heavy quark photoproduction calculations is caused by the large photon-proton centre-of-mass energies W available. Fixed order calculations become unreliable in certain kinematical regions due to the presence of large radiative effects (small x -region). Potentially large logarithms, $\log(W^2/m_Q^2)$, appear, which spoil the convergence of the perturbative expansion. In this case a resummation to all orders of these large logarithms has to be performed. In [49] the uncertainty arising from such small x -effects was estimated. For the direct charm production cross section an uncertainty of 40% is obtained, while for the beauty production cross section this effect is less dramatic (about 20%). The theoretical predictions are therefore much more reliable for beauty production.

In figure 1.19 Feynman diagrams of the virtual corrections to the LO BGF process are shown and in figure 1.20 the NLO contributions due to gluon radiation are illustrated. Due to the virtual corrections and gluon radiation, ultraviolet, infrared and collinear singularities appear. The ultraviolet divergences are removed by renormalisation (charge and mass), the infrared divergences cancel with loop contributions and the collinear divergences are absorbed into the definition of the parton densities [48, 45]. A consequence of this procedure is the direct dependence of the cross section on the renormalisation scale μ_R and the factorisation scale μ_F . By comparing the NLO diagram figure 1.20 d) with the resolved excitation diagram figure 1.18 c) it is obvious that they describe the same process, thus charm excitation is approximately the same as NLO. In NLO it is not possible to distinguish between direct and resolved processes anymore. For beauty production the contribution of the NLO corrections as well as the contributions of the excitation processes were estimated to be both about 35% of the total photoproduction cross section ($Q^2 < 1$). For charm larger differences between these two corrections, NLO about 35% and excitation about 60%, were obtained (by using the programs, which will be introduced in section 2.2 and 2.3).

Measurements at HERA of charm production are all described relatively well by the theory. But in the b -sector, the picture is somewhat unresolved ($p\bar{p}$: [1, 2, 3, 4], γp : [5, 6, 7, 8], $\gamma\gamma$: [9, 10], ep : [11, 12], eN : [13]). The first b -measurements at HERA [5, 6] were about a factor 3-5 above the NLO calculations, while in more recent HERA b -measurements [7, 8] in the visible range better agreement is observed. In this analysis $D^*\mu$ -events are selected and a separation of charm and beauty production is performed by exploiting the charge and angle correlations between the D^* -meson and the muon. This exclusive analysis makes possible the measurement of the charm and beauty cross section closer to threshold than the previous analyses.

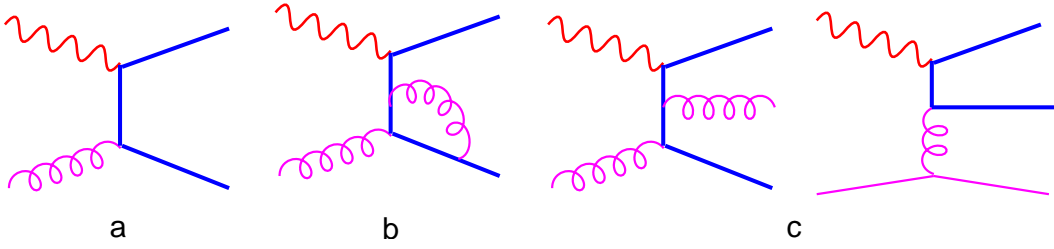


Figure 1.21: *Feynman diagrams of the massive scheme. a) shows the LO contribution, b) an example for a virtual contribution and c) and d) show NLO radiative processes.*

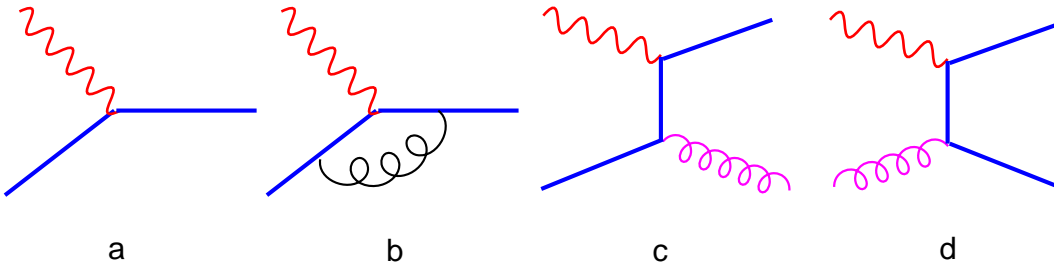


Figure 1.22: *Feynman diagrams of the massless scheme. a) shows the LO contribution, b) an example for a virtual contribution and c) and d) show NLO radiative processes.*

1.5.4 Calculation Schemes

Up to now heavy quark production near threshold has been discussed, where $\mu \sim m_Q$ holds. In this kinematic regime the 3-flavour-fixed-number-scheme (massive scheme) is used. The results of this analysis will be compared with NLO calculations within this approach. For completeness, a brief overview of the other two existing approaches, which apply in different kinematic regimes, is given in this section.

At large scales the heavy quarks can be treated as zero mass partons, like the other light quarks u, d and s . Effectively this means charm or beauty can be treated as an active flavour in the proton. The corresponding scheme is called the 4-flavour-zero-mass-scheme (massless scheme) [50]. The LO contribution in the massless scheme, illustrated in figure 1.22 a), is only of the order α compared to $\alpha\alpha_s$ in the massive scheme, shown in figure 1.21 a). Also the NLO contributions are in this scheme always one order smaller in α_S (figure 1.22 c) and d)).

The massive scheme at large scales and the massless scheme at small scales have large uncertainties and are not of NLO accuracy. This is illustrated in figure 1.23 [51, 50].

The most reliable pQCD prediction is obtained by combining these two schemes together[50]. Here different numbers of flavours are used in the different energy ranges. Near threshold, where $\mu \sim m_Q$ holds, the massive scheme is used and it is evolved upwards. For large scales $\mu \gg m_Q$ a slightly modified mass less scheme with $m_Q \neq 0$ is applied and it is evolved downwards.

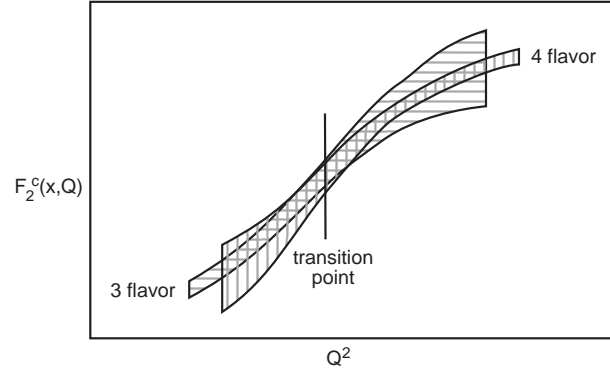


Figure 1.23: Illustration of the accuracy of the NLO calculation in the massive and the massless scheme [50].

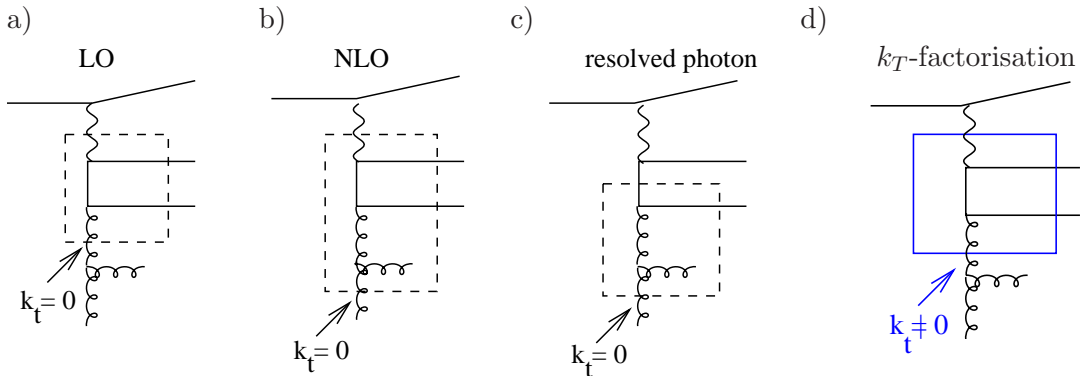


Figure 1.24: Comparison between collinear ($k_T = 0$) and k_T factorisation ($k_T \neq 0$). k_T factorisation contains implicitly higher order contributions as shown and also the gluon propagator diagram of the charm excitation [34].

1.5.5 Small x Cross Sections

The third regime already shown in figure 1.15 is the small x regime with $s \gg \hat{s}$ ($\hat{s} = xys$). In this regime a resummation of $\ln(1/x)$ terms is needed using the CCFM or BFKL approaches (see section 1.3.3 and 1.3.4). This leads to the so-called k_T -factorisation. The cross section of the hard interaction, has to be calculated “off-shell” (meaning that the gluon out of the proton, which takes part in the hard interaction has a non-vanishing virtuality). In these models the gluon density depends also on k_T and is called the unintegrated gluon density. In k_T -factorisation the LO hard process is calculated via $\gamma g^* \rightarrow Q\bar{Q}$ for photoproduction and $\gamma^* g^* \rightarrow Q\bar{Q}$ in the case of DIS, since g is off-mass shell. Figure 1.24 shows a comparison of the k_T -factorisation and the conventional collinear factorisation applied in the DGLAP formalism. In the k_T -factorisation scheme (figure 1.24 d)) some higher order terms of NLO (figure 1.24 b)), NNLO, .. as well as the most important term of the resolved charm excitation contribution (figure 1.24 c)) are taken into account.

Figure 1.25 shows the k_T dependence of the heavy quark cross section $\hat{\sigma}(\gamma^* g^* \rightarrow Q\bar{Q})$ within the k_T -factorisation scheme. The decrease of the cross section towards large values of k_T is stronger for small photon virtualities $Q^2 = k_{t\gamma}^2$.

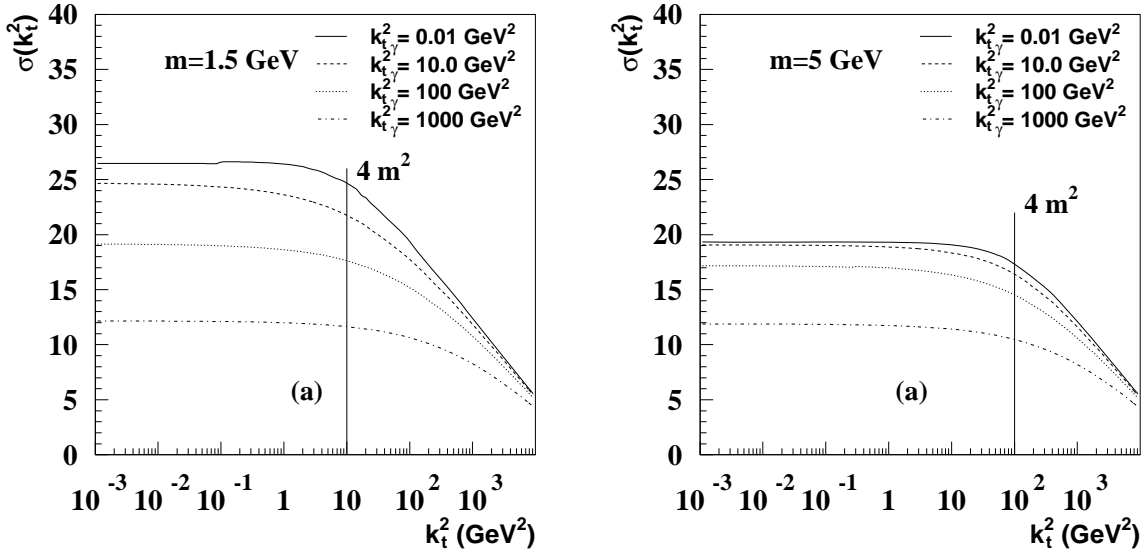


Figure 1.25: k_T^2 dependence of the heavy quark cross section $\gamma^{(*)}g^* \rightarrow Q\bar{Q}$ within the k_T -factorisation. Left: Charm production, right: beauty production. The cross sections are shown for four values of the photon virtuality $Q^2 = k_t^2 \gamma$, [52].

In the case of k_T -factorisation the $\gamma^{(*)}p$ cross section [34, 52] is obtained by the convolution of the unintegrated gluon density $\mathcal{A}(x, k_T, \bar{q}'_T)$ with the k_T dependent hard cross section:

$$\sigma_{\gamma^{(*)}p}(\mu^2, m_Q^2) = \int_0^1 \int_0^\infty \frac{dx_g}{x_g} dk_T^2 \mathcal{A}(x_g, k_T, \bar{q}'_T) \hat{\sigma}_{\gamma^{(*)}g^*} \quad (1.62)$$

After explaining the heavy quark production, the transition of heavy quarks into hadrons via fragmentation is described in the next section.

1.6 Fragmentation

Fragmentation is used to describe the transition of the coloured quarks to colourless hadrons. For this transition only phenomenological models exist due to the fact that the strong coupling constant rises strongly at large distances and thus spoils the perturbative calculations.

The inclusive production cross section for heavy hadrons can be written as:

$$d\sigma_h(p) = \sum_{i \in \text{partons}} \int_0^1 D_i^h(z, \mu_F) d\hat{\sigma}_i\left(\frac{p}{z}, \mu_F\right) \frac{dz}{z} \quad (1.63)$$

Here D_i^h indicates the probability for an initial parton i to produce a hadron h with momentum fraction z and $d\hat{\sigma}_i$ is the hard ep cross section computed at the factorisation scale μ_F (see section 1.5). Implied here is that D_i^h is independent of the hard scattering process, which is referred to as universality of the fragmentation process. This assumption has been verified by the ZEUS collaboration, who have measured the fragmentation

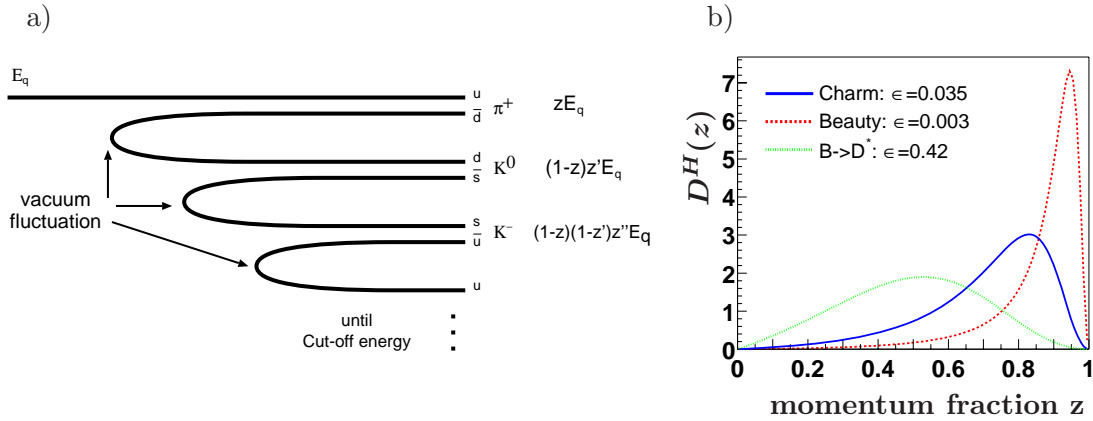


Figure 1.26: a) Illustration of the independent fragmentation. b) Peterson function for the c and b quark in NLO as well as a Peterson function modelling the decay of b -hadrons into D^* [54, 55].

function of the D^* meson in photoproduction using D^* events with an associated jet [53]. Good agreement with the measurements performed at e^+e^- collider experiments OPAL and ARGUS is obtained.

A perturbative treatment is partially possible. For heavy quarks the transition from the quarks produced at a scale μ_F to the quarks on their mass shell is performed via gluon radiation in the perturbative fragmentation function D_i . LO and NLO calculations of these functions are available. In Monte-Carlo generators this part is described perturbatively via parton showers. The second part of the fragmentation describes the non-perturbative transition from the quarks on mass shell to hadrons and is expressed by non-perturbative fragmentation function D^H :

$$D_i^h(z, \mu_F) = \int_z^1 D_i(x, \mu_F) D^H\left(\frac{z}{x}\right) \frac{dx}{x} \quad (1.64)$$

The dependence of D_i on the factorisation scale μ_F is again obtained via the DGLAP evolution equations. In contrast to the proton or the photon case here a boundary condition exists:

$$D_i(x, \mu_F = m_Q) = \delta(1 - x) \quad (1.65)$$

If the heavy quark is produced at $\mu_F = m_Q$ no further gluon radiation is possible and thus D_i is a delta function.

For the non-perturbative part or the confinement part of the fragmentation several models exist. Only the independent fragmentation model with emphasis on Peterson fragmentation [56] and the Lund string model are explained in more detail, because they are used in the simulation for the analysis presented here.

For heavy quarks independent fragmentation according to the Peterson function is at HERA often used instead of the Lund string model. Due to the relative large mass of the heavy quarks no large differences between these two models occur.

In the independent fragmentation model a bound meson $Q\bar{q}$ is formed by creating a $q\bar{q}$ pair from the vacuum (see figure 1.26 a)). Baryons are obtained in this model from vacuum

		Energy [GeV]	LO	NLO
ϵ_c	ARGUS	10.5	0.058	0.035
	OPAL	91.2	0.078	0.040
	ZEUS	near threshold	0.064	–
ϵ_b	ALEPH	91.2	0.0069	0.0033

Table 1.1: Peterson parameter for the transition of a c or b quark into a D^* meson obtained by different experiments and in LO or NLO [57, 53].

fluctuations like $qq\bar{q}$. But in this model an ad hoc requirement of colour and flavour neutralisation with the last quark is needed. The fragmentation function D^H is derived from the transition amplitude \mathcal{P} ($Q \rightarrow h$) and the appropriate longitudinal phase space factor $1/z$ with $z = E_h/E_Q$. \mathcal{P} is related to the energy difference between the initial and final state $\Delta E = E_Q - E_h - E_q$ according to:

$$\mathcal{P} \sim \frac{1}{(\Delta E)^2} = \frac{1}{(E_Q - E_h - E_q)^2} \quad (1.66)$$

The energy difference can be written as:

$$\begin{aligned} \Delta E &= E_Q - E_h - E_q \\ &= \sqrt{m_Q^2 + p_Q^2} - \sqrt{m_h^2 + p_h^2} - \sqrt{m_q^2 + p_q^2} \\ &= \sqrt{m_Q^2 + p_Q^2} - \sqrt{m_h^2 + z^2 p_Q^2} - \sqrt{m_q^2 + (1-z)^2 p_Q^2} \\ &\approx \frac{m_Q^2}{2p_Q} \left(-\frac{1}{z} - \frac{\epsilon_Q}{1-z} + 1 \right) \end{aligned} \quad (1.67)$$

In the last step the relations m_q/p_Q , $m_Q/(zp_Q)$, $m_q/(1-z)p_Q \ll 1$ are used and the approximation $\sqrt{1+x^2} \approx 1 + 1/2 \cdot x$ is applied. $\epsilon_Q = m_q^2/m_Q^2$ is in practice a parameter that is adjusted to describe the data. It refers to the hardness of the fragmentation process. The Peterson fragmentation function can thus be written as:

$$D_Q^H(z) = \frac{N_A}{z} \left(1 - \frac{1}{z} - \frac{\epsilon_Q}{1-z} \right)^{-2} \quad (1.68)$$

N_A is needed to normalise the total probability for hadron formation to unity.

In table 1.1 the Peterson parameters ϵ_c and ϵ_b for the transition of a charm or beauty quark in a D^* meson obtained by different experiments are summarised. The Peterson parameter ϵ_Q depends on the perturbative treatment of the cross sections $d\hat{\sigma}_i$. In NLO additional gluon radiation is considered and the values for ϵ_Q obtained in NLO are smaller than the corresponding LO values. The fragmentation is harder, meaning a smaller ϵ_Q value, if the gluon radiation is considered already in the hard process. The fragmentation of a b quark is harder since hadron fragmentation is less sensitive to the production of light quarks due to the larger b mass. For the heavier b quark it is easier to carry the light quarks away than for the charm quark, leading to a larger momentum fraction z of the hadron in case of beauty fragmentation. In figure 1.26 b) the Peterson function in NLO are shown using as Peterson parameter for charm $\epsilon_c = 0.035$ (for beauty $\epsilon_b = 0.0033$) as it later is used in the NLO calculations.

In the Lund string model [58] the colour field between a $q\bar{q}$ pair is described as a one dimensional colour flux tube, called a string (see figure 1.27 a)). The energy of the string

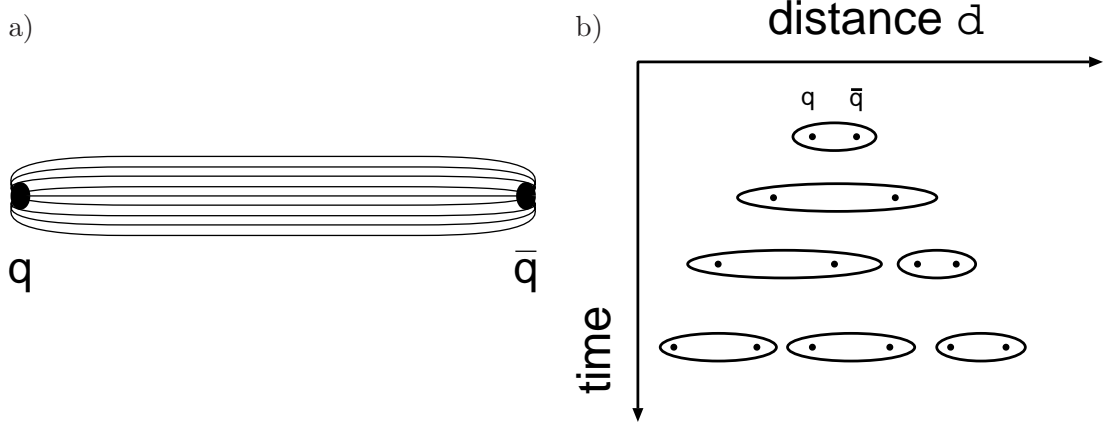


Figure 1.27: Principle of the Lund string fragmentation. a) Colour field between a $q\bar{q}$ pair. b) Fragmentation in the Lund string model.

is given by $E_{string} = \kappa r$. Here r denotes the distance between the two colour charges and κ is the string tension constant or the mass density in the string. κ is of the order of 1 GeV/fm. The linear dependence of the string energy on the distance r is motivated by the QCD potential:

$$V(r) = -\frac{4\alpha_s}{3r} + \kappa r \quad (1.69)$$

Heavy quarkonium spectra can be fitted using this potential.

If the string energy is large enough to produce a new $q\bar{q}$ pair the string breaks up. This is illustrated in figure 1.27 b). The strings evolve until the quarks are on their mass shell and then the quarks are combined to colourless hadrons. Baryons are produced via the pair-wise production of di-quarks during a string break up. The gluons are described in this model as “kinks” in the colour string.

In the independent fragmentation model as well as in the Lund string model the change of the transverse momentum due to the transition of a quark to a hadron has to be implemented by hand. For this a Gaussian distribution in transverse momentum p_T is used. In the Lund string model the string break up can be understood as a tunnelling probability $\mathcal{P} \sim \exp(Am_q^2) \exp(Bp_T^2)$. With this the correct flavour mix $u : d : s : c = 1 : 1 : 0.3 : 10^{-11}$ is obtained. In the case of the independent fragmentation model free parameters are used for baryon and strangeness suppression and also for the correct ratio of vector mesons (VM) to pseudo scalar mesons (PS). In the Lund string model the parameters for baryon suppression and the ratio VM/PS also have to be chosen freely.

After explaining in this chapter the theoretical foundations of the heavy quark production at HERA the next chapter is concerned with the reconstruction of the heavy quark pair final state. In this thesis the heavy quark pair is tagged via a D^* meson and an additional muon.

Chapter 2

Reconstruction of the $Q\bar{Q}$ Final State

The fragmentation and decay of heavy quarks can result in the production of D^* mesons and muons. In this analysis, both of these signatures are used to “tag” heavy quarks, thereby giving a so-called double-tagging analysis.

In this chapter the method used to reconstruct the heavy quarks is explained. The double-tagging of heavy quarks is discussed first. Then a short motivation for the $D^*\mu$ -pair double-tag method is given. After explaining briefly the tagging of heavy quarks with D^* -mesons and via semileptonic decays separately, the $D^*\mu$ variables heavily used later in the analysis are explained and a physical motivation is given for them. The Monte Carlo generators and the NLO program FMNR for photoproduction are introduced and acceptance studies are performed. At the end of this chapter the strategy for determining the unintegrated gluon density is described in more detail.

2.1 Double Tagging of Heavy Quark Events using a D^* -Meson and a Muon

In figure 2.1 the principle of double tagging using a D^* -meson and a muon is shown for charm production. The two heavy quarks (c and \bar{c}) produced are both tagged. The D^* -meson is reconstructed usually via the so-called “golden decay channel” ($D^* \rightarrow D^0\pi_s \rightarrow K\pi\pi_s$). The \bar{c} -quark is tagged by reconstructing the muon μ .

The advantage of the double tagging procedure with respects to single tagging is the almost complete reconstruction of the heavy quark pair final state. This in principle makes it possible to extract the gluon density with smaller theoretical uncertainties than possible in inclusive analyses. Furthermore, sensitive tests of Next-to-leading order (NLO) perturbative QCD calculations can be performed. For example, the vectorial sum of the heavy quark transverse momenta in the photon-gluon rest frame obtains a non-zero contribution at NLO. This can be tested by measuring the transverse momenta of the D^* and muon.

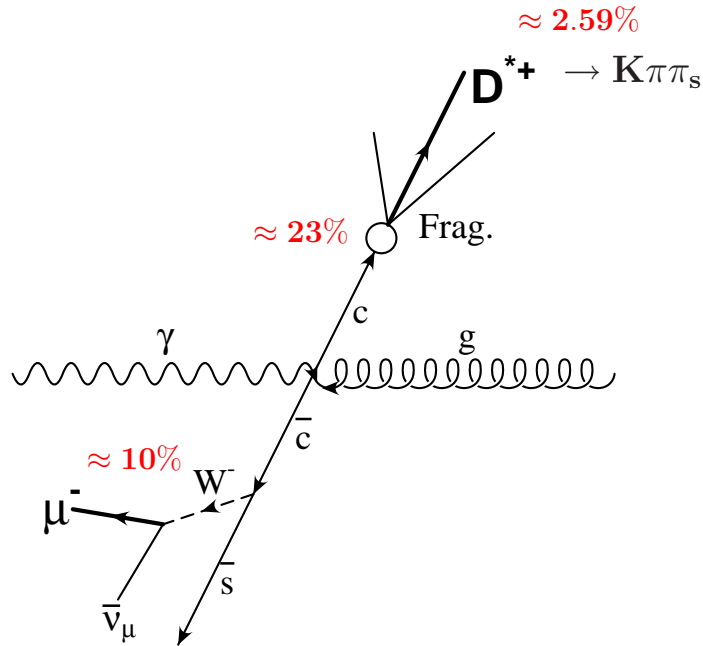


Figure 2.1: *Double tagging of charm production in the photon gluon rest frame. The c -quark is tagged by identifying the D^{*+} meson. The \bar{c} -quark is identified using the semileptonic decay mode $\bar{c} \rightarrow \mu^- \bar{\nu}_\mu X$*

By using the D^* for the reconstruction of a heavy quark a very clean heavy quark sample can be obtained and the D^* provides to good approximation the kinematic quantities of the corresponding quark. The branching ratios however for decay chains which can be used for D^* identification are only of the order of 1% (see figure 2.1), so the resulting heavy quark sample is small.

In the case of muon production, the muon and heavy quark momenta are not so closely correlated with each other and the purity of the sample is much lower, however, due to the large branching ratio for the semileptonic decay of heavy quarks (about 10%) a relatively large sample is obtained. The requirement of a D^* and a muon in a double tagging analysis is therefore a compromise between a high statistics sample and a very clean sample. The size of such a sample is at least a factor 10 smaller than the D^* -meson sample obtained using single tagging.

In the next two subsections the tagging of heavy quarks via a D^* meson and via a semileptonic decay into a muon are described in more detail.

2.1.1 Tagging of Heavy Quarks with D^* -Mesons

The D^{*+} (D^{*-}) meson consists of $c\bar{d}$ ($\bar{c}d$) quarks and has a mass $m_{D^*} = (2010.0 \pm 0.5) \text{ MeV}/c^2$ [59]. In the context of this analysis D^* -meson always means both charge states. The probability, that a c -quark hadronises into a D^{*+} -meson is [60]:

$$f(c \rightarrow D^{*+} X) = (23.5 \pm 0.7 \pm 0.7)\% \quad (2.1)$$

Channel	\mathcal{BR} [%]
$D^0\pi^+$	67.7 ± 0.5
$D^+\pi^0$	30.7 ± 0.5
$D^+\gamma$	1.6 ± 0.4

Table 2.1: Decay channels and branching ratios \mathcal{BR} of D^{*+} -meson [59].

Channel	\mathcal{BR} [%]
$K^-\pi^+$	3.83 ± 0.09
$K^-\pi^+\pi^0$	13.9 ± 0.9
$K^-\pi^+\pi^0\pi^0$	15 ± 5
$K^-\pi^+\pi^+\pi^-$	7.49 ± 0.31
$\bar{K}^0\pi^0$	2.11 ± 0.21
$\bar{K}^0\pi^+\pi^-$	5.4 ± 0.4
$K^0\pi^+\pi^-\pi^0$	10.0 ± 1.2
$K^-e^+\nu_e$	3.64 ± 0.18
$K^-\mu^+\nu_\mu$	3.22 ± 0.17

Table 2.2: Selected decay channels and branching ratios \mathcal{BR} of the D^0 -meson [59].

and the fragmentation fraction of beauty quarks into D^* -mesons is [61]:

$$f(b \rightarrow D^{*+} X) = (17.3 \pm 1.6 \pm 1.2)\% \quad (2.2)$$

The D^* -meson decays via the strong interaction, leading to lifetimes of the order of $10^{-22} - 10^{-24}$ s. It is therefore not currently possible to reconstruct the charged D^* -meson directly (the production and decay vertices cannot be separated by the detector. Therefore the D^* -meson is reconstructed via its decay products (see table 2.1).

In this analysis only the decay to a D^0 -meson ($m_{D^0} = (1864.6 \pm 0.5)$ MeV/ c^2 , [59]) and a charged pion is considered. The advantage of this channel is the small mass difference ΔM between the D^* and D^0 [59]:

$$\Delta M = m_{D^*} - m_{D^0} = (145.436 \pm 0.016)$$
 MeV/ c^2 (2.3)

Since this value lies only slightly above the mass of the pion ($m_\pi = 139.57$ MeV/ c^2), the phase space is strongly restricted for this decay. A much more precise reconstruction of the mass difference ΔM compared to the individual masses of the D^* and the D^0 is therefore possible. Due to the small kinetic energy of the pion it is often referred to as slow pion and indicated as π_s .

The D^0 -meson can decay only via the weak interaction, leading to a larger lifetime $\tau_{D^0} = (0.4126 \pm 0.0028)$ ps [59]. The D^0 decays mostly into a kaon, the charm quark transforming via the radiation of a charged W -boson into a strange quark. In table 2.2 the branching ratios of several decay channels are quoted. In this analysis only the D^0 -decay channel into a negatively charged kaon and a positively charged pion is used. The advantage of this decay channel, compared to other decay channels with larger branching ratios, is that it leaves only two charged decay particles in the final state. The larger the number of particles, which have to be combined, the larger is the combinatorial background.

The reconstruction of further short-lived neutral particles performed also via their decay particles would lead to a further reduction of the overall branching ratio. The reconstruction of low energetic π^0 via the decay into photons is also problematic in events with a relative large particle multiplicity, typical for D^* -events.

Altogether the branching ratio obtained for D^* -mesons decaying via the golden decay channel, $D^* \rightarrow D^0 \pi_s \rightarrow D^0 \pi \pi_s$, is:

$$\mathcal{BR}(D^{*+} \rightarrow K^- \pi^+ \pi_s^+) = \mathcal{BR}(D^{*+} \rightarrow D^0 \pi_s^+) \cdot \mathcal{BR}(D^0 \rightarrow K^- \pi^+) = (2.59 \pm 0.06)\% \quad (2.4)$$

2.1.2 Tagging of Heavy Quarks via Semileptonic Decays

In open heavy quark production heavy quarks transform during fragmentation into hadrons containing one heavy quark. Muons can then be produced by the semileptonic decays of these heavy hadrons. Here the charm or beauty quark transforms via the radiation of a charged W -boson mainly into a strange or a charm quark respectively. A muon and a neutrino are then produced via the decay of the W -boson.

Charm hadrons decay with a probability of nearly 100% into hadrons containing a strange quark, for example negatively charged kaons. Beauty hadrons decay with a probability of about 100% into hadrons containing a charm quark. The decay of a c or b -quark into a d -quark or u -quark is strongly suppressed, since the V_{cd} or V_{ub} elements of the Cabibbo-Kobayashi-Maskawa-Matrix (CKM-matrix) are much smaller than the V_{cs} or V_{cb} elements. In the case of beauty quarks the small size of the V_{cb} element of the CKM-matrix with respect to the size of V_{cs} in the case of charm leads to on average a 1.5 - 3 times larger lifetime of b hadrons than c hadrons, despite the fact that the mass of beauty hadrons is much larger [24].

Charm hadrons arising from the decay of beauty hadrons can also decay semileptonically in a muon, here referred to as cascade decay, while in the case, where the muon is produced directly in the decay of the beauty hadron, this is called direct decay. In this analysis the decay of a beauty hadron into charm or a tau lepton, which then decays into a muon, is collected into the cascade decay mode. The branching ratio $c \rightarrow \mu$ has been measured by the LEP experiments [54]:

$$\mathcal{BR}(c \rightarrow \mu) = (9.8 \pm 0.5)\% \quad (2.5)$$

For beauty the branching ratio for the direct and cascade decays, obtained also by the LEP experiments [62], are:

$$\mathcal{BR}(b \rightarrow \mu) = (10.95_{-0.25}^{+0.29})\% \quad (2.6)$$

$$\mathcal{BR}(b \rightarrow c \rightarrow \mu) = (8.0 \pm 0.4)\% \quad (2.7)$$

$$\mathcal{BR}(b \rightarrow \bar{c} \rightarrow \mu) = (1.6_{-0.5}^{+0.4})\% \quad (2.8)$$

$$\begin{aligned} \mathcal{BR}(b \rightarrow \tau \rightarrow \mu) &= \mathcal{BR}(b \rightarrow \tau X) \cdot \mathcal{BR}(\tau \rightarrow \mu) \\ &= (2.48 \pm 0.26)\% \cdot (17.36 \pm 0.05)\% = (0.43 \pm 0.05)\% \end{aligned} \quad (2.9)$$

In this analysis the total branching ratio used for a b -quark to produce a muon over the cascade decay mechanism is:

$$\begin{aligned} \mathcal{BR}(b \rightarrow \text{cascade} - \mu) &= \mathcal{BR}(b \rightarrow c \rightarrow \mu) + \mathcal{BR}(b \rightarrow \bar{c} \rightarrow \mu) + \\ &\mathcal{BR}(b \rightarrow \tau \rightarrow \mu) = (10.03 \pm 0.64)\% \end{aligned} \quad (2.10)$$

2.1.3 Branching Ratios for $D^*\mu$ Events

The probability, that in a given $c\bar{c}$ event a D^* -meson decays via $D^* \rightarrow K\pi\pi_s$ and a muon is simultaneously produced, is given by:

$$\begin{aligned}\mathcal{BR}(c\bar{c} \rightarrow K\pi\pi_s\mu X) &= 2 \cdot \mathcal{BR}(c \rightarrow \mu) \cdot f(c \rightarrow D^*) \cdot \mathcal{BR}(D^* \rightarrow K\pi\pi_s) \\ &= (0.1194 \pm 0.0076)\%\end{aligned}\quad (2.11)$$

The factor 2 accounts for both possibilities: $c \rightarrow D^{*+} \rightarrow K^-\pi^+\pi_s^+$, $\bar{c} \rightarrow \mu^-$ and the charge conjugated process. In case of beauty the branching ratio consists of three parts:

$$\begin{aligned}\mathcal{BR}(b\bar{b} \rightarrow K\pi\pi_s\mu X) &= 2 \cdot f(b \rightarrow D^*)\mathcal{BR}(D^* \rightarrow K\pi\pi_s) [\mathcal{BR}(b \rightarrow \text{cascade} - \mu) + \\ &\quad \mathcal{BR}(b \rightarrow \mu)] + 2 \cdot \mathcal{BR}(b \rightarrow D^*\mu X)\mathcal{BR}(D^* \rightarrow K\pi\pi_s)\end{aligned}\quad (2.12)$$

The first term is the branching ratio for $D^*\mu$ -events, where the D^* -meson and the muon come from different quarks. This term contains contributions from events, where the muon comes either from a cascade decay (see equation 2.10) or a direct decay. The second term accounts for events, where the D^* and the muon come from the same quark. Almost all $D^*\mu$ -events, which originate from the same b -quark come from the decay of a B^0 or \bar{B}^0 -meson:

$$\bar{B}^0 \rightarrow D^{*+}\mu^-\bar{\nu}_\mu \quad (2.13)$$

The probability, that a $D^*\mu$ -pair is produced from a b -quark is [62]:

$$\mathcal{BR}(b \rightarrow D^{*+}\mu^-\bar{\nu}_\mu) = (2.75 \pm 0.19)\% \quad (2.14)$$

Combining this together with the branching ratios, of the last subsections, a value:

$$\mathcal{BR}(b\bar{b} \rightarrow K\pi\pi_s\mu X) = (0.333 \pm 0.032)\% \quad (2.15)$$

is obtained. The contribution of $D^*\mu$ -events coming from the same b -quark, to the overall branching ratio of $D^*\mu$ -events in beauty production is 43%.

2.1.4 Charge and Angle Correlations

The aim of this thesis is to tag both heavy quarks, one with a D^* -meson and the other one with a muon. In the case of charm the reconstruction of a D^* and a muon guarantees a heavy quark pair (double-tagging), while for beauty the D^* and the muon can come from the same quark. However this case provides a nice opportunity to separate charm and beauty production.

The dominant heavy quark production mechanism at HERA is photon gluon fusion (PGF) as already discussed in the previous chapter. Here the heavy quarks are produced in pairs. In the LO picture the momenta of the produced heavy quarks are exactly opposite in the photon-gluon rest frame. This also holds for the transverse momenta of the quarks in the rest frame of the photon and the incoming proton (γp -frame), since these two frames differ only by a longitudinal boost in the z -direction. The azimuthal angular difference $\Delta\Phi^*$ between the transverse momenta of the two quarks is thus 180° in both frames. In figures 2.2 and 2.3 a),b) and c) the possible charge and angle correlations between the

Charm

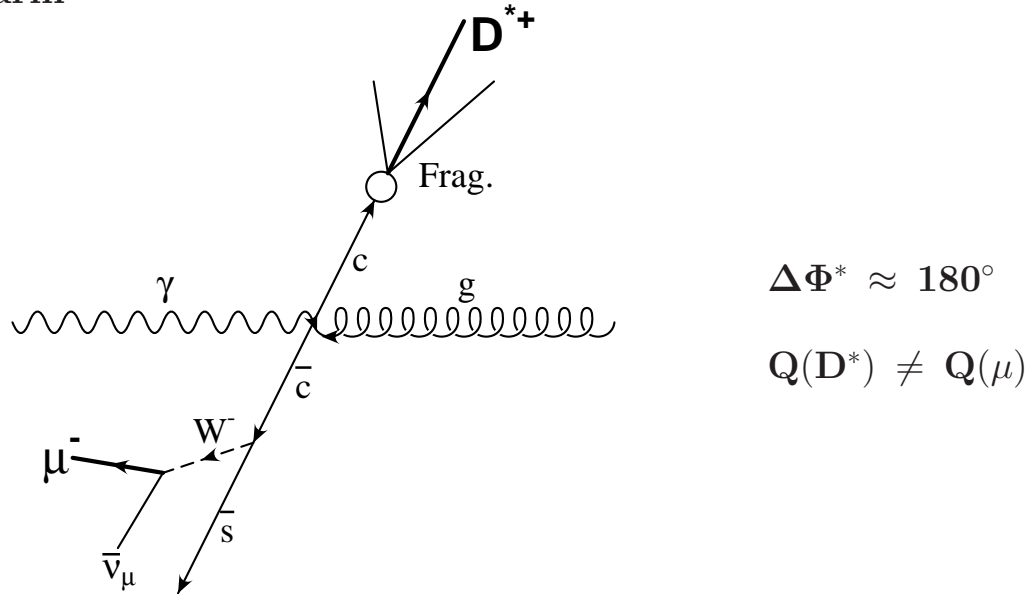


Figure 2.2: Possible charge and angle correlation for **charm events** in the γg rest frame and in the LO direct picture. For simplification the fragmentation and the subsequent decay of a charm hadron into a muon is drawn here only as transition on the quark level.

D^* -meson and the muon are shown for charm and beauty production in the photon–gluon rest frame (γg -frame) in direct leading order.

For charm events the only possible azimuthal angle difference $\Delta\Phi^*(D^*\mu)$ between the D^* -meson and the muon in the γg or γp frame is approximately 180° . The charge of the two particles is opposite, thus $Q(D^*) \neq Q(\mu)$ (figure 2.2). Due to the fragmentation and the decay, the D^* -meson and the muon have only approximately the same direction as the assigned quark.

For beauty events, in addition to the equivalent charge and angle configuration as for charm (fig. 2.3 a)), two further possibilities exist: 1) The D^* -meson and the muon can come from different b quarks, but the muon is produced directly in a b hadron decay (fig. 2.3 b)). This leads to the same charges of the D^* and the muon together with a $\Delta\Phi^*$ of approximately 180° . 2) The D^* -meson and the muon come from the same b -quark (fig. 2.3 c)). Here the two particles again have opposite charges but $\Delta\Phi^*$ is usually small. In figure 2.3 no $B^0-\bar{B}^0$ -mixing or $B_s^0-\bar{B}_s^0$ -mixing configuration is shown since mixing does not lead to an additional charge angle configuration.

Taking into account NLO effects, gluon radiation from the heavy quarks before interacting with the photon is possible (figure 1.20 d)). This leads to an angle $\Delta\Phi^*$ smaller than 180° between the two outgoing heavy quarks in the γg (or γp) frame. Furthermore a possible non-zero initial “intrinsic” transverse momentum of the interacting partons can lead to $\Delta\Phi^*(Q\bar{Q}) \neq 180^\circ$.

Similar statements are true for the resolved processes, the normal resolved as well as the excitation processes, which are expected to contribute mainly in photoproduction.

Beauty

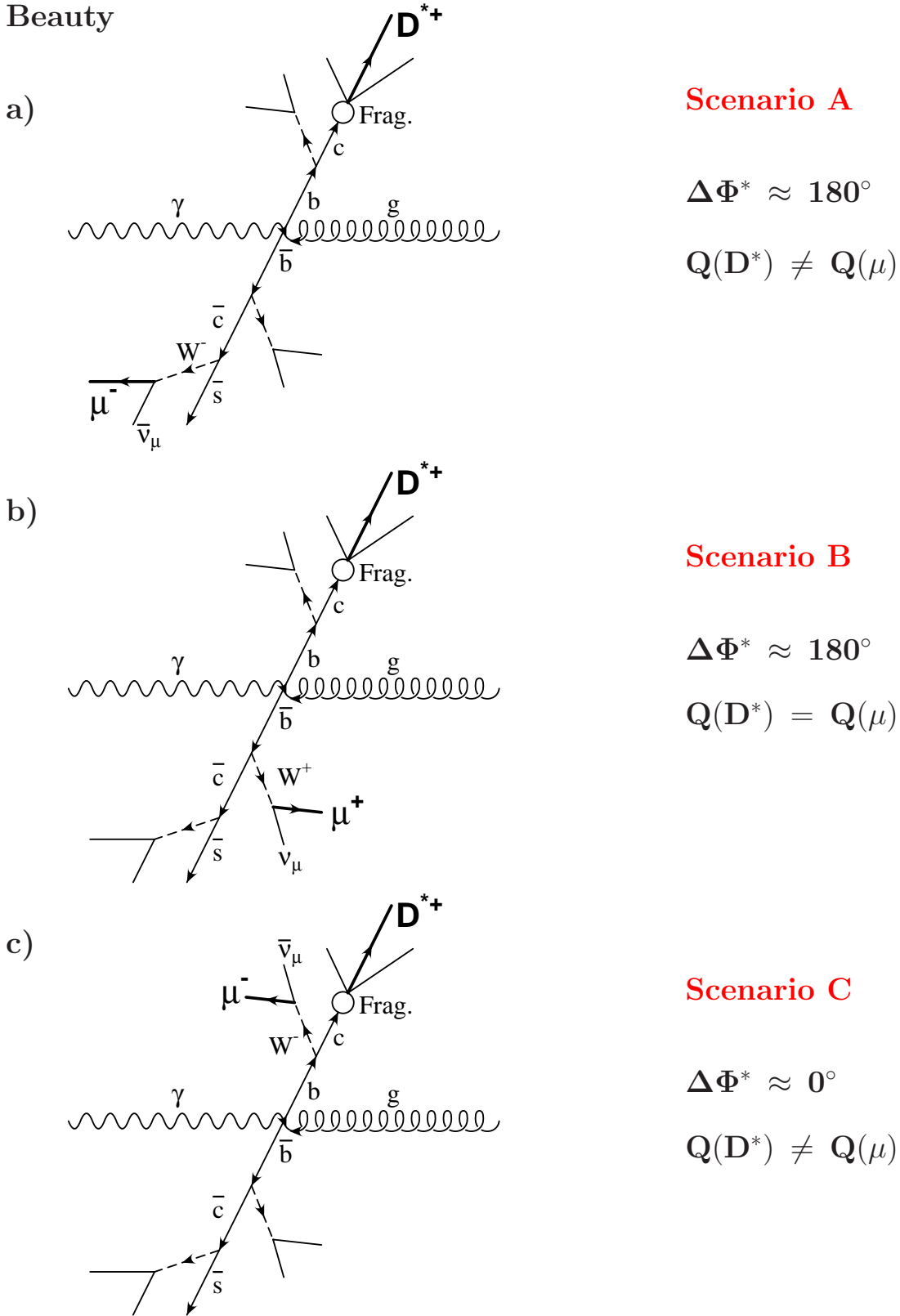


Figure 2.3: Possible charge and angle correlations for *beauty events* in the γg rest frame in the LO direct picture. For simplification the fragmentation and the subsequent decay of a beauty hadron into a muon (direct or cascade decay) or a D^* -meson is drawn here only schematically. a) $b \rightarrow D^{*+}$, $\bar{b} \rightarrow \bar{c} \rightarrow \mu^-$, b) $b \rightarrow D^{*+}$, $\bar{b} \rightarrow \mu^+$, c) $b \rightarrow D^{*+}\mu^-$.

Here the parton out of the photon, which takes part in the hard interaction, can have a transverse momentum with respect to the photon. With such a transverse momentum the γp -frame and the parton-proton frame differ by a boost with a transverse component, leading to a $\Delta\Phi^*(Q\bar{Q})$ in the γp frame smaller than 180° .

These effects smear the charge and angle correlations between the D^* -meson and the muon further. In this analysis a distinction is made between $\Delta\Phi^* \geq 90^\circ$ and $\Delta\Phi^* < 90^\circ$. Taking the charges into account four correlation regions can be defined:

		$\Delta\Phi^* < 90^\circ$	$\Delta\Phi^* \geq 90^\circ$
1. $\Delta\Phi^* < 90^\circ$ and $Q(D^*) = Q(\mu)$.	$Q(\mu) = Q(D^*)$	1 no charm few beauty	2 no charm beauty
2. $\Delta\Phi^* \geq 90^\circ$ and $Q(D^*) = Q(\mu)$.		3 few charm beauty	4 charm beauty
3. $\Delta\Phi^* < 90^\circ$ and $Q(D^*) = -Q(\mu)$.	$Q(\mu) \neq Q(D^*)$		
4. $\Delta\Phi^* \geq 90^\circ$ and $Q(D^*) = -Q(\mu)$.			

2.1.5 $D^*\mu$ -Quantities

The advantage of double tagging with respect to single tagging is that the kinematics of the heavy quark pair final state are almost completely reconstructed, at least in the case of charm. For beauty a clear relation between the two quarks and the $D^*\mu$ -pair is obtained only in a more restricted region of phase space (correlation region 2).

Sensitive tests of Next-to-leading order (NLO) perturbative QCD calculations can be performed. The sum of the heavy quark transverse momentum vectors $p_T^*(Q\bar{Q})$ and the azimuthal angular difference $\Delta\Phi^*(Q\bar{Q})$ between the heavy quarks in the photon-proton rest frame obtain non-zero contributions only at NLO (only if direct processes are considered). The investigation of a possible intrinsic transverse momentum k_T of the initial partons (e.g. the incoming gluon) is possible with these two variables.

Figure 2.4 shows the $\Delta\Phi(D\bar{D})$ and $p_T^2(D\bar{D})$ distributions of the E687-experiment [16]. In this fixed target experiment a photon beam with a mean energy of about 200 GeV was used. For comparison the theoretical prediction is shown in NLO (full line) with $m_c = 1.5 \text{ GeV}/c^2$. The dotted and dashed lines show the impact of an intrinsic momentum k_T of one of the incoming partons. In both plots, the data points have a broader distribution than NLO QCD without assuming an intrinsic k_T . This conclusion is supported by more precise, recent FOCUS data [18].

In this analysis the measured transverse momentum $p_T^*(D^*\mu)$ and the azimuthal angular difference $\Delta\Phi^*$ of the $D^*\mu$ -pair in the photon-proton rest frame is taken as an approximation for the corresponding quark quantities, $p_T^*(Q\bar{Q})$ and $\Delta\Phi^*(Q\bar{Q})$. These two quantities are defined as:

$$p_T^*(D^*\mu) = \sqrt{(p_{x,D^*}^* + p_{x,\mu}^*)^2 + (p_{y,D^*}^* + p_{y,\mu}^*)^2} \quad (2.16)$$

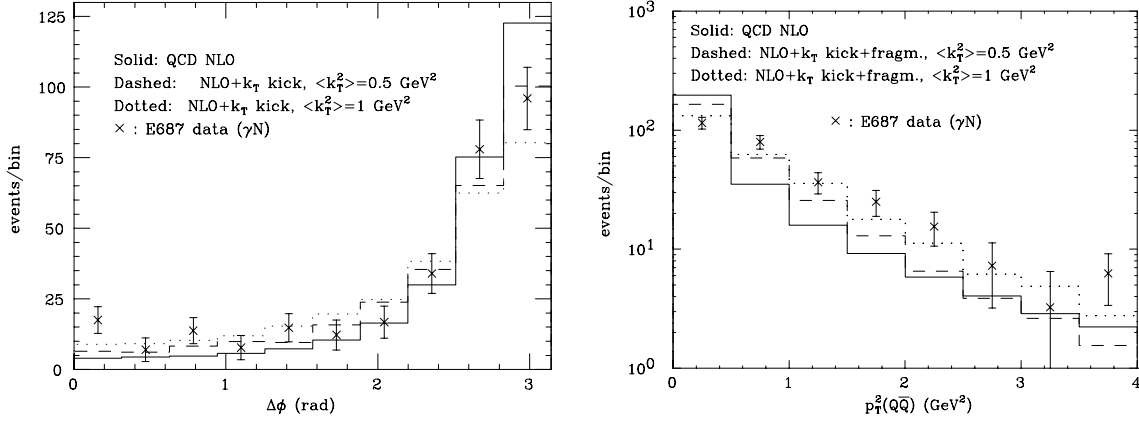


Figure 2.4: $\Delta\Phi(D\bar{D})$ - and $p_T^2(D\bar{D})$ -distribution for charm production in γN -collisions. Shown are the experimental results of the E687-collaboration [17] together with predictions of perturbative calculations in NLO and the impact of an intrinsic transverse momentum k_T of one of the initial partons on the NLO calculations.

$$\Delta\Phi^* = \begin{cases} |\phi_{D^*}^* - \phi_\mu^*| & \text{for } |\phi_{D^*}^* - \phi_\mu^*| \leq 180^\circ \\ 360^\circ - |\phi_{D^*}^* - \phi_\mu^*| & \text{for } |\phi_{D^*}^* - \phi_\mu^*| > 180^\circ \end{cases} \quad (2.17)$$

In addition to these two quantities the invariant mass $M(D^*\mu)$ of the $D^*\mu$ -pair is an approximation to the invariant mass $M(Q\bar{Q})$ of the quark pair. In the LO picture this mass corresponds to the centre-of-mass energy of the incoming photon and the gluon $\sqrt{\hat{s}}$.

The rapidity $\hat{y} = 1/2 \cdot \ln(E(Q\bar{Q}) + p_z(Q\bar{Q}))/E(Q\bar{Q}) - p_z(Q\bar{Q})$ of the quark pair is in the LO picture and in photoproduction directly connected to the ratio of the energies coming from the electron and proton sides, which contribute to the hard interaction. If the process: $parton + g \rightarrow Q + \bar{Q}$ (assuming $k_T = 0$) is considered, the four-momentum of the parton out of the photon which takes part in the hard interaction is $p = x_\gamma \cdot q$. For the incoming gluon out of the proton $g = x_g \cdot P$ is used. Therefore:

$$\begin{aligned} E(Q\bar{Q}) + p_z(Q\bar{Q}) &= x_g \cdot E_p + x_\gamma y \cdot E_e + x_g \cdot E_p - x_\gamma y \cdot E_e = 2x_g E_p \\ E(Q\bar{Q}) - p_z(Q\bar{Q}) &= x_g \cdot E_p + x_\gamma y \cdot E_e - x_g \cdot E_p + x_\gamma y \cdot E_e = 2x_\gamma y E_e \end{aligned} \quad (2.18)$$

$$\text{and } \hat{y}(Q\bar{Q}) = \frac{1}{2} \ln \left(\frac{x_g E_p}{x_\gamma y E_e} \right) \quad (2.19)$$

In this analysis the measured $\hat{y}(D^*\mu)$ is also an approximation for $\hat{y}(Q\bar{Q})$.

Substituting the relation $M^2(Q\bar{Q}) = x_g \cdot x_\gamma y \cdot s$, a formula for the momentum fraction x_γ of the parton with respect to the photon momentum can be obtained:

$$\begin{aligned} \hat{y}(Q\bar{Q}) &= \frac{1}{2} \ln \left(\frac{M^2(Q\bar{Q}) E_p}{x_\gamma^2 y^2 E_e s} \right) = \frac{1}{2} \ln \left(\left(\frac{M(Q\bar{Q}) \sqrt{E_p}}{x_\gamma y \sqrt{E_e s}} \right)^2 \right) \\ &= \ln \left(\frac{M(Q\bar{Q}) \sqrt{E_p}}{\sqrt{s}} \sqrt{\frac{1}{E_e y x_\gamma}} \right) \\ x_\gamma &= \frac{M(Q\bar{Q}) \sqrt{E_p}}{\sqrt{s}} \sqrt{\frac{1}{E_e y}} \cdot \exp(-y(Q\bar{Q})) \end{aligned} \quad (2.20)$$

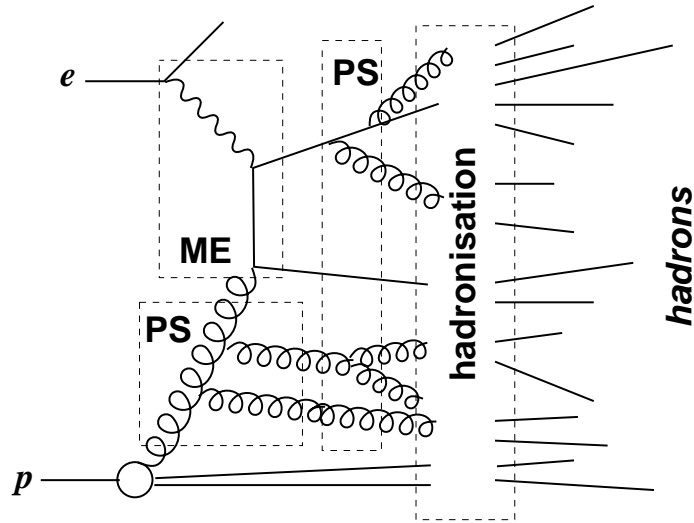


Figure 2.5: *Elements of an ep event generator.*

In this analysis $x_\gamma(D^*\mu)$ is used to check, whether the data are compatible with the resolved excitation component predicted by the theory.

2.2 Monte Carlo Simulation

In order to compare theoretical models with measurements, Monte Carlo programs are used. Furthermore these programs are used to correct the data for resolution, triggering and efficiency effects. The Monte Carlo programs simulate scattering processes based on theoretical models. Since the output of these Monte Carlo programs has the same format as the measured data, data and Monte Carlo prediction can be compared directly. For this the following three steps are necessary:

- **Generation:** The four-vectors of the particles in the final state are generated according to the distributions predicted by the theoretical model.
- **Detector Simulation:** Using the previously generated particle four-vectors the trajectories of the particles through the detector are calculated and particle decays are simulated according to particle lifetimes. Signals in the detector are simulated.
- **Reconstruction:** The tracks, momenta and energies of the particles are reconstructed from the detector signals, using the same program used for the reconstruction of the data.

The Monte Carlo event generation step has several stages. The starting point is a fixed-order matrix element (ME) used to describe the hard partonic subprocess, which is convoluted with the parton densities. In present Monte Carlo generators the hard process is implemented only in LO. To simulate higher orders, initial and final state parton showers (PS) are used. The initial PS are always evolved backwards from the hard process to the

proton. During the initial as well as during the final state PS additional partons are produced. All produced partons hadronise subsequently. The complete procedure is sketched in figure 2.5. Apart from the hard process all stages are in the generators based on leading logarithmic approximations and phenomenological models.

In this analysis the Monte Carlo generators PYTHIA [63] and RAPGAP [64] are used for the determination of the trigger and reconstruction efficiencies, the fraction of beauty events in the selected data and to correct for hadrons mis-identified as muons. Furthermore, they are compared directly with the data. For the simulation of photoproduction events PYTHIA is taken. Within this Monte Carlo generator the simulation of direct and resolved processes, normal resolved as well as excitation, is possible. For DIS events the Monte Carlo Generator RAPGAP is used, which includes real photon emissions from the incoming electron and virtual contributions at the electron vertex, simulated in the program HERACLES [65], which is contained within the RAPGAP generator. The Monte Carlo generator CASCADE [66] is used in addition as an alternative in both photoproduction and DIS.

In all generators the hard subprocess is boson gluon fusion, at least in case of direct processes. PYTHIA simulates also the resolved processes discussed in the last chapter. For the Monte Carlo generators PYTHIA and RAPGAP, which are both based on the DGLAP evolution model of the structure functions, the matrix element is calculated on-shell. Since the CASCADE generator is based on the CCFM evolution model, the virtuality of the incoming gluon and thereby the k_T dependence of the matrix element have to be taken into account explicitly. For the initial parton shower evolution of the RAPGAP and PYTHIA generators the probability for a parton to branch is given by the DGLAP evolution equation, while for the CASCADE generator the branching probabilities are based on the CCFM evolution model. Final state parton showers are always based on the DGLAP evolution model. The hadronisation of light quarks is performed using the Lund string model and for the hadronisation of the heavy quarks the Peterson fragmentation function is used in this analysis. For charm production the Peterson parameter was set to the LO value $\epsilon_c = 0.078$ and in case of beauty production $\epsilon_b = 0.008$ is used (see also chapter 1). For all Monte Carlo generators used the fragmentation is simulated using the program JetSet/PYTHIA 6 [67].

For both Monte Carlo generators RAPGAP and PYTHIA, CTEQ5L [68] is used to parameterise the parton density functions in the proton and for the photon GRV-G LO [69] is used (if resolved processes are considered). In case of CASCADE an unintegrated gluon density $\mathcal{A}(x_g, k_T, \bar{q}_t)$ is used. This gluon density was determined by requiring a good description of the structure function F_2 [38, 39, 37].

The mass m_c of the charm quark was set to $m_c = 1.5 \text{ GeV}/c^2$ and the beauty mass m_b was chosen to be $m_b = 4.8 \text{ GeV}/c^2$ (CASCADE and PYTHIA) and as $m_b = 4.75 \text{ GeV}/c^2$ in the case of the Monte Carlo generator RAPGAP.

For the $B^0 - \bar{B}^0$ mixing a value of 0.73 was chosen for the mixing parameter $x_d = \Delta m_{B^0}/\Gamma_{B^0}$ according to [62]. The corresponding parameter for $B_s^0 - \bar{B}_s^0$ mixing is $x_s = 18$. In the case of $B_s^0 - \bar{B}_s^0$ mixing only a measured lower limit of $x_s > 14$ exists [62].

For the photoproduction sample the kinematic range was restricted to $Q^2 < 1 \text{ GeV}^2$ and for the DIS sample $1 \text{ GeV}^2 < Q^2 < 100 \text{ GeV}^2$. Only such events are selected, which contain at least one D^* -meson, which decays via a D^0 into a $K\pi\pi_s$ system.

Channel	\mathcal{BR}^{MC} [%]	$\mathcal{BR}^{meas.}$ [%]	f_{cor}
$D^* \rightarrow K\pi\pi_s$	2.5	2.59 ± 0.06	1.036
$c \rightarrow D^*$	30	23.5 ± 0.7	0.783
$c \rightarrow \mu$	9.4	9.8 ± 0.5	1.043
$1/2 \cdot c\bar{c} \rightarrow D^*\mu$	2.82	2.30 ± 0.14	0.82
$b \rightarrow D^*$	30	17.3 ± 1.6	0.577
$b \rightarrow \mu$	10.5	10.95 ± 0.27	1.043
$b \rightarrow \text{cascade} - \mu$	10.7	10.03 ± 0.64	0.937
$b \rightarrow D^*\mu$	2.19	2.75 ± 0.19	1.256
$1/2 \cdot b\bar{b} \rightarrow D^*\mu$ cascade decay (scenario A)	3.15	1.74 ± 0.19	0.54
$1/2 \cdot b\bar{b} \rightarrow D^*\mu$ direct decay (scenario B)	3.21	1.89 ± 0.18	0.60
$b \rightarrow D^*\mu$ (scenario C)	2.19	2.75 ± 0.19	1.256
$1/2 \cdot b\bar{b} \rightarrow D^*\mu$	8.46	6.38 ± 0.32	0.754

Table 2.3: Important branching ratios used in the Monte Carlo simulation compared to the measured branching ratios [54, 62]. A correction factor f_{cor} is quoted for each branching ratio.

Channel	f^{MC} [%]	$f^{meas.}$ [%]	f_{cor}
$b\bar{b} \rightarrow D^*\mu$ cascade decay (scenario A)	38	27	0.71
$b\bar{b} \rightarrow D^*\mu$ direct decay (scenario B)	37	30	0.81
$b \rightarrow D^*\mu$ (scenario C)	25	43	1.72

Table 2.4: Comparison of the contributions f^{MC} between the three beauty scenarios in the Monte Carlo Simulation with the measured ones $f^{meas.}$. A correction factor f_{cor} for each beauty scenario is indicated.

Table 2.3 gives an overview of the important branching ratios used in the Monte Carlo simulation together with the measured values. For beauty production the correct contributions of the three different cases has to be ensured. Table 2.4 compares the fractions obtained by the Monte Carlo simulations with the measured fractions. In addition a correction factor is quoted. These correction factors are applied to the corresponding beauty scenarios in all Monte Carlo simulations used. The remaining differences concern only normalisation effects. In order to calculate cross sections the corresponding correction factors of the branching ratios $c\bar{c} \rightarrow D^*\mu$ and $b\bar{b} \rightarrow D^*\mu$ have to be applied as quoted in table 2.3 (marked with bold font).

Samples with different beam energies and detector setup were generated. The relative luminosities of the different samples correspond to those in the data. For the charm Monte Carlo the total luminosity is $\mathcal{L}^{c-MC} = 1.0 \text{ fb}^{-1}$ and for beauty $\mathcal{L}^{b-MC} = 20 \text{ fb}^{-1}$.

2.3 NLO Calculations: FMNR

Next-to-leading order (NLO) perturbative QCD calculations for charm and beauty production in ep scattering are available for deep-inelastic-scattering (HVQDIS [70, 43]) and for photoproduction (FMNR [49, 71, 72]). A comparison of the data with NLO calculations is done only in photoproduction.

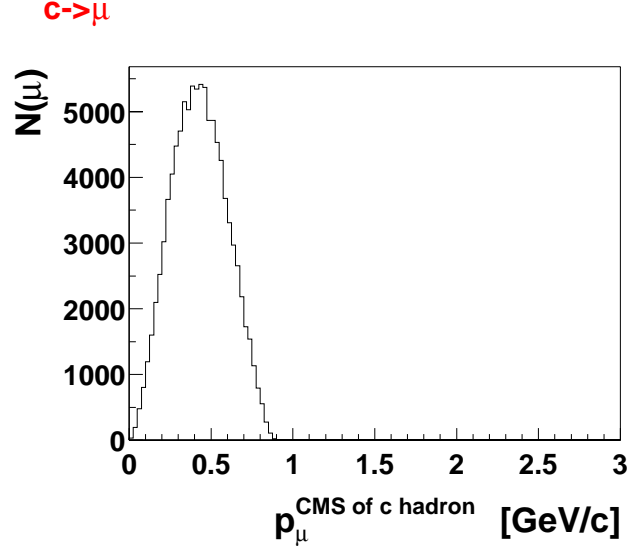


Figure 2.6: *Muon momentum spectrum in the rest frame of a charm hadron as obtained from the PYTHIA Monte Carlo.*

FMNR performs the calculations in the fixed order massive scheme and all NLO processes shown in the previous chapter are considered. Normal resolved processes can also be taken into account. However, since these contributions are small, they are neglected in this analysis. The FMNR output contains the transverse momenta \vec{p}_T and the rapidities \hat{y} of the heavy quarks and the radiated light parton (gluon or quark) in the case of NLO processes. These are given in the rest frame of the electron and the proton. The energy and the momentum in the z -direction are obtained via:

$$p_z = m_T \cdot \sinh(\hat{y}) \quad \text{with} \quad m_T = \sqrt{\vec{p}_T^2 + m^2} \quad (2.21)$$

$$E = m_T \cdot \cosh(\hat{y}) \quad (2.22)$$

In order to compare the results of the calculations to the data, the fragmentation of the heavy quarks into hadrons, and also the semileptonic decay of heavy hadrons into a muon (direct and cascade) has to be modelled. Starting from the four-momenta of the quarks the four-momenta of a D^* -meson and a muon, are calculated as follows:

For charm production the four momenta of the c and \bar{c} quark are evolved into a charm hadron using the Peterson fragmentation function with $\epsilon_c = 0.035$. This value corresponds to the Peterson parameter obtained for the D^* , and is typical of many charmed hadrons in NLO. The four-momenta are scaled with the momentum fraction z (different for both quarks) of the charm hadron with respect to the initial c or \bar{c} quark. This fraction is generated according to the Peterson fragmentation function. This is done in a frame, in which $p_z(Q) = -p_z(\bar{Q})$ holds for the z -component of the two quarks. A boost is then applied back into the ep rest frame. The c quark is evolved already in its final state, the D^* -meson. The two modified four vectors are then transformed into the laboratory frame.

The decay of the \bar{c} hadron into a muon is calculated in the hadrons rest frame. The cosine of the polar angle $\cos(\theta)$ and azimuthal angular distribution of the decay muon are isotropic in

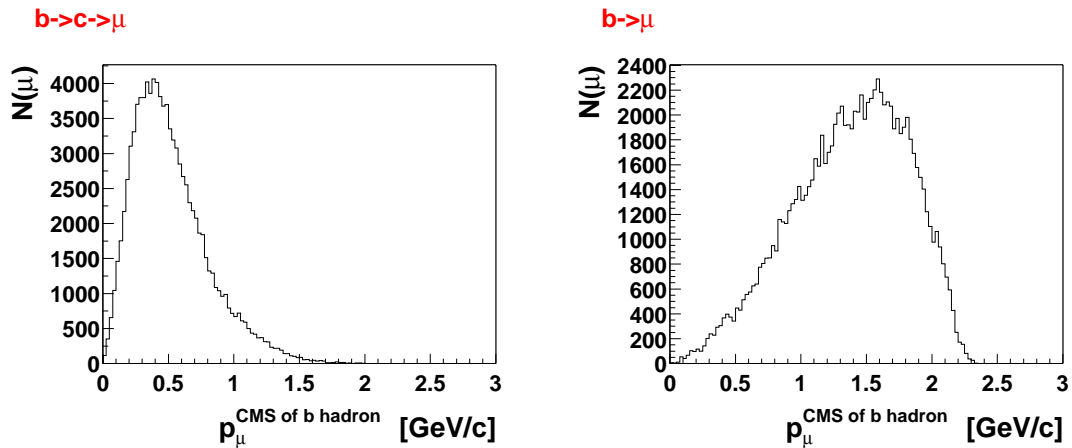


Figure 2.7: Muon momentum spectra in the rest frame of the initial beauty hadron as obtained from the PYTHIA Monte Carlo. Left: Cascade decay; right: direct decay.

this frame and the momentum distribution is adopted from the LO Monte Carlo generator PYTHIA (see figure 2.6). All charm hadrons are considered in this distribution. The four-momentum of the muon in the rest frame of the \bar{c} hadron is then obtained by generating the values for the two angles and the absolute value of the momentum p according to the required muon momentum spectrum. A Lorentz boost back into the laboratory frame is then performed. The modified four-vectors now represent the D^* -meson and muon.

For beauty the procedure is more complicated due to the fact that three different scenarios exist (not considering $B - \bar{B}$ mixing):

- A. $\mu^- \leftarrow \bar{c}\text{-hadron} \leftarrow \bar{b}\text{-hadron} \leftarrow \bar{b}b \rightarrow b\text{-hadron} \rightarrow D^{*+}$
- B. $\mu^+ \leftarrow \bar{b}\text{-hadron} \leftarrow \bar{b}b \rightarrow b\text{-hadron} \rightarrow D^{*+}$
- C. $b\text{-hadron} \rightarrow D^{*+}\mu^-$

The fragmentation of the $b\bar{b}$ -pair into a b or \bar{b} hadron is performed in an analogous way as explained for charm production. The only difference is that here the Peterson fragmentation function parameter ϵ is chosen as $\epsilon_b = 0.0033$. For scenario A and B the decay of the b hadron into a D^* -meson is modelled by using a second Peterson fragmentation function with $\epsilon = 0.42$ [54, 55] (see figure 1.26, page 29). In the rest frame of the b hadron the azimuthal and polar angular distributions of the D^* -meson are isotropic and their values are chosen from an uniform distribution. The absolute value of the momentum of the D^* -meson corresponds to the maximum possible momentum scaled with a factor z corresponding to the Peterson fragmentation function. From these three variables the four-momentum of the D^* -meson is calculated and afterwards a boost into the laboratory frame is performed.

The decay of the beauty hadron into a muon is implemented in a similar way as for charm production, using for the scenario A a muon momentum spectrum from the cascade decay and for scenario B from the direct decay of the initial b hadron. These muon momentum spectra in the rest frame of the initial b hadron are again obtained from the PYTHIA Monte Carlo program and again all beauty hadrons are considered. The distributions are shown in figure 2.7.

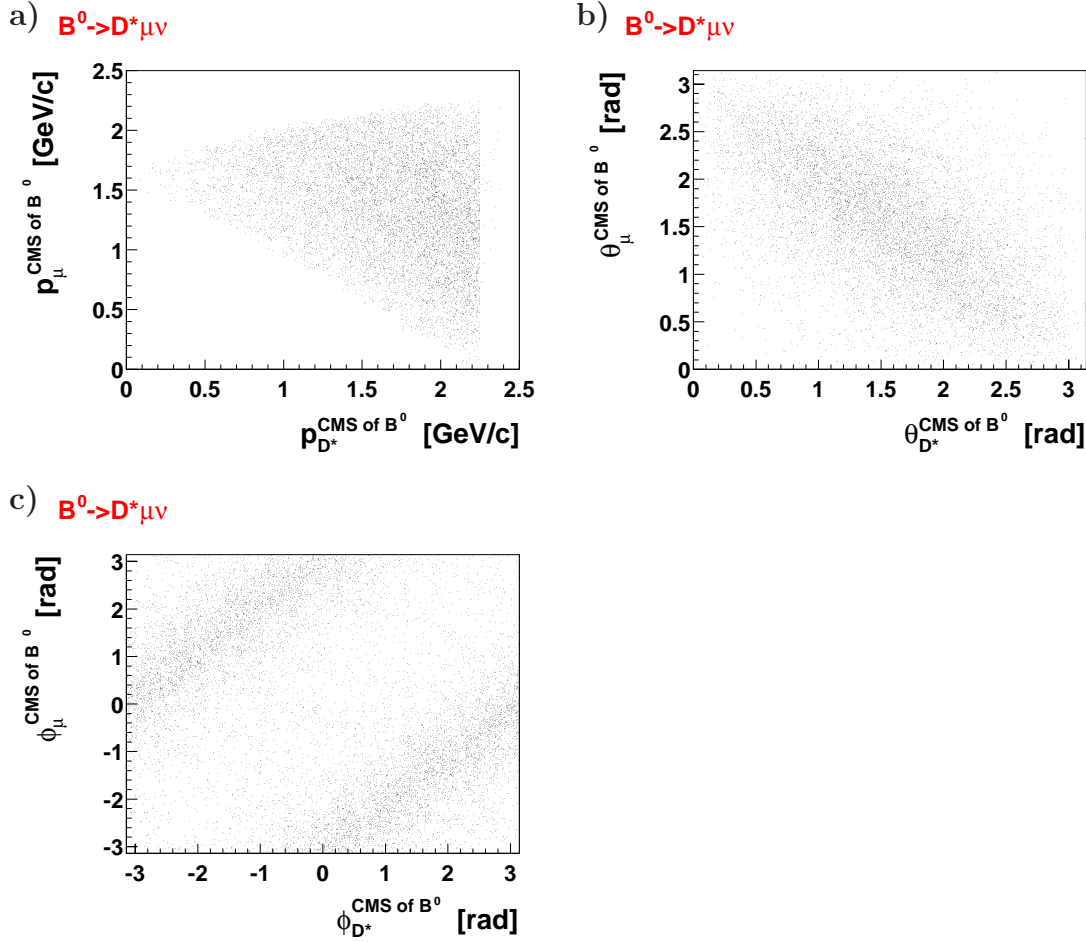


Figure 2.8: Correlations of the polar (b) and azimuthal (c) angles and the momenta (a) of the $D^* \mu$ -pair from b hadron decays. These quantities are calculated in the rest frame of the b hadron.

For scenario C, where a b hadron decays into a $D^* \mu$ -pair, the correlation between the two particles is taken into account. The correlation between the polar and azimuthal angles of the $D^* \mu$ -pair as well as the correlation of the momenta of the D^* -meson and the muon are taken from the PYTHIA Monte Carlo generator. They are shown in figure 2.8. Since most of the $D^* \mu$ -events of scenario C originate from a B^0 decay (about 70%), only the B^0 -decay is considered and the three quantities above are shown in the rest frame of the B^0 -meson. The values of these quantities for the two particles are generated according to their correlations. After calculating the four-momenta of the D^* and the muon a boost back into the laboratory frame is applied.

The cross sections obtained after the modification of the $Q\bar{Q}$ cross sections with the fragmentation procedure are indicated with σ_Q^{FMNR} . Only the four-momenta of the quark pair were changed during the fragmentation procedure. To get $D^* \mu$ cross sections, as determined from the data, the branching ratios and a factor 2 to account for the two quarks have to be taken into account:

$$\sigma_c = 2 \cdot \mathcal{BR}(c \rightarrow D^*) \mathcal{BR}(c \rightarrow \mu) \cdot \sigma_c^{FMNR} \quad (2.23)$$

$$\sigma_b(\text{A}) = 2 \cdot \mathcal{BR}(b \rightarrow D^*) \mathcal{BR}(b \rightarrow \text{cascade} - \mu) \cdot \sigma_b^{FMNR}(\text{A}) \quad (2.24)$$

$$\sigma_b(\text{B}) = 2 \cdot \mathcal{BR}(b \rightarrow D^*) \mathcal{BR}(b \rightarrow \mu) \cdot \sigma_b^{FMNR}(\text{B}) \quad (2.25)$$

$$\sigma_b(\text{C}) = 2 \cdot \mathcal{BR}(b \rightarrow D^* \mu) \cdot \sigma_b^{FMNR}(\text{C}) \quad (2.26)$$

Here (A), (B), (C) denote the three different beauty scenarios.

For differential cross sections in the quantities $\Delta\Phi^*$, $p_T^*(D^*\mu)$, the invariant mass $M(D^*\mu)$ and the rapidity $\hat{y}(D^*\mu)$ of the $D^*\mu$ -pair, the data from all correlation regions 1-4 are used. Correlation region 4 only is used for the extraction of the gluon density leading to a large charm contribution and thus to an acceptable correlation between the quark pair and the reconstructed $D^*\mu$ -pair. With the future anticipated increase in statistics correlation region 2 will provide for beauty a good correlation between the quark pair and the $D^*\mu$ -pair. The data of correlation region 3 lead to a clean $b \rightarrow D^*\mu$ cross section.

In data more than one $D^*\mu$ -pair can be found and since there is no reasonable criteria to select a pair, all found $D^*\mu$ -pairs are counted. $D^*\mu$ -pairs are not uncorrelated in the case of multi $D^*\mu$ events. But because the fraction of multi $D^*\mu$ events is small, the effect of the correlation on the error of the data points can be neglected. The cross sections, extracted in this analysis, can be written as:

$$\sigma_c^{cor\ 1-4} = \sigma_c \quad (2.27)$$

$$\sigma_c^{cor\ 4} = \sigma_c^{\Delta\Phi^* > 90^\circ} \quad (2.28)$$

$$\sigma_b^{cor\ 1-4} = \sigma_b(\text{A}) + \sigma_b(\text{B}) + \sigma_b(\text{C}) \quad (2.29)$$

$$\begin{aligned} \sigma_{b, no\ b \rightarrow D^*\mu}^{cor\ 4} &= \left((1 - A_{B-osc})^2 + A_{B-osc}^2 \right) \cdot \sigma_b^{\Delta\Phi^* > 90^\circ}(\text{A}) + \\ & 2 \cdot (1 - A_{B-osc}) \cdot A_{B-osc} \cdot \sigma_b^{\Delta\Phi^* > 90^\circ}(\text{B}) \end{aligned} \quad (2.30)$$

$$\begin{aligned} \sigma_b^{cor\ 3} &= \sigma_b^{\Delta\Phi^* < 90^\circ}(\text{C}) + \left((1 - A_{B-osc})^2 + A_{B-osc}^2 \right) \cdot \sigma_b^{\Delta\Phi^* < 90^\circ}(\text{A}) + \\ & 2 \cdot (1 - A_{B-osc}) \cdot A_{B-osc} \cdot \sigma_b^{\Delta\Phi^* < 90^\circ}(\text{B}) \end{aligned} \quad (2.31)$$

For beauty production B^0 -mixing is also considered and it is assumed that the probability for an oscillated B^0 -hadron is $A_{b-osc} = 12\%$. The cross section contribution of beauty scenario A and B are very small for $\Delta\Phi^* < 90$, while the contribution of beauty scenario C for $\Delta\Phi^* > 90$ is of course smaller than the $\Delta\Phi^* < 90$ contribution (but still sizeable). Indeed this contribution is, in the visible range of this analysis, larger than the naively expected dominant contribution from scenario A, since the acceptance for beauty events from scenario A is much smaller than for that of scenario C.

In the program FMNR a charm mass $m_c = 1.5 \text{ GeV}/c^2$ and a beauty mass $m_b = 4.75 \text{ GeV}/c^2$ are used. The parton densities of the proton are parametrised using CTEQ5D [68]. For beauty production the mean value of the factorisation scale is chosen to be

Selection	cross section [pb]		
	direct	normal res.	excitation
Charm			
$c\bar{c}$ incl.	571540	76515	358110
D^*	267000	33400	162000
+ $0.05 < y < 0.75$	156000	24500	118000
+ $p_T(D^*) > 1.5$ GeV/c	38600	5650	42400
+ $ \eta(D^*) < 1.5$	28100	1640	28900
+ μ	2770	165	2840
+ $p(\mu) > 2.0$ GeV/c	2150	83	2189
+ $ \eta(\mu) < 1.735$ (vis.)	142	4	100
Beauty			
$b\bar{b}$ incl.	3742	677	1139
D^*	1288	185	397
+ $0.05 < y < 0.75$	984	149	322
+ $p_T(D^*) > 1.5$ GeV/c	535	76	189
+ $ \eta(D^*) < 1.5$	396	23	128
+ μ	196	12	64
+ $p(\mu) > 2.0$ GeV/c	164	8	53
+ $ \eta(\mu) < 1.735$ (vis.)	55	3	17

Table 2.5: Predicted cross sections for inclusive charm and beauty production from the PYTHIA Monte Carlo generator. The total $D^*\mu$ cross section in the measured visible range and several stages between these two extremes are given. The direct, normal resolved and the resolved excitation component are indicated separately.

equal to the renormalisation scale μ_R and equal to the transverse mass m_T : $\mu_F = \mu_R = m_T = \sqrt{((p_T(b) + p_T(\bar{b}))/2)^2 + m_b^2}$. For charm production $\mu_F = 2\mu_R = 2 \cdot m_T$ with $m_T = \sqrt{((p_T(c) + p_T(\bar{c}))/2)^2 + m_c^2}$ is taken. The value of Λ_{QCD} is set to 0.226 and α_s to 0.118. All the calculations are performed in the DIS renormalisation scheme.

2.4 Monte Carlo Studies of $D^*\mu$ Events

Some of the expected distributions from the Monte Carlo simulations are now discussed.

Table 2.5 shows predictions for the charm and photoproduction cross sections separately for the direct and resolved contributions. The latter is separated into normal resolved and excitation contributions. The first row in each case shows the inclusive charm or beauty production cross sections. Several intermediate stages between these inclusive cross sections and the visible $D^*\mu$ cross sections (last row) are quoted. In the case of direct photoproduction the cross section reduces by a factor of 4025 for charm production and by a factor of 68 for beauty production. These factors contain the branching ratios and the acceptances \mathcal{A} , $\mathcal{A}_c^{direct} = 1.0\%$ and $\mathcal{A}_b^{direct} = 11\%$.

The requirement of $p(\mu) > 2$ GeV/c together with the requirement of D^* -mesons and muons identified in the central detector ($|\eta(D^*)| < 1.5$ and $|\eta(\mu)| < 1.735$) leads to a strong enrichment of events from beauty production.

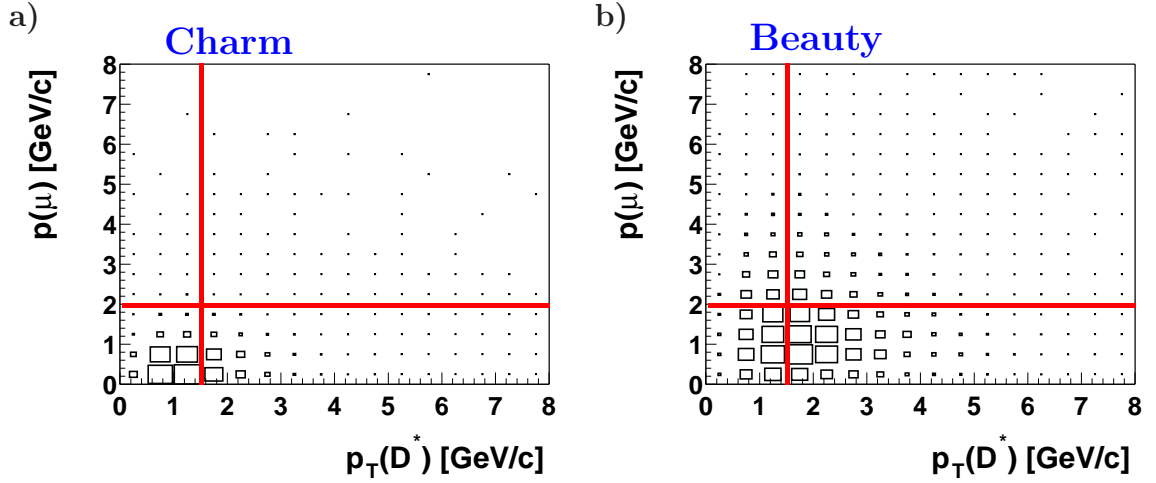


Figure 2.9: Correlation between the transverse momentum $p_T(D^*)$ of the D^* and the momentum $p(\mu)$ of the muon for photoproduction in the visible range before applying p_T and p cuts. a) charm production, b) beauty production.

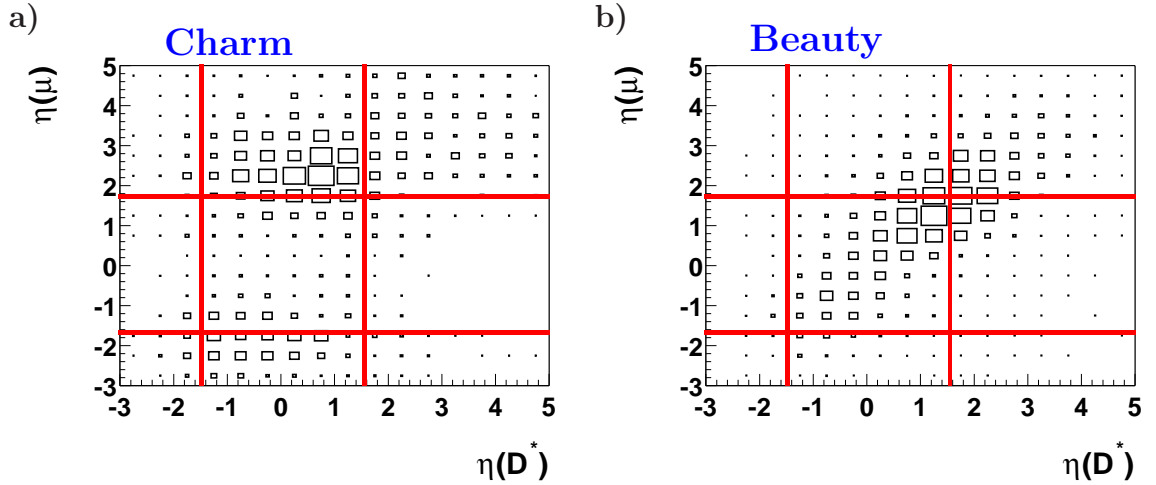


Figure 2.10: Correlation between the pseudorapidities η of the D^* and the muon for photoproduction in the visible range before applying η cuts. Left: charm production, right: beauty production.

The acceptances for events from excitation processes are only slightly smaller than those of the direct processes. For charm production an acceptance of $A_c^{ex} = 0.8\%$ and for beauty production an acceptance of $A_b^{ex} = 11\%$ are obtained. The cross section of the normal resolved component is already for the inclusive cross section significantly smaller than the direct or excitation cross sections. The contribution of the normal resolved component to the total inclusive charm photoproduction cross section is 7.6%. For beauty production a fraction of 12% is obtained. The selection of $D^*\mu$ -pairs leads to a further strong suppression of this component. In particular the cut on the pseudorapidity of the D^* and the momentum of the muon reduce this fraction significantly. Since the predicted fraction in the visible range for charm production is smaller than 1.7%, and for beauty production $\lesssim 4.0\%$, the normal resolved component is neglected in this analysis.

b -scenario	B^0 -osc.	correlation regions [%]				
		1	2	3	4	1-4
A $D^*\mu$ from diff. quarks cascade decay	-	1.4	14.5	17.7	43.4	76.9
	D^* -side	1.0	7.5	1.6	2.6	12.7
	μ -side	0.5	6.0	0.2	1.2	7.9
	both sides	-	0.2	1.2	1.0	2.4
	Σ	2.9	28.2	20.7	48.2	100
B $D^*\mu$ from diff. quarks direct decay	-	10.9	55.7	0.6	7.8	75.1
	D^* -side	0.1	0.5	2.0	10.3	12.9
	μ -side	0.1	0.6	1.6	7.8	10.1
	both sides	0.3	1.5	-	0.2	2.0
	Σ	11.3	58.3	4.3	26.1	100
C $D^*\mu$ from same quark	-	-	-	65.2	19.3	84.5
	D^* -side	-	-	11.8	3.7	15.5
	Σ	-	-	77.0	23.0	100

Table 2.6: Contributions of the three different beauty decay scenarios (see page 45) depending on the correlation regions for photoproduction. The contributions are split further into those without any (or two of the same b -side) B^0 -meson oscillation, with one, where this oscillation is assigned to the D^* or muon side, and with two oscillations for the beauty scenarios A and B, where the two particles are coming from different heavy quarks.

In figures 2.9 and 2.10 the correlations between the transverse momentum $p_T(D^*)$ of the D^* -meson and the momentum $p(\mu)$ of the muon and the correlations of the pseudorapidities η of the D^* -meson and of the muon are shown for charm and beauty production in photoproduction. The distributions in figure 2.9 and 2.10 are shown in the visible range ($Q^2 < 1 \text{ GeV}^2$, $0.05 < y < 0.75$, $p_T(D^*) > 1.5 \text{ GeV}/c$, $|\eta(D^*)| < 1.5$, $p(\mu) > 2.0 \text{ GeV}/c$, $|\eta(\mu)| < 1.735$) before applying the p_T and p cuts and the η cuts respectively. The visible range is marked by lines within both figures. For charm only the tails of the $p_T(D^*)$ and $p(\mu)$ distributions fall in the visible range of the detector. For beauty the situation is slightly better. In case of beauty the dominant region of $D^*\mu$ event production lies in the $\eta(D^*)$ range $0.5 < \eta(D^*) < 2.5$ and in the $\eta(\mu)$ -range $0.5 < \eta(\mu) < 2.5$. For charm the contribution of $D^*\mu$ events, with a central D^* -meson and a muon in the forward or backward direction is largest. The contribution, where both particles are in the central region is small. An extension of the visible range towards the forward region should lead to a strong increase in the number of $D^*\mu$ events.

The transverse momentum distribution of the D^* -meson and the muon momentum distribution as well as the pseudorapidity distributions of the D^* -meson and the muon in photoproduction are shown for charm production in figure 2.11 and for beauty production in figure 2.12. The effect of applying step-by-step the p_T , p and η cuts to these distributions is also presented. In particular the cut on the momentum of the muon leads to a strong modification of the shape of the pseudorapidity of the muon (figure 2.11 d)). After applying this cut a minimum is observed in the central region, where a maximum was before. For beauty the same cut has a much less dramatic effect (figure 2.12 d)). The reason for this behaviour is the soft muon momentum spectrum in case of charm production.

The simplified picture of the possible charge and angular correlations for the different beauty scenarios can be extended using the Monte Carlo simulation. Table 2.6 shows

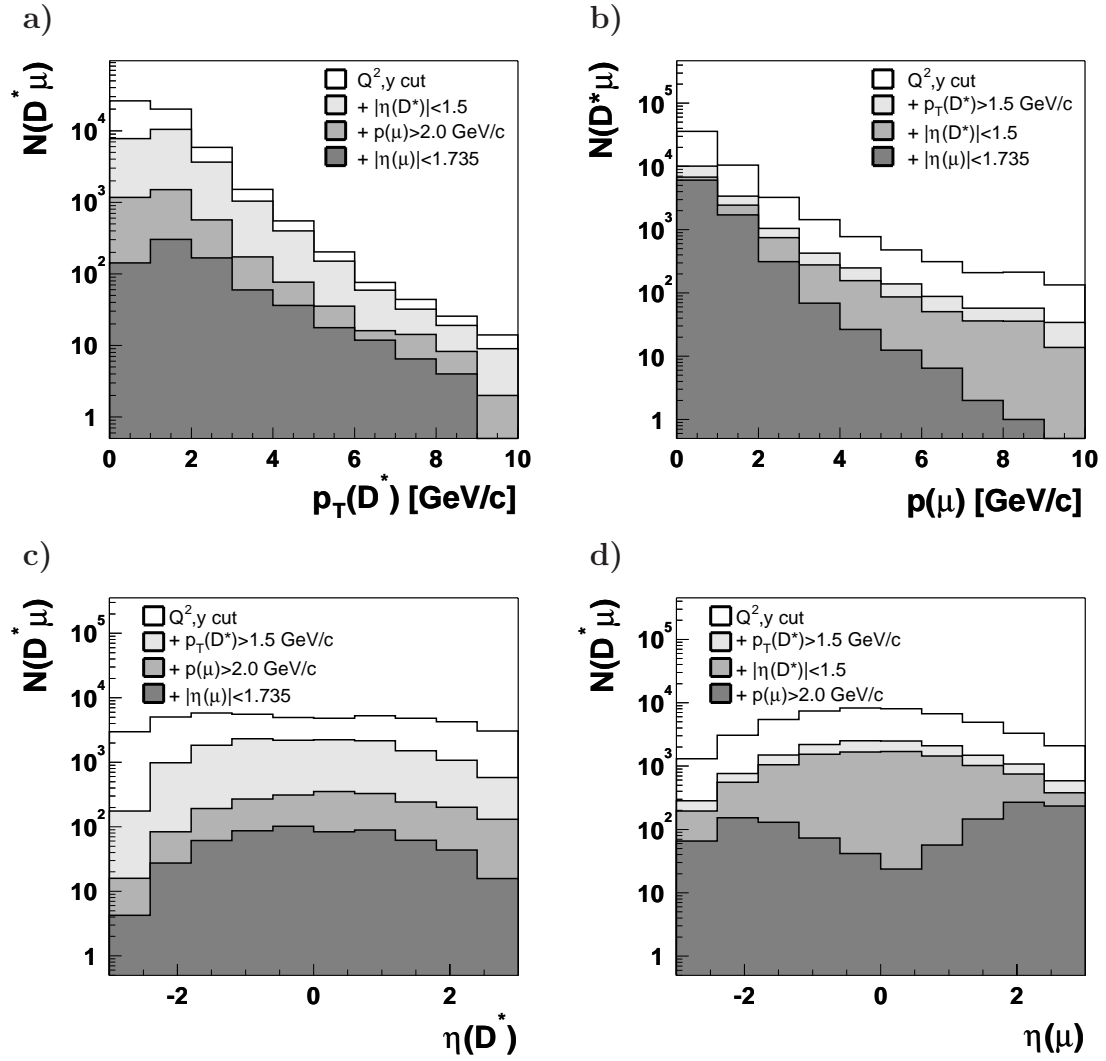


Figure 2.11: Transverse momentum $p_T(D^*)$ (a), muon momentum $p(\mu)$ (b), pseudorapidity of the D^* -meson $\eta(D^*)$ (c) and the pseudorapidity of the muon $\eta(\mu)$ (d) in **photoproduction charm** events. The change of these distributions in size and shape by applying the other three kinematical constraints step by step is also presented (see legend).

the contributions of the three different beauty scenarios (see page 45) depending on the correlation regions. The contributions are divided further into those without any B^0 -meson oscillation, those with one oscillation assigned to the D^* or muon side, and those with two oscillations for the beauty scenarios A and B (where the two particles are coming from different heavy quarks). In the case of beauty scenario A a large contribution in correlation region 2 is obtained, which is not expected naively. In the case of no B^0 -meson oscillation this contribution is due to processes like $b \rightarrow c\tau^-\bar{\nu}_\tau \rightarrow c\bar{\nu}_\tau\mu^-\bar{\nu}_\mu\nu_\tau$ and $b \rightarrow c\bar{c}s$. In the case of beauty scenario B (considering no B^0 oscillation) contributions are obtained also in correlation region 3 and 4, although naively no contributions are expected. These contributions are caused by the process $b \rightarrow c\bar{c}s$. Furthermore it is obvious, that in case of the third beauty scenario, a significant fraction is obtained for $\Delta\Phi^* > 90^\circ$, and therefore in correlation region 4.

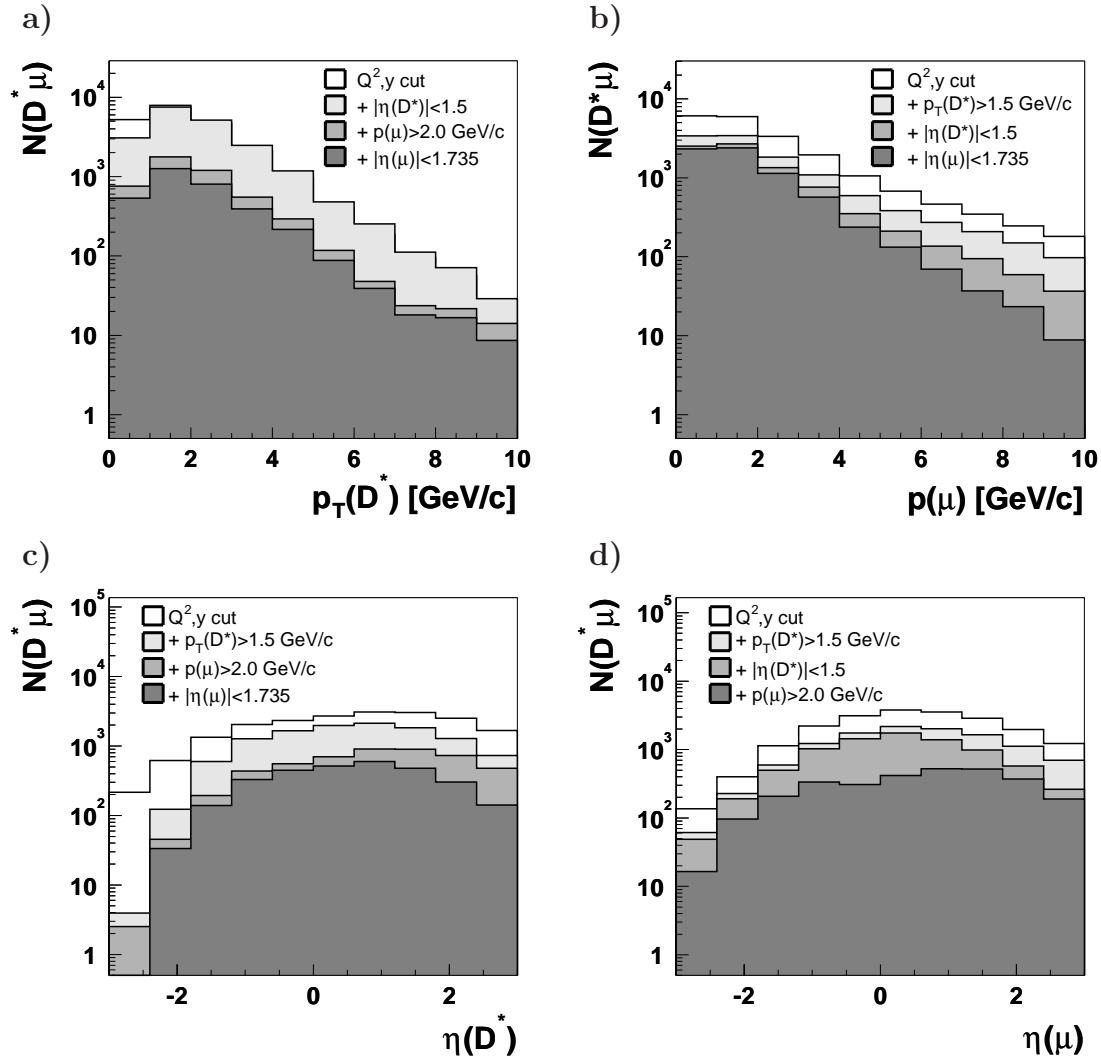


Figure 2.12: Transverse momentum $p_T(D^*)$ (a), muon momentum $p(\mu)$ (b), pseudorapidity of the D^* -meson $\eta(D^*)$ (c) and the pseudorapidity of the muon $\eta(\mu)$ (d) in **photoproduction beauty** events. The change of these distributions in size and shape by applying the other three kinematical constraints step by step is also presented (see legend).

Table 2.7 summarises the contributions of the three different beauty scenarios to each correlation region. The dominant contribution to correlation region 2 comes from scenario B. For correlation region 3 the main contribution is from scenario C. In correlation region 4 the largest contribution is not given by scenario A but scenario C. This is due to the smaller acceptance for muons from cascade decays (e.g. soft $p(\mu)$ spectrum) than for those from the other two scenarios.

correlation region	beauty scenario [%]		
	A	B	C
1	5.8	94.2	-
2	10.5	89.5	-
3	3.1	2.5	94.4
4	14.9	27.9	57.3
1-4	7.7	30.3	62.0

	$\Delta\Phi^* < 90^\circ$	$\Delta\Phi^* \geq 90^\circ$
$Q(\mu) = Q(D^*)$	1 no charm few beauty	2 no charm beauty
$Q(\mu) \neq Q(D^*)$	3 few charm beauty	4 charm beauty

Table 2.7: Contributions of the three different beauty decay scenarios (see page 45) in each correlation region for photoproduction.

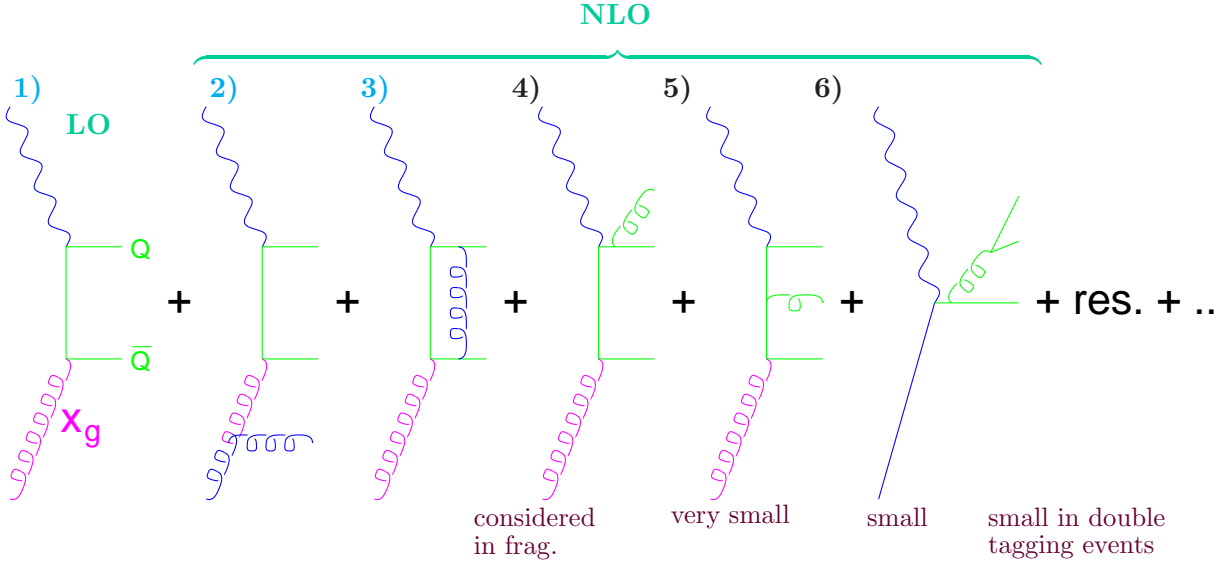


Figure 2.13: Contributions to the heavy quark cross section up to NLO.

2.5 Procedure for Extracting the Unintegrated Gluon Density

As already discussed in the last chapter the unintegrated gluon density is extracted using CCFM evolution model. The unintegrated gluon density $\mathcal{A}(x_g, k_T, \vec{q}'_t)$ depends on three quantities: the momentum fraction x_g of the incoming parton taking part in the hard interaction (in systems without a transverse momentum of the initial parton), the transverse momentum of this parton k_T and the maximum allowed angle \vec{q}'_t (see section 1.3.4).

These quantities can be calculated from the four-momenta of the two heavy quarks. Figure 2.13 shows the different processes contributing to the heavy quark cross section up to NLO. The normal resolved contribution can be neglected as previously discussed (section 2.4). The production of heavy quarks via gluon splitting is very small ($< 5\%$ [73]) in all kinematic ranges and has no strong impact on the distributions of the three relevant quantities. The excitation processes are given in principle by the second Feynman diagram and by the one, where a gluon is radiated from an internal quark line (Feynman diagram 5)). The latter contribution is very small. The radiation of a gluon from an external heavy quark line is automatically included in the final state parton showers modelled in the Monte Carlo simulations.

The dominant contributions are the processes 1-3. For these the following formulae hold:

$$x_g = \frac{M^2(Q\bar{Q}) + Q^2}{y \cdot s} \quad (2.32)$$

$$k_T = p_T^*(Q\bar{Q}) \quad (2.33)$$

$$\vec{q}'_t = x_g \cdot \sqrt{s \cdot \frac{E_p}{E_e} \cdot \exp(-2\hat{y}_{Q\bar{Q}})} \quad (2.34)$$

Here $M(Q\bar{Q})$ is the invariant mass of the heavy quark pair, $p_T^*(Q\bar{Q})$ its transverse momentum measured in the photon proton rest frame, and $\hat{y}(Q\bar{Q})$ is the rapidity of the quark pair in the laboratory frame. E_p and E_e give the energy of the incoming proton or electron respectively and Q^2 is the virtuality of the photon. y is the Björken variable. Equation 2.34 was already derived in section about 1.3.4. Equation 2.33 is obtained from momentum conservation and the fact that in the photon-proton rest frame, the photon has no transverse momentum with respect to the z -axis. Only the incoming gluon can then have a non-zero transverse momentum and this momentum has to be balanced by the two heavy quarks, equation 2.33 has to hold.

In case of photoproduction equations 2.32 and 2.33 reduce to:

$$x_g = \frac{M^2(Q\bar{Q})}{y \cdot s} \quad (2.35)$$

$$k_T = p_T^*(Q\bar{Q}) \approx p_T(Q\bar{Q}) \quad (2.36)$$

Here the transverse momentum of an arbitrary particle in the photon-proton rest frame is unchanged in the laboratory frame.

A short derivation of equation 2.32 is given below for those events, where x_g is connected to the relative momentum fraction of the proton carried by the gluon (all systems with $k_T = 0$). The reaction $\gamma g \rightarrow Q\bar{Q}$ is considered for this purpose. The four-momenta of the gluon $g = (x_g \cdot E_p, 0, 0, x_g \cdot E_p) = x_g \cdot (E_p, 0, 0, E_p) = x_g \cdot P$, the photon momentum q ($q^2 = -Q^2$) and the four momenta of the heavy quarks p_Q and $p_{\bar{Q}}$ are related as:

$$\begin{aligned} g + q &= p_Q + p_{\bar{Q}} \\ \Rightarrow (g + q)^2 &= (p_Q + p_{\bar{Q}})^2 = M^2(Q\bar{Q}) \\ \Leftrightarrow g^2 + 2 \cdot qg + q^2 &= M^2(Q\bar{Q}) \\ \Rightarrow 2 \cdot x_g \cdot qP - Q^2 &= M^2(Q\bar{Q}) \\ \stackrel{x=Q^2/\langle 2q \cdot P \rangle}{\Leftrightarrow} Q^2 \cdot \frac{x_g}{x} - Q^2 &= M^2(Q\bar{Q}) \\ \Leftrightarrow x_g &= \frac{M^2(Q\bar{Q}) + Q^2}{Q^2/x} \\ \stackrel{Q^2 \stackrel{=}{\Leftrightarrow} x \cdot y \cdot s}{\Leftrightarrow} x_g &= \frac{M^2(Q\bar{Q}) + Q^2}{y \cdot s} \end{aligned}$$

Since x_g depends only on Lorentz invariant quantities it is also Lorentz invariant. Therefore this definition of x_g holds in all frames. However the interpretation of x_g as the relative momentum fraction of the gluon to the proton momentum is only valid in systems where $k_T = 0$.

In [73] a slightly different x_g definition is proposed for the photoproduction regime (laboratory frame):

$$x_g = \frac{M(Q\bar{Q})}{\sqrt{s}} \cdot \sqrt{\frac{E_e}{E_p}} \cdot \exp(\hat{y}(Q\bar{Q})) \quad (2.37)$$

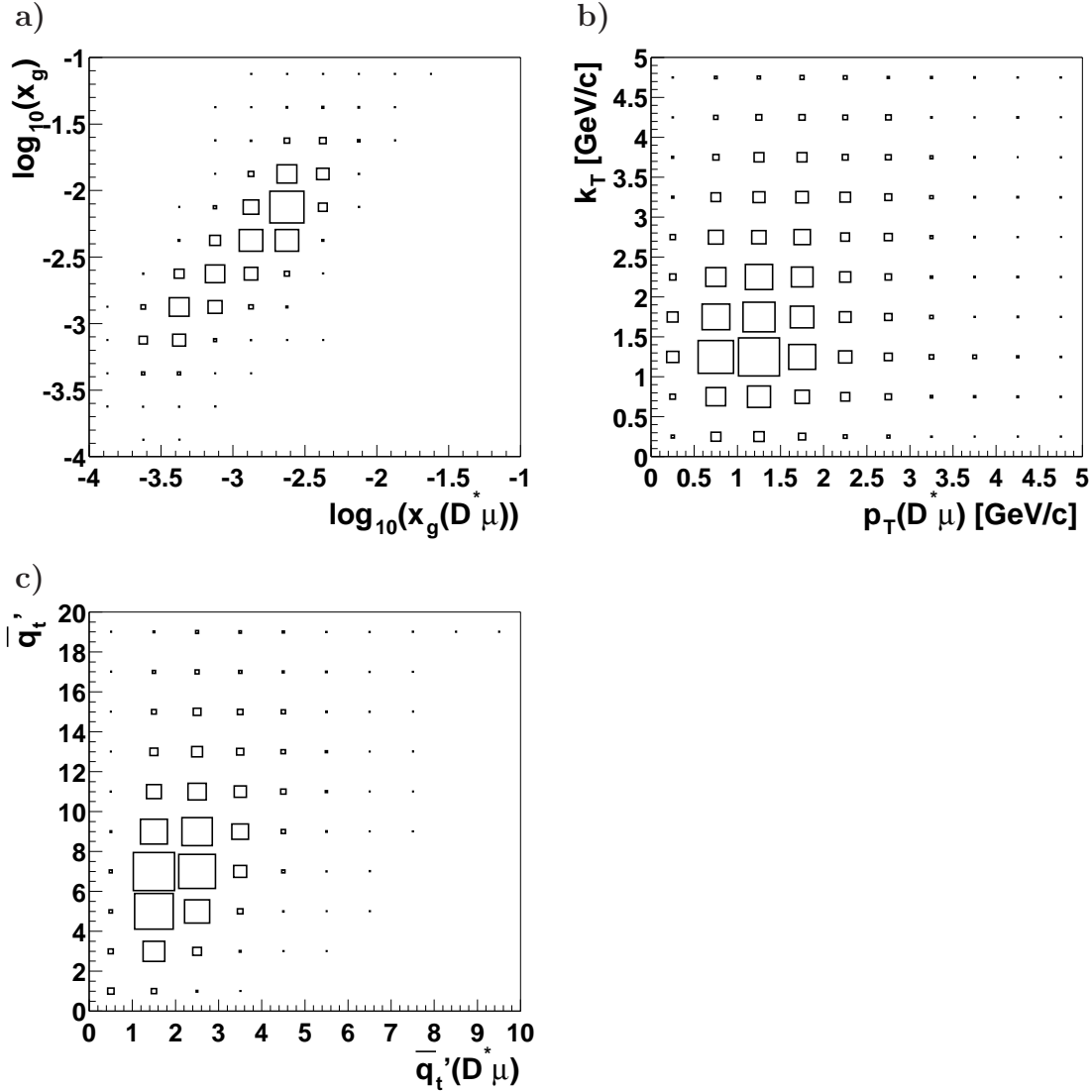


Figure 2.14: Correlation between variables, on which the unintegrated gluon density depends, a) x_g , b) k_T and c) \bar{q}_t' reconstructed via the quark and via the $D^*\mu$ quantities. The correlation is shown for charm production in the photoproduction domain. Only events of the correlation region 4 ($\Delta\Phi^* \geq 90^\circ$ and different charges) are selected.

This formula holds also for the normal resolved processes, however it is valid only for $k_T = 0$. Therefore this formula is not suitable for the extraction of the unintegrated gluon density, where $k_T = 0$ can no longer be assumed.

In this analysis the unintegrated gluon density is extracted using definition of x_g given in equation 2.32. The four-momenta of the heavy quarks are approximated by those of the D^* -meson and the muon. Figure 2.14 shows for charm production in photoproduction the correlation between x_g , k_T and \bar{q}_t' obtained from $D^*\mu$ quantities and obtained from $Q\bar{Q}$ -quantities. For x_g a relatively good correlation between the $D^*\mu$ and the quarks is observed, while for the two other variables k_T and \bar{q}_t' the correlations is worse, due to fragmentation effects and in particular the semileptonic decay in the case of the muon.

The correlations would improve strongly, if the heavy quark pair were tagged using two D -mesons and the correlation would be much worse, if the heavy quark pair were tagged using two muons.

The distributions based on the $Q\bar{Q}$ variables will be obtained via an unfolding (see chapter 9). Here the correlation between the $D^*\mu$ and the $Q\bar{Q}$ quantities (figure 2.14) are exploited. In the unfolding detector effects can also be considered, if the unfolding matrix is obtained from a Monte Carlo simulation. Since in this double-tagging analysis the unfolding has to correct only for fragmentation effects and does not rely on any assumption about the heavy quark momenta or their correlation, a LO-Monte Carlo can be used for the unfolding. An unfolding with NLO calculations is not expected to yield better results, because the fragmentation is treated in a much simpler way. The unintegrated gluon density depends on three variables and thus in principle a threefold differential distribution has to be determined and unfolded. Since the data are statistically limited, only single and double differential distributions with a few bins can be considered.

The differential cross sections depending on x_g , but calculated in bins of k_T and \vec{q}'_t , are related to the unintegrated gluon density $x_g\mathcal{A}(x_g, k_T, \vec{q}'_t)$ as follows:

$$\frac{d\sigma(k_T, \vec{q}'_t)}{dx_g} = x_g\mathcal{A}(x_g, k_T, \vec{q}'_t) \cdot \frac{d\sigma^{g=1}(k_T, \vec{q}'_t)}{dx_g} \quad (2.38)$$

The cross section on the right-hand side corresponds to the hard subprocess cross section ($\gamma g^* \rightarrow Q\bar{Q}$ in case of photoproduction and $\gamma^* g^* \rightarrow Q\bar{Q}$ in case of DIS) in the visible range convoluted with the photon flux. The “g=1” indicates that it is obtained by a constant gluon density ($k_T^2 \cdot x_g\mathcal{A}(x_g, k_T, \vec{q}'_t) = 1$). This cross section can be calculated with the CASCADE Monte Carlo event generator with a gluon density which is flat in all variables instead of using the the normal parton density function of the proton. Since an unintegrated gluon density is directly related to an off-shell calculation of the hard subprocess, the Monte Carlo event generator CASCADE has to be used instead of a Monte Carlo generator based on the DGLAP evolution model.

The calculated cross section is given for a specific factorisation scale μ_F . Due to the statistical method used this scale μ_F^2 modifies to an average $\langle\mu_F^2(i)\rangle$ calculated over all events in the i -th interval of the different distributions. In each bin i the averaged factorisation scale is different and to obtain an unintegrated gluon density at an overall averaged factorisation scale $\langle\mu_F^2\rangle$, which holds for all events and not only for a single bin, the data points have to be propagated in μ_F^2 using a given parametrisation. With that equation 2.38 modifies to:

$$x_g\mathcal{A}_i(x_g, k_T, \vec{q}'_t, \langle\mu_F^2\rangle) = \frac{x_g\mathcal{A}(x_g, k_T, \vec{q}'_t, \langle\mu_F^2\rangle)}{x_g\mathcal{A}(x_g, k_T, \vec{q}'_t, \langle\mu_F^2(i)\rangle)} \cdot \frac{d\sigma(k_T, \vec{q}'_t)}{dx_g} \cdot \left(\frac{d\sigma^{g=1}(k_T, \vec{q}'_t)}{dx_g}\right)^{-1} \quad (2.39)$$

In [74] it was shown that the effect of this propagation factor is very small compared to the large statistical errors, since within the errors no strong dependence of the gluon density on the factorisation scale μ_F^2 is observed. Therefore in this analysis no such propagation factor is applied and equation 2.38 will be used.

Chapter 3

The H1 Experiment at HERA

The data used in this analysis were taken by the H1 detector at the HERA machine. At HERA electrons and protons are accelerated in two separate beams and the two beams collide inside the H1 and ZEUS detectors. The particles produced during an interaction are measured by different components of the detector.

The electron-proton collider HERA is introduced first and then the H1 detector is described focussing on the components which are important for this analysis.

3.1 The HERA Accelerator

The ep storage ring HERA (see figure 3.1) is situated at the DESY laboratory in Hamburg, Germany. It has a circumference of 6.4 km and consists of two separate storage rings, one

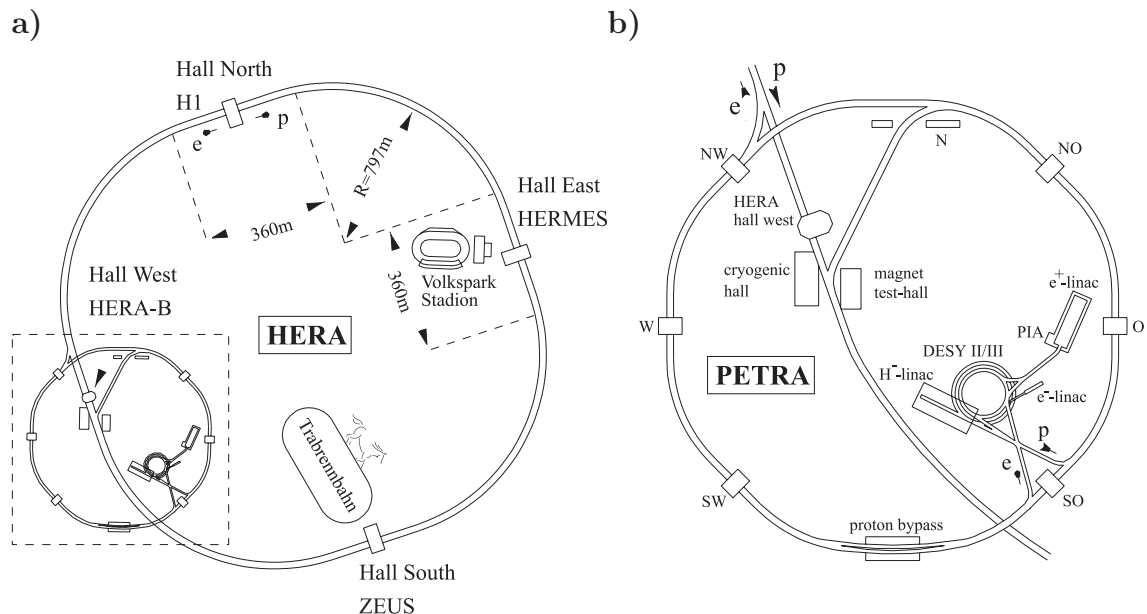


Figure 3.1: a) The HERA accelerator and its four experiments H1, ZEUS, HERMES and HERA-B. b) HERA pre-accelerators.

for protons and one for electrons or positrons. The electron and proton beams collide in two interaction regions where the detectors H1 and ZEUS are located. There are two more experiments, HERMES and HERA-B, which use only one of the beams. The HERMES experiment uses the longitudinally polarised electron beam to study the spin structure of the nucleons. The HERA-B experiment uses the proton beam from HERA. The beam is focussed on a wire target to produce B -mesons. In ep -ring-accelerators, transversally polarised electrons are automatically produced, while for longitudinal polarisation spin rotators are needed. During the data taking period 1992-2000 (referred to as HERA I) only the HERMES experiment had a longitudinally polarised electron beam. After the HERA upgrade (HERA II), longitudinally polarised electron beams are also possible in the ZEUS and H1 detectors. Furthermore, a second aim of the HERA upgrade is to increase the luminosity by a factor 3-5.

Before injection into the HERA storage ring the electrons as well as the protons are accelerated in so-called pre-accelerators. They are accelerated further in the HERA ring itself. The electrons achieve a maximum energy of 27.5 GeV and the protons an energy of 820 GeV / 920 GeV before / since 1998 respectively. This results in a centre-of-mass energy of $\sqrt{s} \approx 300$ GeV before 1998 and $\sqrt{s} \approx 318$ GeV since 1998 respectively. In the year 1998 and in the first part of 1999 electrons were used instead of the positrons used usually.

The beam particles are stored in up to 220 bunches with a bunch crossing interval of 96 ns, corresponding to a rate of 10.4 MHz. The bunches consist of about $10^{10} - 10^{11}$ particles. A small number of non-colliding bunches, so-called pilot bunches, are used for background studies. The lifetime of the lepton beam is about 10 hours for positrons and only 6 hours for the electron beam. In contrast to positrons, electrons can recombine with the ions of the residual gas in the beam pipe. This leads to a shorter electron beam lifetime. The typical lifetime of the proton beam is with several 100 hours much larger.

3.2 The H1 Detector

The H1 detector is a typical multi-purpose detector designed to measure the momentum and the energy of particles produced in an ep interaction. To ensure an almost complete reconstruction of such an ep collision event, the detector has an almost hermetic coverage around the beam axis. The asymmetric construction of the detector takes the different beam energies of the electron and proton into account. Due to the larger energy of the protons the centre-of-mass system is not at rest but shifted in the direction of the proton. Therefore a large number of produced particles have a momentum in proton direction. The instrumentation in this direction is enhanced.

The right-handed coordinate system used at H1 has its origin at the nominal interaction point. The z -axis points in the proton beam direction. The region with positive z is called the “forward” region. The x -axis points towards the centre of the HERA ring and the y -axis points perpendicularly upwards. The azimuthal angle ϕ is given by the angle with respect to the x -axis in the xy -plane. The polar angle θ is the angle with respect to the z -axis. Thus the polar angle is $\theta = 0^\circ$ in the proton direction and $\theta = 180^\circ$ in electron beam direction.

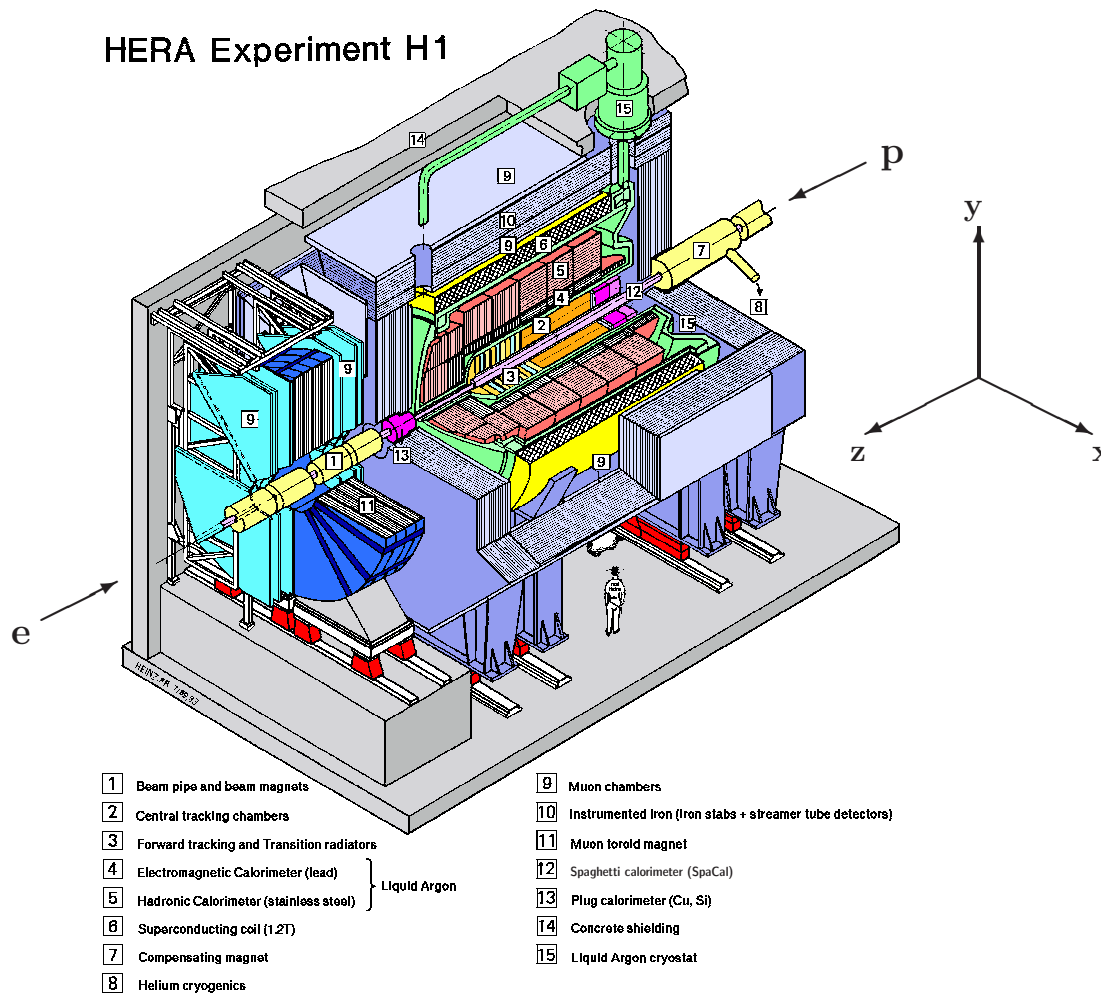


Figure 3.2: *Construction of the H1 detector.*

The components of the H1 detector (figure 3.2) are arranged around the beam axis. The tracking system as well as the calorimeter are located inside the super conducting coil, which produces a magnetic field for momentum measurement. This layout reduces the dead material in front of the calorimeter. The detector components from the inner components to the outer are:

- **Silicon Tracker:** The central and backward silicon tracker (CST and BST respectively) measure the hits of charged particles via ionisation in semiconductors. Since they are located near to the interaction point and since the spatial resolution is very high, they can be used to determine primary and secondary vertices. The BST covers the angular range $162^\circ \leq \theta \leq 176^\circ$ and makes a very precise measurement of the scattered electron possible. The CST is described in more detail in section 3.2.2. More information on the silicon trackers can be found in [75]. Since 2002 a third silicon tracker exists in the forward region (FST, forward silicon tracker).
- **Tracking detectors:** The central tracking detector (CTD) consists of two central jet chambers (CJC1 and CJC2), two central z -drift chambers (central inner/outer

z -drift chamber, CIZ/COZ) and two proportional chambers (inner/outer proportional chamber CIP/COP). In the jet chambers (see section 3.2.1) the momentum and the direction of charged particles are measured via ionisation in a gas. Since the measurement of the z -coordinate is with a resolution of $\sigma_z = 6\text{-}7$ cm much less precise than the measurement in the xy -plane ($\sigma_{xy} = 150 \mu\text{m}$), the z -coordinate is improved by an additional z determination in the z -chambers, which have a better resolution of $\sigma_z = 350 \mu\text{m}$.

The forward tracking detector (FTD) consists of three so-called super modules each segmented in a forward proportional chamber (FPC), radial and planar drift chambers and a transition radiator. The FTD covers the angular range $5^\circ \leq \theta \leq 30^\circ$.

To measure the momentum of charged particles in the backward direction ($151^\circ \leq \theta \leq 177.5^\circ$) the backward drift chamber (BDC) is used. The BDC is mainly used to detect the scattered electrons.

More information about the tracking detectors can be found in [76], and references therein.

- **Calorimeter:** The tracking detectors are surrounded by a liquid argon calorimeter (LAr) [77] in the central and forward region. The main task of the calorimeter is the identification of neutral and charged particles and also jets and the energy measurement of these objects. The LAr is a sandwich calorimeter consisting of an inner electromagnetic (EM) and an outer hadronic (HAD) part. The HAD calorimeter covers the angular range $4^\circ \leq \theta \leq 135^\circ$ and the angular coverage of the electromagnetic calorimeter ($4^\circ \leq \theta \leq 153^\circ$) extends more into the backward direction. To identify hadrons in the very forward range $0.6^\circ \leq \theta \leq 4^\circ$ the so-called plug calorimeter is used. In the backward direction the spaghetti calorimeter (SpaCal) (see section 3.2.3 and [78]) is installed, which is mainly used to measure the energy and the angle of the scattered beam electron.
- **Super conducting coil:** The LAr calorimeter is located inside a super conducting coil, which produces a magnetic field of 1.15 Tesla. Charged particles are deflected and make a momentum measurement of these particles possible.
- **Muon system:** The muon system consists of two subdetectors, the central muon detector (CMD) and the forward muon detector (FMD). Both are designed for the identification of muons. The CMD is described in more detail in section 3.2.4. More information on the CMD can be found in [79]. The FMD [80] covers the polar angular range $3^\circ < \theta < 17^\circ$. It is a spectrometer consisting of a toroid magnet between three double layers of drift chambers at both sides. For muons with momenta $p > 5 \text{ GeV}/c$ a momentum measurement with a resolution of up to 24% is possible. The resolution decreases slowly for larger momenta.
- **Time-of-flight system:** The time-of-flight system (ToF) consists of scintillators located at both ends of the detector along the beam pipe. The scintillators have a good time resolution of 1 ns and are used to reject beam-induced background arriving out-of-time in the H1 detector.
- **Luminosity system:** The luminosity is measured via the Bethe-Heitler process $ep \rightarrow ep\gamma$, for which the cross section is very well known. The luminosity system is situated downstream from the H1 detector in the direction of the electron beam. It consists of a photon detector (PD) at $z = -103\text{ m}$ and the electron tagger (ET33)

at $z = -33$ m. In the offline reconstruction only the photon measurement is used. This leads to a precision of better than 2% for the measurement of the integrated luminosity. For online luminosity measurement electron identification in the ET33 is also used.

Furthermore, ET33 and the other electron taggers (ET44 at $z = -44$ m and the ET8 at $z = -8$ m) can be used to detect the scattered electron in photoproduction events at very small scattering angles ($\theta_{e'} \approx 180^\circ$), corresponding to photon virtualities $Q^2 < 0.01 \text{ GeV}^2$.

A more detailed description of the H1 detector can be found in [81] and [82] or on the web-page [83]. In the next subsections the components important for this presented analysis are described in more detail.

3.2.1 Central Jet Chamber

The central jet chamber consists of two gas-filled coaxial cylinders situated along the beam axis from $z = -1.1$ m to $z = +1.1$ m. The first chamber CJC1 has an inner radius of 20.3 cm and an outer radius of 45.1 cm. Thus the polar angular range $11^\circ \leq \theta \leq 169^\circ$ is covered by the CJC1. The inner radius of the second chamber is 53.0 cm and the outer radius 84.4 cm. This leads to a slightly smaller angular coverage of $26^\circ \leq \theta \leq 154^\circ$.

The inner chamber CJC1 consists of 720 anode sense wires running parallel to the z -axis, distributed over 24 radial layers each with 30 azimuthal cells in ϕ (see figure 3.3). The outer chamber has 32 radial layers each with 60 cells, containing 1920 anode sense wires. The drift field is formed by cathode wires, which separate the sense wires in ϕ . A jet chamber cell extends azimuthally from the sense wire plane to both adjacent cathode wire planes. Radially it extends over the full radial length of the CJC1 or CJC2 respectively. The adjacent sense wires in such a cell are separated by two potential wires, which are set to ground. Thus there are four potential wires around each sense wire forming a square. This arrangement makes it possible to adjust drift field and gas amplification nearly independently. To get an almost uniform drift field the distance of the cathode wires to the sense wire plane is taken into account in the chosen voltage of the cathode wires. At the inner and outer end of each cell field wires are situated to ensure that the field is also at the end of the cells sufficiently uniform. The sense wires are offset from the nominal wire plane by $\pm 150 \mu\text{m}$ because of the electrical forces between them. This offset ensures that the position of the sense wire is always well known and it helps to identify mirror hits.

The jet chamber cells are tilted by 30° with respect to the radial direction. This provides two advantages: First the particles traversing the CJC cross a larger number of sense wire planes, meaning more drift cells are penetrated on average. This leads to a better track reconstruction and avoids track ambiguities (wrong track segments, consisting of mirror hits, no longer match). Secondly the Lorentz angle is approximately compensated by this tilt. The Lorentz angle is the angle between the electrical field and the drift direction of the electrons, which are deflected by the Lorentz force of the magnetic field.

The chambers are filled with a gas mixture, which is ionised if a charged particle traverses the chamber. The positive ions drift to the cathode wires and the electrons to the sense

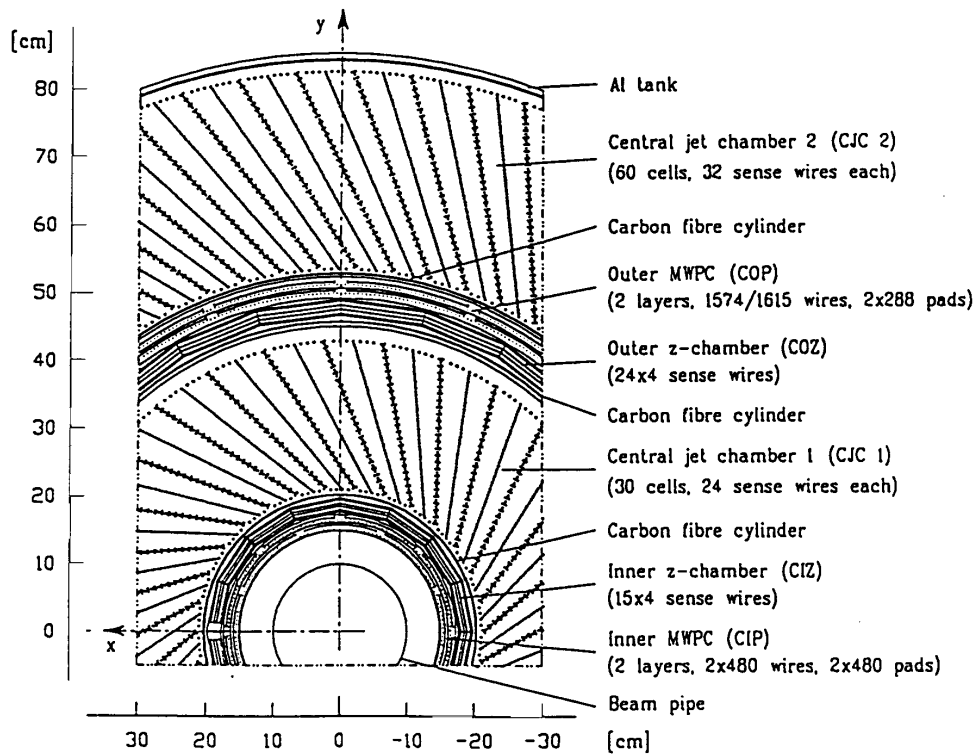


Figure 3.3: *Cross section view of the central jet chambers.*

wires. Between the cathode wires and the potential wires the field is almost uniform and thus the drift velocity of the electrons is almost constant. In the gas amplification range between potential wires and the sense wires, the electric field is proportional to $1/r$, where r indicates the distance of the electron to the sense wire. The electron gains sufficient energy to cause secondary ionisation and a chain of such processes leads to an avalanche of secondary electrons. On the sense wire the deposited charge of such an avalanche, caused by a charged particle, is measured and read out via an electronic circuit.

The distance of the track of a charged particle to the sense wire in the xy -plane is determined from the drift time. A spatial resolution of $\sigma_{xy} = 150 \mu\text{m}$ is achieved. The sense wires are read out at both ends and the z -coordinate is determined from the ratio of the measured charges at both ends (charge division). The resolution of the z -coordinate is $\sigma_z = 6 - 7 \text{ cm}$. A significant improvement is obtained by taking the z -chambers CIZ and COZ into account. Since their sense wires are perpendicular to the z -axis a two orders of magnitude better resolution is achieved.

A three dimensional hit for the track of a charged particle is determined from the drift distance as well as from the z -coordinate. The hits are assigned to tracks and a helix trajectory is fitted. From this fit the track parameters are obtained.

Further information, obtained by the drift chamber, is the energy loss per distance dE/dx . This quantity can be determined from the total collected charge on a sense wire. Since the energy loss depends on the momentum and on the mass of the particle it can be used together with the Bethe-Bloch formula [59] to get some information about the particle type.

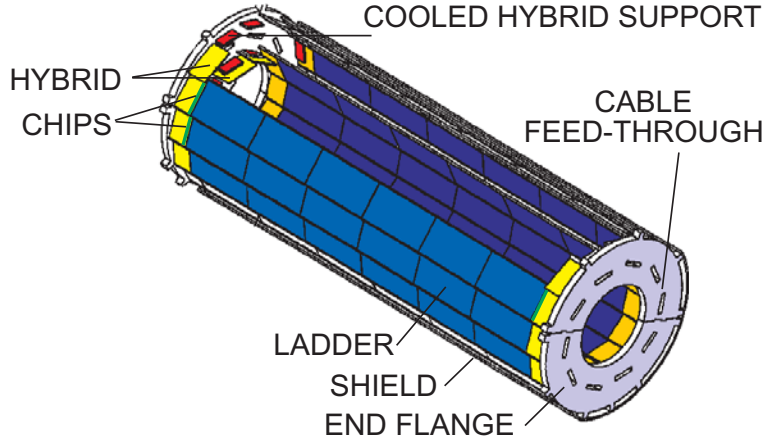


Figure 3.4: *Construction of the central silicon tracker CST.*

3.2.2 Central Silicon Tracker CST

The CST consists of two cylindrical layers of semiconductor (silicon) sensors. The inner radius is 5.57 cm and the outer 9.7 cm. The length of the CST is 44.2 cm. Thus the CST covers the polar angular range $30^\circ \leq \theta \leq 150^\circ$. The inner layer contains 12 so-called ladders, which are arranged around the z -axis. Each of the ladders consists in the z -direction of six silicon sensors and readout electronics at both ends. The outer layer is composed of 20 ladders (see figure 3.4).

When a charged particle traverses the CST an electron-hole pair is produced in the silicon. Due to the voltage between the inner and outer surface of the sensors, the electrons and holes drift to the inner or outer side. Here strips are mounted, from where the deposited charge is read out. Since the strips of both sides are perpendicular to each other it is possible to measure the $r\phi$ -coordinate as well as the z -coordinate. In $r\phi$ a resolution of $\sigma_{r\phi} = 12 \mu\text{m}$ is achieved and in z a resolution (depending on the polar angle) of up to $\sigma_z = 22 \mu\text{m}$ is obtained.

A three dimensional hit is determined from the position of the sensor and the two coordinates. Possible CST hits are then assigned to tracks measured in the CJC and the improved track parameters are found.

A more detailed description of the CST can be found in [84].

3.2.3 Spaghetti Calorimeter

The backward 'spaghetti' type calorimeter (SpaCal) covers the polar angular range $151^\circ \leq \theta \leq 178^\circ$ and is mainly used for the energy and angle measurement of the scattered electron. The acceptance of the SpaCal corresponds to photon virtualities in the range $1 \leq Q^2 \leq 100 \text{ GeV}^2$.

The SpaCal consists of scintillating fibres embedded in lead. If a particle reaches the calorimeter, secondary particles are produced via interactions with lead atoms. The secondary produced particles carry a large fraction of the energy loss of the initial particle.

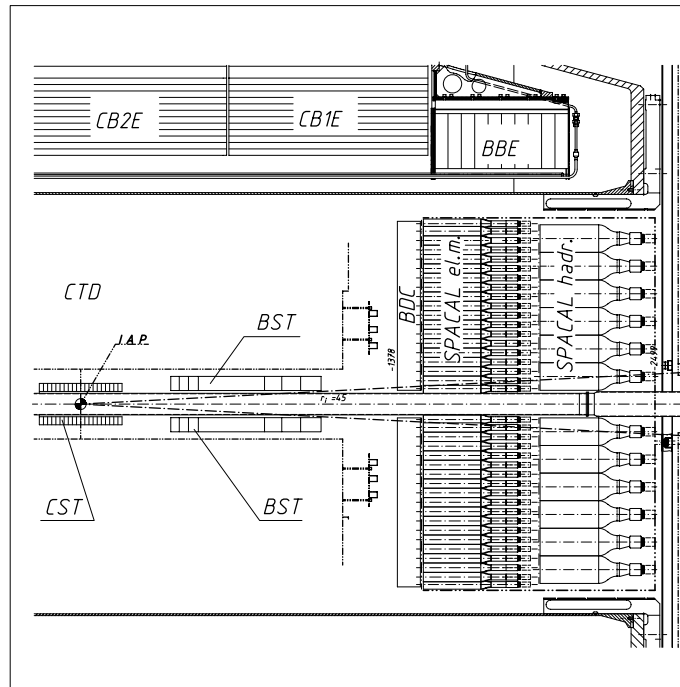


Figure 3.5: Cross section view of the backward spaghetti type calorimeter SpaCal.

A chain of such processes leads to a particle shower. In the scintillating fibres the energy of the secondary particles is measured. From the energy and their spatial distribution the total energy and the position of the primary particle is determined.

The SpaCal is divided into an electromagnetic and a hadronic section. Both sections have a thickness of 25 cm (see figure 3.5). Since the SpaCal is mainly used for the identification of the scattered electron, the hadronic part is only about one interaction length deep. An electron will deposit its total energy in the electromagnetic section, while a hadron will deposit only a small part of its energy in the hadronic section due to the larger extension of hadronic showers. Furthermore the segmentation is much finer in the electromagnetic part than in the hadronic part of the SpaCal. The electromagnetic part consists of 1192 quadratic cells with a length of 4 cm and the hadronic part of 136 cells with a cross-section of $12 \times 12 \text{ cm}^2$. The energies are measured with $\sigma_E/E = 7.5\% \sqrt{E [\text{GeV}]} \otimes 1\%$ in the electromagnetic and with $\sigma_E/E = 30\% \sqrt{E [\text{GeV}]} \otimes 7\%$ in the hadronic part of the SpaCal.

More information about the SpaCal can be found in [85].

3.2.4 Central Muon Detector

In contrast to all the particles (except neutrinos), which are in general stopped in the inner detector (up to the LAr), the energy loss of muons is typically very small in the calorimeter. Thus the muon systems are located outside the inner detector. The central muon detector consists of the iron return yoke of the magnet coil and limited streamer tubes which are situated in several slits of the iron yoke. The CMD is divided into four regions: the forward and backward barrel, which cover together the angular range $35^\circ \leq \theta \leq 135^\circ$, and

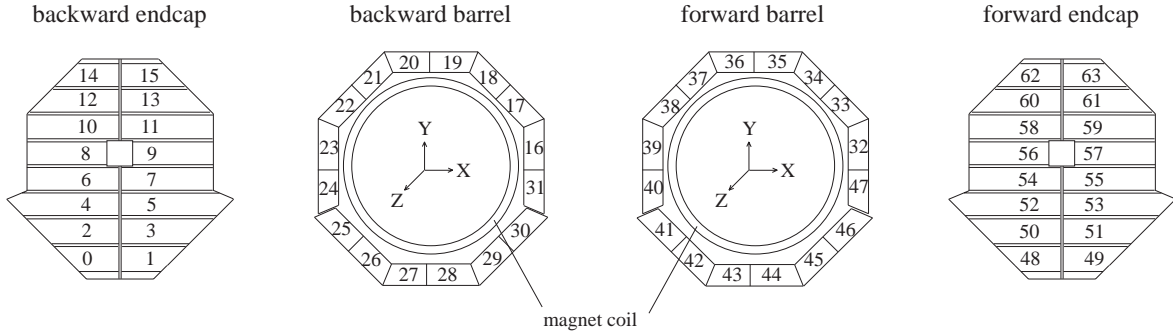


Figure 3.6: *Layout of the 64 modules of the instrumented iron.*

the forward and backward endcap. The forward and backward endcaps have an angular acceptance of $5^\circ \leq \theta \leq 35^\circ$ and $130^\circ \leq \theta \leq 175^\circ$ respectively. Each of these parts again consists of 16 modules (see figure 3.6). Altogether the CMD contains 64 modules. Each of these modules consists of 10 iron plates with a thickness of 7.5 cm in the radial direction (barrel) or in the z -direction (endcaps). In each slit of the iron one layer of streamer tubes is located, except for the slit between the fourth and fifth iron layer where two layers of streamer chambers are situated. In addition in front of and behind the instrumented iron so-called muon boxes are installed, each of them consisting of three layers with streamer chambers (see figure 3.7). These additional muon boxes improve the track measurement. Altogether 16 streamer chamber layers exist.

Two different types of streamer chambers are used: five layers with strips and 11 layers with pads. Each streamer chamber consists of several gas tight elements, which are again built up of two so-called 8-fold profiles. A profile contains 8 sense wires orientated along the z -axis in the barrel and along the x -axis in the endcaps. The muon chambers are also equipped on the top of those elements either with strips perpendicular to the wires or with pad electrodes to provide a two-dimensional measurement. The cross section of a muon chamber is $1 \times 1 \text{ cm}^2$ (see figure 3.8).

In analogy to the case of the CJC, the muon chambers are filled with a gas mixture, and in the same way as in the CJC, the momentum and direction of the penetrating muons is measured via ionisation in the gas. The resolution of the position measurement obtained by the wires reaches about 3 to 4 mm perpendicular to the direction of the wires and thus also perpendicular to the streamer tubes. The resolution for strip hits is about 10 to 15 mm along the sense wires and the pads define coarse space points with a precision of about 10 cm. The track reconstruction starts with the wire hits. The found track segments are fitted by a straight line and to get a curve several track segments are connected. Then the strip information is used to get a three-dimensional track. The strongly varying magnet field inside the CMD and the large energy loss of at least 80 MeV in one iron plate is taken into account for the track reconstruction. The pad information is used to resolve track ambiguities and to detect hadronic energy leaking from the LAr and SpaCal calorimeters. Details on the track reconstruction algorithm can be found in [86].

For trigger purposes the wire signals of layers 3, 4, 5, 8 and 12 are used. The endcap modules are grouped into an inner part containing the modules 6-11 (forward endcap) and 54-59 (backward endcap) and into an outer part. For each module a coincidence is evaluated for the n planes used out of total 5.

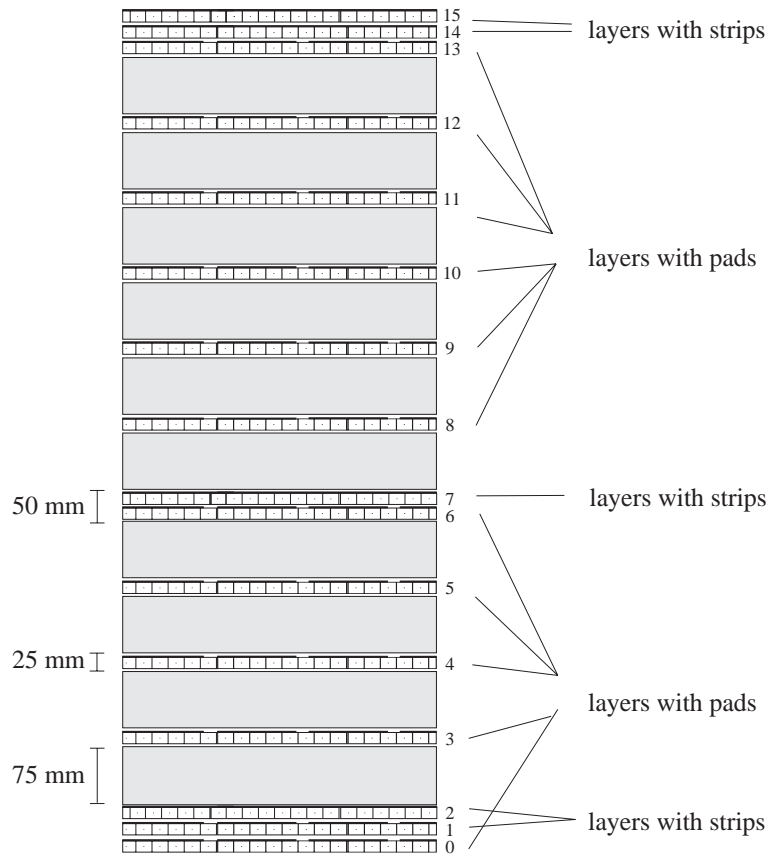


Figure 3.7: Cross Section of the central muon detector CMD.

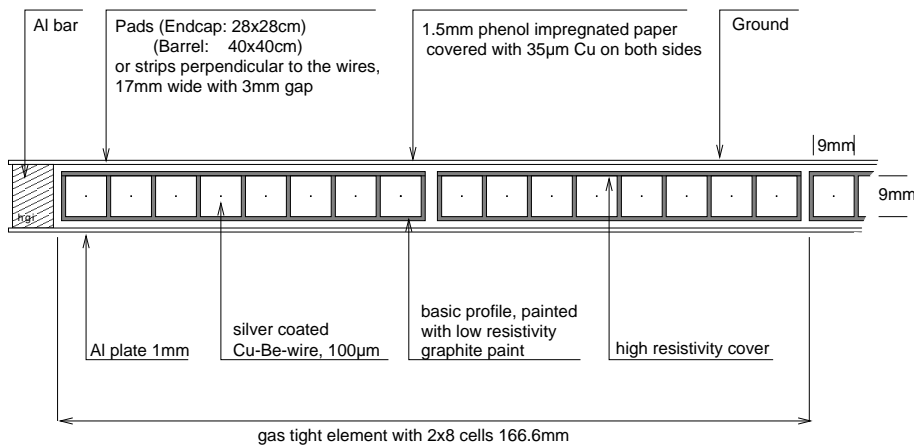


Figure 3.8: Cross section view of the basic chamber unit.

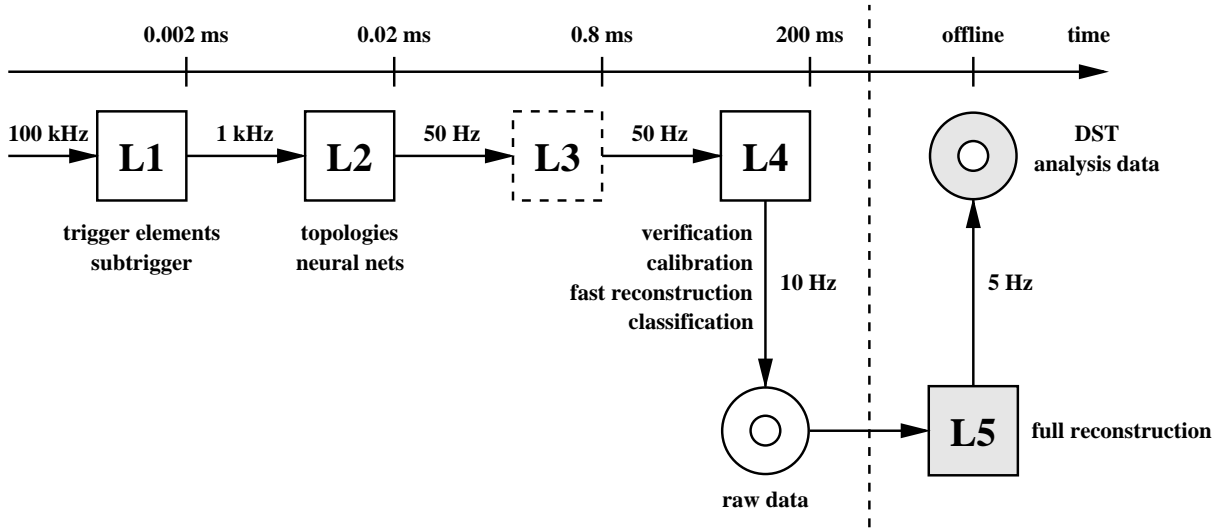


Figure 3.9: Overview of the trigger system.

3.2.5 Trigger System

The bunch crossing time of the electron and proton bunches at HERA is 96 ns, corresponding to a frequency of 10.4 MHz. Only in a small fraction of bunch crossings does this lead to an ep -reaction. Furthermore the rate of the background processes is several orders of magnitude higher than the ep event rate. The background arises mainly from collisions of the beam protons with rest gas atoms within the beam-pipe (beam-gas interactions). It is also possible that off-orbit protons hit accelerator or detector components which lead to so-called beam-wall background events. Furthermore cosmic muons and synchrotron radiation have to be considered in addition. Due to the short time interval between two bunch crossings of only 96 ns it is not possible to read out the whole detector and to select afterwards the interesting events (the dead time would be too high). Thus a trigger system is used. The task of triggers is to select in a short time (to minimise the dead time) the physically interesting events and to reject the background events in order to reduce the rate, at which the events are then later stored.

At H1 the trigger system consists of four levels (see figure 3.9), which reduce the rate in several steps. The input rate decreases from about 100 kHz at the first level (L1) down to 50 Hz at the fourth level (L4). At the same time the maximally allowed time on which a decision is made increases from $2.3 \mu\text{s}$ on L1 to 100 ms on L4.

First trigger level L1: Since the decision time of some detector components is significantly above 96 ns, the detector information of the last bunch crossings is stored intermediately in buffers (pipelines). This avoids dead time until the decision on L1 is made. The pipeline storage depth is $2.5 \mu\text{s}$ and thus determines the maximum allowed L1 decision time. In case of a positive trigger decision (L1 keep) no further signals are put into the buffer and the dead time of the experiment starts. The L1 decision is based on special trigger signals of the detector components, referred to as trigger elements. The 192 trigger elements are logically combined to 128 so-called subtriggers. If an event is accepted by at least one of the subtriggers the trigger decision is positive. L1 reduces the rate typically from about 100 kHz to 1 kHz.

Depending on the run and background conditions the level 1 subtriggers are prescaled to get an acceptable output rate. A prescale factor of n means, that only every n -th event which fulfills the subtrigger condition is accepted by L1.

Second trigger level L2: The second trigger level uses neural networks and topological correlations to reduce the rate. The maximum allowed decision time on L2 is 20 μ s. In the case of a negative decision on L2 the writing of detector signals of the following bunch crossings into the buffer starts again. Otherwise the detector readout starts. L2 reduces the rate to about 50 Hz. Trigger level L3, on which larger-scale analyses of the detector signals can be done, was not implemented during the HERA I data-taking period (1992-2000) but was an upgrade project for the HERA II data taking period.

Fourth trigger level L4: The fourth trigger level is a multi-processor farm, which performs a fast event reconstruction.

Until 1997 a trigger verification was done, which mimicked the L1 subtrigger conditions. Since 1997 a system of so-called hard scales and final state finders exists. Events, which fulfill at least one of the hard scales, like a track with a high transverse momentum, a muon with a transverse momentum above 1 GeV/c or a high energy cluster in the calorimeter, are accepted directly. If not, the events have to pass one of the final state finders, which depend on the verified L1 subtriggers. For this $D^*\mu$ analysis the open heavy flavour finder, which looks for D -mesons in general, and the closed heavy flavour finder, which looks in addition to the J/Ψ also for single muons, are important. In the context of this thesis the closed heavy flavour finder is called the muon finder and the open heavy flavour finder the D^* finder.

In 1998 the trigger verification in its original sense was replaced by the system of hard scales and finders. The event classification, which had been done previously on L5 until 1997, is performed since 1998 on L4. The hard scales were re-defined, but in general with harder conditions than in 1997. Also the finder algorithms were changed partly. Only if an event is assigned to at least one physics class, defined via a hard scale or finder requirement, the event is accepted by L4 without a prescale. In case of prescale a L4 weight is assigned to this event. For this analysis the relevant classes are class 15 (D -mesons) and class 16 (J/Ψ and single muons).

Offline Reconstruction L5: The last level performs a complete offline reconstruction of the events accepted by L4 using the software package H1REC [87] and also the final calibration. Until 1997 the events were classified in physics classes. Open heavy flavour events with a muon were assigned to class 24 and D^* events to class 16. If an event belonged to at least one physics class the reconstructed data were stored on tape (physics output tape, POT). If no class could be assigned to an event it was rejected. This procedure lead to a reduction of about a factor 2. The part of the data used for analyses is stored in a more compressed way on disc (data summary tape, DST).

Since the classification was taken over by L4 in 1998, no rejection of events have been performed on L5 and all events originally assigned to a physics class on L4 are kept. The offline reconstruction with the final calibration and the POT and DST storage are retained.

Table 3.1 gives an overview of the trigger levels L4 and L5 in the years 1997-2000.

	1997	1998-2000
L4	trigger verification hard scales and finders	hard scales and finders classification (class 15, 16)
L5	final reconstruction classification (class 16, 24)	final reconstruction

Table 3.1: *Overview of trigger levels L4 and L5 in 1997 to 2000. The classes relevant for this analysis are indicated in braces.*

Chapter 4

Data Selection

In this chapter the selection of events with charm or beauty production in photoproduction and in Deep-Inelastic-Scattering (DIS) are described. Data taken by the H1 detector during the years 1997 to 2000 are used.

Charm and beauty events are selected by requiring at least one D^* and at least one muon in the final state. The D^* is reconstructed via the decay channel $D^* \rightarrow D^0 \pi_s \rightarrow K \pi \pi_s$ and for the muon the identification in the instrumented iron is essential to reduce hadron mis-identification.

In this analysis several data sets are used (see table 4.1). The D^* photoproduction and DIS samples are used to check D^* variables and also muon mis-identification. The final data sets used for the cross section measurements are the $D^* \mu$ photoproduction and the total $D^* \mu$ data sample including also events from DIS.

Due to the complex trigger and classification scheme at H1, which was in addition changed after 1997, a rather complex selection chain using a different set of cuts for the inclusive D^* samples and the final $D^* \mu$ samples is necessary.

	number of events
D^* in photoproduction	955
D^* in DIS	3351
$D^* \mu$ in photoproduction	184
$D^* \mu$ in DIS	45
$D^* \mu$ in photoproduction and DIS (total)	229

Table 4.1: *Data samples. The D^* data sets are used to check the D^* variables and also hadron mis-identification, while the $D^* \mu$ data sets are the final data samples used in this analysis.*

4.1 Run Selection and Detector Status

During the period 1997 to 2000 the beam energy of the protons changed from 820 GeV in 1997 to 920 GeV since 1998. The HERA storage ring was operated either with electrons

Correction	\mathcal{L} [pb] ⁻¹
Delivered	124
Good and medium runs	112
Detector status	92
Satellite bunch correction	88.8

Table 4.2: *Integrated luminosity (1997,1999-2000) before and after the applied corrections.*

Year	lepton	E_p [GeV]	\mathcal{L} [pb] ⁻¹
1997	e^+	820	18.6
1999a	e^-	920	10.1
1999b	e^+	920	13.8
2000	e^+	920	46.3
Σ			88.8

Table 4.3: *Integrated luminosity after detector status and satellite bunch correction.*

(1998 and first part of 1999) or with positrons. For this analysis no distinction between positrons and electrons is made.

In the year 1998 a high beam-induced background during electron-running caused several problems especially in the tracking detectors. Furthermore, the L4 triggering important for this analysis was frequently changed. The useful luminosity for this data period is only very small and therefore the data period is omitted. So-called minimum bias runs with different trigger settings and runs with a shifted vertex are also excluded. Only runs with a good or medium quality are selected. In poor runs, important detector components like LAr or CJC were not operational or these runs contain only few events. This requirement leads to a reduction of the luminosity from 124 pb⁻¹ to 112 pb⁻¹ (see table 4.2).

Only those data-taking periods are considered, where the detector components important for this analysis were operational: central jet chambers (CJC1 and CJC2), central proportional chambers (CIP and COP), liquid argon calorimeter (LAr), spaghetti calorimeter (SpaCal), backward drift chamber (BDC), central muon system (CMD), time-of-flight system (ToF) and the luminosity system (Lumi). With these High-Voltage (HV) requirements the luminosity reduces to $\mathcal{L} = 92$ pb⁻¹. In contrast to the final $D^*\mu$ data set the HV condition is relaxed for the inclusive D^* data sets. Here no requirement on the CMD is demanded.

In the electron and proton beam so called satellite bunches exist before and after those at the nominal interaction point. These bunches arise during electron or proton injection into the HERA ring. To suppress background events from interactions in satellite bunches a cut on the z -coordinate of the interaction point is applied. The distance of the z -vertex to the nominal interaction point has to be smaller than 35 cm. The loss of events due to this cut is considered in a correction of the luminosity. After the satellite bunch correction the luminosity is $\mathcal{L} = 88.8$ pb⁻¹. Table 4.2 summarises the integrated luminosity after each correction discussed above. In table 4.3 the integrated luminosities taken in the different data-taking periods are shown after all corrections.

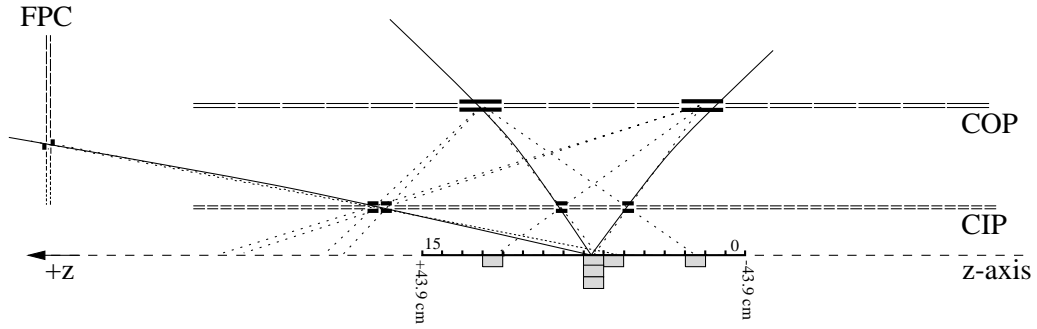


Figure 4.1: *Z-vertex histogram obtained by extrapolating rays, defined by hits in the proportional chambers. Wrong combination of hits are marked by dotted lines.*

ST	Definition	mean prescaling
2	(SPCLe_IET>1 SPCLe_IET_Cen_2)&& DCRPh_THig && zVtx_sig	1.69
19	Mu_Bar && DCRPh_CNH && zVtx_sig	1.06
22	Mu_ECQ && DCRPh_CNH && zVtx_sig	1.06
56	Mu_Any && DCRPh-Ta && (SPCLe_IET>1 SPCLe_IET_Cen_2)	1.00
61	(SPCLe_IET>2 SPCLe_IET_Cen_3)&& DCRPh_THig&& zVtx_sig	1.16
83	eTAG && DCRPh_Tc && zVtx_sig (until 1997) DCRPh_Tc && zVtx_sig && LU_ET !&& LU_PD_low (since 1999)	1.16

Table 4.4: *Definition and mean prescaling factors of the subtriggers used in this analysis. Only the most important trigger elements are shown. The symbols ||, && and !&& signify a logical OR, a logical AND and a logical AND NOT.*

4.2 Level 1 Trigger Selection

The photoproduction $D^*\mu$ data set is triggered by the muon subtriggers (ST) 19, 22 and 56 (since 1999), each requiring a signal in the central muon system, while the inclusive photoproduction D^* sample is triggered using the electron taggers. Here subtrigger 83 is used demanding an energy deposition in ET33 covering the region $Q^2 < 0.01 \text{ GeV}^2$ in contrast to $Q^2 < 1 \text{ GeV}^2$ for the former sample.

DIS events for the D^* inclusive as well as for the $D^*\mu$ samples are triggered using an energy deposition in the SpaCal. Since the trigger conditions have been changed in the middle of the year 1997, the subtrigger 61 is used after run 193442. For the first part of 1997 subtrigger 2 is used. For the $D^*\mu$ sample in DIS the muon triggers are used in addition.

In table 4.4 all subtriggers used in this analysis are shown. These subtriggers are made up of the following trigger elements (see table 4.5):

- The **DCRPh Trigger** uses the tracks of the central jet chambers. Here 10 of the 56 wire layers are used for the trigger, 7 in CJC1 and 3 in CJC2. The signals of these wire layers are compared with predefined masks in the $r\phi$ plane. Positive and negative tracks with low ($450 \lesssim p_T \lesssim 800 \text{ MeV}$) or high ($p_T \gtrsim 800 \text{ MeV}$) transverse momentum can be separated. For the definitions of the different individual DCRPh trigger elements see table 4.5.

Trigger element	Definition
Trigger elements of the central drift chambers CJC1 and CJC2	
DCRPh-Ta	at least one fired track mask with $p_T \gtrsim 450$ MeV/c
DCRPh-Tc	at least three fired track masks with $p_T \gtrsim 450$ MeV/c
DCRPh-TNeg	at least one fired negative track mask with $p_T \gtrsim 450$ MeV/c
DCRPh-THig	at least one fired track mask with $p_T \gtrsim 800$ MeV/c
DCRPh-CNH	short cut for DCRPh-Tc && DCRPh-TNeg && DCRPh-THig
Trigger elements to detect a significant vertex using CIP, COP and FPC	
zVtx_sig	significant maximum in z-vertex-histogram
Trigger elements to detect the scattered electron in the SpaCal	
SPCLe_IET>1	measured electron in the SpaCal, $E \geq 2$ GeV
SPCLe_IET_Cen_2	similar to SPCLe_IET>1 but for the central region in SpaCal
SPCLe_IET>2	measured electron in the SpaCal, $E \geq 6$ GeV
SPCLe_IET_Cen_3	similar to SPCLe_IET>2 but for the central region in SpaCal
Trigger elements of the instrumented iron	
Mu_FIEC	muon candidate in the forward inner endcap
Mu_FOEC	muon candidate in the forward outer endcap
Mu_BOEC	muon candidate in the backward outer endcap
Mu_BIEC	muon candidate in the backward inner endcap
Mu_Bar	muon candidate in the barrel
Mu_ECQ	muon candidate in the endcaps except in the forward inner: Mu_FOEC Mu_BOEC Mu_BIEC
Mu_Any	muon candidate in the endcaps or the barrel: Mu_FIEC Mu_FOEC Mu_BOEC Mu_BIEC Mu_Bar
Trigger elements to detect the scattered electron in the ET33	
eTAG	signal in the ET33 and no large energy deposition in the PD
LU_ET	signal in ET33
LU_PD_low	energy deposition in the PD

Table 4.5: *Trigger elements, which are used for the subtriggers in this analysis.*

- The **zVtx Trigger** uses the information of the central proportional chambers, CIP and COP, and the first layer of the forward proportional chamber FPC to provide a rough estimation of the z-coordinate of the ep interaction. In 16 ϕ sectors straight 'rays' are fitted through the hits in the three proportional chambers. The intersections of these rays with the z-axis are filled into a histogram (see figure 4.1). All rays which intersect the region around the nominal vertex lead in this histogram to z-values close to the vertex. Wrong combinations of hits lead to randomly distributed values in this histogram. The trigger element $zVtx_sig$ is set, if a histogram bin exists containing significantly more entries than the average of the others.
- The **inclusive electron trigger (IET)** of the SpaCal sums the energy depositions in 16 cells (4x4 arrangement), forming a trigger tower. Altogether 320 trigger towers exist, half overlapping in size in both the x and y directions (the sliding window method). This avoids trigger inefficiencies as a function of the impact point. The energy deposition in the trigger towers is then compared to three adjustable energy thresholds and the trigger elements are formed in an inner (IET_Cen, $R < 16$ cm) and an outer (IET, $R > 16$ cm) region. The detailed definitions of the SpaCal

triggers used are given in table 4.5.

- The **muon** (or iron) **trigger** uses five layers (3, 4, 5, 8, and 12) of the central muon detector (CMD), see chapter 3. The number of required layers differs between the different detector regions. In the barrel (Mu_Bar) two out of the innermost four trigger layers are required, in the backward inner or outer endcap (Mu_BIEC or Mu_BOEC) and in the forward outer endcap (Mu_FOEC) three out of five layers are required. In the forward inner endcap (Mu_FIEC) four out of five layers are required. The detailed definitions of the muon trigger elements are listed in table 4.5.
- The **trigger of the electron tagger ET33** requires an energy deposition above an adjustable threshold and at the same time the energy deposition in the photon detector (PD) has to be smaller than a given threshold. In the year 1997 the trigger element eTAG was used. For this trigger element the energy threshold for the scattered electron was 4 GeV and the energy deposition in the photon detector had to be smaller than 2 GeV. In the years 1999 and 2000 the trigger element LU_ET requiring an energy deposition in the ET33 above 6 – 9 GeV was used in combination with the veto of the trigger element *LU_PD_Low*, which demands an energy deposition in the photon detector below 5 – 7 GeV.

4.2.1 L1 Prescales and Weights

Since the level 1 subtriggers used each carry a different prescale factor, this is taken into account in the luminosity calculation for the used trigger set. The trigger set contains N subtriggers. For the trigger set N_{comb} possible combinations of *fired* triggers exist:

$$N_{comb} = \sum_{k=1}^N \binom{N}{k} \quad (4.1)$$

For the case in which a trigger set contains only two triggers, for example s19 and s56, the possible trigger combinations are: s19 only, s56 only and s19 and s56. Without prescaling all triggers within a combination would have accepted the event. For each trigger combination j the probability P_{jk} that the event was accepted by one of the subtriggers of the combination is calculated for run k according to (see [88]):

$$P_{jk} = 1 - \prod_{i=1}^{N_{subtr}} \left(1 - \frac{1}{d_{ik}}\right) \quad (4.2)$$

Here N_{subtr} is the number of subtriggers in the trigger combination j and d_{ik} indicates the prescaling factor of a subtrigger i , which belongs to the trigger combination j in run k .

The data are divided into periods p with unchanged trigger definitions, for example the year 1997, 1999 e^- and 1999 e^+ /2000. The periods consist of a huge number of runs k . To keep the statistical errors as small as possible the run dependent prescale factors $d_{jk} = 1/P_{jk}$ for a trigger combination j are averaged over a period. The luminosity weighted average prescale factor d_{jp} is:

$$d_{jp} = \frac{\sum_{kep} \mathcal{L}_k}{\sum_{kep} \mathcal{L}_k \cdot P_{jk}} \quad (4.3)$$

For each $D^*\mu$ -event the corresponding weight $w_{jp} = 1/d_{jp}$ is applied to the Monte Carlo simulation to account for the L1 prescaling. The overall prescale factor \bar{d} for the selected $D^*\mu$ events is determined from the corresponding weights for each event. The prescaled luminosity in the data is obtained by applying the overall averaged prescale factor.

The averaged prescale factors d_{jp} are found to be very close to unity or even equal 1.0 for all periods and all trigger combinations, except for the trigger combination s2 (used only in the first part of 1997 data). For the trigger s2 a prescale factor of 1.69 is obtained.

4.3 Level 4 Trigger Selection and Level 5 Classification

The selection on the fourth trigger level is based mainly on the concept of “hard scales” and “final state” finders. If an event does not fulfill any of the hard selections it has to pass one of the finders.

In the year 1997 the most important hard scale condition for $D^*\mu$ events is: “at least one reconstructed muon track in the CMD which matches to a track in the CTD or FTD in θ and ϕ with a transverse momentum of $p_T(\mu) > 1 \text{ GeV}/c$ ”. The D^* final state finders did not run on the used muon triggers, but on subtriggers like 61 (2) or 83. The muon finders running on subtriggers 19 and 22 require a matching between the reconstructed CMD track and a track in the CTD or FTD. Since only a J/Ψ muon finder ran on subtrigger 56 this trigger is not used for the year 1997. The physics classification is done on L5 using the final calibrations. The important classes are the open heavy flavour class 16 (D mesons), and the closed heavy flavour class 24 (J/Ψ , μ , e). For the year 1997, only $D^*\mu$ events, which belong either to L5 class 16 or to L5 class 24, are selected. The D^* inclusive events are selected via the L5 class 16.

After 1997 the hard scales were tightened and were very rarely fulfilled by the $D^*\mu$ events. Thus the influence of the final state finders is much stronger here than in the year 1997. The D^* finders did not run on the muon subtriggers but again on for example the DIS trigger 61 and on the ET trigger 83. The D^* finder therefore in the case of the photoproduction data set was running only if in addition to a muon trigger another trigger was set. For these events both, the muon finder as well as the D^* -finder was running and the contribution is non-negligible. The muon finder subclass AOPEN requiring a matching between the reconstructed CMD or FMD track and a good inner track runs on all muon subtriggers 19, 22, 56. A transverse momentum $p_T(\mu) \geq 2.0 \text{ GeV}/c$ for $\theta_\mu > 20^\circ$ and $p(\mu) > 5.0 \text{ GeV}/c$ for $\theta_\mu < 20^\circ$ was required. From the period 1999 e^+ (since run 246240) this condition was relaxed to $p_T(\mu) \geq 1.5 \text{ GeV}/c$ for $\theta_\mu > 18^\circ$ and $p(\mu) > 5.0 \text{ GeV}/c$ for $\theta_\mu < 18^\circ$. Since 1998 the classification was performed directly during the online reconstruction on trigger level four. The new classes are 15 (open heavy flavour class) and 16 (closed heavy flavour class). In this analysis $D^*\mu$ events since 1999 are selected, if they belong to these L4 classes 15 or 16. The D^* inclusive events are selected via the L4 class 15.

Table 4.6 summarises the required L4 or L5 classes, the important finders together with the L1 subtriggers on which the finders ran (here defined as precondition for the finders).

Year	Class	Important finder	Preconditions (L1 subtriggers)
1997	24	muon finder AOPEN: matching of a muon track with an inner track. Most important cut: $p(\mu) > 1.0 \text{ GeV}/c$	19, 22
	16	D^* -finder	61, (2 until 193442), 83, ..
since 1999	16	muon finder AOPEN: matching of a muon track with an inner track. Most important cut: $p_T(\mu) > 2.0 \text{ GeV}/c$ (1.5 GeV/c since run 246240)	19, 22, 56
	15	D^* -finder	61, 83, ..

Table 4.6: Overview of $L4$ (since 1999) or $L5$ classes (until 1997) required in this analysis, the associated $L4$ -finders and the corresponding preconditions (L1 subtriggers, on which the finders ran), separately for the year 1997 and 1999-2000. In addition to the DIS subtrigger 61 (2 for first part of 1997) and the ET33 trigger 83 the D^* finder also ran on other L1 subtriggers, which are all based on the identification of a scattered electron, either in the SpaCal (DIS) or in the electron taggers or the Very Low Q^2 Spectrometer (VLQ). In addition to these triggers the D^* -finder ran also on an untagged D^* trigger, which is highly prescaled.

4.4 Kinematic Selection

4.4.1 Selection of DIS Events

The kinematic variables of the event are reconstructed from the energy E'_e and the angle θ_e of the scattered electron:

$$Q_e^2 = 4 \cdot E_e \cdot E'_e \cos^2 \left(\frac{\theta_e}{2} \right) \quad (4.4)$$

$$y_e = 1 - \frac{E'_e}{E_e} \sin^2 \left(\frac{\theta_e}{2} \right) \quad (4.5)$$

$$x_e = \frac{Q_e^2}{s \cdot y_e} \quad (4.6)$$

Here E_e is the energy of the incoming electron. The identification of the scattered electron in the DIS sample is performed via the energy measurement in the SpaCal calorimeter. The energy deposition in the calorimeter cells is combined to clusters and the cluster with the highest energy in the electromagnetic part of the calorimeter is taken as the candidate for the scattered electron. In this analysis only a very rough selection of DIS events is performed. The main aim is to suppress photoproduction background. The energy of the electron candidate has to be at least 8 GeV, the virtuality $2 < Q_e^2 < 100 \text{ GeV}^2$ and the inelasticity $0.05 < y_e < 0.7$. The cut on the virtuality corresponds approximately to the geometric acceptance of the SpaCal. The upper limit of the accepted y_e values corresponds to the cut on the energy of the electron and the lower limit corresponds to the minimum possible value if a lower cut on $Q_e^2 = 2 \text{ GeV}^2$ is applied. The DIS cuts are summarised for the D^* inclusive and $D^*\mu$ samples in table 4.7 and 4.9 respectively.

4.4.2 Selection of Photoproduction Events

The kinematic variables of the event are reconstructed from the energy of the scattered electron if it is detected in ET33. Here the polar angle of the electron candidate is large and $Q^2 \lesssim 0.01 \text{ GeV}^2$ (due to the ET33 acceptance). When $\theta_e \approx 180^\circ$, equation 4.5 reduces to:

$$y_e = 1 - \frac{E'_e}{E_e} = \frac{E_e - E'_e}{E_e} \quad (4.7)$$

If an electron is identified in ET33 the energy deposition of the reconstructed electron candidate has to be above 4 GeV to ensure a good signal and a cut on the position of the electron $|x_0| < 6.5 \text{ cm}$ is applied to ensure a valid energy measurement. The requirement of no large energy deposition ($E_\gamma < 2 \text{ GeV}$) in the photon detector at the same time reduces the background arising from bremsstrahlung and Bethe-Heitler events.

To ensure an ET33 detector acceptance above 10 percent for all periods a cut on the inelasticity $0.29 < y_e < 0.65$ is applied. The mean acceptance is about 40%. This selection is used in the following for the inclusive D^* data set (see table 4.7).

For the $D^*\mu$ -sample photoproduction events are not defined via a scattered electron in the electron taggers, but with an appropriate anti-tag condition (untagged photoproduction). In this case the Jacquet-Blondel [89] method is used, which is based on the reconstruction of the energy E_i and the momentum \vec{p}_i of all particles i of the hadronic final state (HFS). The kinematic variables are reconstructed as follows:

$$y_{JB} = \frac{\sum_{i \in \text{HFS}} (E_i - p_{z,i})}{2E_e} \quad (4.8)$$

$$Q_{JB}^2 = \frac{\left(\sum_{i \in \text{HFS}} p_{x,i} \right)^2 + \left(\sum_{i \in \text{HFS}} p_{y,i} \right)^2}{(1 - y_{JB})} \quad (4.9)$$

$$x_{JB} = \frac{Q_{JB}^2}{s \cdot y_{JB}} \quad (4.10)$$

The hadronic final state is reconstructed from tracks and clusters in the calorimeter. Tracks and clusters are combined in such a way, that no energy is counted twice [90, 91]. Central tracks with a transverse momentum below 8 GeV/c are extrapolated into the calorimeter. Energy depositions in a cylinder of radius 25 cm (electromagnetic calorimeter) and of radius 50 cm (hadronic calorimeter) around the extrapolated track are considered. The cell energies are assigned to the tracks in such a way, that the energy measurement in the calorimeter and the momentum measurement, the resolution of which is better for small energies, are consistent. Tracks with $p_T > 8 \text{ GeV}/c$ are not used, since the energy resolution of the calorimeter is at large energies better than the resolution of the tracking chambers. These tracks as well as forward tracks and neutral particles are taken into account using cluster energies in the calorimeter.

The untagged photoproduction events are selected by rejecting events with electromagnetic energy clusters above 8 GeV in the SpaCal or the LAr calorimeter. This restricts the photon virtuality to $Q^2 < 1 \text{ GeV}^2$. For the inelasticity a cut $0.05 < y_{JB} < 0.75$ is applied. For the $D^*\mu$ photoproduction data set the cuts are summarised in table 4.9.

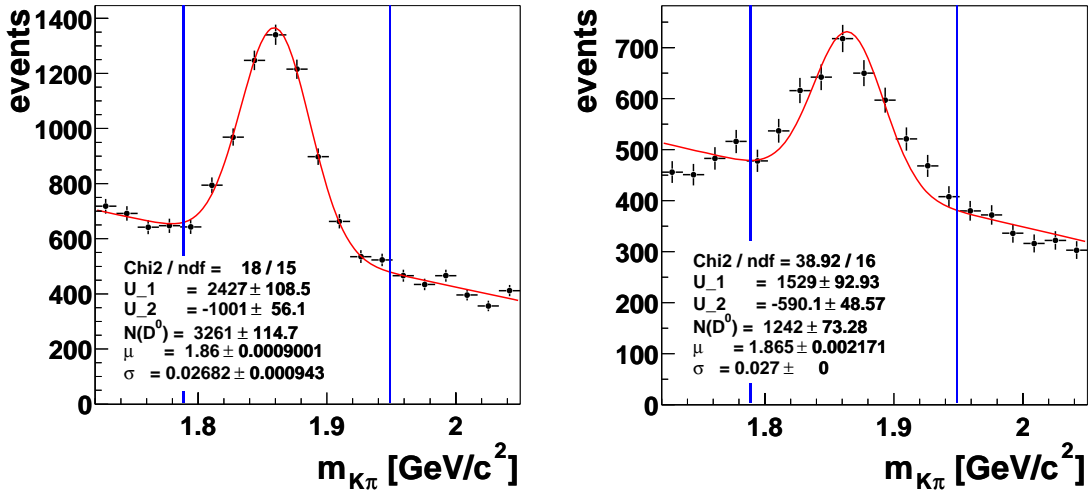


Figure 4.2: Invariant mass of the D^0 candidates for D^* candidates with a mass difference $\Delta M = m_{K\pi\pi_s} - m_{K\pi}$ of the D^* - and D^0 -candidate of $2.5 \text{ MeV}/c^2$ around the nominal value of $0.1454 \text{ GeV}/c^2$. Left: DIS selection. Right: Photoproduction selection. The sum of a Gaussian and a straight line is used as fit function.

4.5 Selection of D^* Events

Events with charm or beauty quark production are selected via the identification of the charmed D^* meson. The D^* meson is reconstructed via its decay products. In this analysis the decay channels $D^{*+} \rightarrow D^0\pi_s^+ \rightarrow K^-\pi^+\pi_s^+$ and $D^{*-} \rightarrow \bar{D}^0\pi_s^- \rightarrow K^+\pi^-\pi_s^-$ are used.

4.5.1 Reconstruction of the D^*

The tracks of charged particles are reconstructed in the CTD. The momentum vectors of the charged particles are calculated using the track parameters. The tracks of the D^* decay products have to have a radial length R of at least 10 cm to ensure a good momentum reconstruction. If a track traverses the CST and hits in the CST can be associated to this track, these hits are used to improve the track parameters. Another improvement of the track parameters comes from a fit to the primary and possible secondary vertices.

To reconstruct the D^0 meson all possible two-track combinations from an event are considered. The two tracks must have opposite charges and the transverse momenta have to be both above $300 \text{ MeV}/c$. Furthermore the distance in $r-\phi$ d'_{ca} of the corresponding non-vertex fitted track with respect to the primary vertex has to be less than 1 cm. Assuming one of the considered particles is a kaon and the other a pion the invariant mass of the pair is calculated. Figure 4.2 shows the distribution of the D^0 candidate mass for events in DIS and in photoproduction. If the invariant mass lies in a window $\pm 80 \text{ MeV}/c^2$ around the nominal D^0 mass ($m_{D^0} = 1.865 \text{ GeV}/c^2$), the combination is kept as a D^0 candidate.

To avoid the rejection of D^0 candidates with a long radial decay length (b candidate events) D^0 candidates from track pairs fitted to the same secondary vertex are selected if

	DIS	Photoproduction
Data taking period	1997 and 1999-2000	
Run selection	good and medium runs	
Detector status	CJC, CIP/COP, LAr, SpaCal, BDC, ToF, Lumi	
Z-vertex	$ z_{vertex} < 35$ cm	
Trigger selection	s61 or s2 (until run 19443)	s83
	L5 class 16 (1997) or L4 class 15 (since 1999)	
Kinematic selection	$E'_e > 8$ GeV $0.05 < y_e < 0.7$ $2 < Q^2 < 100$ GeV ²	$E'_e > 4$ GeV $E_\gamma < 2$ GeV $ x_0 < 6.5$ cm $0.29 < y_e < 0.65$
D^* selection	Decay channel $D^* \rightarrow D^0 \pi_s \rightarrow K \pi \pi_s$ $p_T(D^*) > 2.0$ GeV/c $ \eta(D^*) < 1.5$ $R(K, \pi, \pi_s) > 10$ cm $d_{ca}^l(K, \pi) < 1$ cm $p_T(K, \pi) > 0.4$ GeV/c $p_T(\pi_s) > 0.12$ GeV/c $ m(K\pi) - m_{D^0} < 80$ MeV/c ² $\Delta M < 0.1685$ GeV/c ²	

Table 4.7: Selection cuts of both inclusive D^* data sets: DIS and photoproduction.

no D^0 candidate from primary vertex fitted track hypotheses of the same tracks could be reconstructed.

To reconstruct the D^* candidate the D^0 candidate is combined with a third track from the same event. Only tracks with transverse momenta of at least 120 MeV/c and an opposite charge to the kaon candidate are considered. The four-momentum of the D^* candidate is calculated using the momenta of the three decay particles. The mass difference $\Delta M = m(K\pi\pi_s) - m(K\pi)$ between the D^* and D^0 candidates has to be less than 0.1685 GeV/c². Furthermore only D^* candidates with a transverse momentum of at least 1.5 GeV/c and a pseudorapidity $|\eta(D^*)| < 1.5$ (central region) are selected. The pseudorapidity is defined as:

$$\eta = \frac{1}{2} \ln \left(\frac{p + p_z}{p - p_z} \right) = -\ln \left(\tan \frac{\theta}{2} \right) \quad (4.11)$$

This D^* selection is used for the $D^* \mu$ event selection.

For the inclusive D^* sample harder cuts on the transverse momenta of the decay particles and on the D^* itself are necessary especially in the photoproduction region to reduce the combinatorial background. The cuts on the transverse momenta of the kaon and pion candidates are both increased in the inclusive D^* data sample to 0.4 GeV/c and the

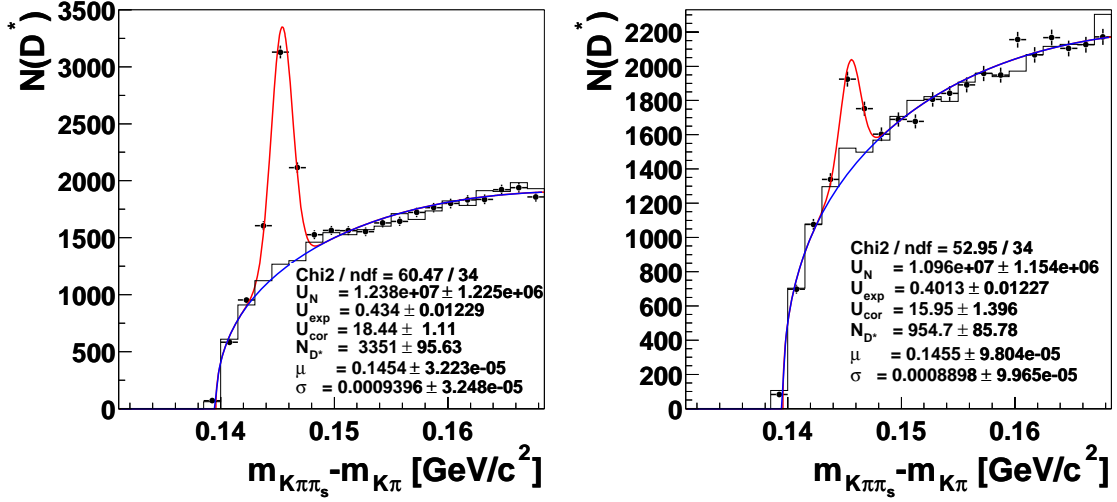


Figure 4.3: Mass difference $\Delta M = m(K\pi\pi_s) - m(K\pi)$ for D^* candidates (points) and background events (histogram) with the fit. Left: DIS selection. Right: Photoproduction selection.

transverse momentum of the D^* has to be greater than 2.0 GeV. The selection cuts for both inclusive D^* data sets are summarised in table 4.7. The mass difference distributions of the selected inclusive D^* events in DIS or photoproduction are shown in figure 4.3.

4.5.2 D^* Fit Method

The selected D^* candidates consist of D^* mesons and combinatorial background. The number of D^* events is obtained from the ΔM distributions. The ΔM values peak around the nominal ΔM value of 0.1454 GeV/c^2 for D^* mesons and can be described by a Gaussian distribution:

$$f_{D^*}(\Delta M) = \frac{N_{D^*}}{\sqrt{2\pi}\sigma} \cdot \exp\left(-\frac{(\Delta M - \mu)^2}{2\sigma^2}\right) \quad (4.12)$$

This D^* signal function depends on three parameters: the number of D^* mesons N_{D^*} , the mean ΔM value μ and the width σ . The combinatorial background can be described approximately via a square-root function intersecting the x -axis at the pion mass. The parameterisation function for the background used is a power law with a quadratic correction term in ΔM , which leads to a significant improvement of the fit quality [92]:

$$f_{BG}(\Delta M) = U_N \cdot (\Delta M - m_\pi)^{U_{\text{exp}}} \cdot (1 - U_{\text{cor}} \cdot \Delta M^2) \quad (4.13)$$

The normalisation factor U_N , the exponent U_{exp} and U_{cor} are fit parameters. The sum of the D^* -signal and background functions is fitted to the measured ΔM distributions. Taking the bin size d_{bin} of the ΔM histogram into account the fit function is modified to:

$$f_{RC}(\Delta M) = d_{\text{bin}} \cdot (f_{D^*}(\Delta M) + f_{BG}(\Delta M)) \quad (4.14)$$

For the fit the maximum-likelihood-method is used assuming a Poisson distribution. In order to improve the background description the fit is done simultaneously to the ΔM distribution of the D^* candidates and background events.

The background events are selected with the same algorithm described previously but with the exception that the charge combination is different. The three-particle combinations $K^+\pi^+\pi_s^-$ or $K^-\pi^-\pi_s^+$ are selected. These are called wrong charge (WC) combinations in contrast to right charge (RC) combinations in the case of a D^* meson decay. For the wrong charge combinations the kaon and pion pair would originate from a doubly charged particle while for the right charge combinations the charge is zero. Since in both cases two particles with the same charge and one with the opposite charge are selected, the same combinatorial background distribution in ΔM is expected. For the total data sample a scaling of the background distribution is not necessary. However, it is important for some differential quantities so the scaling of the background is included in the fit. The fit function to the wrong charge data set is given by:

$$f_{WC}(\Delta M) = d_{bin} \cdot N_{scal} \cdot f_{BG}(\Delta M) \quad (4.15)$$

N_{scal} indicates the scaling factor between the right charge and wrong charge combinatorial background:

$$N_{Scal} = \frac{\sum_{bin} N_{bin}^{WC}}{\sum_{bin} N_{bin}^{RC}} \quad \text{for } \Delta M\text{-bins between } 0.155 \text{ and } 0.1685 \quad (4.16)$$

A simultaneous fit of the function f_{WC} to the ΔM distribution of the background events and of the right charge function f_{RC} to the ΔM distribution of the D^* candidates is performed. In figure 4.3 the ΔM distributions of both data samples are shown together with the result of this fit. For the total D^* inclusive and $D^*\mu$ data set N_{scal} is approximately unity. In differential distributions deviations from one of up to 30% occur. This is especially true for the correlation regions in the case of the $D^*\mu$ -sample.

For the inclusive DIS D^* sample 3351 ± 96 D^* signal events are obtained from the fit and for the tagged photoproduction sample 955 ± 86 D^* signal events. In the following the signal region is defined using a window ± 2.5 MeV/ c^2 around the nominal ΔM value for the D^* ($\Delta M_{D^*} = 0.1454$ GeV/ c^2).

4.6 Selection of Muons in D^* Events

The aim of this analysis is to tag both heavy quarks produced via the boson-gluon fusion process. Therefore in addition to the reconstructed D^* an additional muon is required to tag the second heavy quark. Typically the energies of muons from heavy hadron decays at HERA are smaller than 10 GeV. For muons from charmed hadrons the momentum is on average smaller than for muons from beauty hadron decays (due to the smaller mass of the charm quark and therefore the smaller charmed hadron mass). Only muons with a momentum above 1.5 GeV/ c can be identified in the central muon detector (CMD). A good muon identification is possible if the muons traverse the whole CMD. This holds if the energy of the muons is larger than 2.5 GeV. By identifying muons using the LAr calorimeter only the reconstruction of muons is possible with momenta down to 0.8 GeV/ c .

The muon selection in this analysis is performed using the program packages described in [93, 94]. To ensure that the muon most likely originates from the decay of a charm or beauty hadron the associated inner track is fitted to the primary vertex. This reduces the

contribution of muons from the decay of strange particles like kaons since the lifetime of these is large enough to be resolved in the CJC.

Only tracks classified as good tracks are used for the muon selection. Good tracks are selected according to [93], which resolves track ambiguities and rejects bad and unphysical track hypotheses. The cuts used in this selection are summarised in appendix B. For a iron muon candidate the selected good track has to be linked to a track in the instrumented iron. Often several good tracks reconstructed in the CJC can be linked to a reconstructed iron track. The muon selection chooses the combination with the largest link probability. Furthermore several quality criteria (see appendix B) are applied to the iron track, for example a cut on the number of layers with hits. The identification of muons in the calorimeter is based on the extrapolation of the track helix in the calorimeter and the energy deposition within two cones with two different radii around this helix. In the case of a minimum ionising particle (i.e. muon) the energy should be almost completely deposited in the inner cone ($R_a = 15$ cm), while almost no energy should be deposited in the outer cone ($R_b = 30$ cm). Different calorimeter muon qualities are defined [93]:

- $Q_\mu^{Cal} = 3$: very good quality
- $Q_\mu^{Cal} = 2$: good quality
- $Q_\mu^{Cal} = 1$: weak quality
- $Q_\mu^{Cal} = 0$: no calorimeter muon

Muons identified in the iron are given the muon quality $Q_\mu^{iron} = Q_\mu^{Cal} + 10$. In this analysis a new muon quality 10_{new} is used. This quality is defined as muon quality 10 with the additional requirement that the number of wire layers, which have hits, has to be above 5 and the first layer with hits has to be less than or equal 5, if the polar angle θ_μ is above 135° . This additional requirement is similar to that already demanded for the forward endcaps and is motivated by the fact, that at polar angles above this cut no hadronic calorimeter exists and so more hadrons can reach the iron. Thus the following qualities are considered:

$$0, 1, 2, 3, 10, 10_{new}, 11, 12, 13$$

In the following muons are selected by requiring $Q_\mu \geq 2$ or higher. To select muons in D^* events a minimal momentum $p(\mu)$ of the muon of 2.0 GeV/c is required and only muons in the central region with $|\eta(\mu)| < 1.735$ are selected. To obtain a good signal to background ratio in the D^* signal region a cut on the ratio of the transverse energy fraction $f_{ET}(D^*\mu)$ of the $D^*\mu$ -pair to the transverse energy of all particles with $\theta > 10^\circ$ is applied:

$$f_{ET}(D^*\mu) = \frac{E_T(D^*\mu)}{\sum_{i, \theta > 10^\circ} E_T(i)} > 0.15 \quad (4.17)$$

Here $E_T(D^*\mu) = p_T(\mu) + p_T(D^*)$ and $E_T(i) = p_T(i)$. Furthermore a cut on the track length of the muon $R > 10$ cm is applied as for the decay particles of the D^* . In addition all four tracks are required to be different ensuring four different particles and reducing the number of kaons or pions mis-identified as muons.

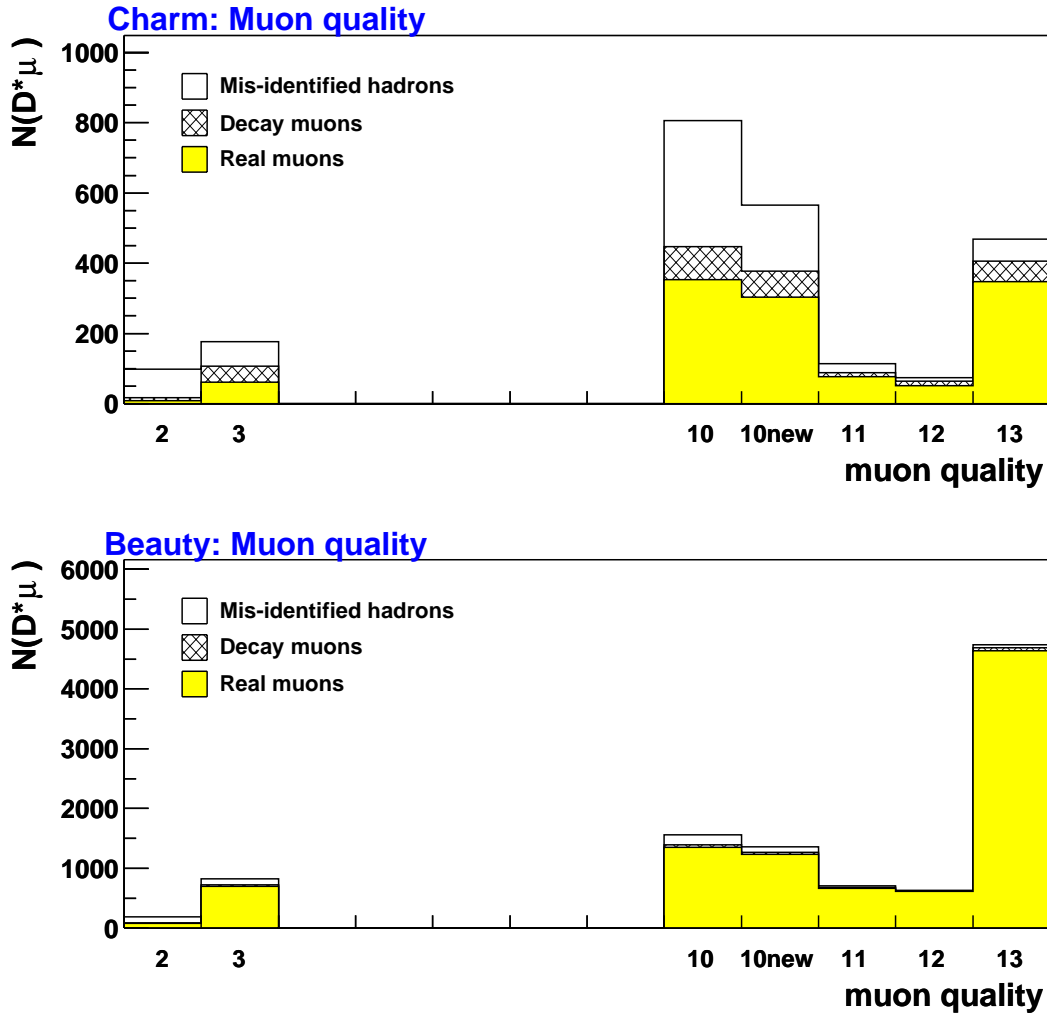


Figure 4.4: Distribution of the muon quality for muons in D^* events in photoproduction from the PYTHIA Monte Carlo simulation. For this plot the usual $D^*\mu$ cuts (see table 4.9) are used but the cut on the muon quality of $Q_\mu \geq 10_{new}$ was relaxed to $Q_\mu \geq 2$.

In figure 4.4 the number of real muons in the Monte Carlo simulation are presented for each muon quality for the photoproduction $D^*\mu$ data set. The number of muons coming from an in-flight decay of light hadrons and the number of hadrons mis-identified as muons are also shown. The sum of the two contributions is referred to as muon background or as muon fake in the following.

The purity of the muons with calorimeter qualities is very low in the case of charm production, 9% for $Q_\mu = 2$ and about 35% for $Q_\mu = 3$. Due to the muon triggers and the L4 setup, where $p_T(\mu) > 2.0$ GeV/c or $p_T(\mu) > 1.5$ GeV/c is required in the muon finders since 1999, the number of real muons reconstructed in the calorimeter only is relatively small, about 8% for charm and about 10% for beauty. Therefore muons identified only in the calorimeter are not used. Instead the normal iron muons with muon qualities 11, 12 and 13 and the iron muons with 10_{new} are selected ($Q_\mu \geq 10_{new}$). With this selection the purity improves from about 57% to 64% in the case of charm and the loss of real muon events is about 5%. For beauty production the loss of real muon events is even smaller,

Muon quality	Charm		Beauty	
	P [%]	ϵ [%]	P [%]	ϵ [%]
2	9	1	42	1
3	35	7	84	9
10	44	39	86	17
10_{new}	54	34	91	15
11	68	9	94	8
12	70	6	98	8
13	74	39	98	58
2+3,10,11-13	52	100	93	100
10,11-13	57	92	95	90
10_{new}, 11-13	64	87	96	89

Table 4.8: Purity P and efficiency ϵ depending on the muon qualities (see text) for $D^*\mu$ events. The quoted values are for the photoproduction sample. For the combined DIS and photoproduction sample the values are almost the same.

only about 1%, and the already excellent purity improves from 95% to 96%.

Table 4.8 summarises the purities and the efficiencies for each muon quality and also for the combined sets. The values are quoted for the photoproduction sample, but almost the same values are obtained for the combined DIS and photoproduction sample.

For beauty production the purity predicted by the PYTHIA Monte Carlo for a $D^*\mu$ photoproduction sample with $Q_\mu \geq 10_{new}$ is 96% and therefore much larger than the purity of 64% predicted for charm production (table 4.8). The muon background for charm production is therefore predicted to be about a factor 9 larger than the muon background for beauty production. The reason is, that the ratio of D^* events with an additional real muon in the visible range per D^* event is for beauty considerably larger than for charm production (see table 2.5). The total amount of muon background events however is for beauty and charm production only slightly different. Therefore the purity is for beauty production larger than for charm production.

In table 4.9 all cuts applied for the selection of $D^*\mu$ events are summarised separately for the selection of the photoproduction data set and the DIS data set. The combined photoproduction and DIS data sample is then obtained by applying a logical OR of the two subsets. The kinematic range of the combined data set is $Q^2 < 100 \text{ GeV}^2$ and $0.05 < y < 0.75$. The requirement of $p(\mu) > 2 \text{ GeV}/c$ together with the requirement of D^* -mesons and muons identified in the central detector leads to a strong enrichment of events from beauty production (see table 2.5).

Two events with a reconstructed D^* and an additional muon are shown in figures 4.5 and 4.6. Both events are beauty candidates. More details of the events can be found in the figure captions.

The distributions of the mass difference ΔM between the D^* and the D^0 particle candidates are shown for the final $D^*\mu$ data sets in figure 4.7. The distributions are shown separately for both data classes in each figure, the right charge data (points) containing the D^* signal and the wrong charge data (histogram), together with the fit introduced already for the inclusive D^* -meson data. 184 ± 26 and 229 ± 30 $D^*\mu$ events are obtained

	DIS	Photoproduction
Data taking period	1997 and 1999-2000	
Run selection	good and medium runs	
Detector status	CJC, CIP/COP, CMD, LAr, SpaCal, BDC, ToF, Lumi	
Z-vertex	$ z_{vertex} < 35$ cm	
Trigger selection	s19, s22, s56 (since 1999), s61 or s2 (until run 19443)	s19, s22, s56 (since 1999)
	L5 class 16, 24 (1997) or L4 class 15, 16 (since 1999)	
Kinematic selection	$E'_e > 8$ GeV	$E'_e < 8$ GeV
D^* selection	Decay channel $D^* \rightarrow D^0 \pi_s \rightarrow K \pi \pi_s$ $R(K, \pi \pi_s) > 10$ cm $d'_{ca}(K, \pi) < 1$ cm $p_T(K, \pi) > 0.3$ GeV/c $p_T(\pi_s) > 0.12$ GeV/c $ m(K\pi) - m_{D^0} < 80$ MeV/c ² $\Delta M < 0.1685$ GeV/c ²	
μ selection	At least one iron muon with $Q_\mu \geq 10_{new}$ $R > 10$ cm $\text{track}(\mu) \neq \text{track}(K, \pi, \pi_s)$	
$D^* \mu$ selection	$f_{ET}(D^* \mu) > 0.15$	
Kinematic range	$p_T(D^*) > 1.5$ GeV/c $ \eta(D^*) < 1.5$ $p(\mu) > 2$ GeV/c $ \eta(\mu) < 1.735$	
	$0.05 < y < 0.7$ $2 < Q^2 < 100$ GeV ²	$0.05 < y < 0.75$ $Q^2 < 1$ GeV ²

Table 4.9: Selection cuts of the final $D^* \mu$ subsets: Photoproduction and DIS. The combined photoproduction and DIS data set is the sum of both subsets. The kinematic range of the combined data set is $Q^2 < 100$ GeV² and $0.05 < y < 0.75$.

by the fit for the photoproduction sample and the total data set containing also DIS events respectively. The values are within the expected deviations in agreement with the number of $D^* \mu$ events obtained by subtracting the wrong charge distribution from the right charge distribution in the signal region (± 2.5 MeV/c² around the nominal value of $\Delta M = 0.1454$ GeV/c²). In table 4.10 the parameters of the fits are presented for both data sets.

To obtain a differential distribution in a particular arbitrary quantity the number of D^*

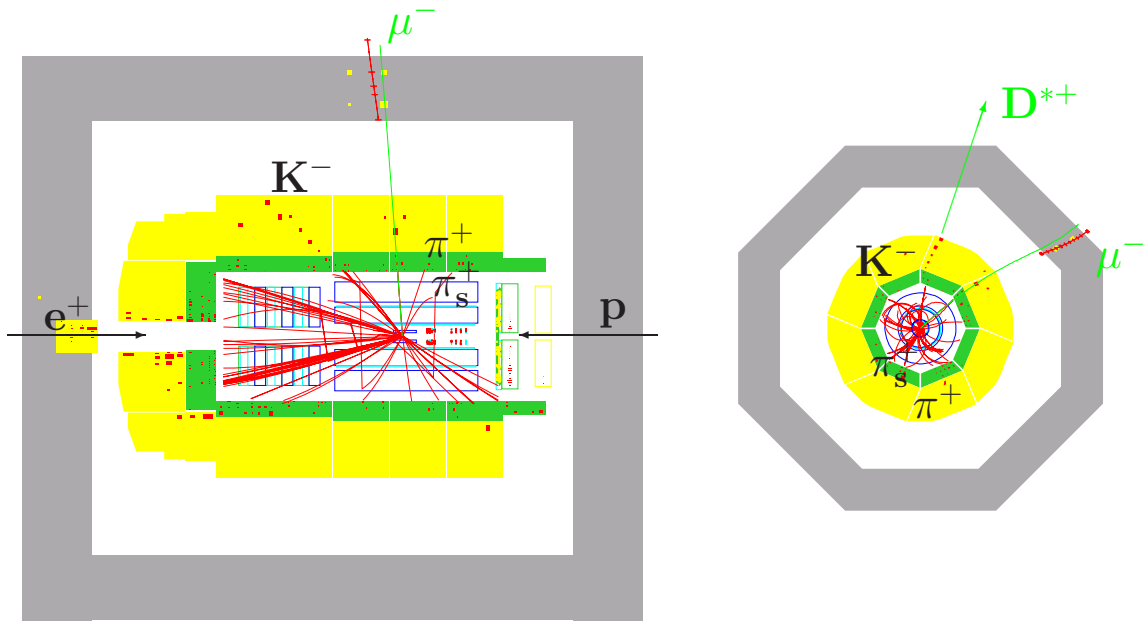


Figure 4.5: Illustration of a $D^*\mu$ candidate, which belongs to the third correlation region. Here the azimuthal angle between the D^* and the muon is below 90° and the two particles have opposite charges.

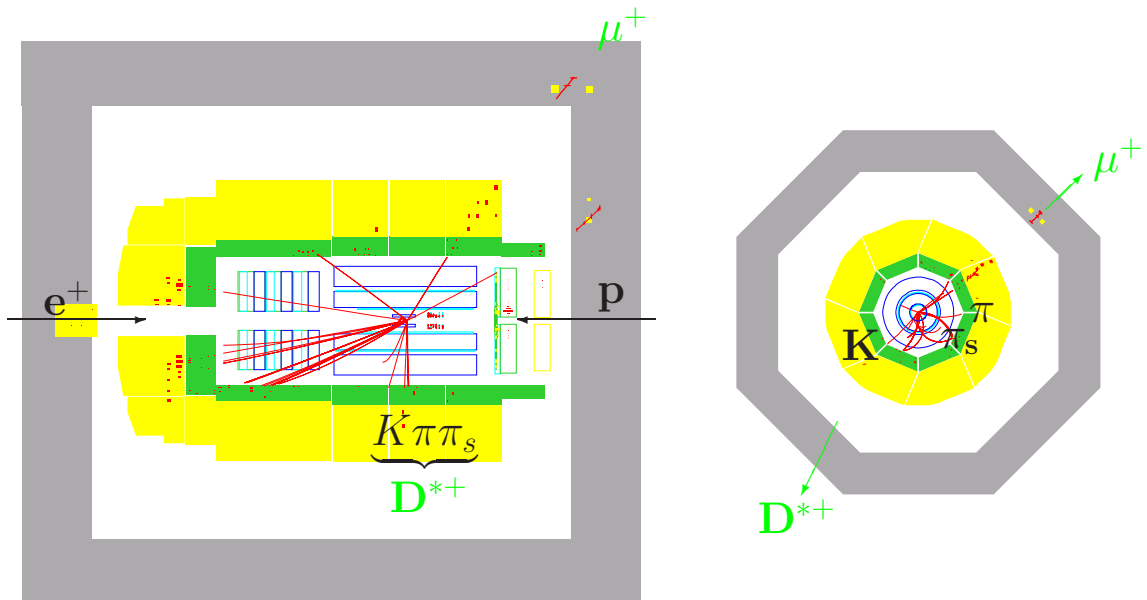


Figure 4.6: Illustration of a $D^*\mu$ candidate, which belongs to the second correlation region. Here the azimuthal angle between the D^* and the muon is above 90° and the two particles have same charges.

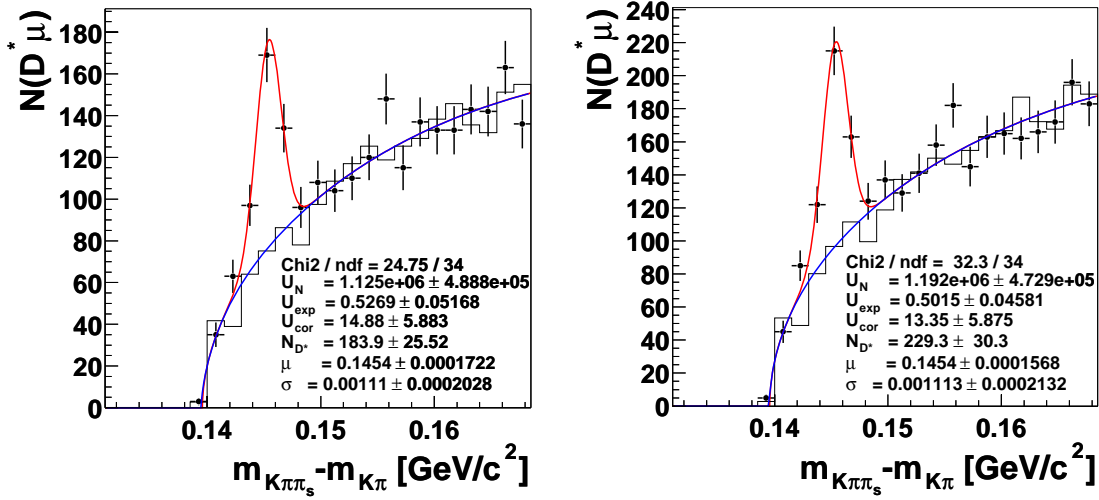


Figure 4.7: Mass difference $\Delta M = m(K\pi\pi_s) - m(K\pi)$ for $D^*\mu$ candidates (points) and background events (histogram) together with the fit. Left: photoproduction. Right: DIS + photoproduction.

Parameter	Photoproduction	DIS + photoproduction
N_{D^*}	184 ± 26	229 ± 30
μ [MeV/c ²]	145.4 ± 0.2	145.4 ± 0.2
σ [MeV/c ²]	1.1 ± 0.2	1.1 ± 0.2
U_N [10 ⁶]	1.1 ± 0.5	1.2 ± 0.5
U_{exp}	0.526 ± 0.051	0.501 ± 0.046
U_{cor} [c ⁴ /MeV ²]	14.9 ± 5.9	13.4 ± 5.9

Table 4.10: Fit parameters of the ΔM distribution for both $D^*\mu$ data sets.

or $D^*\mu$ events in a bin is determined by simultaneously fitting the ΔM distribution of the right and wrong charge combinations in this bin. Since the number of events can be very small in some bins, the number of free parameters is reduced for these fits. Only N_{D^*} and U_N are left as free parameters, the others are fixed to the values obtained from the fit to the total samples (see table 4.10 ($D^*\mu$) and figure 4.3 (inclusive D^*)). The mean value μ is always fixed to the nominal value of 0.1454 MeV/c².

Due to the ΔM fit the differential distributions do not contain combinatorial background anymore. Nevertheless the distributions still contain muon background in addition to signal events. This background is corrected later using the Monte Carlo simulation.

4.7 Investigations to increase the Number of Selected $D^*\mu$ Events

Since the number of selected $D^*\mu$ events is small for a differential analysis, several investigations to increase the number of events were performed.

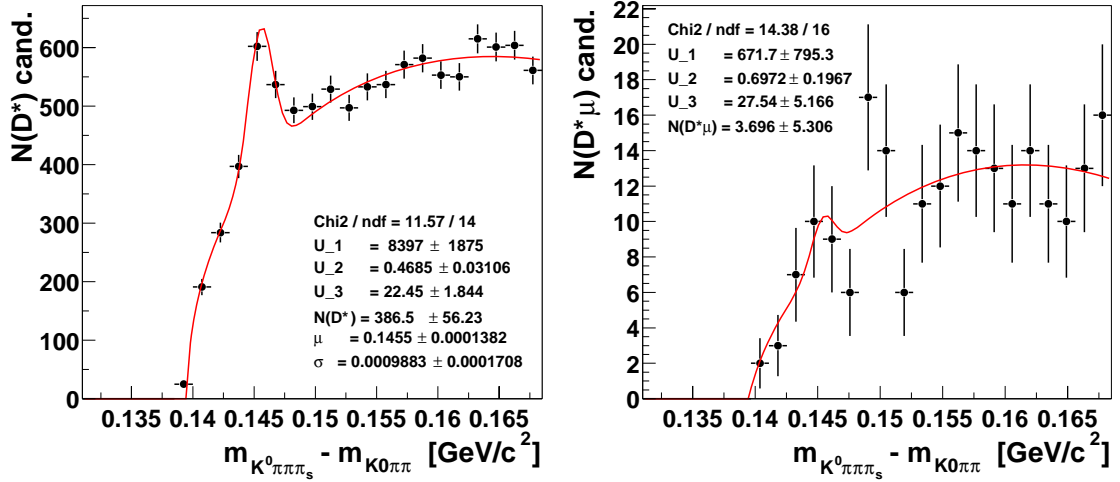


Figure 4.8: Mass difference $\Delta M = m(K^0\pi\pi\pi_s) - m(K^0\pi\pi)$ for D^* candidates (points) together with the fit. Left: All inclusive D^* events without any trigger and DIS or photoproduction selection. Right: $D^*\mu$ events with photoproduction selection. The data taking period 1999 e^+ /2000 is used.

In addition to the “golden” D^* decay channel $D^* \rightarrow D^0\pi_s$ with $D^0 \rightarrow K^-\pi^+$, also two other D^0 channels, namely $D^0 \rightarrow \bar{K}^0\pi^+\pi^-$ with $\bar{K}^0 \rightarrow \pi^+\pi^-$ and $D^0 \rightarrow K^-\pi^+\pi^-\pi^-$, can be used for the reconstruction of D^* -mesons. The branching ratio of $D^0 \rightarrow \bar{K}^0\pi^+\pi^-$ is 5.4%, larger than the 3.83% for $D^0 \rightarrow K^-\pi^+$. However, since less than half of the produced K^0 mesons can be reconstructed in the detector as K_S^0 and because of a $K_S^0 \rightarrow \pi^+\pi^-$ decay rate of 67.7% the effective decay rate of the D^0 is in this case only 2.02% and thus the number of identified D^0 mesons smaller than in the golden channel. The decay channel $D^0 \rightarrow K^-\pi^+\pi^+\pi^-$ has a larger decay rate of 7.49%, but due to the larger multiplicity the combinatorial background is also larger.

An explicit selection based on [95] was nevertheless performed for the decay channel $D^* \rightarrow D^0\pi_s \rightarrow K^0\pi^+\pi^-\pi_s$. Some cuts were relaxed: the minimal transverse momenta of the pion candidates, from which the K^0 is reconstructed, was required to be above 0.15 GeV/c, no maximal start radius for all tracks was required, the mass of the D^0 candidate was allowed to be within a window of ± 80 MeV/c² around the nominal D^0 mass. A cut on the sum of the absolute transverse momenta of the two pion candidates forming the K^0 was however demanded: $p_T(\pi^+) + p_T(\pi^-) > 0.4$ GeV/c. For the inclusive D^* data set a cut $p_T(D^*) > 2.5$ GeV/c was required however for the $D^*\mu$ data set this cut was relaxed to 1.5 GeV/c. In figure 4.8 the ΔM distribution obtained for this decay channel is shown for the inclusive data sample and for the $D^*\mu$ sample selecting only photoproduction events and taking only the data periods 1999 e^+ and 2000. Since the resulting number of events is very small this decay channel was not included in this analysis.

In the case of the channel $D^{*+} \rightarrow D^0\pi_s^+ \rightarrow K^-\pi^+\pi^+\pi^-\pi_s^+$ the combinatorial background is larger, because the D^0 decays directly into four particles. A signal acceptable and comparable to that obtained in the golden decay channel could only be obtained using very hard cuts on the transverse momentum of the D^* meson [96]. The gain in the number of $D^*\mu$ events would therefore be relatively small. At the same time however the data set would become completely inhomogeneous. Thus this channel is excluded as well.

Another way to increase $D^*\mu$ statistics is to extend the muon reconstruction also to the forward range. Muons identified in the forward muon detector (FMD) are reconstructed generally with a momentum above 5 GeV/c and a polar angle between 8° and 16° . The muon momentum distribution is harder for beauty than for charm, but the beauty events are produced more centrally in the detector. In the visible range, restricted in y , p_T and η , the estimated gain is only between 10 – 15% according to the Monte Carlo simulation. With the improved forward detector at HERA II the situation could be better. Detecting D^* -mesons also in the forward region would increase the statistics but at the same time more muons should also be found in the FMD in events with a forward D^* since the heavy quark event is boosted into the forward direction.

A third way to increase the statistics in double tagged events is to add D^*e events. No trigger however was installed for electrons with such low energies as typical of heavy quark events. Only tagged photoproduction can therefore be triggered with s83 or DIS events with s61. These samples however only give a small part of the overall sample (untagged photoproduction and DIS) and the cut on the transverse momentum has to be increased strongly compared to the muon case. Also a cut on the minimum angular difference between the electron track and a second track is necessary to ensure a small fraction of mis-identified hadrons. In the future a technically improved electron finder and an untagged trigger based on the Fast Track Trigger (FTT) at HERA II could improve this situation. For this analysis no D^*e events were used. Thus this analysis will be based on $D^*\mu$ events with a D^* reconstructed via the golden decay channel in the central detector and a muon reconstructed in the iron as discussed in the section before.

After selecting $D^*\mu$ events either in untagged photoproduction or in a combined sample containing DIS events in addition the following chapters determine the beauty contribution in the two data sets. For this purpose the charge and angle correlations between the D^* and the muon are used. Due to the cut on the transverse momentum of the muon and also due to trigger requirements the beauty contribution is enriched. First however the Monte Carlo simulation is compared to the data. It is used later for the separation of charm and beauty events, to correct for the muon background and also to monitor efficiencies and to determine cross sections.

Chapter 5

Comparison of Data and Simulation

In this chapter the description of the data by the Monte Carlo program is investigated, since this is to be used for the separation of charm and beauty, the muon background correction and the efficiency calculation.

The description of the kinematic variables in photoproduction and in DIS are checked first using the inclusive D^* samples selected in the previous chapter, where the number of events is relatively large. The kinematic variables are then also checked for the $D^*\mu$ samples. Then event topological variables, for example the number of tracks or the number of $D^*\mu$ -candidates, are considered. In a third step D^* quantities are checked for the inclusive D^* selection and the final $D^*\mu$ selection. Afterwards the muon variables and $D^*\mu$ quantities are compared. In the last section the muon background in D^* events is investigated in more detail. For this purpose a D^* sample containing a high-momentum track of the D^* decay particles (kaon or pion) is selected and it is investigated whether-or-not this track is falsely identified as a muon.

For all variables the data distributions are obtained using the simultaneous D^* fit to the ΔM distribution of the right and wrong charge data samples in each bin (see section 4.5.2). The Monte Carlo predictions for charm and beauty production are both normalised to the data. A shape comparison between the data and the predicted distributions is performed. For the inclusive D^* sample the beauty fraction is negligible in the data and good agreement between the data and the charm Monte Carlo distributions is expected. For the $D^*\mu$ sample the beauty fraction is sizeable, about 30% as it will be obtained in chapter 6. Quantities, which have different shape for charm and beauty, cannot be described by only one Monte Carlo simulation. In the next chapter a comparison of the most important D^* and muon quantities are redone using the extracted beauty fraction.

5.1 Reweighting of the Monte Carlo Simulation

For photoproduction the MC generator PYTHIA [63] is used. As discussed in chapter 2 the “normal” resolved component in photoproduction is expected to be very small in

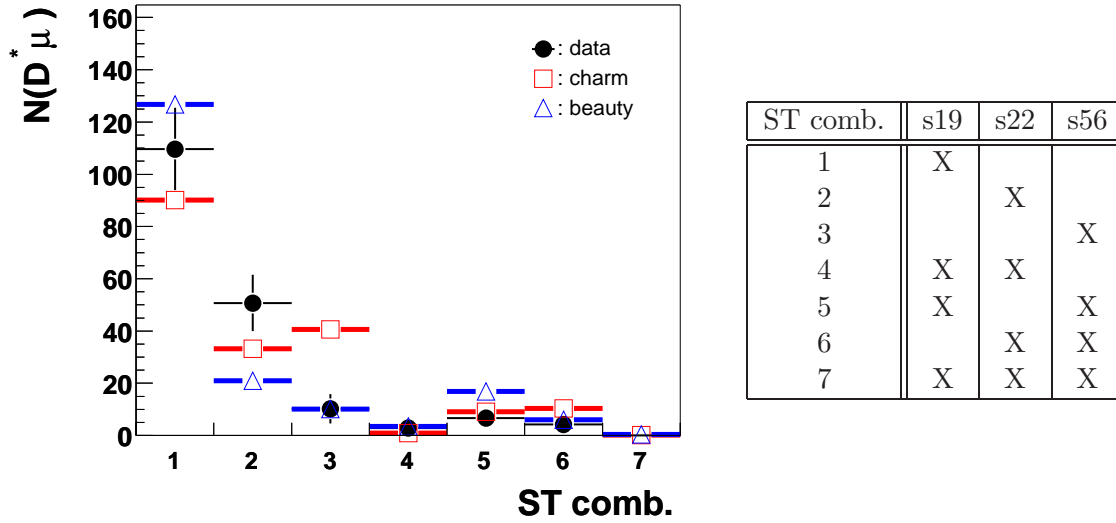


Figure 5.1: Number of $D^*\mu$ events depending on the trigger combinations of the photoproduction sample. The numbers indicate the following trigger combinations: 1: s19 only, 2: s22 only, 3: s56 only, 4: s19 and s22 but no s56, 5: s19 and s56 but no s22, 6: s22 and s56 but no s19, 7: s19 and s22 and s56 (see table on the right hand side, here X indicates a fired trigger). The points represent the data, the triangles the beauty and the squares the charm Monte Carlo simulation. For the Monte Carlo simulation the total number of events is scaled separately for charm and beauty to the number of events in the data. The Monte Carlo simulation contains the final weighting procedure.

the $D^*\mu$ sample. Therefore in photoproduction only the direct component and the charm (beauty) excitation component are taken into account. In the following the sum of the direct and the excitation components as predicted by the Monte Carlo simulation is always shown.

In DIS the remaining resolved components (normal and excitation) are neglected and RAPGAP [64] is chosen as Monte Carlo generator. In the Monte Carlo generator RAPGAP the initial state radiation of the electron is simulated. For the total $D^*\mu$ data set the Monte Carlo predictions shown always consist of the direct and excitation photoproduction part and the DIS part. In the total $D^*\mu$ sample the contribution of DIS events is about 20% (see table 4.1). In order to adjust this contribution in the Monte Carlo simulation to that of the data the DIS events are weighted by a factor 1.35 for charm and for beauty production. For the final $D^*\mu$ sample several effects, which are not or not correctly described in the Monte Carlo simulation, are taken into account via reweighting of the Monte Carlo. In the Monte Carlo simulation the L1 prescale factors of the considered subtriggers are not modelled. Thus the prescale factors determined in the last chapter for each trigger combination in the two different data sets (photoproduction: s19, s22, s56; total: s19, s22, s56, s2 or s61) and for each data taking period are applied in the Monte Carlo simulation. The number of $D^*\mu$ -events depending on the fired trigger combinations is shown for the photoproduction sample in figure 5.1. The data contain events from charm as well as from beauty production. The agreement between data and Monte Carlo simulation is in most bins reasonable.

For the period 1999 e^+ /2000 the efficiencies of the muon finder or the logical OR of both

		precondition of	
		μ finder	both finders
γp			
1999 e^+ /2000	c-MC	1.69	0.50
	b-MC	1.37	0.60
1999 e^-	c-MC	1.09	0.93
	b-MC	0.96	1.04
1997	c-MC	1.25	0.80
	b-MC	1.20	0.83
$\gamma p + \text{DIS}$			
1999 e^+ /2000	c-MC	1.74	0.69
	b-MC	1.48	0.68
1999 e^-	c-MC	1.0	1.0
	b-MC	0.90	1.07
1997	c-MC	1.56	0.74
	b-MC	1.35	0.79

Table 5.1: *Weights for the Monte Carlo simulation of the two possible L4 finder preconditions: events, where only the μ finder or where both finder preconditions are fulfilled. The weights indicated in this table are obtained via the calculation of the fractions of the two precondition classes (where the muon finder precondition is fulfilled alone or where in addition also the D^* finder precondition is fulfilled) in the data and in the Monte Carlo simulation. For the determination of these fractions in the data the number of D^* candidates in the signal region is used.*

finders are described by the Monte Carlo simulation, while for the other two periods the efficiency of the muon finder has to be adjusted to the data. In the year 1997 the efficiency of the muon finder is almost constant in $p_T(\mu)$ at around 80%. In the Monte Carlo simulation thus an overall efficiency of 80% is used. In the period 1999 e^- the efficiency at threshold ($p_T(\mu) > 2.0$ GeV/c required in the L4 finder) is adjusted to the 20% value obtained in the data. For all other regions a good agreement between data and Monte Carlo simulation is found.

The Monte Carlo simulation however does not describe correctly the fraction of events, where only one of the both of the L4 preconditions for the muon finder and the D^* finder or where the precondition for both finders are fulfilled. The L4 preconditions in this analysis are defined as the L1 triggers, on which the L4 finders ran (see table 4.6). These numbers are adjusted in the Monte Carlo simulation depending on the data set and the data taking period. The case, where only the D^* -finder precondition is fulfilled, does not occur in the data.

In table 5.1 the weights applied to the fraction of events, in which the muon finder L4 precondition or both D^* and muon finder L4 preconditions are fulfilled, are shown. These weights are determined after requiring the corresponding L4 finder. Since the efficiencies of the muon finder or the logical OR of both finders are described by the Monte Carlo simulation – at least in the adjusted Monte Carlo simulation – the applied correction factors between data and Monte Carlo simulation do not change if the L4 finder is not required. Different weighting factors are obtained for charm and beauty and for the photoproduction or the total sample.

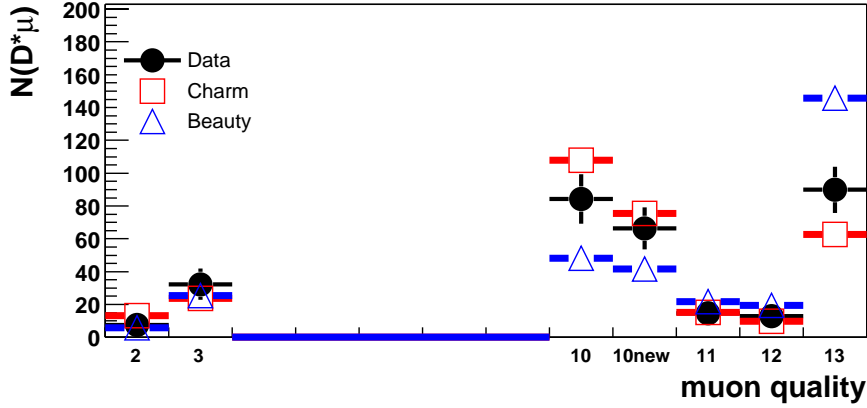


Figure 5.2: Muon quality of $D^*\mu$ events in photoproduction. The Monte Carlo simulation contains the final weighting procedure. In order to produce this figure the usual cut on the muon quality $Q_\mu \geq 10$ was relaxed to $Q_\mu \geq 2$.

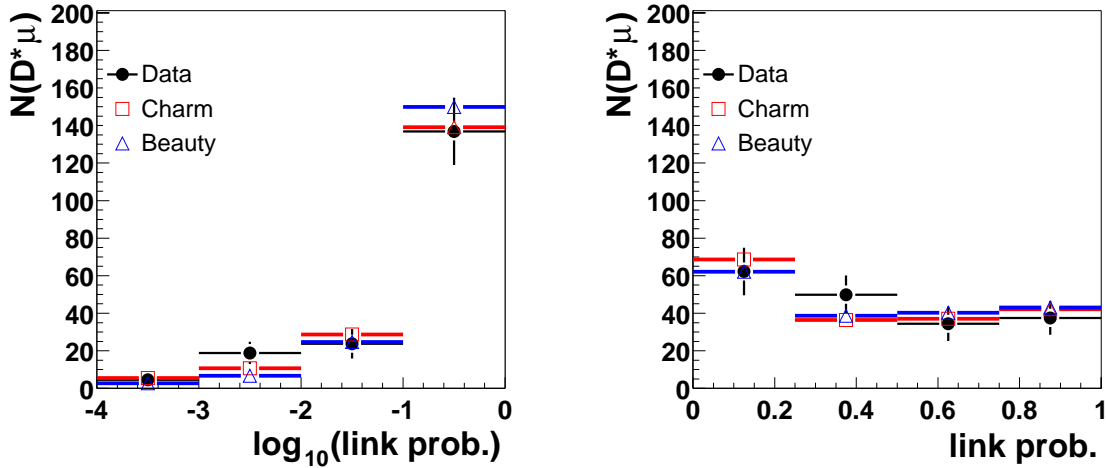


Figure 5.3: Link probability of the reconstructed muon track in the iron and the CJC track for $D^*\mu$ events in photoproduction. The same data are shown twice in a logarithmic and a linear scale. The Monte Carlo simulation contains the final weighting procedure.

An additional reweighting of the Monte Carlo simulation is performed in the transverse momentum and the polar angle of the muon, depending on the muon qualities. Here the same reweighting as used for an elastic $J/\Psi \rightarrow \mu^+\mu^-$ analysis [97] is applied. Only small differences between data and Monte Carlo simulation occur for muons reconstructed in the iron before reweighting. For muons reconstructed only in the calorimeter the discrepancies between data and Monte Carlo are significantly larger before the reweighting. The event topologies of $D^*\mu$ events which have many tracks and elastic J/Ψ two-track events differ. But the efficiency of muons reconstructed in the instrumented iron are equivalent since iron muons are also in $D^*\mu$ events quasi isolated objects in the iron. The same weighting as in the J/Ψ analysis is therefore applied, even if it has only a very small impact on the muon distributions.

The muon quality and the link probability between the reconstructed muon track in the

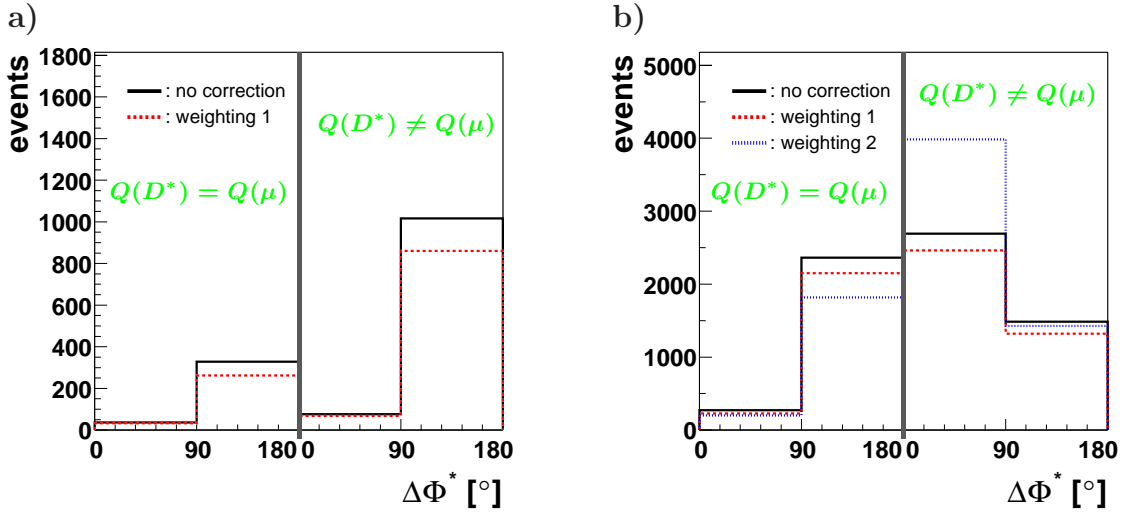


Figure 5.4: *Reweighting of the photoproduction $D^*\mu$ sample in the Monte Carlo simulation. a) Charm; b) Beauty. Weighting 1 includes the Monte Carlo simulation adjustment due to L1 prescaling, L4 finder efficiencies and the fractions of the number of events fulfilling the L4 finder precondition for the muon finder or for both finders (D^* and muon finder). Weighting 2 includes in addition the adjustment of the fractions for the different beauty decay topologies.*

iron and the track in the CJC are well described by the Monte Carlo in $D^*\mu$ events, as shown in figure 5.2 and 5.3 for the photoproduction sample. For the total sample the description is as good as in the photoproduction case. No further adjustments are therefore applied.

As already discussed in chapter 2 weights for the branching ratios of the three different beauty decay topologies, where the D^* meson and the muon come either from different quarks (here the cascade or direct decay of a beauty hadron into a muon are distinguished) or from the same quark, are applied. This ensures the correct fractions of these beauty topologies. In case of charm production no such weighting is applied.

To summarise, the $D^*\mu$ Monte Carlo samples used in the next sections and chapters are always adjusted for the following quantities:

- DIS contribution in the case of the total sample
- L1 Prescaling
- Muon L4 finder efficiency for 1997 and 1999 e^-
- Fractions of the number of events fulfilling the L4 finder precondition for the muon finder or for both finders (D^* and muon finder)
- Momentum and polar angle distribution of the muon
- Fractions for the different beauty decay topologies

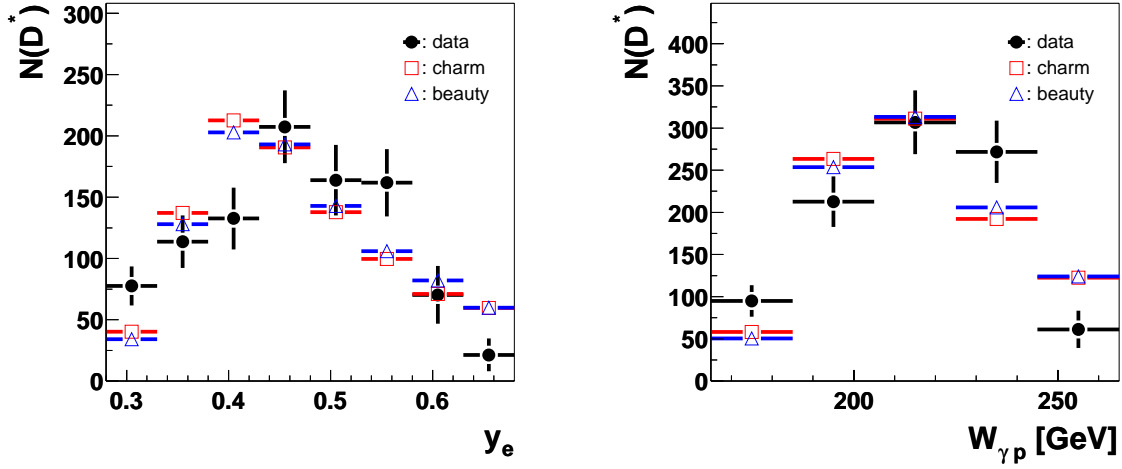


Figure 5.5: Description of the important kinematic variables in *photoproduction*: y and $W_{\gamma p}$. The black dots indicate the *inclusive D^* data*, the squares the charm Monte Carlo and the triangles the beauty Monte Carlo prediction.

Figure 5.4 shows the population of the Monte Carlo simulation in the four correlation regions without adjustment and with adjustment. The adjustments due to L1 prescaling, L4 finder efficiencies and the fractions of the number of events fulfilling the L4 finder precondition for the muon finder or for both finders (D^* and muon finder) have only a small impact on the relative population of the correlation regions, while the adjustment of the fractions for the different beauty decay topologies, which is only applied to the beauty Monte Carlo simulation, has a strong impact on the population as expected.

For the inclusive D^* data sets (mainly charm) no such reweighting of the Monte Carlo simulation was applied, since here only one subtrigger with one finder is used. For a shape comparison the distributions directly obtained from the Monte Carlo simulation are thus sufficient.

5.2 Description of ep Scattering

For photoproduction the description of the shape of the inelasticity y and the centre of mass energy $W_{\gamma p}$ of the photon-proton system are checked using the inclusive D^* data set as well as the final $D^*\mu$ data set. In figure 5.5 the inclusive D^* data set is compared to the prediction of the charm and beauty Monte Carlo simulations. Here the number of events in the Monte Carlo simulation is normalised to the number of events in the data. The data of the inclusive D^* sample contains mainly events from charm production. The acceptance of ET33 is y -dependent and this detector acceptance is not simulated in the Monte Carlo program. Here no ET33 acceptance weighting factors are applied, but the description of the data by the Monte Carlo simulation is already reasonable. The corresponding distributions obtained for the final $D^*\mu$ photoproduction data set is shown in figure 5.6. The final $D^*\mu$ sample contains both, events from charm and events from beauty production. The Monte Carlo simulations also describe this data quite well.

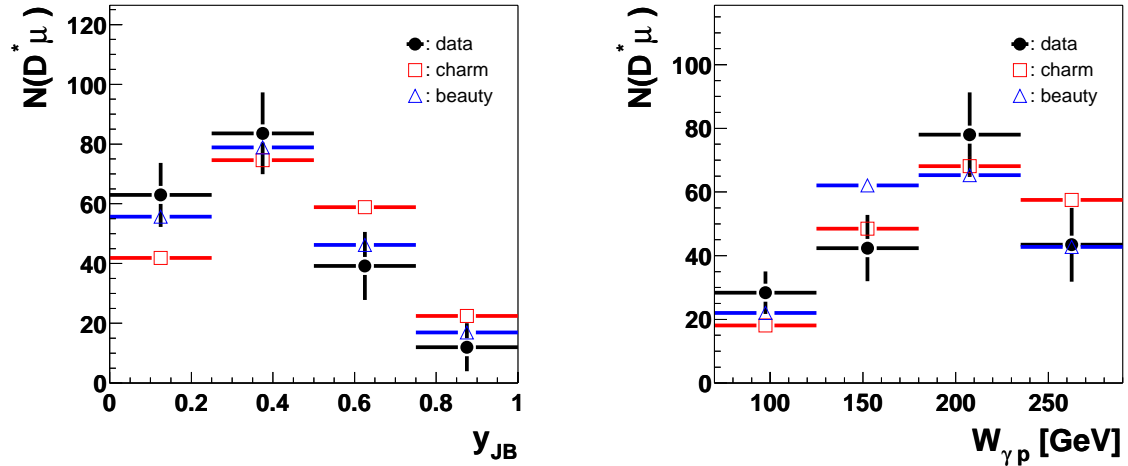


Figure 5.6: Description of the important kinematic variables in *photoproduction*: y and $W_{\gamma p}$. The black dots indicate the final $D^*\mu$ data, the squares the charm Monte Carlo and the triangles the beauty Monte Carlo prediction.

In DIS the correct description of the reconstruction of the electron candidate has to be ensured in the Monte Carlo simulation. Thus for the inclusive D^* as well as for the $D^*\mu$ DIS sample the energy $E_{e'}$, the polar angle $\theta_{e'}$ and the azimuthal angle $\Phi_{e'}$ of the scattered electron are compared. Furthermore the kinematic variables obtained from those quantities, like the virtuality of the photon Q_e^2 , the inelasticity y_e and the Björken variable x_e are also compared.

Figure 5.7 shows these six variables for the inclusive D^* sample and figure 5.8 for the $D^*\mu$ DIS data sample. Especially in case of $E'_{e'}$ and y_e larger differences between charm and beauty production are obtained. Since the data in the case of the inclusive D^* sample are expected to contain almost no beauty events the charm Monte Carlo simulation describes the data well. For the $D^*\mu$ sample a reasonable description by the Monte Carlo simulation is also obtained. From the energy distribution of the scattered electron, the photoproduction background in the data can be estimated. For a data sample with a sizable photoproduction background a large peak at small $E_{e'}$ would be obtained. Since there is no apparent peak at small energies of the scattered electron $E_{e'}$ (see figure 5.7 and 5.8), the photoproduction background in the data is very small.

The number of reconstructed central tracks (with $p_T > 0.3$ GeV/c), D^* -mesons, muons and $D^*\mu$ -candidates are important variables, which characterise the topology of the event. The description of these quantities is essential to get a correct estimation of any double counted D^* or $D^*\mu$ events in the Monte Carlo simulation. Furthermore, if the number of tracks is not described by the Monte Carlo simulation, also the fraction of muon background events will be incorrectly simulated. Figure 5.9 shows the number of muon, D^* and $D^*\mu$ candidates as well as the number of tracks per event for the photoproduction $D^*\mu$ sample. Reasonable agreement between data and Monte Carlo simulation is obtained. Good description of the data by the Monte Carlo simulation is obtained also for the total $D^*\mu$ data sample, which is not shown here.

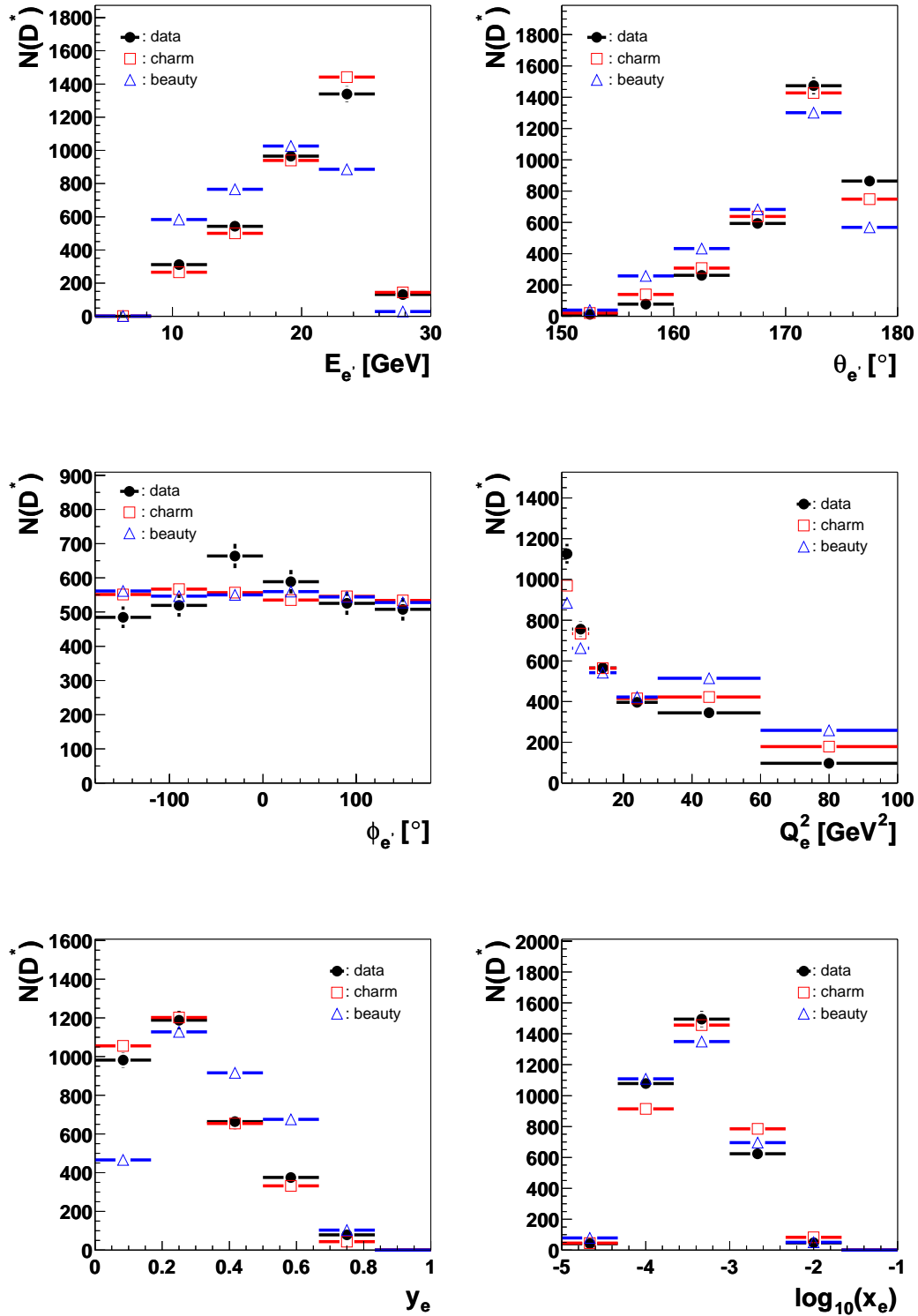


Figure 5.7: Description of the important kinematic variables in DIS: $E_{e'}$, $\theta_{e'}$, $\Phi_{e'}$, Q_e^2 , y_e and x_e . The black dots indicate the *inclusive D^* data*, the squares the charm Monte Carlo and the triangles the beauty Monte Carlo prediction.

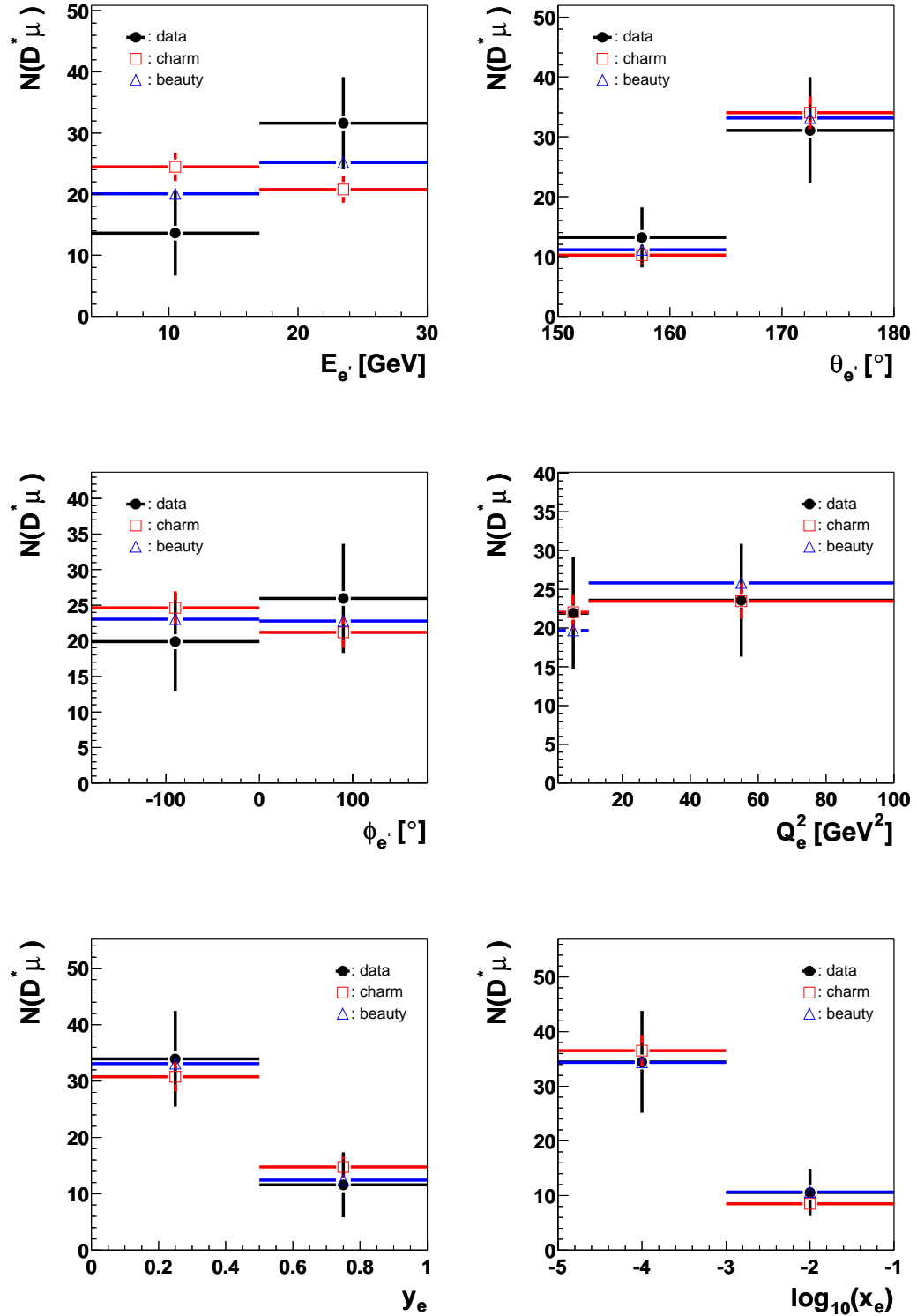


Figure 5.8: Description of the important kinematic variables in DIS: $E_{e'}$, $\theta_{e'}$, $\Phi_{e'}$, Q_e^2 , y_e and x_e . The black dots indicate the $D^*\mu$ data, the squares the charm Monte Carlo and the triangles the beauty Monte Carlo prediction.

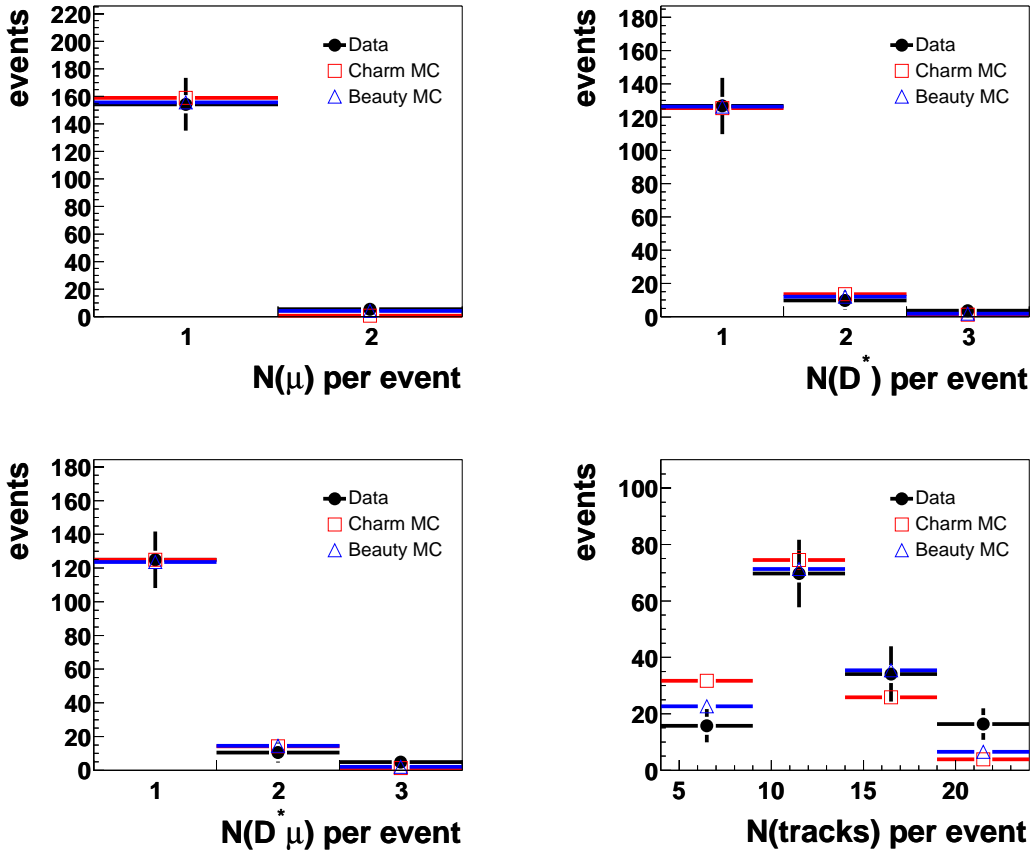


Figure 5.9: Event variables of the *photoproduction* $D^*\mu$ data sample. Shown are the number of muon, D^* and $D^*\mu$ candidates as well as the number of reconstructed central tracks. The black dots indicate the data, the squares the charm Monte Carlo and the triangles the beauty Monte Carlo prediction.

5.3 Description of D^* Kinematical Variables

The D^* -meson is reconstructed via its decay products. The description of variables, on which cuts are applied in the D^* reconstruction – the radial track length R , the transverse momentum p_T and the minimal distance d'_{ca} of the corresponding non-vertex fitted track with respect to the primary vertex – are shown for the kaon together with the pseudorapidity η and the azimuthal angle ϕ , in figures 5.10 or 5.11. For the kaon in the inclusive D^* or $D^*\mu$ photoproduction samples the agreement between data and Monte Carlo simulation for all distributions is reasonably good. For the other decay particles as well as for the total data set a similar good description of the data by the Monte Carlo simulation is obtained. For most variables the differences between charm and beauty Monte Carlo are small, but for the distribution of the pseudorapidity larger differences occur. The $D^*\mu$ data contain events from charm as well as from beauty production. A Monte Carlo simulation containing a mixture of beauty and charm events should describe the data in an acceptable way.

For the inclusive D^* or the final $D^*\mu$ photoproduction data the transverse momentum,

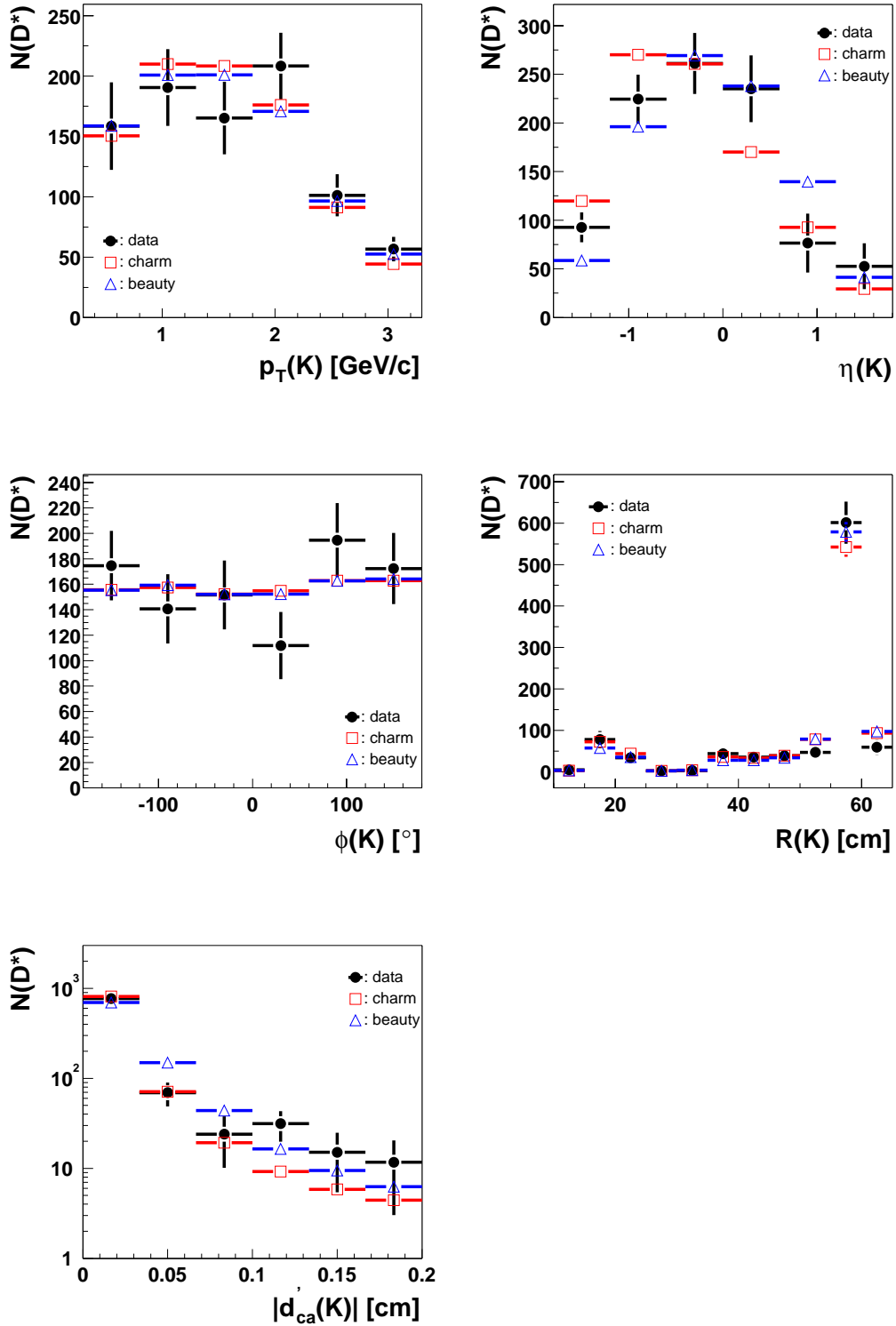


Figure 5.10: Description of the *kaon* variables in the *inclusive D^* photoproduction sample*. The black dots indicate the data, the squares the charm Monte Carlo and the triangles the beauty Monte Carlo prediction. The transverse momentum p_T , the pseudo-rapidity η , the azimuthal angle ϕ , the radial track length R and the minimal distance d_{ca}^l of the corresponding non-vertex fitted track with respect to the primary vertex of the kaon are shown.

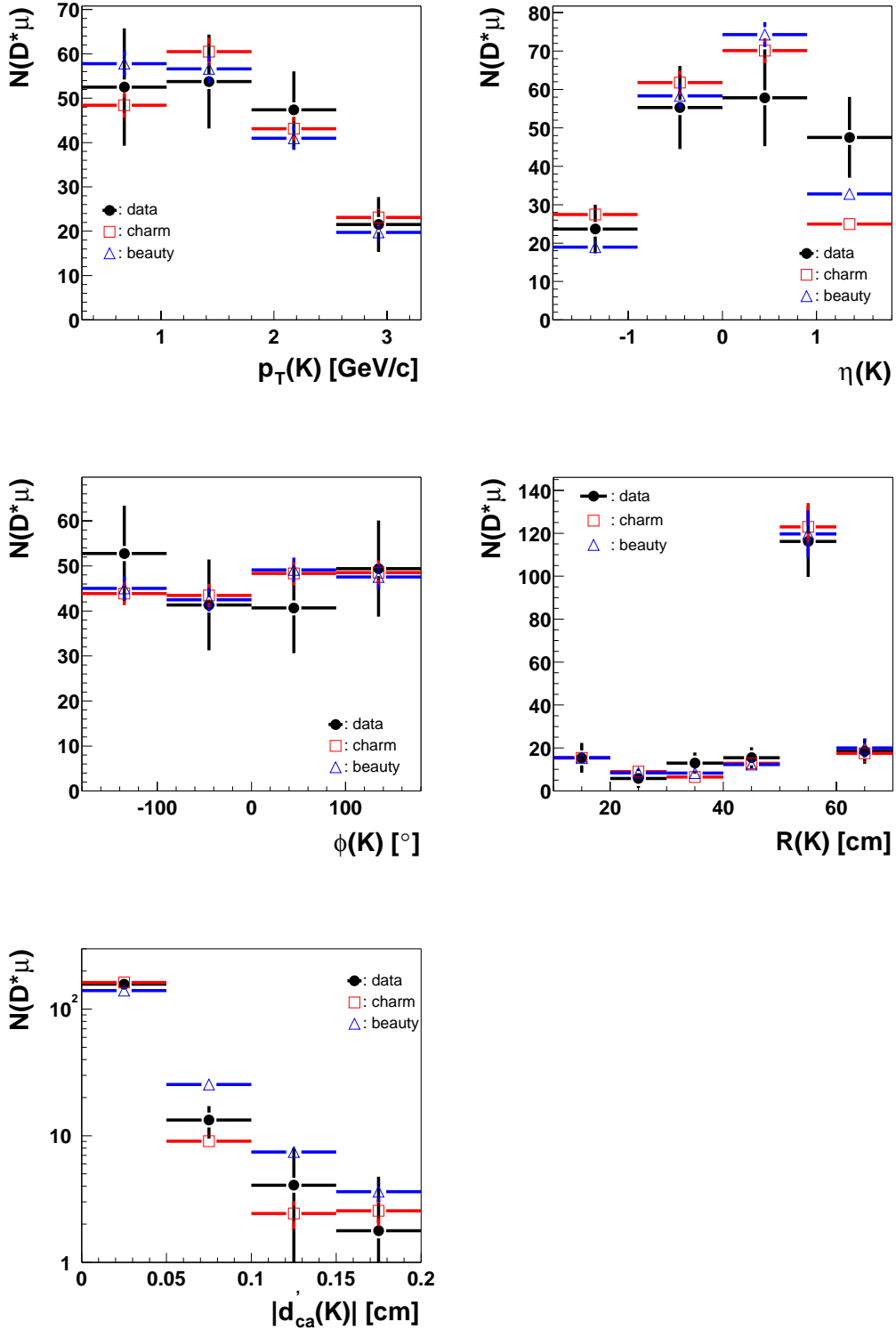


Figure 5.11: Description of the *kaon variables* in the $D^*\mu$ photoproduction sample. The black dots indicate the data, the squares the charm Monte Carlo and the triangles the beauty Monte Carlo prediction. The transverse momentum p_T , the pseudorapidity η , the azimuthal angle ϕ , the radial track length R and the minimal distance d'_{ca} of the corresponding non-vertex fitted track with respect to the primary vertex of the kaon are shown.

the pseudorapidity and the azimuthal angle of the D^* -meson are shown in figure 5.12. In addition to the D^* -variables which are shown, also the D^0 -variables are all described reasonably by the Monte Carlo simulation. For the inclusive DIS D^* data sample and the overall $D^*\mu$ sample a similar description is obtained for the D^* and D^0 -meson quantities.

5.4 Description of Muon and Combined Variables

In this section the same variables as considered for the decay particles of the D^* -meson are checked for the muon: The transverse momentum $p_T(\mu)$, the pseudorapidity $\eta(\mu)$, the azimuthal angle $\phi(\mu)$, the radial track length $R(\mu)$ and the minimal distance $d'_{ca}(\mu)$ of the corresponding non-vertex fitted track with respect to the primary vertex. These variables are shown in figure 5.13 for the photoproduction sample and again reasonable agreement between data and the Monte Carlo simulation is obtained. Also for the total $D^*\mu$ sample including the DIS events in addition a similar description is obtained.

Further combined quantities obtained using the four-momentum of the D^* -meson and the muon four-momentum are considered. Figure 5.14 shows for photoproduction the transverse momentum $p_T^*(D^*\mu)$, the rapidity $\hat{y}(D^*\mu)$ and the invariant mass $M(D^*\mu)$ of the $D^*\mu$ -pair as well as the azimuthal angle difference $\Delta\Phi^*$ between the D^* -meson and the muon. In addition the transverse energy fraction $f_{ET}(D^*\mu)$ of the $D^*\mu$ -pair with respect to the transverse energy of all final state particles with a polar angle above 10° is shown. For these variables reasonable agreement between data and Monte Carlo simulation is obtained for the photoproduction sample as well as for the total $D^*\mu$ sample (not shown here).

5.5 Description of the Muon Background

The remaining background in $D^*\mu$ events after performing a ΔM fit consist of hadrons, mis-identified as muons, as well as muons from inflight decays. By reconstructing a D^* -meson the background from u , d , s events is negligible. The description of the remaining background, called muon background or muon fake, by the Monte Carlo simulation is investigated in this section.

The probability \mathcal{P} to mis-identify a hadron as a muon depends on the flight path and the material traversed in the H1 detector and also on the hadron type itself. For example the muon mis-identification probability is larger for kaons than for pions.

In the first measurement of open beauty at HERA [6, 98] the muon mis-identification probability was obtained by an inline Monte Carlo generator, which simulates and reconstructs only one hadron per event. With this method a large amount of Monte Carlo events could be produced. The obtained mis-identification probabilities determined as a function of p and θ are in good agreement with those obtained from the data. In the data these probabilities were extracted using elastic $\Phi \rightarrow K^+K^-$ and $K^0 \rightarrow \pi^+\pi^-$ events. The hadron composition in the final data sample was taken from the Monte Carlo simulation and the muon background in the final data sample was then obtained by applying the

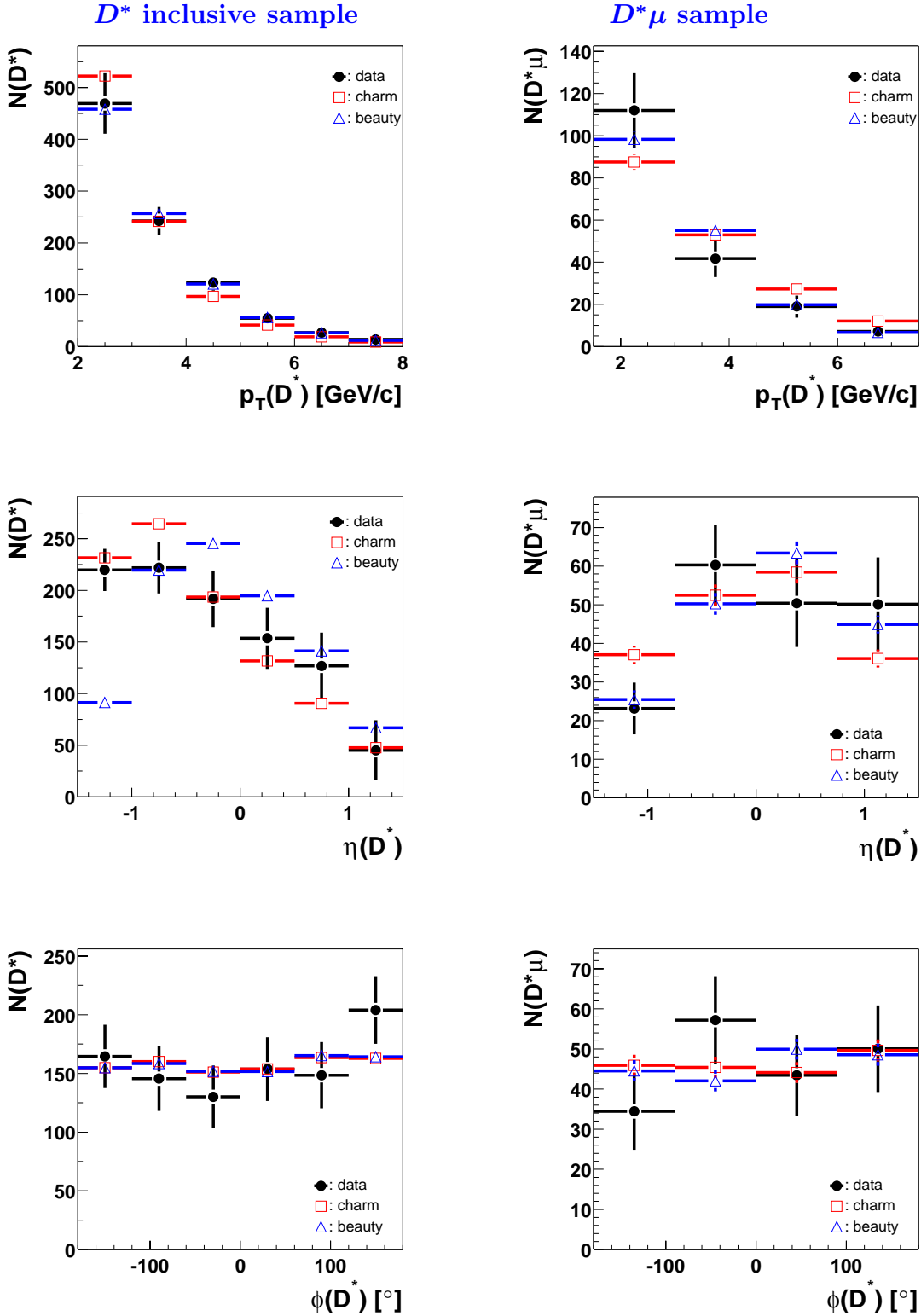


Figure 5.12: Description of the D^* variables in the *inclusive* D^* (left side) and in the $D^*\mu$ (right side) *photoproduction* samples. The black dots indicate the data, the squares the charm Monte Carlo and the triangles the beauty Monte Carlo prediction. The transverse momentum p_T , the pseudorapidity η , the azimuthal angle ϕ of the D^* -candidate are shown.

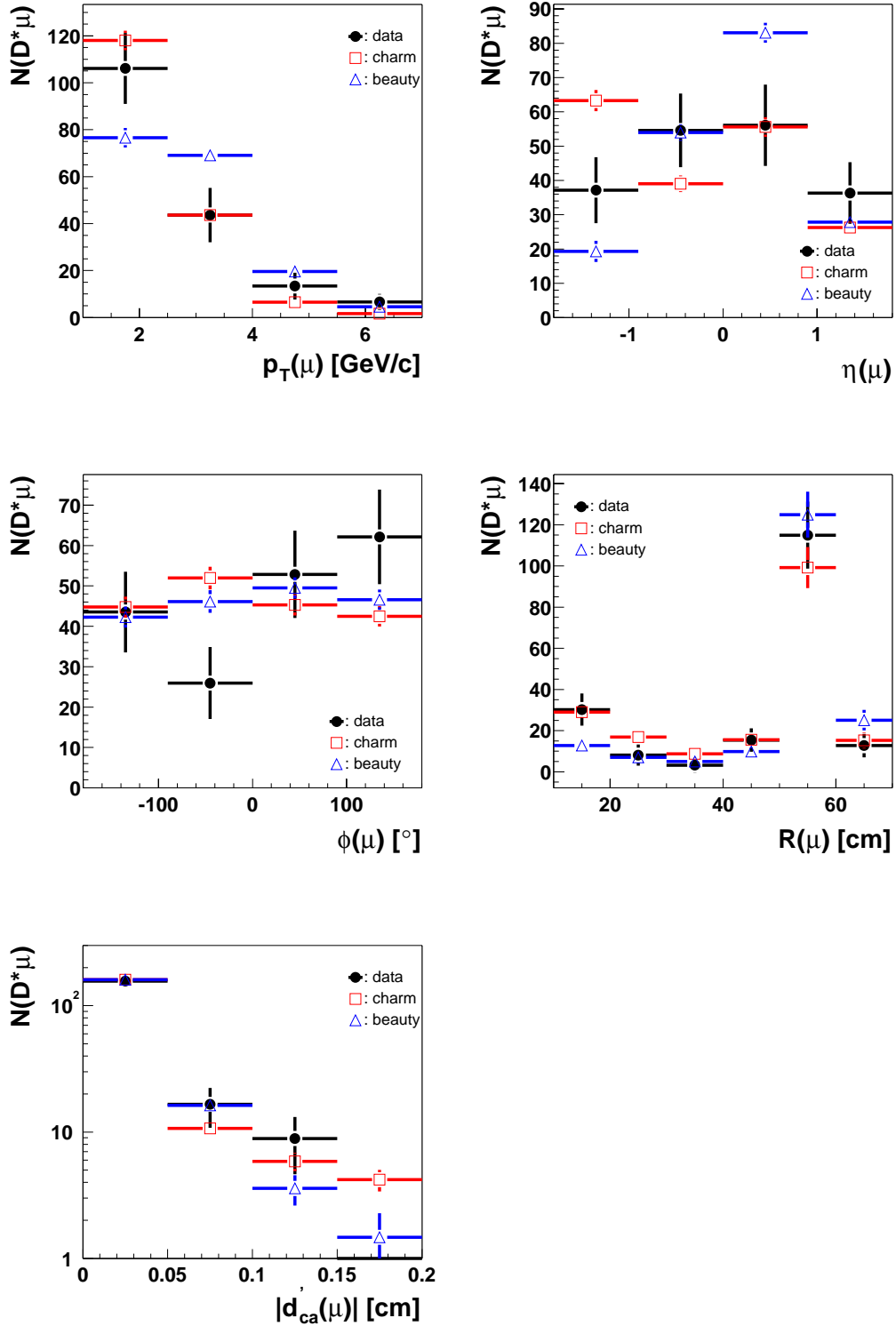


Figure 5.13: Description of the muon variables in the $D^*\mu$ photoproduction sample. The black dots indicate the data, the squares the charm Monte Carlo and the triangles the beauty Monte Carlo prediction. The transverse momentum $p_T(\mu)$, the pseudorapidity $\eta(\mu)$, the azimuthal angle $\phi(\mu)$, the radial track length $R(\mu)$ and the minimal distance $d'_{ca}(\mu)$ of the corresponding non-vertex fitted track with respect to the primary vertex are shown.

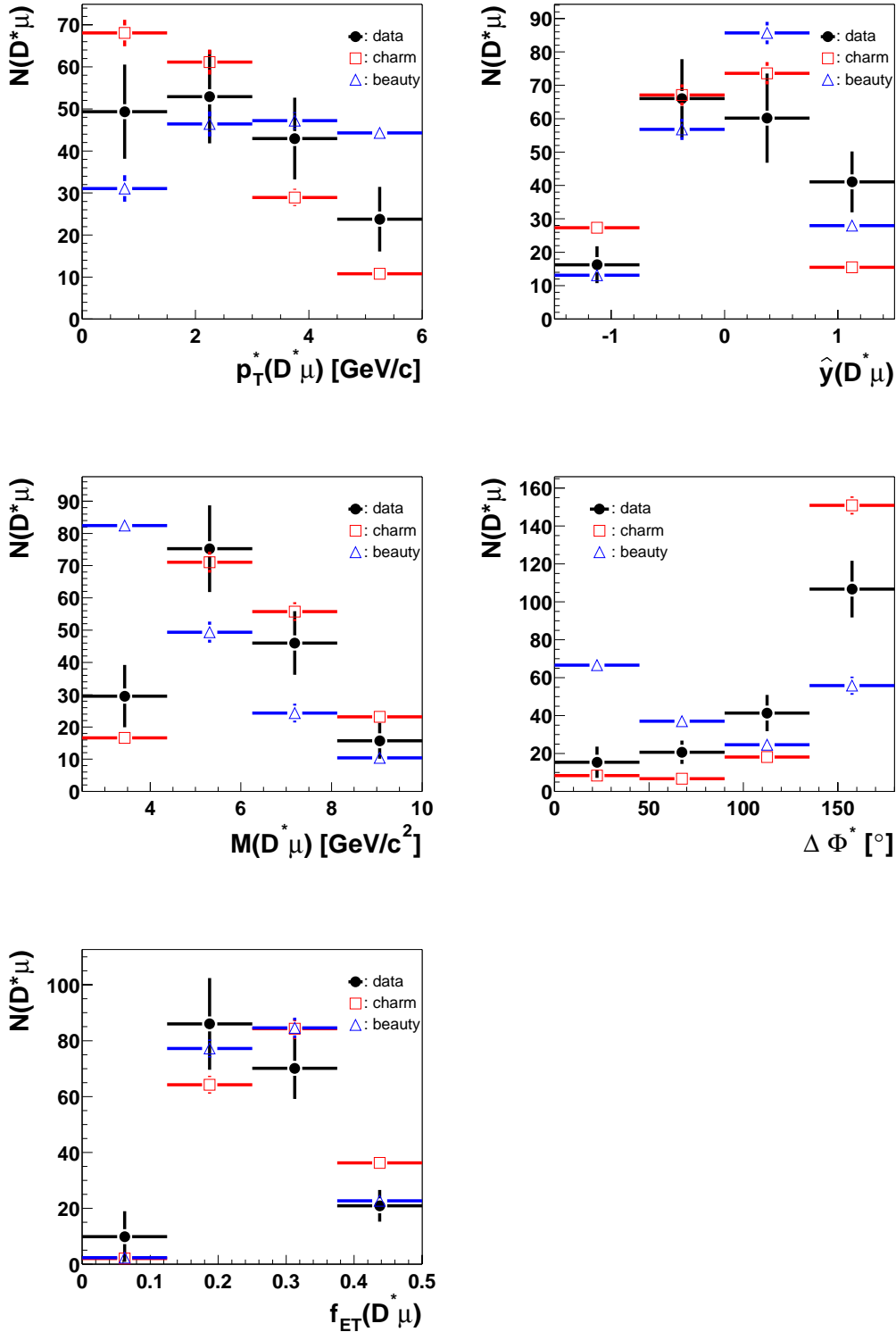


Figure 5.14: Description of the combined $D^*\mu$ variables in the $D^*\mu$ photoproduction sample. The black dots indicate the data, the squares the charm Monte Carlo and the triangles the beauty Monte Carlo prediction. Shown are the transverse momentum $p_T^*(D^*\mu)$, the rapidity $\hat{y}(D^*\mu)$, the invariant mass $M(D^*\mu)$ of the $D^*\mu$ -pair and the azimuthal angle difference $\Delta\Phi^*$ between the D^* -meson and the muon. In addition the transverse energy fraction $f_{ET}(D^*\mu)$ of the $D^*\mu$ -pair with respect to the transverse energy of all final state particles with a polar angle above 10° is shown.

muon fake probabilities on a data sample, with no real muons and a similar topology as the final data set.

In this analysis a data sample with similar event topology as the final data set and without real muons are the inclusive D^* samples in tagged photoproduction and DIS. Here, however the obtained muon fake contribution would be statistically very limited. A further problem in using these samples is, that a different kinematic reconstruction is used for the inclusive D^* -selection and the $D^*\mu$ selection in photoproduction.

In a recent open beauty ($b \rightarrow \mu$) measurement [7], detailed studies [99] showed, that the mis-identification probability depends not only on p and θ , but also on the energy deposition in the calorimeter (important for hadrons, mis-identified as muons, so-called punch through) and the decay kinematics of the hadrons (important for decay muons). In principle these dependencies should be simulated also with an inline generator and probabilities as a function of the energy deposition and the decay kinematics are in principle calculable. However due to at least two more dependencies much more statistics is needed to get precise probabilities and furthermore possible effects due to other particles or tracks cannot be simulated.

Due to these reasons, in this analysis the muon background is taken directly from the Monte Carlo simulation, which contains significantly more events than the data and which takes care of all hidden dependencies of the mis-identification probability.

The hadron mis-identification probability is checked with the decay particles of the D^0 meson using the inclusive D^* samples. This method has the advantage that the mis-identification probability is determined for particles in a realistic environment. The particles are in jets and correlations due to overlapping tracks or shower signals are taken into account.

Since for the selected muon a cut $p(\mu) > 2.0$ GeV/c is applied, only inclusive D^* events with a momentum of one of the two D^0 decay particles – kaon or pion – of above $p(K \text{ or } \pi) > 2.0$ GeV/c are used. This sample is referred to as the starting sample. For this starting sample the distribution in the azimuthal angle ϕ , the momentum p and the polar angle θ of the kaon or pion are shown in figure 5.15. It is then checked, whether the kaon or pion, fulfilling the above condition, is falsely reconstructed as a muon, leading to the muon background distributions. To ensure that the kaon or pion of the D^* -candidate is not a real muon, in each bin of the considered distributions, the simultaneous ΔM -fit to the right and wrong charge combination distribution is performed. The hadron mis-identification probability depending on a variable x is then obtained as the ratio of the muon background distribution to the distribution of the starting sample.

The probabilities determined in this way hold for a certain ratio of kaons and pions in the sample and it has to be ensured, that this ratio is also described by the Monte Carlo simulation in the correct way. The ratio between reconstructed kaon and pion candidates, obtained via the usual ΔM -fit to reduce the amount of wrong candidates, is about one in the starting sample. For the data a ratio of 1.03 ± 0.05 is obtained and for charm or beauty a ratio of 1.07 or 1.1 is obtained respectively in the photoproduction sample. Since the momentum distribution of the heavier kaon is slightly harder than the momentum distribution of the pion this ratio is slightly above one. However, this ratio is reasonably described for both inclusive D^* -samples by the Monte Carlo simulation.

Figure 5.15 shows the muon mis-identification probability \mathcal{P} as a function of the azimuthal angle ϕ , the momentum p and the polar angle θ of the kaon or pion for the inclusive D^* DIS sample. The DIS sample is chosen, since it contains significantly more events. Good agreement between data and Monte Carlo is obtained and as expected the single differential hadron mis-identification probabilities do not depend strongly on the type of the heavy quark. The small differences between the two heavy quark types can be explained by the dependence of the muon mis-identification probability on θ and small differences in the θ starting distribution.

After showing, that the hadron mis-identification probabilities and the muon-, event-, D^* -, $D^*\mu$ -, and kinematic variables are described by the MC in a correct way, one can conclude, that the Monte Carlo simulation describes the muon background reasonably well. Thus the Monte Carlo simulation is used in the following to correct for the muon background in the data. Due to the small differences observed between charm and beauty in the muon mis-identification probabilities and the small discrepancies in $\eta(\mu)$ between data and Monte Carlo simulation in the final $D^*\mu$ sample a relative systematic uncertainty of 20% is estimated for the muon background for charm as well as for beauty.

In this chapter the Monte Carlo simulation was compared to the data. Since there are several effects for the $D^*\mu$ samples, which are not or not correctly described in the Monte Carlo simulation, a reweighting of the Monte Carlo simulation was introduced. Using this reweighting reasonable agreement between data and Monte Carlo simulation is obtained in all variables. The muon background was checked with real data using the kaon and the pion from the D^0 decay. No discrepancy to the Monte Carlo simulation has been found. In the next chapters the Monte Carlo simulation after reweighting will be used to determine the beauty fraction in the $D^*\mu$ samples, for the correction of muon background and for the calculation of efficiencies.

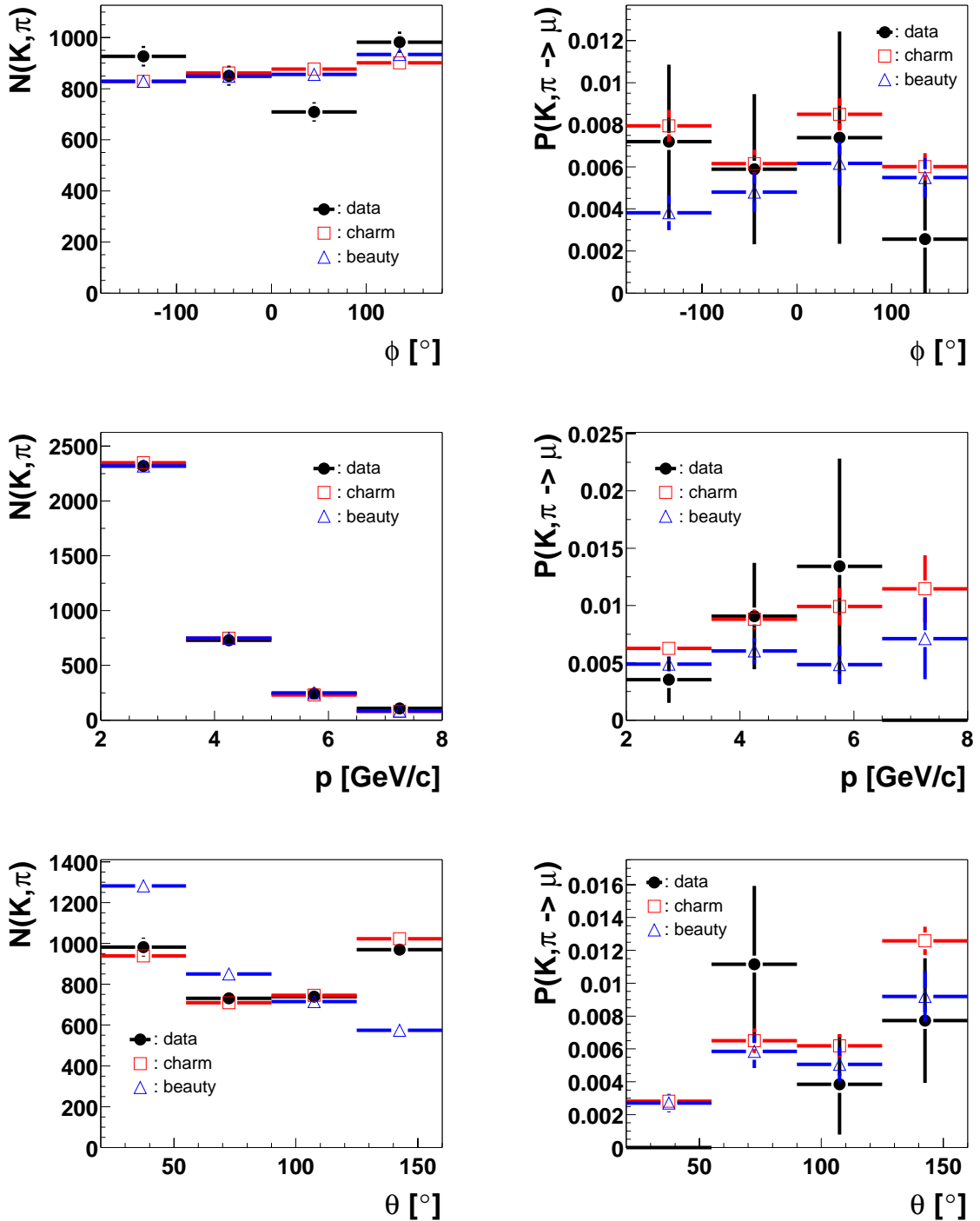


Figure 5.15: Muon mis-identification probabilities for the inclusive DIS D^* -sample. A cut on the momentum of the kaon or pion track of the D^* candidate above 2 GeV/c is applied. On the left side the distributions of the azimuthal angle ϕ , the momentum p and the polar angle θ are shown for the starting sample. On the right side the probabilities depending on the azimuthal angle ϕ , the momentum p and the polar angle θ are shown. The black dots indicate the data, the squares the charm Monte Carlo and the triangles the beauty Monte Carlo prediction. In case of a zero entry for data, the number of events in the final sample has not been sufficient to determine a probability with the ΔM -fit.

Chapter 6

Separation of Charm and Beauty Production

In this chapter the charm and beauty fractions in the selected $D^*\mu$ -events are determined. The four different charge and angle correlation regions are well suited for the separation of charm and beauty. The fraction of charm and beauty events is determined using a two dimensional Log-Likelihood-Fit. In the fit the mass difference between the D^* and D^0 candidate (ΔM) and the charge and angle correlations are used.

The beauty fraction determined in this way is then checked using control distributions, where the data are compared to the normalised sum of the charm and beauty Monte Carlo predictions, using the obtained beauty fraction. The Monte Carlo simulation used in this chapter is always adjusted according to the procedure introduced in chapter 5.

It is shown, that the mean measured distance between the primary vertex and the D^0 decay vertex increases with increasing beauty fraction due to the lifetime of the beauty hadron.

Furthermore this method of separating charm and beauty in $D^*\mu$ -events is compared to the results of other methods, which use slightly different variables for the separation or which apply the separation only to a restricted range of the data.

6.1 Charge and Angle Correlations between the D^* and the Muon

As already introduced in chapter 2 charm and beauty production can be separated by exploiting the charge and angular correlations between the D^* and the muon. The following four correlation regions were defined (see chapter 2):

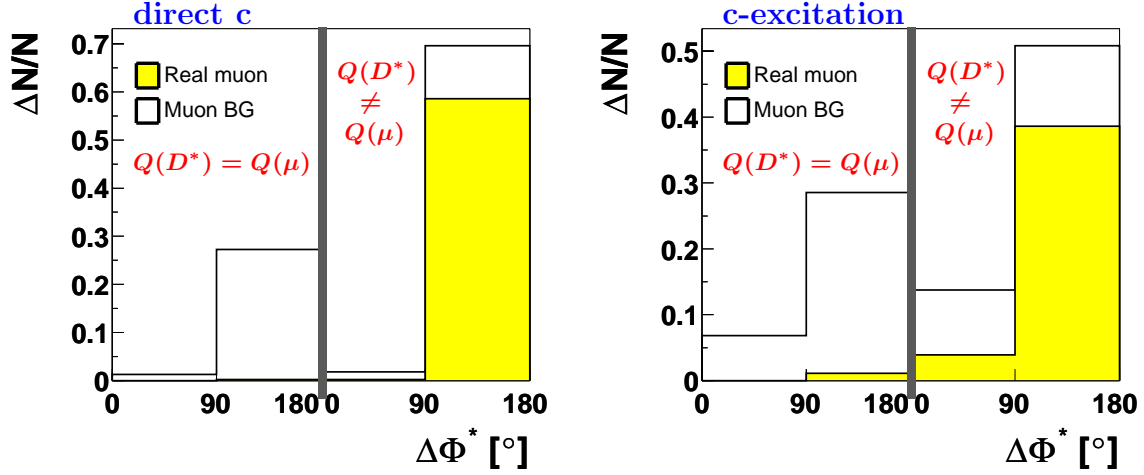


Figure 6.2: Population of the four correlation regions for the direct (left) and excitation (right) component for the charm photoproduction Monte Carlo events. All reconstructed $D^*\mu$ events (open histogram) and the real $D^*\mu$ events (gray histogram) are shown.

Contribution [%]	Charm	Beauty
γp		
direct	63	78
excitation	37	22
$\gamma p + \text{DIS}$		
γp direct	51	62
γp excitation	30	17
DIS direct	19	21

Table 6.1: Different contributions of the two $D^*\mu$ samples as predicted by the PYTHIA Monte Carlo simulation after reweighting.

In general the muon background is larger in correlation regions 2 and 4 with $\Delta\Phi^* > 90^\circ$ than in the other two correlation regions (see e.g. figure 6.2). The reason is that the decay particles of the D^* cannot be mis-identified as muons due to the requirement that the muon track $\text{track}(\mu) \neq \text{track}(K, \pi, \pi_s)$. This leads to fewer possibilities for mis-identifying a hadron as muon for $\Delta\Phi^* < 90^\circ$ (correlation regions 1 and 3).

It is striking that the absolute values of mis-identified muons in charm is larger for correlation region 2 than for correlation region 4 (both with $\Delta\Phi^* > 90^\circ$). In the case that the D^* -meson and the muon have opposite charges (correlation region 4), "real" muons can be found, while this is not possible if the D^* and the muon have the same charge as in correlation region 2 (at least for the direct component). In correlation region 2 the leading particle carrying the same charge as the D^* , is mostly the kaon from the corresponding charm hadron decay ($c\text{-hadron} \rightarrow K^-, \bar{c} \rightarrow D^{*-}$). In correlation region 4 this possibility is excluded due to the charge requirement and almost only pions produced via the semileptonic decay of the charm hadron are possible candidates for a mis-identification ($c\text{-hadron} \rightarrow \pi^+, \bar{c} \rightarrow D^{*-}$). Since the mis-identification probability is larger for kaons than for pions the muon background is larger in correlation region 2 than in correlation region 4.

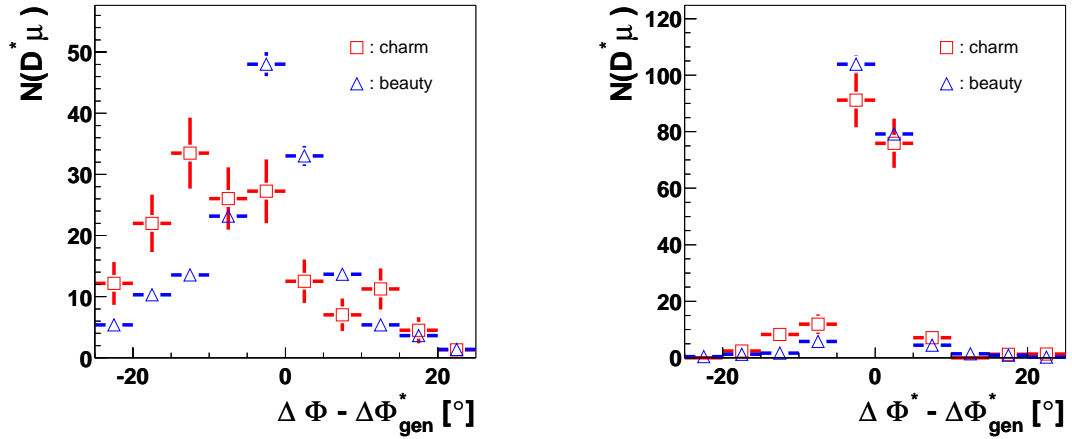


Figure 6.3: Correlation between (left) reconstructed $\Delta \Phi$ and (right) $\Delta \Phi^*$ and the generated $\Delta \Phi_{gen}^*$ for the DIS sample. Variables marked with a star are calculated in the γp -rest frame. The beauty Monte Carlo (triangles) and the charm Monte Carlo (squares) predictions are shown separately.

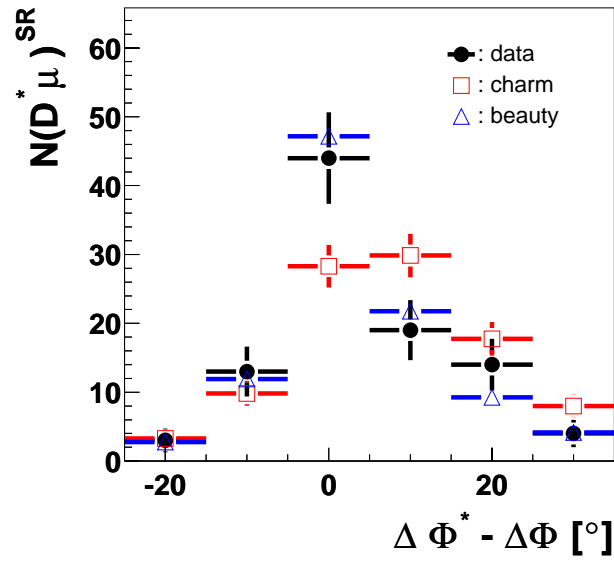


Figure 6.4: Correlation between reconstructed $\Delta \Phi$ and $\Delta \Phi^*$ for DIS $D^* \mu$ events. Variables marked with a star are calculated in the γp -rest frame. The black points indicate the data (events in the D^* -signal region), the triangles the beauty Monte Carlo and the squares the charm Monte Carlo prediction.

In photoproduction the azimuthal angle difference between the D^* -meson and the muon measured in the laboratory frame is identical to that determined in the photon-proton rest frame. The situation changes for DIS events since the scattered electron carries a non-negligible transverse momentum. Therefore a Lorentz transformation into the photon-proton rest frame is performed in this analysis for the DIS events. The differences between the reconstructed $\Delta \Phi$ determined in the laboratory frame and the reconstructed $\Delta \Phi^*$ calculated in the γp -rest frame to the generated values $\Delta \Phi^*$ are shown in figure 6.3, respec-

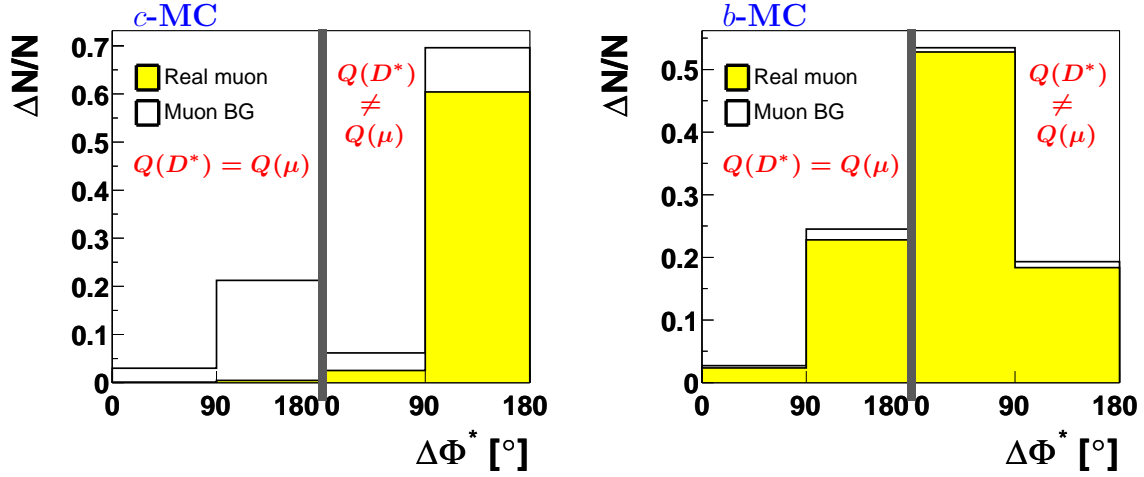


Figure 6.5: Population of the four correlation regions for charm (left) and beauty (right) Monte Carlo events (DIS + photoproduction). All reconstructed $D^*\mu$ events (open histogram) and the real $D^*\mu$ events (gray histogram) are shown.

corr. region	$\Delta N_{rec}/N_{rec}$ [%]				$f_{\mu-BG}$ [%]					
	1	2	3	4	1	2	3	4	1-4	
charm γp										
dir.+exc.	3	21	6	70	100	98	66	13	36	
dir.	1	21	1	77	100	99	89	11	31	
exc.	5	23	13	59	100	96	62	17	45	
c γp + DIS	3	21	6	70	96	98	58	13	37	
beauty γp										
dir.+exc.	3	24	54	19	14	7	1	5	4	
dir.	2	27	50	21	16	7	1	5	4	
exc.	7	16	66	11	12	9	2	4	4	
b γp + DIS	3	25	53	19	13	7	1	5	4	

Table 6.2: Population $\Delta N/N$ and muon background fraction $f_{\mu-BG}$ of the four correlation regions for the charm and beauty Monte Carlo simulations.

tively. As expected the correlation between the reconstructed and the generated variable is much worse, if no transformation is performed. Resolution effects of the measured Q^2 , polar angle θ'_e and azimuthal angle ϕ'_e of the scattered electron, which are used for the boost into the γp -rest frame, are small compared to the effect of the boost itself. Figure 6.4 demonstrates, that the relation between the reconstructed $\Delta\Phi$ and $\Delta\Phi^*$, and with that also the boost in general, is described by the Monte Carlo. Due to the restricted number of $D^*\mu$ events in the DIS sample all events within the D^* -signal region are considered.

The population of the four correlation regions for the total $D^*\mu$ -sample containing also DIS events is shown in figure 6.5 for charm and beauty Monte Carlo predictions. A similar behaviour as in the pure photoproduction case is observed.

Table 6.2 summarises the contributions and the muon background fraction in each correlation region for the charm and beauty Monte Carlo. This is done separately for photo-

production and the total data sample.

The distribution of the correlation regions is sufficiently different for reconstructed charm and beauty D^* - μ -events to use this quantity for a determination of the beauty fraction in the data (see figures 6.1 and 6.5).

6.2 Determination of the Charm and Beauty Fraction

To extract the charm and beauty fraction in the data a two dimensional Log-Likelihood fit is used. For the fit a two dimensional distribution of the data, depending on the mass difference ΔM of the D^* and D^0 -candidate and on a ‘‘separation variable’’ is used. The corresponding two dimensional theoretical distribution is fitted to the data. This procedure exploits the complete information of the ΔM and the separation variable and a separation of charm and beauty is possible. As separation variables the four correlation regions are used in this analysis.

The Log-Likelihood fit is based on the assumption of Poisson distributed data in the bins and the following function has to be minimised in the case of a two dimensional binned distribution [100]:

$$F(\vec{P}) = \sum_{i=1}^{\#i\text{-bins}} \sum_{j=1}^{\#j\text{-bins}} F(i, j) \quad (6.1)$$

with:

$$F(i, j) = 2 \cdot \left[(\mu(i, j) - r(i, j)) + r(i, j) \cdot \ln \left(\frac{r(i, j)}{\mu(i, j)} \right) \right] \quad (6.2)$$

Here $r(i, j)$ indicates the observed number of events in an analysis bin (i, j) and $\mu(i, j)$ the number of expected events in this bin. \vec{P} is the parameter vector. The function $F(i, j)$ behaves approximately like a χ^2 function. A derivation of equation 6.2 is given in appendix C.

As for the one dimensional ΔM -fit a simultaneous fit to the right charge (RC) and wrong charge (WC) data samples is performed. The index i denotes the ΔM bins and j the correlation region or in general the separation variable. The function, which has to be minimised is therefore:

$$F(\vec{P}) = \sum_{i=1}^{\#\Delta M\text{-bins}} \sum_{j=1}^{\#\text{sep.var. bins}} \left(F^{RC}(i, j) + F^{WC}(i, j) \right) \quad (6.3)$$

with:

$$F^{RC/WC}(i, j) = 2 \cdot \left[\left(\mu^{RC/WC}(i, j) - r^{RC/WC}(i, j) \right) + r^{RC/WC}(i, j) \cdot \ln \left(\frac{r^{RC/WC}(i, j)}{\mu^{RC/WC}(i, j)} \right) \right] \quad (6.4)$$

for the right or wrong charge data set.

In the fit 25 bins in ΔM and 4 bins for the correlation regions or another separation variable are used. Altogether six free parameters are used, $\vec{P} = (N_c, N_b, U(1), U(2), U(3), U(4))$:

N_c and N_b give the number of $D^*\mu$ -events from charm and beauty respectively, and one background parameter $U(j)$ is needed for each bin of the separation variable.

The data consist of true $D^*\mu$ -events and also background events. The signal can be subdivided into real $D^*\mu$ events from charm and beauty production and the background in combinatorial background ($U_{comb.}$) of the D^* -selection and into real D^* events, where the reconstructed muon is either a mis-identified hadron or a decay muon (muon background: $U_\mu = U_\mu^c + U_\mu^b$). The combinatorial D^* background however also contains real muons as well as hadrons mis-identified as muons or decay muons. Therefore the reconstructed $D^*\mu$ -events consist of:

$$\text{C-}D^*\mu\text{-signal} + \text{B-}D^*\mu\text{-signal} + \text{comb. background} + \text{muon background}$$

This can be rewritten as:

$$\underbrace{\text{C-}D^*\mu\text{-signal} + U_\mu^c}_{\text{'Charm } D^* \text{ signal'}} + \underbrace{\text{B-}D^*\mu\text{-signal} + U_\mu^b}_{\text{'Beauty } D^* \text{ signal'}} + U_{comb.}$$

With the aid of the two dimensional Log-Likelihood fit the number of $D^*\mu$ -events from charm and beauty-production in the signal is determined. For the fit the muon background fractions for charm and beauty predicted by the Monte Carlo are used. In chapter 5 it was shown that the muon background predicted by the Monte Carlo describes the data.

The normalised distribution in the separation variable (see for example figure 6.1) is multiplied with a ΔM dependent Gaussian function for charm and beauty. The width σ and the position μ of the Gaussian function are fixed to the corresponding D^* values obtained from the fit to the ΔM distribution in chapter 4 ($\mu = 145.4 \text{ MeV}/c^2$ and $\sigma = 1.1 \text{ MeV}/c^2$). The background is described by the modified square root function, discussed in chapter 4, multiplied with a free parameter for each bin in the separation variable. The function $\mu^{RC}(i, j)$, which is fitted to the right charge combination data set, therefore has the form:

$$\mu^{RC}(i, j) = \underbrace{N_c \cdot [f_c^{norm.}(j) \cdot f_{D^*}^{norm.}(i)]}_{\text{Charm } D^* \text{ signal}} + \underbrace{N_b \cdot [f_b^{norm.}(j) \cdot f_{D^*}^{norm.}(i)]}_{\text{Beauty } D^* \text{ signal}} + \underbrace{U(j) \cdot f_{BG}^{norm.}(i)}_{\text{RC Background}} \quad (6.5)$$

and the equation for the function $\mu^{WC}(i, j)$ is:

$$\mu^{WC}(i, j) = \underbrace{U(j)N_{scal}(j) \cdot f_{BG}^{norm.}(i)}_{\text{WC Background}} \quad (6.6)$$

Here the variables have the following definitions:

- $f_c^{norm.}(j)$: Normalised distribution of the separation variable for charm
- $f_b^{norm.}(j)$: Normalised distribution of the separation variable for beauty
- $f_{D^*}^{norm.}(i)$: Normalised Gaussian depending on ΔM
- $f_{BG}^{norm.}(i)$: Normalised background function depending on ΔM
- $N_{scal}(j)$: Scaling factor between the RC and WC combinatorial background

The scaling factor $N_{scal}(j)$ is determined in the same way as for the one dimensional ΔM -fit:

$$N_{scal}(j) = \frac{\sum_{bin} N_{bin}^{WC}(j)}{\sum_{bin} N_{bin}^{RC}(j)} \quad \text{for } \Delta M\text{-bins between } 0.155 \text{ and } 0.1685 \quad (6.7)$$

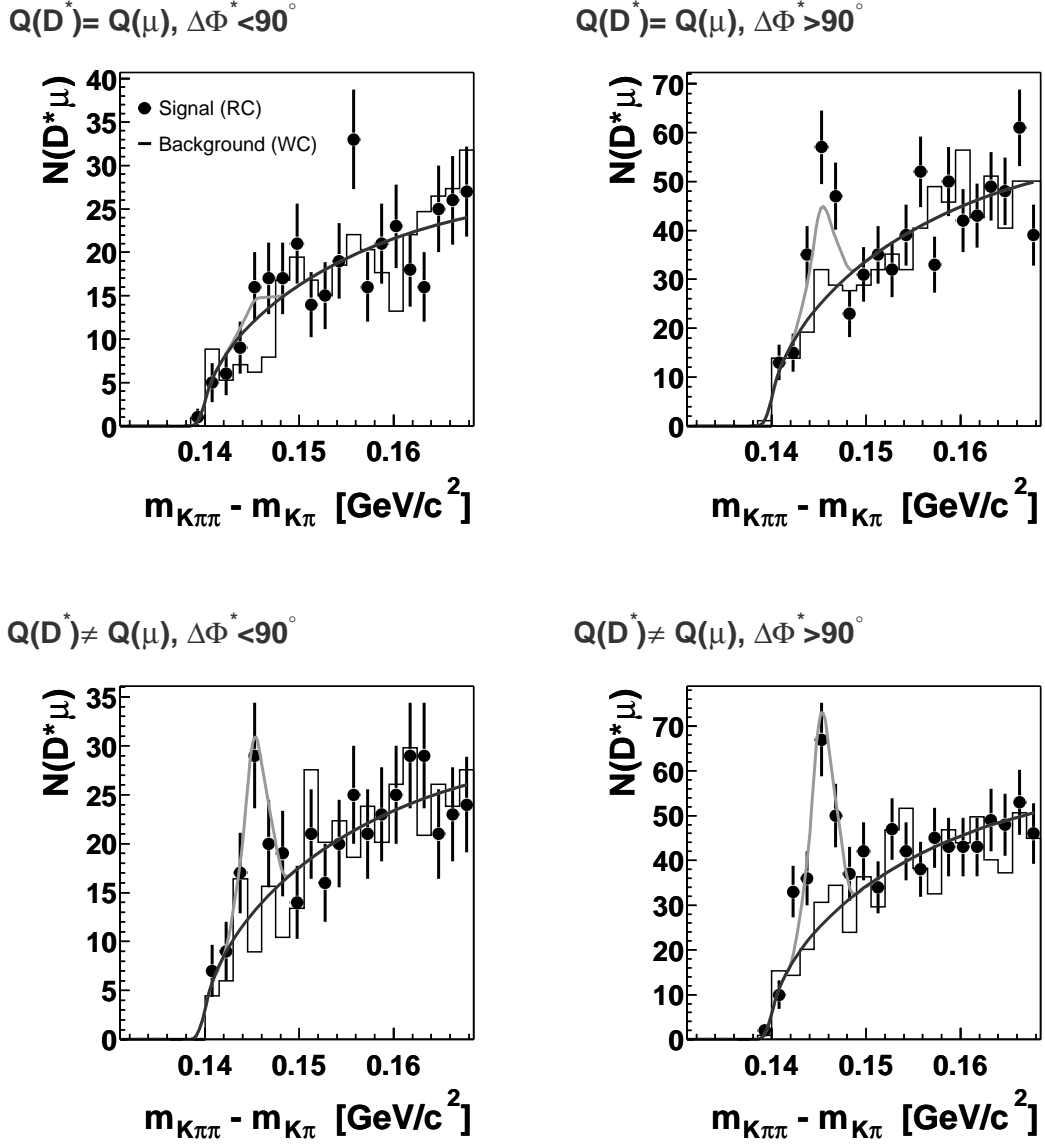


Figure 6.6: ΔM distribution of the *photoproduction data* (right charge combination (RC): dots, wrong charge combination (WC): histogram) together with the function obtained from the *two dimensional fit* (depending on the four correlation regions and ΔM). The light line indicates the RC fit curve and the dark line the WC fit curve. At large ΔM values the two curves are identical.

$f_c^{norm.}(j)$ and $f_b^{norm.}(j)$ can be expressed by two functions, one containing the real $D^*\mu$ events $f_{Q=c,b}^{true}$ and one for those classified as muon background $f_{Q=c,b}^{\mu-BG}$:

$$f_Q^{norm.}(j) = \frac{f_Q^{true}(j) + f_Q^{\mu-BG}(j)}{\sum_k^{\#sep.var.bins} (f_Q^{true}(k) + f_Q^{\mu-BG}(k))} \quad \text{with } Q = c, b \quad (6.8)$$

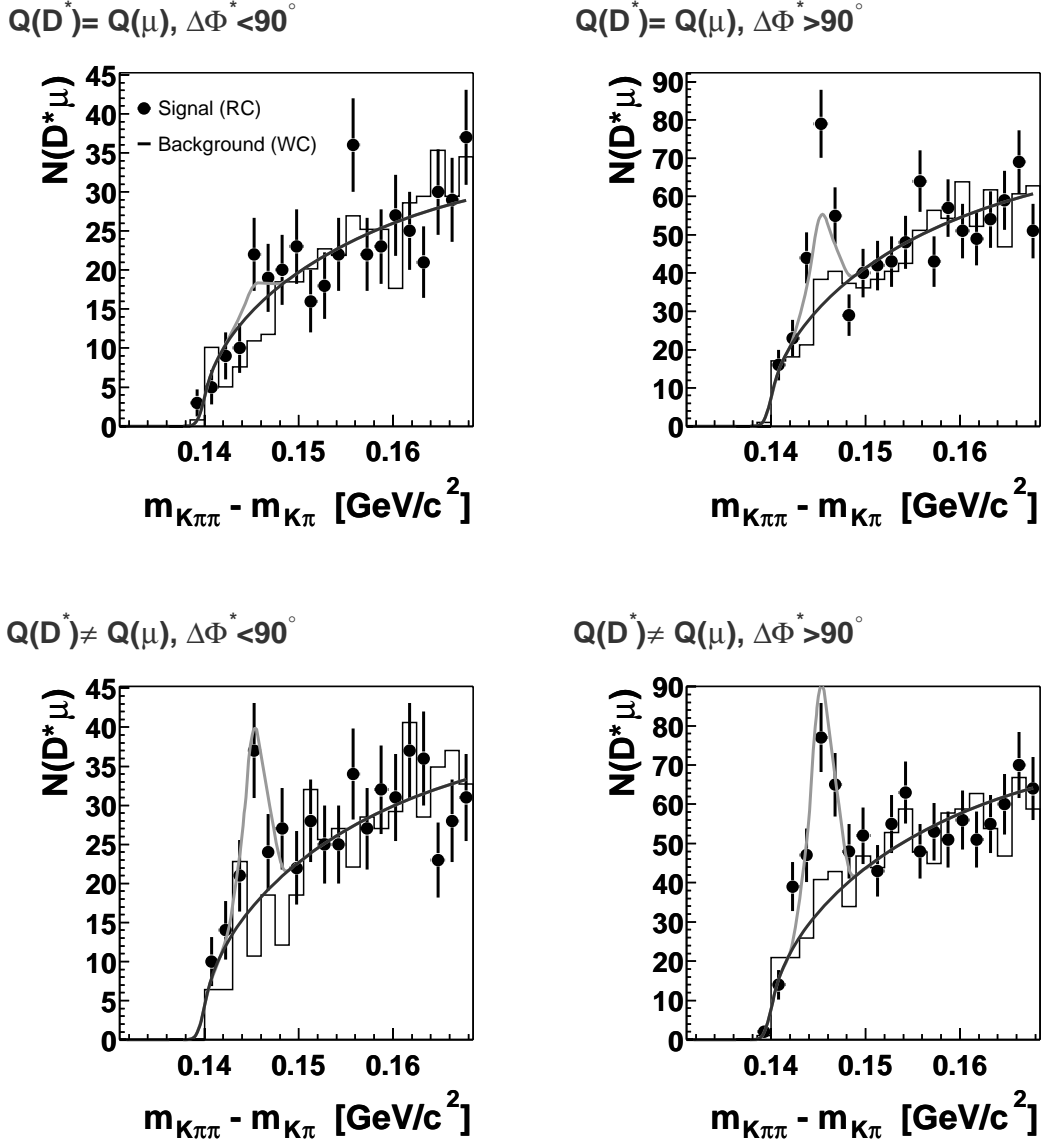


Figure 6.7: ΔM distribution of the *photoproduction + DIS* data (right charge combination (RC): dots, wrong charge combination (WC): histogram) together with the function obtained from the *two dimensional fit* (depending on the four correlation regions and ΔM). The light line indicates the RC fit curve and the dark line the WC fit curve. At large ΔM values the two curves are identical.

The function $f_{D^*}^{norm.}(i) = f_{D^*}(i) / \sum_l^{\#\Delta M - bins} f_{D^*}(i)$ is determined from:

$$f_{D^*}(i) = \frac{1}{d_{bin}} \int_{\Delta M_l(i)}^{\Delta M_u(i)} \frac{1}{\sqrt{2\pi}\sigma} \exp\left(-\frac{(\Delta M - \mu)^2}{2\sigma^2}\right) d\Delta M \quad (6.9)$$

The background function $f_{BG}^{norm.}(i) = f_{BG} / \sum_i f_{BG}(i)$ is obtained in a similar way:

$$f_{BG}(i) = \frac{1}{d_{bin}} \int_{\Delta M_l(i)}^{\Delta M_u(i)} (\Delta M - m_\pi)^{U_{exp}} \cdot (1 - U_{cor} \cdot \Delta M^2) d\Delta M \quad (6.10)$$

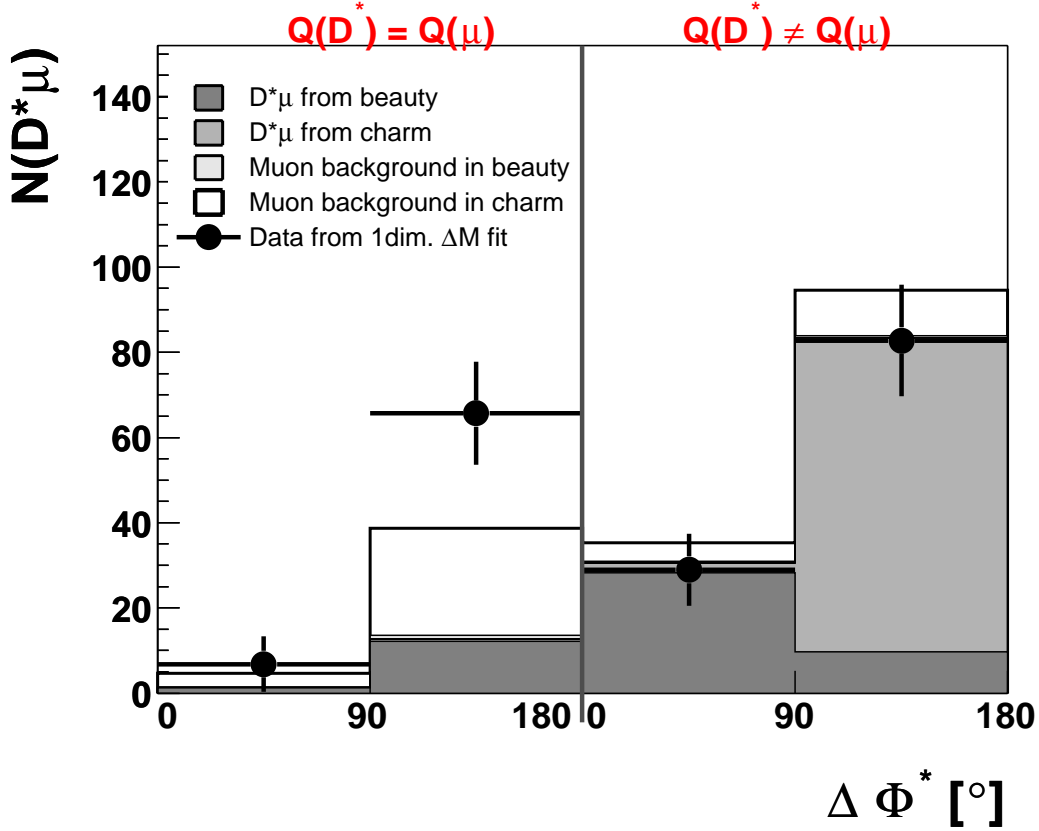


Figure 6.8: Population of the four correlation regions in the *photoproduction data sample* as obtained by the two dimensional fit. The black dots are the data, which are obtained from a one dimensional ΔM fit in each correlation region.

Here d_{bin} indicates the bin width, $\Delta M_l(i)$ and $\Delta M_u(i)$ the ΔM values of the lower and upper limits of the i -th bin respectively.

The product of either $f_c^{norm.}(j)$ or $f_b^{norm.}(j)$ and $f_{D^*}^{norm.}$ in equation 6.5 is normalised in such a way, that the parameter N_c (N_b) represents the number of reconstructed charm (beauty) events. $f_c^{norm.}(j)$ and $f_b^{norm.}(j)$ are determined with the aid of the adjusted Monte Carlo program, and they correspond to the "open" histograms of figure 6.1 in case of photoproduction and to figure 6.5 in case of the total sample.

Figures 6.6 (photoproduction) and 6.7 (photoproduction + DIS) show for the two dimensional Log-Likelihood fit the ΔM -distributions of the RC and WC data and the functions $\mu^{RC}(i, j)$ and $\mu^{WC}(i, j)$ obtained from the fit to the data in the four correlation regions. The data are described reasonably well by the fitted function. The largest discrepancy is observed for $\Delta\Phi^* > 90^\circ$. The minimum F_{min} of the function $F(\vec{P})$ is 139.7 for the photoproduction sample and 156.0 for the total sample. This is for both samples in good agreement with the number of degrees of freedom ndf . ndf is given by the total number of bins minus the number of bins which have a zero bin content in the data as well as in the Monte Carlo simulation ($2 \cdot 4 \cdot (25 - 5) = 160$), and minus the number of free parameters (6), leading to 154. The probability P , that the distribution of the data is consistent with

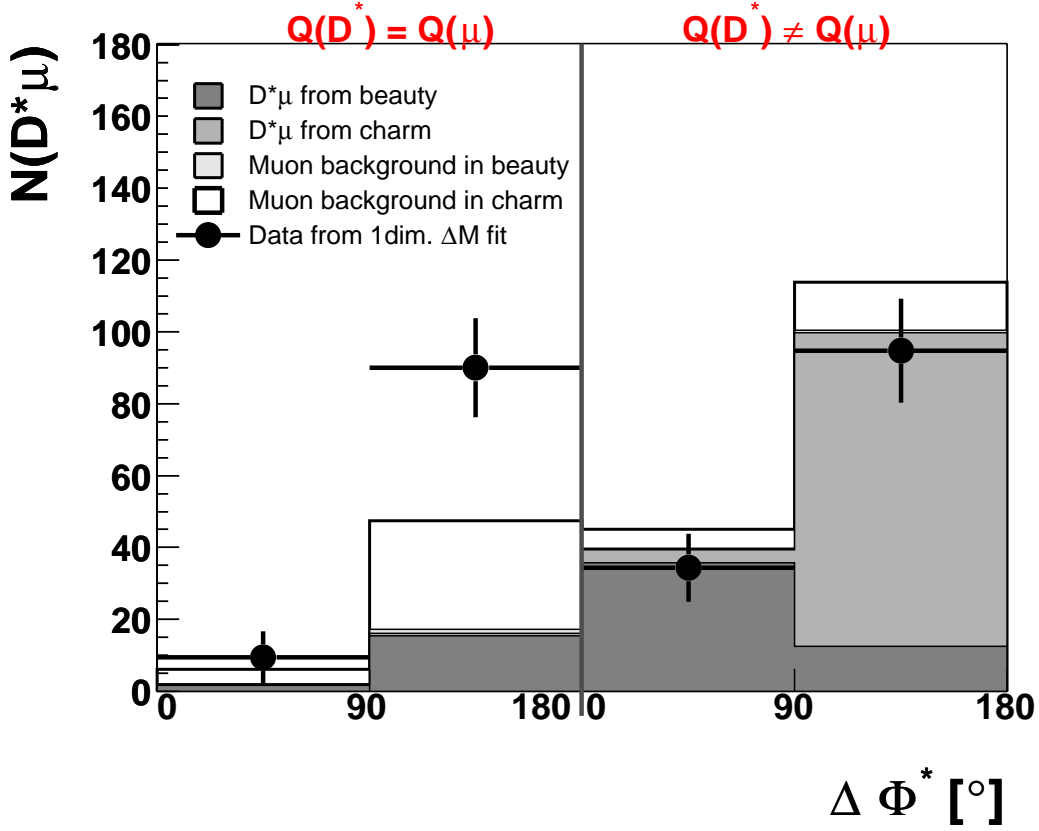


Figure 6.9: Population of the four correlation regions in the *photoproduction + DIS data sample* as obtained by the two dimensional fit. The black dots are the data, which are obtained from a one dimensional ΔM fit in each correlation region.

the theoretical curve obtained by the fit, can be calculated via the χ^2 distribution [100]:

$$P = \text{prob}(F_{min}, ndf) = \frac{1}{\sqrt{2^{ndf}}\Gamma(ndf/2)} \int_{F_{min}}^{\infty} e^{-\frac{1}{2}t} t^{\frac{1}{2}ndf-1} dt \quad (6.11)$$

For the photoproduction sample a probability of 0.789 and for the total sample of 0.444 is obtained. The correlation coefficient between N_c and N_b , which is a measure for the separation power of a quantity, results in -0.447 for the photoproduction sample and -0.473 for the total sample. The correlation coefficient value is 0, if both distributions are completely separated.

The result of the two dimensional fit is shown in figures 6.8 (photoproduction) and 6.9 (photoproduction + DIS). The populations of the four correlation regions of the data are shown subdivided into true $D^*\mu$ -events from charm and beauty production and those events classified as muon background, again shown separated for charm and beauty. The summed results are compared to the values obtained from the one dimensional ΔM fits. Reasonable agreement between the one and two dimensional fits is observed. For the photoproduction sample a total beauty fraction of $f_b = (31 \pm 6)\%$ is obtained, while for the total sample the beauty fraction is $f_b = (32 \pm 6)\%$. The statistical uncertainty

fit		correlation region				
		1	2	3	4	Σ
rec. $D^*\mu$						
γp	N_c	3.2 ± 0.5	26 ± 4	7 ± 1	84 ± 14	120 ± 20
	N_b	1.4 ± 0.5	13 ± 4	29 ± 9	10 ± 3	54 ± 17
	f_b [%]	31 ± 6	34 ± 6	81 ± 4	11 ± 3	31 ± 6
$\gamma p + DIS$	N_c	4.3 ± 0.7	31 ± 5	9 ± 1	101 ± 16	145 ± 23
	N_b	1.8 ± 0.5	17 ± 5	36 ± 11	13 ± 4	68 ± 20
	f_b [%]	30 ± 5	35 ± 6	80 ± 4	11 ± 3	32 ± 6
μ-BG corrected $D^*\mu$						
γp	N_c	0	0.5 ± 0.1	2.2 ± 0.4	74 ± 12	76 ± 13
	N_b	1.2 ± 0.4	12 ± 4	28 ± 9	10 ± 3	51 ± 16
	f_b [%]	100	96 ± 1	93 ± 2	12 ± 3	40 ± 7
$\gamma p + DIS$	N_c	0.16 ± 0.03	0.7 ± 0.1	3.6 ± 0.6	87 ± 14	92 ± 15
	N_b	1.6 ± 0.5	15 ± 5	36 ± 10	12 ± 4	65 ± 19
	f_b [%]	91 ± 2	96 ± 1	91 ± 2	12 ± 3	41 ± 6

Table 6.3: Results from the two dimensional fits: Number of $D^*\mu$ -events from charm and beauty production and the beauty fraction f_b in the two data samples in the four correlation regions. Both values, before and after muon background correction, are quoted. Only statistical errors are indicated. Only the total number of $D^*\mu$ events from charm and beauty production are a direct result of the fit (marked with bold font). The number of charm and beauty events in the four correlation regions are scaled down from the total fitted number of charm and beauty events using the Monte Carlo simulation. Therefore the relative ratios between the correlation regions are assumed to be described by the Monte Carlo simulation, while the total normalisation is obtained from the fit.

indicated is obtained via error propagation taking the correlation between the number of charm and beauty events into account. Correcting for the muon background (using table 6.2) these fractions modify to $f_b = (40 \pm 7)\%$ and $f_b = (41 \pm 6)\%$ respectively, since charm events contain more muon background than beauty events.

The fit result is once more summarised in table 6.3. The number of $D^*\mu$ -events from charm and beauty production in the two selected data samples are stated. This is separately shown for $D^*\mu$ events before muon background correction and after muon background correction. Only the total number of $D^*\mu$ events from charm and beauty production are direct results of the fit, while the number of charm and beauty events in the four correlation regions are obtained by scaling down the total fitted number of charm and beauty events using the Monte Carlo simulation. The relative ratios between the correlation regions are taken from the Monte Carlo simulation, while the total normalisation is obtained from the fit. In the next chapter total charm and beauty ep cross sections will be calculated using the values summarised in the table 6.3.

6.3 Control Distributions

As a check whether the beauty fraction determined by the two dimensional fit is reasonable, figures 6.10 (photoproduction) and 6.11 (photoproduction + DIS) show the transverse

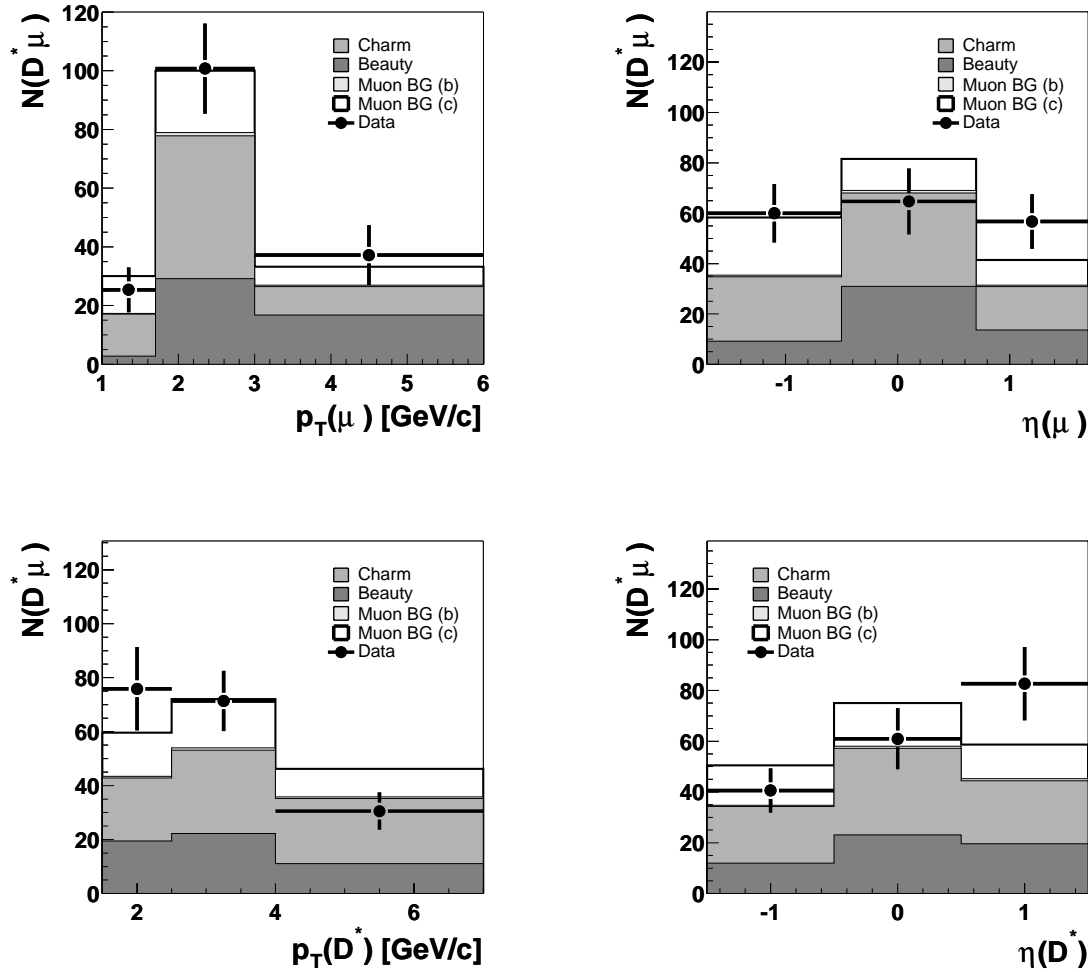


Figure 6.10: *Differential distribution of the transverse momentum p_T and pseudorapidity η of the muon and the D^* -meson for the **photoproduction data** (dots). Furthermore the sum of charm and beauty, using the beauty fraction $f_b = 31\%$ as obtained from the two dimensional Log-Likelihood fit, is drawn (upper black line). The individual contributions of pure beauty, pure charm and muon background of beauty and charm are also shown.*

momentum and the pseudorapidity of the D^* -meson and the muon together with the corresponding Monte Carlo distribution obtained using the b -fraction obtained by the fit ($f_b = 31\%$ for the photoproduction sample and $f_b = 32\%$ for the total sample). No correction for the muon background is applied here. The total Monte Carlo distributions are normalised to the data. The number of $D^*\mu$ events and the assigned statistical error are determined in each bin of the considered variable from the simultaneous ΔM fit to the right and wrong charge data.

All distributions of the two particles are described reasonably well by the Monte Carlo. However, in both pseudorapidity distributions some small differences do appear. For the D^* -meson an excess in forward direction (large η) is observed, similar to those reported in previous measurements at ZEUS and H1 ([31, 30, 14]). The pseudorapidity distribution

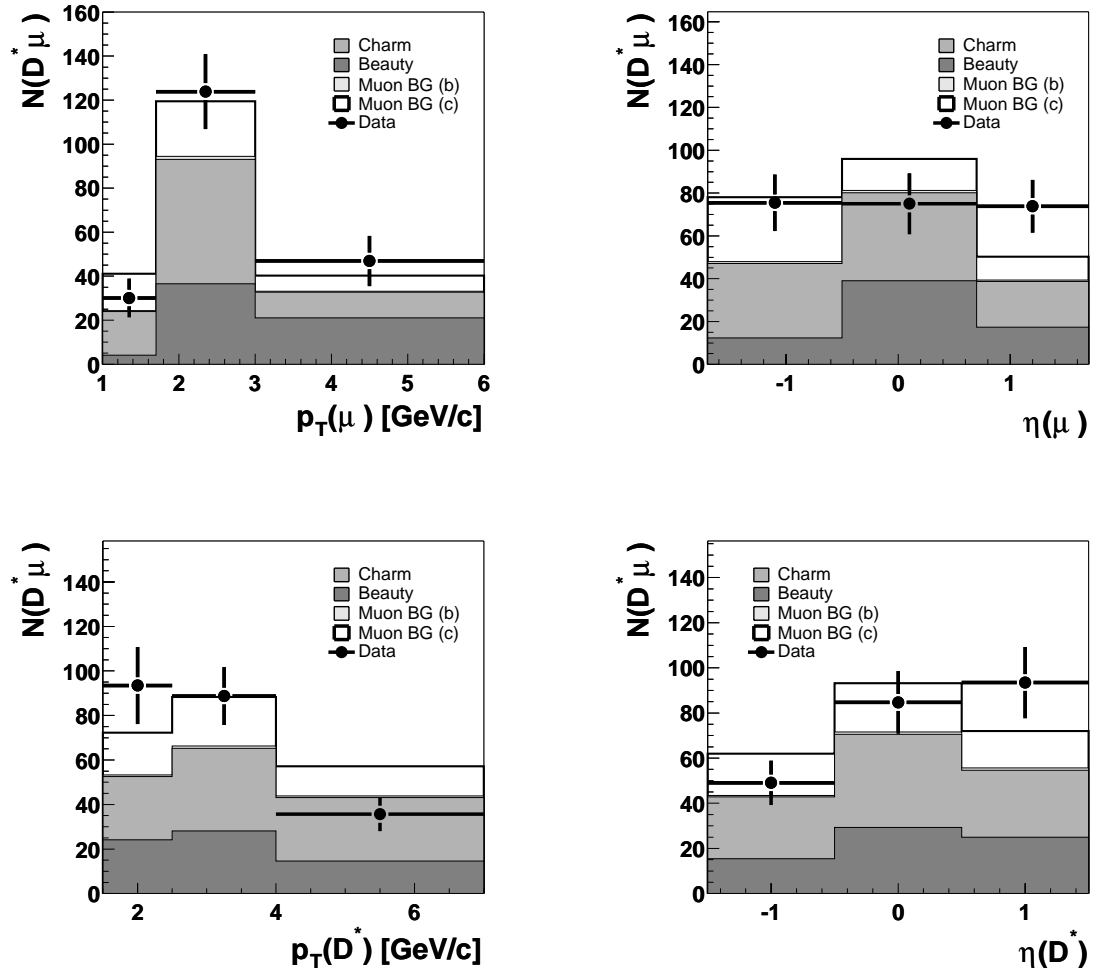


Figure 6.11: Differential distribution of the transverse momentum p_T and pseudorapidity η of the muon and the D^* -meson for the **photoproduction + DIS data** (dots). Furthermore the sum of charm and beauty, using the beauty fraction $f_b = 32\%$ as obtained from the two dimensional Log-Likelihood fit, is drawn (upper black line). The individual contributions of pure beauty, pure charm and muon background of beauty and charm are also shown.

of the muon seems to be somewhat flatter in the data than predicted by the Monte Carlo.

The reasonable description of the data by the Monte Carlo using the charm and beauty fractions determined from the fit shows that the separation procedure leads to a reasonable result, which can be applied also to other distributions.

In order to check, whether the excitation contribution as predicted by the PYTHIA Monte Carlo simulation is also reasonable, $x_\gamma(D^*\mu)$ is considered as an approximation for the relative momentum fraction of the parton, taking part in the hard interaction, with respect to the photon momentum (see section 2.1.5, equation 2.20). In figure 6.12 the distributions obtained using the Monte Carlo simulation with and without the excitation contribution are compared to the data for the photoproduction sample. In the Monte Carlo simulation

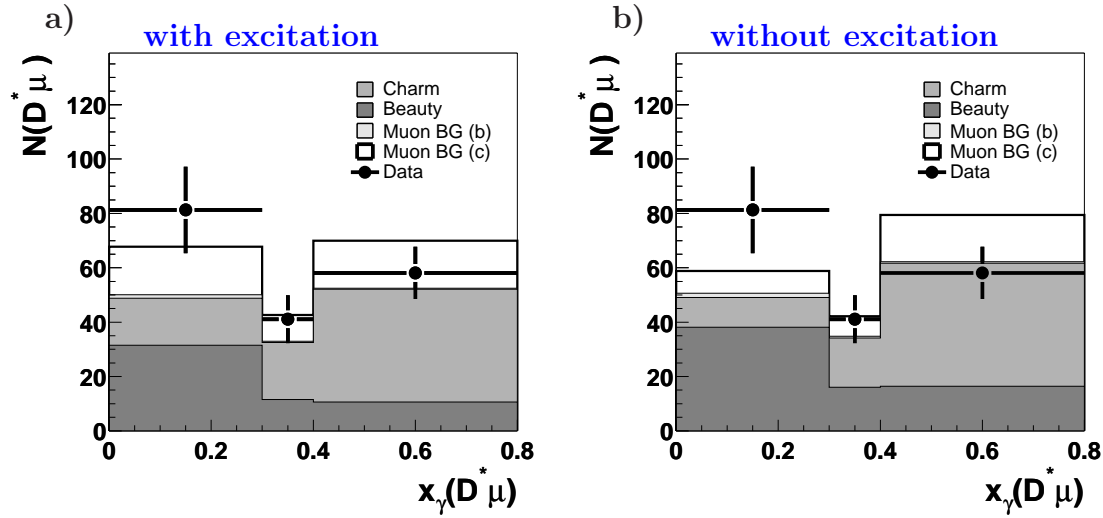


Figure 6.12: Check of the excitation resolved contribution in the photoproduction data. Shown is the $x_\gamma(D^*\mu)$ distribution (dots). a) Comparison with the PYTHIA Monte Carlo simulation with resolved excitation contribution, b) without such a contribution. Furthermore the sum of charm and beauty, using the beauty fraction as obtained from the two dimensional Log-Likelihood fit, is drawn (upper black line). The individual contributions of beauty, charm and muon background from beauty and charm are also shown.

the beauty fraction obtained from the fit is again used. In the plot without excitation contribution, the beauty fraction is determined by fitting only direct charm and beauty Monte Carlo simulations, giving a beauty contribution of $f_b = (41 \pm 6)\%$. Again no muon background correction is applied. No large difference between the Monte Carlo prediction with and without resolved excitation contribution is observed. There is a tendency, that the data are described better by the Monte Carlo prediction with excitation contribution.

As a second check of the result of the two dimensional fit, the measured lifetime $t(D^0)$ of the D^0 -meson is considered in the charm enriched correlation region 4, the beauty enriched correlation regions 2+3 and in the total sample.

The lifetime of the D^0 -meson in its rest frame is related to its decay length $l(D^0)$ via:

$$t(D^0) = \frac{1}{\gamma} \cdot \frac{l(D^0)}{\beta c} \quad (6.12)$$

with $\beta = v/c$ and $\gamma = 1/\sqrt{1 - \beta^2}$.

In charm events the D^0 -mesons are produced at the primary vertex. Since the lifetime $t(D^0)$ of the D^0 -meson is defined in the rest frame of the D^0 -meson, the distribution $t(D^0)$ corresponds to an exponential function convoluted with a resolution function. Negative decay times can occur due to resolution effects.

In beauty events the D^* -meson is not produced directly at the primary vertex, but at the decay vertex of a b -hadron. The large lifetime of the b -hadron contributes directly to the measured lifetime. Thus the measured lifetime of the D^0 -meson is on average larger for beauty than for charm events.

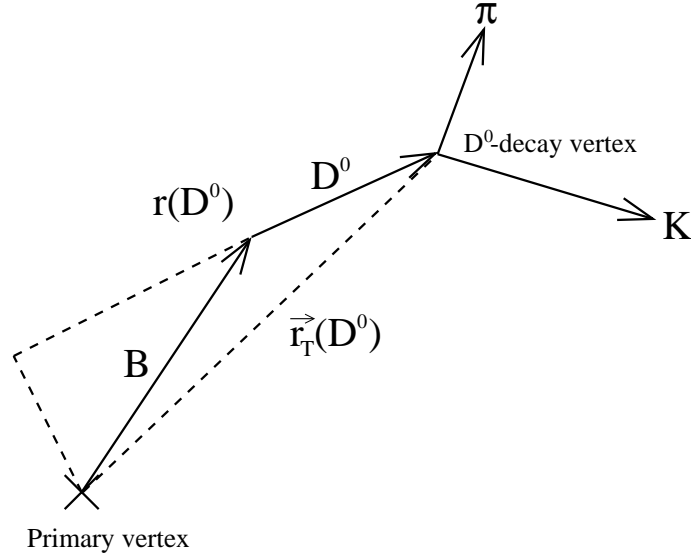


Figure 6.13: Decay length $r(D^0)$ in an event with a b hadron B .

For the determination of the decay length the D^0 -decay vertex has to be reconstructed precisely. Thus the kaon and pion track have to have associated hits in the central silicon tracker (CST). The additional requirement on the number of CST-hits $N_{CST-hits}$:

$$N_{CST-hits}(K) \cdot N_{CST-hits}(\pi) \geq 2 \quad (6.13)$$

is applied for this investigation. The decay length is defined by the distance vector $\vec{r}(D^0)$ from the primary vertex to the D^0 -decay vertex. Since the measurement of the x and y -coordinates of the vertices is much more precise than the measurement of the z -coordinate, only the transverse component of the distance vector $\vec{r}_T(D^0)$ is used (compare figure 6.13). The D^0 -decay vertex is reconstructed from the intersection point of the non-vertex fitted kaon and pion track in the xy -plane. The position of the primary vertex is determined by a fit of the beam position and selected tracks. The kaon, pion and muon tracks are not used in this fit, because they might bias the fit towards a secondary vertex. The D^0 -decay length $r(D^0)$ is then defined as the projection of the distance vector $\vec{r}_T(D^0)$ on the transverse momentum direction $\vec{p}_T(D^0)$ of the D^0 -candidate:

$$r(D^0) = \vec{r}_T(D^0) \cdot \frac{\vec{p}_T(D^0)}{p_T(D^0)} \quad (6.14)$$

The lifetime of the D^0 -meson can then be calculated using:

$$\begin{aligned} t(D^0) &= \frac{1}{\gamma} \cdot \frac{l(D^0)}{\beta c} = \frac{r(D^0)/\sin(\theta(D^0))}{\gamma\beta c} = \frac{r(D^0)}{\sin(\theta(D^0))p(D^0)/m(D^0)} \\ &= \frac{r(D^0)m(D^0)}{p_T(D^0)} \end{aligned} \quad (6.15)$$

The $t(D^0)$ -distribution in photoproduction data is shown in figure 6.14 for the correlation regions 2+3 and 4 separately. It is obvious, that the distribution for the correlation

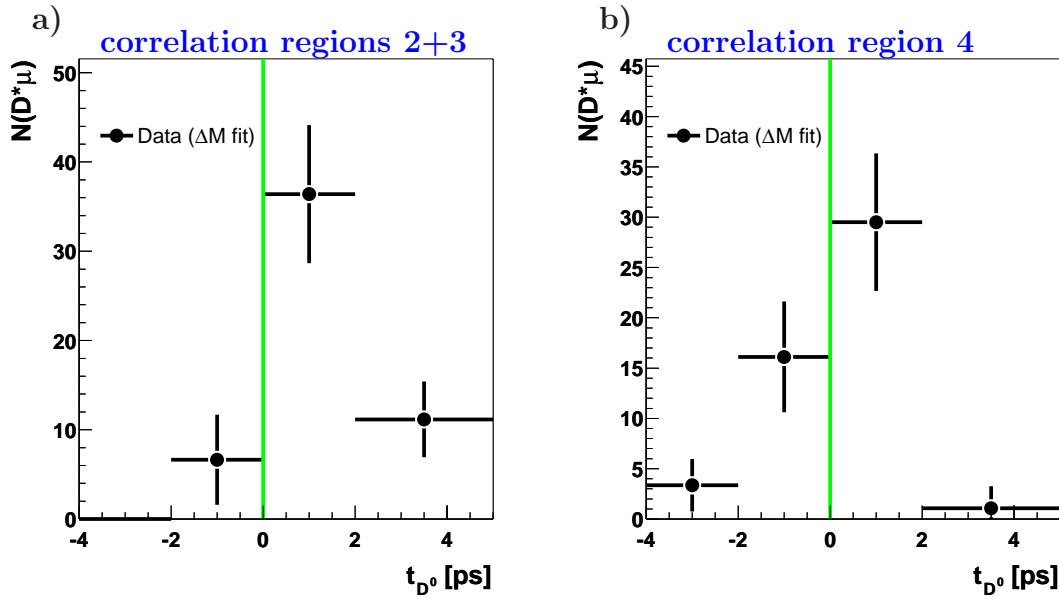


Figure 6.14: Life time of the D^0 -meson $t(D^0)$ obtained for the photoproduction data. a) Correlation region 2+3, b) correlation region 4. In correlation region 2+3 a large beauty fraction is predicted by the fit, while 4 is dominated by charm.

region 2+3 ($\bar{t}(D^0) = (1.24 \pm 0.09)$ ps) is shifted towards larger values compared to that for correlation region 4 ($\bar{t}(D^0) = (0.16 \pm 0.28)$ ps), as expected for a strongly enriched b -sample. Thus these studies confirm the result of the two dimensional fit further.

The number of $D^*\mu$ events is reduced significantly by applying the cut on the number of CST-hits. About 35% of the data are rejected by this cut, due to the smaller acceptance of the CST compared to the CJC and due to some inefficiencies of the CST.

A two dimensional fit to the CST photoproduction data using $t(D^0)$ as separation variable yields a beauty fraction of $f_b = (31 \pm 9)\%$ (see figure 6.15). This is compatible with the result obtained for this sample using the correlation regions: $f_b = (38 \pm 7)\%$. For the total sample the agreement between these two methods is even better: a beauty fraction of $f_b = (34 \pm 8)\%$ is obtained if $t(D^0)$ is used as separation variable while $f_b = (39 \pm 7)\%$ is obtained when the correlation regions are used as a separation variable. Due to the relatively large absolute value of the correlation coefficient between the number of charm and beauty events of 0.86 in case of using $t(D^0)$ the significance of the beauty fraction and the number of charm and of beauty events is smaller than in the case of using the correlation regions.

Even in the case of an increased number of $D^*\mu$ -events, it is questionable, whether the separation of charm and beauty could be improved, if the two methods are combined. The loss of events due to the CST requirement is quite sizable, while on the other hand the gain in separation power is only small.

To use the lifetime information itself to separate charm and beauty, the description by the Monte Carlo simulation of all quantities used for the lifetime determination, like the primary and decay vertex, would have to be good. Since the Monte Carlo incorporates for example an over-optimistic resolution of the primary vertex [91], the Monte Carlo would have to be modified. Several other effects also have to be taken into account [99]. To get

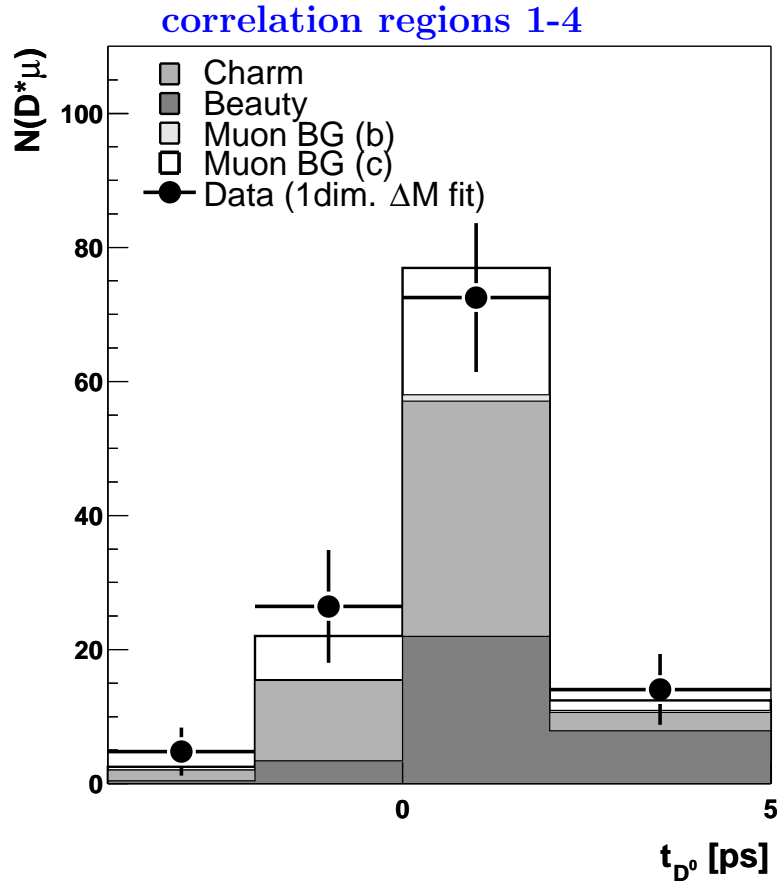


Figure 6.15: Result of the two dimensional fit to the CST photoproduction data sample using the lifetime of the D^0 -meson as separation variable. The black dots are the data, which are obtained from a one dimensional ΔM fit in each bin of $t(D^0)$.

a well measured lifetime, the data sample may have to be reduced further. Since no real gain is expected, the D^0 lifetime was not considered further in this analysis.

6.4 Comparison with other Methods

In this section the results of the separation of charm and beauty production based on the four correlation regions are compared to those obtained with differently defined separation variables.

The ZEUS collaboration uses a slightly different method for the separation of charm and beauty production in $D^*\mu$ -events [101, 102], than the “correlation region method” used in this analysis. The variable ΔR is used defined as:

$$\Delta R = \sqrt{\Delta\Phi^2 + \Delta\eta^2} \quad , \quad (6.16)$$

$\Delta\Phi$ is measured in the laboratory frame and $\Delta\eta$ is the pseudorapidity difference of the D^* -meson and the muon. The beauty fraction is determined here by a fit in ΔR to a

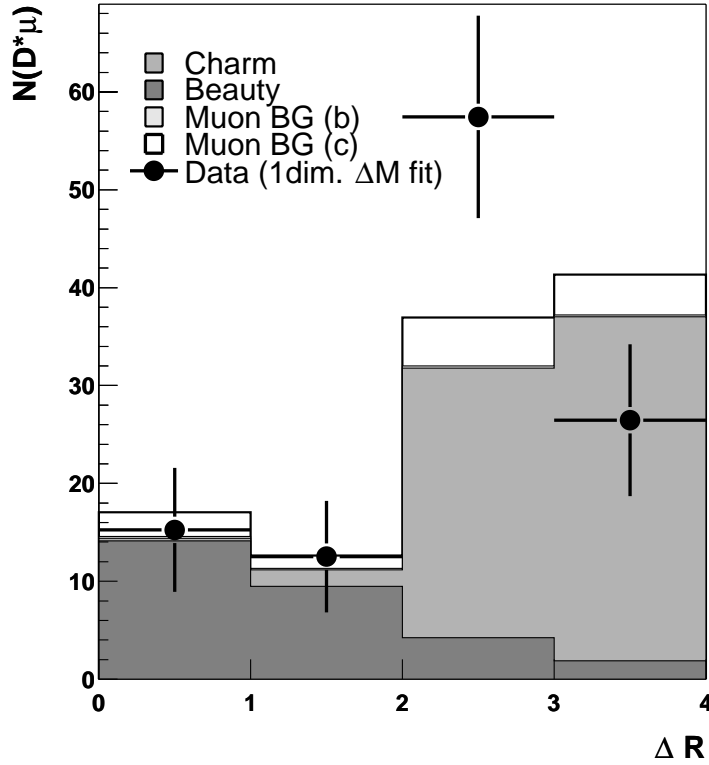


Figure 6.16: Result of the two dimensional fit using $\Delta R = \sqrt{\Delta\Phi^2 + \Delta\eta^2}$ as separation variable. Only the unlike sign photoproduction data set is used. The black dots are data, which are obtained from a one dimensional ΔM fit in each bin.

data subsample, which contains only $D^*\mu$ -events with unlike sign charge (called unlike sign data). The data sample used by the ZEUS collaboration corresponds to the data of correlation regions 3 and 4. Applying this fit method to the H1 photoproduction data sample gives the result shown in figure 6.16. From the fit the following numbers of charm and beauty events are obtained: $N_c = 78 \pm 14$ and $N_b = 30 \pm 11$. These values are to be compared with 91 ± 15 charm and 39 ± 12 beauty events, which are obtained by scaling the result of this analysis using the Monte Carlo simulation (table 6.4). A difference is therefore observed not only in the separation of charm and beauty but also in the total number of $D^*\mu$ events obtained between the two methods. The quality of the ΔR fit yields a probability P of 0.167 and is significantly worse than the fit with the correlation regions ($P = 0.631$). The quantity ΔR depends in addition to $\Delta\Phi$ also on $\Delta\eta$. It is therefore also susceptible to systematic effects in the $\Delta\eta$ variable. The η distribution of the D^* -meson as well as that of the muon are not so well described by the Monte Carlo as the $\Delta\Phi$ distribution. The separation power in ΔR is slightly better than in the four correlation regions. The significance $N/\sigma(N)$ of the number of charm events and beauty events respectively is therefore only slightly worse with 5.6 and 2.7 compared to 6.1 and 3.1, although here the data set is reduced. Using the total data nevertheless leads to a slightly improved significance.

For a consistency check also a fit in $\Delta\Phi$ (measured in the laboratory frame) alone to the unlike sign data sample is performed. In addition "modified correlation regions" using

fit	cor. region	N_c	N_b	f_b	P
γp					
normal	1-4	120 ± 20	53 ± 17	31 ± 6	0.789
→	3+4	91 ± 15	39 ± 12	30 ± 6	
mod. cor	1-4	101 ± 19	71 ± 18	41 ± 6	0.543
→	3+4	77 ± 15	52 ± 13	40 ± 6	
ΔR	3+4	78 ± 14	30 ± 11	28 ± 7	0.308
$\Delta \Phi$	3+4	71 ± 14	37 ± 12	34 ± 7	0.868
$\gamma p + DIS$					
normal	1-4	145 ± 23	68 ± 20	32 ± 6	0.444
→	3+4	110 ± 18	49 ± 15	28 ± 5	
mod. cor	1-4	134 ± 23	74 ± 20	36 ± 6	0.314
→	3+4	101 ± 17	54 ± 15	35 ± 6	
ΔR	3+4	95 ± 16	31 ± 13	25 ± 7	0.446
$\Delta \Phi$	3+4	89 ± 16	39 ± 13	31 ± 7	0.788

Table 6.4: Comparison of different fit methods. For each method the number of charm N_c and beauty N_b events as well as the probability of the fit P are shown. The arrow indicates, that the numbers in this row are not obtained by an independent fit, but are scaled down from the fit result of the total sample, which is given one row above. Here the relative ratios between the correlation regions are assumed to be described by the Monte Carlo simulation, while the total normalisation is obtained from the fit.

ΔR instead of $\Delta \Phi$ are also used. They are defined as:

1. $\Delta R < 2$ and $Q(D^*) = Q(\mu)$.
2. $\Delta R > 2$ and $Q(D^*) = Q(\mu)$.
3. $\Delta R < 2$ and $Q(D^*) = -Q(\mu)$.
4. $\Delta R > 2$ and $Q(D^*) = -Q(\mu)$.

In table 6.4 a quantitative comparison of the results of these four fit methods is shown. The comparison of the two methods based on $\Delta \Phi$ (normal correlation regions and $\Delta \Phi$ itself) show similar discrepancies in the total number of events as the two methods based on ΔR (modified correlation regions and ΔR itself) leading thus to an almost same quality of consistency. However, the fit quality seems to be better for $\Delta \Phi$ than for ΔR (see probability P of the fit in table 6.4). Due to the potential additional source of systematic errors and the fact, that the modified and normal correlation regions are quasi-identical in terms of significance, the “normal” correlation regions are used in this analysis.

In this chapter the separation of charm and beauty was performed by using the charge and angle correlations between the D^* -meson and the muon. Four correlation regions have been defined, which then are used as separation variable in a Log-Likelihood fit. The determined number of charm and beauty events will be used in the next chapter to extract the total visible $D^*\mu$ cross sections for charm as well as for beauty production. The beauty fraction is used to determine differential charm+beauty cross sections as a function of several $D^*\mu$ quantities and as a function of x_g , k_T and \bar{q}'_t in photoproduction.

Chapter 7

Total Charm and Beauty Cross Sections

In this chapter the total charm and beauty cross sections in the visible range are determined and compared to theoretical predictions and to other measurements.

7.1 Cross Section Definitions

The visible range, in which the cross section measurement is performed, depends on event kinematical quantities and on the muon and D^* -meson kinematics. The visible range for the two data samples used differs only in the Q^2 region as shown in table 7.1.

For both kinematic ranges however three different visible cross sections are defined. First $D^*\mu$ -events from all four correlation regions are used. In events which contain more than one $D^*\mu$ -pair each pair is included in the visible cross section. In the case of beauty production the sample contains also $D^*\mu$ -events, which come from a single b hadron. The second cross section uses only $D^*\mu$ -events with an azimuthal angle difference $\Delta\Phi^* > 90^\circ$ and different charges (correlation region 4). Since this region is dominated by charm the momentum of the D^* meson and muon can be used to approximate the momenta of the produced quark (antiquark). The third cross section uses $D^*\mu$ -events, which come mainly from one b hadron (correlation region 3). The different defined cross sections are summarised in table 7.2.

photoproduction	photoproduction + DIS
$Q^2 < 1 \text{ GeV}^2$	$Q^2 < 100 \text{ GeV}^2$
$0.05 < y < 0.75$	
$p_T(D^*) >$	$1.5 \text{ GeV}/c$
$ \eta(D^*) <$	1.5
$p(\mu) >$	$2.0 \text{ GeV}/c$
$ \eta(\mu) <$	1.735

Table 7.1: Definition of the visible range of the total $D^*\mu$ cross sections.

	correlation region	additional vis. cuts	quark type Q	contributing event topologies
$\sigma_{vis}^{Q,all}$	1-4	-	c, b	all possible combinations
$\sigma_{vis}^{Q,cor\ 4}$	4	$\Delta\Phi^* > 90^\circ$ $Q(D^*) \neq Q(\mu)$	c	$\mu^- \leftarrow \bar{c}c \rightarrow D^{*+}$
$\sigma_{vis}^{Q,cor\ 3}$	3	$\Delta\Phi^* < 90^\circ$ $Q(D^*) \neq Q(\mu)$	b	mainly $b \rightarrow D^{*+}\mu^-$

Table 7.2: Definition of the visible regions of total cross sections. The contributing event topologies are indicated only in a simplified way. The muons come from a semileptonic decay of a heavy hadron and the beauty quark first fragments into a b hadron before decaying into the D^* -meson.

The visible cross sections are calculated according to:

$$\sigma_{vis}^{Q,i}(ep \rightarrow e'D^*\mu X) = \frac{N_{rec,trig,L4}^{Q,i}(D^*\mu)}{\epsilon_{rec}^{Q,i} \cdot \epsilon_{trig}^{Q,i} \cdot \epsilon_{L4}^{Q,i} \cdot \mathcal{BR}(D^* \rightarrow K\pi\pi_s) \cdot \mathcal{L}_{presc.}} \quad (7.1)$$

Here $N_{rec,trig,L4}^{Q,i}(D^*\mu)$ is the number of $D^*\mu$ -events from charm or beauty production obtained in the previous chapter. The correction for the muon background is already performed. The upper index i indicates which events are included: all = all events, $cor\ 4$ = only the events of the correlation region 4, $cor\ 3$ = events of correlation region 3. $\mathcal{L}_{presc.}$ is the integrated luminosity (prescaled) of the analysed data and ϵ_{rec} , ϵ_{trig} and ϵ_{L4} are the efficiencies for reconstructing the $D^*\mu$ -events and selecting them by the trigger or L4-finder respectively. \mathcal{BR} represents the branching ratio of the decay channel $D^* \rightarrow K\pi\pi_s$.

7.2 Luminosity

Due to the prescaling of the subtriggers on level 1 the effective integrated luminosity ($\mathcal{L}^{total} = 88.8 \text{ pb}^{-1}$) after detector status and satellite bunch corrections is reduced further. In order to obtain the prescaled luminosity $\mathcal{L}_{presc.}$ for the selected $D^*\mu$ events the Monte Carlo simulation is used to estimate the distribution of trigger combinations in the data. In the Monte Carlo simulation the prescaling of the subtriggers is not simulated. Thus the prescale factors $d_{j,p}$, depending on the data taking period p and the trigger combination j , were determined in chapter 4 for the two different data sets, photoproduction and the total data sample. The prescale factor $d_n = d_{n,j,p}$ of a $D^*\mu$ -pair n depends on the trigger combination, which is set before the prescaling and the period p . The overall prescale factor \bar{d} of the $D^*\mu$ -events is the average of the prescaling factor $d_{n,j,p}$ for each $D^*\mu$ -pair:

$$\bar{d} = \frac{N(D^*\mu)}{\sum_n^{N(D^*\mu)} \frac{1}{d_{n,j,p}}} \quad (7.2)$$

The sum runs over all $D^*\mu$ -pairs in the Monte Carlo simulation. The prescaled luminosity \mathcal{L} is then obtained by:

$$\mathcal{L}_{presc.} = \frac{\mathcal{L}^{total}}{\bar{d}} \quad (7.3)$$

For both data samples an overall averaged prescale factor $\bar{d} = 1.04$ is obtained, leading to a prescaled luminosity of $\mathcal{L} = 85.4 \text{ pb}^{-1}$. Since the prescale factors are all very close to one, especially for the longest period $1999e^+/2000$, no difference in the overall prescale factor of the two data samples is obtained. The averaged prescale factor in each correlation region is to very good approximation identical to the overall averaged prescale factor. A maximal relative difference of 0.2% is observed.

7.3 Efficiencies

Not all events in the visible range are reconstructed and analysed. Events are lost due to inefficiencies of triggers, L4-finders and detector components as well as due to cuts during the event selection. This loss is taken into account by the efficiencies. The total efficiency is factorised as follows:

$$\epsilon = \epsilon_{rec} \cdot \epsilon_{trig} \cdot \epsilon_{L4} \quad (7.4)$$

The single efficiencies are defined as:

$$\epsilon_{rec} = \frac{N^{rec}(D^*\mu)|_{vis}}{N^{gen}(D^*\mu)|_{vis}} \quad (7.5)$$

$$\epsilon_{trig} = \frac{N^{rec,trig}(D^*\mu)|_{vis}}{N^{rec}(D^*\mu)|_{vis}} \quad (7.6)$$

$$\epsilon_{L4} = \frac{N^{rec,trig,L4}(D^*\mu)|_{vis}}{N^{rec,trig}(D^*\mu)|_{vis}} \quad (7.7)$$

The reconstruction efficiency ϵ_{rec} gives the ratio of the number of reconstructed $D^*\mu$ -pairs $N^{rec}(D^*\mu)$ (without muon background) after applying all selection cuts (excluding trigger and L4-finder requirements) and all generated $D^*\mu$ -pairs in the visible range. The trigger efficiency is defined as the ratio of the reconstructed $D^*\mu$ -pairs $N^{rec,trig}(D^*\mu)$ with a positive trigger decision and the number of reconstructed $D^*\mu$ -pairs. The L4-finder efficiency is then defined in an analogous way. The number of reconstructed $D^*\mu$ pairs $N^{rec,trig,L4}(D^*\mu)$ found by the trigger and the L4-finder is divided by the number of reconstructed and triggered $D^*\mu$ -pairs.

In the reconstruction efficiency the number of generated events in the visible range is compared to those defined by the reconstructed quantities. The reconstructed transverse momentum and the pseudorapidity of the D^* and the muon reproduce the generated quantities well. y , reconstructed via the Jacquet-Blondel method (see section 4.4.2), does not reproduce the generated value as good as the other quantities. However, migration effects are considered in the reconstruction efficiency as defined in equation 7.5.

The efficiencies used for the cross section calculation are determined using the Monte Carlo simulation. As discussed in chapter 5 the Monte Carlo simulation does not describe all aspects observed in the data and is therefore adjusted where necessary. For the efficiency determination the weighting factors are taken into account.

As a cross check some efficiencies are determined also from the data and compared to those determined by the Monte Carlo simulation. No correction for the muon background

TE	MT	ϵ_c [%]	ϵ_b [%]	ϵ_{cb} [%]	ϵ_{data} [%]
zVtx_sig	0,56,87	91 ± 4	95 ± 1	92 ± 3	92 ± 1
DCRPh-Ta	0,56,87	97 ± 1	98 ± 1	98 ± 1	100
DCRPh_CNH	0	91 ± 4	94 ± 1	92 ± 3	97 ± 0.4
Mu_Bar	0,61,83	86 ± 2	86 ± 4	86 ± 2	85 ± 2
Mu_ECQ	0,61,83	20 ± 6	41 ± 5	23 ± 6	30 ± 2
Mu_Any	0,61,83	81 ± 1	84 ± 2	82 ± 1	82 ± 1
SPCLe_IET>1 SPCLe_IET_Cen>2	19,22	100	100	100	99 ± 1

Table 7.3: Efficiencies of the trigger elements (TE) used for the photoproduction data set and for all correlation regions. The subtriggers used as monitor triggers (MT) are also quoted. Only statistical errors are shown.

contribution is applied in contrast to the efficiencies used later for the cross section calculation. Since the data contain charm as well as beauty events the efficiencies of the data have to be compared with the combined efficiencies ϵ_{cb} , composed of the single efficiencies for charm ϵ_c and beauty ϵ_b :

$$\epsilon_{cb} = \frac{\epsilon_c \cdot \epsilon_b}{f_b \cdot \epsilon_c + (1 - f_b) \cdot \epsilon_b} \quad (7.8)$$

In this case f_b is the beauty fraction of the data, where the muon background is not subtracted. The statistical error of ϵ_{cb} is obtained by error propagation, taking the correlation coefficient between the number of charm and the number of beauty events into account.

Table 7.3 shows the efficiencies of the trigger elements (TE) used in case of photoproduction and for all correlation regions. In the data the number of $D^*\mu$ -events is not determined via a ΔM -fit due to the low number of events, but is taken to be equal to the number of $D^*\mu$ -events in the D^* signal region. Only the binomial statistical errors are quoted:

$$\sigma_\epsilon = \sqrt{\frac{\epsilon \cdot (1 - \epsilon)}{N_1}} \quad \text{with} \quad \epsilon = \frac{N_2}{N_1} \quad \text{and} \quad N_1 \geq N_2 \quad (7.9)$$

Here, N_1 is the initial number of $D^*\mu$ -pairs and N_2 the number of $D^*\mu$ -events after applying the selection with efficiency ϵ . For the determination of the trigger element efficiency monitor triggers are used. These are reference triggers, which do not require the considered trigger element. For most trigger elements used in this analysis more than one monitor trigger is used and thus the logical "OR" of these monitor triggers is required. For all efficiencies good agreement between data and Monte Carlo simulation is observed. Since in photoproduction not all events have an energy deposition in the SpaCal, an energy deposition of at least 2 GeV was required to determine the efficiency of the trigger element SPCLe_IET>1 || SPCLe_IET_Cen>2. For the determination of the barrel or endcap muon trigger element (Mu_Bar or Mu_ECQ) only $D^*\mu$ events with a muon identified in the barrel or endcap of the muon system are considered. However, the efficiencies of the trigger elements Mu_ECQ and SPCLe_IET>1 || SPCLe_IET_Cen>2 cannot be checked reliably due to the limited number of $D^*\mu$ -events. In the inelastic photoproduction of J/Ψ mesons [103] good agreement was obtained also for these two trigger elements. For the total sample and also for correlation region 3 and 4 in both samples the same picture is obtained. The SpaCal trigger elements of subtrigger 2 and 61 used for the DIS data are

L4 pre cond.	ϵ_c [%]	ϵ_b [%]	ϵ_{cb} [%]	ϵ_{data} [%]	rel. ϵ_{syst} [%]
1997					
μ -finder	80 ± 3	80 ± 1	80 ± 2	80 ± 7	—
D^* - or μ -finder	90 ± 3	97 ± 1	92 ± 2	90 ± 5	—
1999e^-					
μ -finder	67 ± 4	86 ± 1	72 ± 3	71 ± 11	—
D^* - or μ -finder	95 ± 2	99 ± 1	96 ± 2	93 ± 5	—
1999e^+/2000					
μ -finder	70.0 ± 1.5	87.9 ± 0.5	74.4 ± 1.1	84 ± 4	5
D^* - or μ -finder	93.3 ± 1.0	97.1 ± 0.3	94.4 ± 0.7	99 ± 1	3

Table 7.4: *Efficiencies of the L4-finders for the photoproduction data set and for all correlation regions. The efficiencies of the muon finder and of the logical OR of the D^* -finder and the muon finder are quoted separately for the different data taking periods. ϵ_{syst} is the systematic uncertainty.*

very efficient, almost 100%, but could not be checked reliably using $D^*\mu$ -data. In [91] this was checked for inclusive D^* -events and no discrepancy between data and Monte Carlo simulation was observed. Thus no systematic error is given for the trigger efficiency.

The efficiency of the L4 muon finder and of the logical OR of the L4 D^* -finder and the L4 muon finder are listed in table 7.4, again using as an example only the photoproduction data in all correlation regions. To determine the efficiencies for the muon finder the L4 (L5 in the year 1997) open heavy flavour class (15 or 16 (1997)) has to be set:

$$\epsilon^{\mu \text{ finder}} = \frac{N(D^*\mu) |_{\mu \text{ class}, D^* \text{ class}}}{N(D^*\mu) |_{\mu \text{ precond.}, D^* \text{ class}}} \quad (7.10)$$

Here $N(D^*\mu) |_{\mu \text{ precond.}, D^* \text{ class}}$ indicates the number of $D^*\mu$ events, which fulfill the L4 muon finder precondition and which are assigned in addition to the open heavy flavour class. $N(D^*\mu) |_{\mu \text{ class}, D^* \text{ class}}$ is the number of $D^*\mu$ events which are assigned to the closed heavy flavour class as well as to the open heavy flavour class. In the case of the efficiency of the logical “OR” of the L4 D^* finder and the L4 muon finder L4 weights (see section 3.2.5) are considered, since no independent finder exists. Furthermore the L4 precondition of the investigated finder has to be fulfilled (see table 4.6):

$$\epsilon^{\mu | D^* \text{ finder}} = \frac{N(D^*\mu) |_{\mu \text{ class or } D^* \text{ class}}}{\sum_{i=1}^{N(D^*\mu) |_{\mu \text{ precond.}, D^* \text{ precond.}}} \text{L4-weight}(i)} \quad (7.11)$$

$N(D^*\mu) |_{\mu \text{ precond.}, D^* \text{ precond.}}$ is the number of $D^*\mu$ events, which fulfill the muon finder as well as the D^* finder precondition and $N(D^*\mu) |_{\mu \text{ class or } D^* \text{ class}}$ is the number of $D^*\mu$ events, which are assigned to the open or closed heavy flavour class in addition. The agreement between data and Monte Carlo prediction is reasonable (table 7.4). The indicated systematic error is obtained by calculating the probability of the remaining difference. If this probability is below 0.1 (corresponding to a 90% confidence level) a systematic error is added, which yields a probability of 0.1. In the total sample and for the different correlation regions the systematic errors for the muon-finder and the combined finder is never larger than 5% and they are all of the same order of magnitude. Thus a systematic error of 5% is taken for the L4-finder efficiency. A further systematic uncertainty entering the L4-finder efficiency comes from the fraction of events which fulfill the muon finder, the

$f_{ET}(D^*\mu)$ -cut	ϵ_c [%]	ϵ_b [%]	ϵ_{cb} [%]	ϵ_{data} [%]
γp				
cor. 1-4	97.3 ± 0.4	95.6 ± 0.2	96.7 ± 0.3	95 ± 4
cor. 4	98.0 ± 0.5	96.5 ± 0.6	97.6 ± 0.4	95 ± 5
cor. 3	93.0 ± 3	96.8 ± 0.3	96.1 ± 0.6	79 ± 14
$\gamma p + DIS$				
cor. 1-4	91.5 ± 0.6	88.9 ± 0.3	90.7 ± 0.5	96 ± 3
cor. 4	92.7 ± 0.7	86.5 ± 0.7	91.9 ± 0.7	92 ± 5
cor. 3	83 ± 3	92 ± 4	90 ± 1	83 ± 12

Table 7.5: Efficiencies of the cut on the relative transverse energy $f_{ET}(D^*\mu)$ of the $D^*\mu$ -pair. This is shown separately for the two data sets and for the different correlation regions. The efficiencies of the data are obtained by a ΔM -fit of the data sample with and without the cut on $f_{ET}(D^*\mu)$.

	Charm		Beauty	
	correlation region		correlation region	
	1-4	4	1-4	3
N	76 ± 13	74 ± 12	51 ± 16	28 ± 9
ϵ_{rec}	0.220	0.225	0.252	0.272
ϵ_{trig}	0.578	0.580	0.690	0.700
ϵ_{L4}	0.803	0.806	0.903	0.907
\mathcal{L} [pb^{-1}]	85.4			
\mathcal{BR}	0.0259			
σ [pb]	337 ± 58	318 ± 52	147 ± 46	73 ± 23

Table 7.6: Total visible $D^*\mu$ cross sections in **photoproduction**, separately for the different correlation regions, together with all quantities entering the cross section formula. Only the statistical error is indicated. The event numbers are taken from table 6.3.

D^* -finder or both finder preconditions. These fractions are adjusted in the Monte Carlo simulation to the data for the two data samples, but the number of events is limited and it is not done separately for each correlation region or any other variable. Varying these fractions by $\pm 10\%$ for the μ -finder and combined finder class leads to variations of 1% in the cross section for both samples. This uncertainty can be neglected compared to the systematic uncertainty already indicated.

The next efficiency check concerns the efficiency of the cut on the relative transverse energy $f_{ET}(D^*\mu)$. Table 7.5 shows this efficiency separately for the two data sets and for the different correlation regions used. The efficiencies for the data are obtained by a simultaneous ΔM -fit to the right and wrong charge data with and without the cut on $f_{ET}(D^*\mu)$. The error of the efficiency is obtained by error propagation taking the correlation coefficient between the initial and final data set into account. As can be seen from table 7.5 good agreement between data and Monte Carlo simulation is obtained and thus no systematic uncertainty concerning this cut is quoted.

With the efficiencies determined in this section and with the prescaled luminosity from the last section the total visible $D^*\mu$ cross sections for charm and beauty production can

	Charm		Beauty	
	correlation region		correlation region	
	1-4	4	1-4	3
N	92 ± 15	87 ± 14	65 ± 19	36 ± 10
ϵ_{rec}	0.213	0.217	0.257	0.271
ϵ_{trig}	0.658	0.659	0.753	0.759
ϵ_{L4}	0.832	0.832	0.915	0.919
\mathcal{L} [pb ⁻¹]	85.4			
\mathcal{BR}	0.0259			
σ [pb]	357 ± 58	331 ± 53	166 ± 49	86 ± 24

Table 7.7: Total visible $D^*\mu$ cross sections in $\gamma p + DIS$, separately for the different correlation regions, together with all quantities entering the cross section formula. Only the statistical error is indicated. The event numbers are taken from table 6.3.

be calculated using equation 7.1. The result is given in table 7.6 for the photoproduction data set together with all quantities entering this equation. The analogous result is shown in table 7.7 for the total data sample. As expected the charm cross section obtained in the correlation region 4 is only slightly smaller than the total charm cross section. For beauty production however, the cross section in correlation region 3 is about half of the total beauty cross section.

7.4 Systematic Errors

In addition to the statistical uncertainties several effects exist, which lead to a systematic uncertainty on the cross section determination. These effects have been partly discussed already in the last section. Below the systematic errors are summarised.

The systematic errors on the calculation of the total visible charm and beauty cross sections are listed in table 7.8. A total relative systematic uncertainty of 16% (charm) or 19% (beauty) is obtained.

Some systematic errors are estimated by varying uncertain parameters. For a uniform distribution between two results a and b the variance is $(a - b)^2/12$ [100]. Therefore a systematic error of the maximum deviation, which occurs in a variation of an uncertain parameter, divided by $\sqrt{12}$ is assigned to the measurement.

A first check concerns the definition of the correlation regions. For this purpose the definition of the correlation regions was modified in $\Delta\Phi^*$ by moving the cut from 90° by $\pm 2^\circ$, $\pm 5^\circ$ and $\pm 10^\circ$ respectively. This was done for data and Monte Carlo simulation. The variation by 2° for data and Monte Carlo simulation leads to a maximal difference of the order of 5 (photoproduction) or 6 (total sample) events, which does not grow with a larger movement of the $\Delta\Phi^*$ -cut, but fluctuates as expected. The stability of the fit with respect to the $\Delta\Phi^*$ -cut was found to be reasonable. No systematic error is assigned.

The $\Delta\Phi^*$ model dependence is estimated by using the CASCADE Monte Carlo simulation instead of the PYTHIA Monte Carlo simulation. From the difference of the number

of reconstructed charm and beauty events as well as the difference of the beauty fraction, obtained by the two different Monte Carlo simulations, for the photoproduction sample as well as for the total sample a systematic uncertainty of 1.5% on the charm cross section and of 8% on the beauty cross section and the beauty fraction is obtained.

The uncertainty of the **muon background** description has a direct impact on the number of charm and beauty events determined by the fit and also on the muon background correction. Both effects were investigated together by varying the muon background fraction by $\pm 20\%$ separately for charm and beauty. This leads to a systematic uncertainty of 1% for the charm cross section, to a systematic uncertainty of 5% and 3% for the beauty cross section and the beauty fraction respectively.

A further systematic uncertainty on the determination of the number of charm and beauty events with the fit are the **fragmentation fractions for the muons** in the Monte Carlo. The data consist in case of beauty of three types of $D^*\mu$ events. The D^* and the muon can come either from one b -quark or the two particles can come originally from different b -quarks. For the latter case, the direct ($b \rightarrow \mu$) or cascade ($b \rightarrow c \rightarrow \mu$) decays have to be distinguished. The distribution of the correlation regions depends on the fragmentation fractions of the three classes. Therefore the fractions of the three $D^*\mu$ -classes in the Monte Carlo simulation have been modified by varying one fragmentation fraction at the time by the quoted uncertainty (see chapter 2). The two dimensional fit is performed for each variation. The positive or negative deviations for the number of charm and beauty events as well as for the beauty fraction obtained by the variation of the three fragmentation fractions are added linearly. Dividing the total deviations by $\sqrt{12}$ an uncertainty of 1% for the charm cross section and 6% for the beauty cross section and beauty fraction is obtained. Adding the three systematic uncertainties in quadrature, a systematic uncertainty of 10.5% is obtained for the beauty fraction.

The dependence of the result of the two dimensional fit – the number of charm and beauty events N_c or N_b – on the procedure of the simultaneous ΔM -fit was checked. A fit only to the right charge data was used as well as allowing more free parameters for the simultaneous fit. In photoproduction the maximum obtained difference is, with one event for N_c and N_b , much smaller than the statistical uncertainty. Also for the total sample the differences are three events at most. Thus the behaviour of the ΔM -fit was found to be reasonable and no systematic uncertainty is indicated.

The systematic uncertainty of the **signal extraction** with the two dimensional fit is estimated by varying the width of the Gaussian assumed for the D^* signal events. In the analysis this width is fixed to the value obtained by a one dimensional ΔM fit to the total data. An uncertainty of $\pm 0.2 \text{ MeV}/c^2$ for the width is obtained for both data samples. Varying the width of the Gaussian by this amount an uncertainty of 4% for the charm cross section and of 2.5% for the beauty cross section as well as for the beauty fraction is obtained.

The reconstruction efficiency determined in the last section can be factorised into the efficiency of the D^* -reconstruction, the muon reconstruction and the kinematic reconstruction. The uncertainty on the muon reconstruction depends on the uncertainty of the muon identification and the uncertainty of the muon track reconstruction. The **muon identification** was extensively checked with elastic J/Ψ mesons [97]. The relative systematic uncertainty of 1.5% determined in this analysis, from which the muon weighting

	source	$\epsilon_{syst.} [\%]$	
		Charm	Beauty
1.	$\Delta\Phi^*$ -model dependence	1.5	8
2.	μ -BG	1	5
3.	signal extraction	4	2.5
4.	fragmentation fractions	1	6
5.	reflections of D^*	5	
6.	muon identification	1.5	
7.	track reconstruction for $D^*\mu$	13	
8.	L4 finder efficiency	5	
9.	$\mathcal{BR}(D^{*+} \rightarrow K^- \pi^+ \pi_s^+)$	2	
10.	\mathcal{L}	1.5	
total syst. error		16	19

Table 7.8: Relative systematic errors of the total visible charm and beauty cross sections.

factors were taken, is applied here as well.

The D^* -reconstruction uncertainty depends again on the uncertainty of the track reconstruction efficiency and on the momentum and mass resolution. Since the uncertainty of the **track reconstruction** is smaller with larger p_T of the particles, for the kaon, pion and muon a relative uncertainty of the track reconstruction efficiency of 3% is assumed [104], while for the slow pion a relative error of 4% is assumed. Assuming a maximal correlation between the four particles a value of 13% is obtained.

The uncertainty on the **kinematic reconstruction** depends in the case of photoproduction events on the energy measured in the SpaCal and in case of the DIS selection also on the polar angle of the scattered electron. To estimate the systematic uncertainty of the efficiency of the selection of photoproduction events or DIS events, the measured energy of the electron candidate was varied by $\pm 3\%$ and the polar angle was changed in addition by ± 1 mrad. From the deviation in the number of selected $D^*\mu$ events a systematic uncertainty of 0.5% is obtained, which is negligible.

The systematic error on the **L4-finder efficiency** is 5% as described in the previous section. Any further systematic uncertainty on the trigger efficiency is found to be negligible.

A systematic effect on the ΔM -fit can be caused by **reflections**. Other D^0 decay channels apart from $D^0 \rightarrow K^- \pi^+$ can contribute in the D^* -signal region. In [105] this effect was estimated for a D^* selection in DIS to be $(3.5 \pm 1.5)\%$. In this analysis, the effect of reflections is taken into account by a relative systematic uncertainty of 5%.

The relative error of the **branching ratio of the D^* meson** $\mathcal{BR}(D^* \rightarrow K \pi \pi_s)$ is indicated in chapter 2 as 2%. The **integrated luminosity** is with a systematic uncertainty of 1.5% relatively precisely known [106].

Due to the small prescaling factors the impact of slightly wrong prescaling factors on the cross section determination can be neglected.

7.5 Comparison to Theoretical Predictions

After calculating the total visible $D^*\mu$ cross section for charm and beauty production and after the determination of the systematic uncertainties of the cross section calculation, the final result is compared in this section with the LO + parton shower prediction of the Monte Carlo generators PYTHIA and CASCADE and with NLO calculations. A comparison with the NLO predictions is performed only for the photoproduction data set. The comparisons are given in table 7.9 for the photoproduction sample and in table 7.10 for the total sample including DIS events. The calculation of the NLO cross section in photoproduction is extensively discussed in chapter 2. For the Monte Carlo cross section the number of $D^*\mu$ events in the visible range was counted and the cross section is then given by:

$$\sigma_{vis}^{Q, MC} = \frac{N_{vis}^Q(D^*\mu)}{\mathcal{L}^{MC}} \cdot \frac{f(Q\bar{Q} \rightarrow D^*\mu)}{f^{MC}(Q\bar{Q} \rightarrow D^*\mu)} \quad (7.12)$$

The last factor takes into account, that the fragmentation factors and branching ratios in the Monte Carlo simulation do not correspond to the most recent measurements quoted in table 2.3 of chapter 2.

The ratios of data to theory are shown in table 7.9 (photoproduction) and 7.10 (total sample). The charm cross sections are in good agreement with the Monte Carlo prediction of the generator PYTHIA, taking the direct as well as the excitation resolved component into account, and even better with the prediction of the Monte Carlo generator CASCADE. The prediction of the NLO calculations in photoproduction, is in good agreement with the measured charm cross section, too. For beauty production, a factor 3.1 between data and NLO calculation is obtained in photoproduction using all correlation regions. For correlation region 3 this factor is 4.2. The beauty cross section of the CASCADE Monte Carlo prediction and of the PYTHIA Monte Carlo prediction (direct + excitation resolved component) are larger than the NLO prediction. In case of the CASCADE Monte Carlo generator only a factor 1.5 (all correlation regions) or 1.4 (correlation region 3) is obtained, while for the CASCADE Monte Carlo generator for both cases a factor 2.0 is obtained. For the total data set a similar factor between data and Monte Carlo prediction is obtained as in photoproduction.

The theoretical uncertainties for the NLO calculations as indicated in table 7.9 are determined as proposed in [107]. The heavy quark mass, the factorisation scale and the renormalisation scale are each varied and the variations obtained are added linearly. The charm mass is varied by $\pm 0.2 \text{ GeV}/c^2$ around the default value of $m_c = 1.5 \text{ GeV}/c^2$, while the beauty mass is varied by $\pm 0.25 \text{ GeV}/c^2$ around the default value of $m_b = 4.75 \text{ GeV}/c^2$. For the lower values of the scales half of the default value of the scales is chosen, while for the upper value twice the default value for the scales is chosen. The relative theoretical uncertainty of the NLO calculations for charm and beauty is about 40%.

A rough estimation of the theoretical uncertainties of the predictions of the two Monte Carlo generators, by varying the heavy quark mass in the same way as for the NLO calculations and the scales simultaneously, was performed in addition. The uncertainties obtained are of the same order of magnitude or slightly smaller.

Figure 7.1 shows a comparison of the ratio of the measured b -cross section and the NLO prediction for this analysis and other measurements of the H1 and ZEUS collaboration.

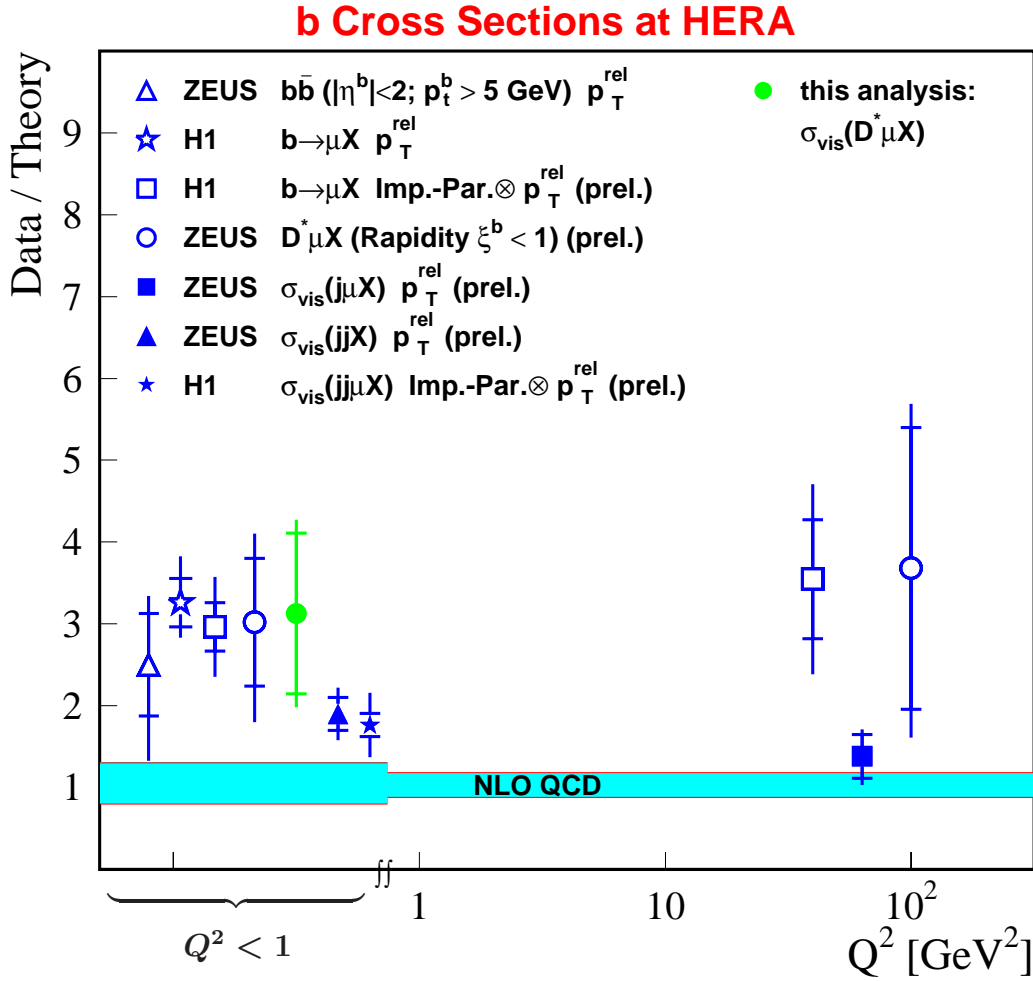


Figure 7.1: Ratio of the measured b production cross sections at HERA and the theoretical predictions based on NLO QCD calculations. The ratio for this analysis is indicated for all correlation regions in photoproduction. The theoretical uncertainty of the NLO calculation (error band) for photoproduction is about 25% and for DIS about 15%. These numbers are only indicative. The estimated theoretical uncertainties for the NLO calculations for this analysis is about 40% (table 7.10).

The ratio, obtained in this analysis, is in very good agreement with that from the $D^* \mu$ -analysis of the ZEUS-collaboration. Although this ratio seems to be above the ratios, obtained in the recent $b \rightarrow \mu$ measurements of the H1 and ZEUS collaboration [7, 8], they are still compatible due to the large error.

In the recent $b \rightarrow \mu$ measurement of H1 [7] the ratio between NLO and data was determined to be 1.7. The ratios for the two Monte Carlo predictions are larger, 2.5 for the PYTHIA Monte Carlo generator and 1.9 for the CASCADE Monte Carlo generator, than the ratio for the NLO prediction in the $b \rightarrow \mu$ measurement, while it is the other way around in this analysis. In the $b \rightarrow D^*$ measurement at HERA presented in [91] the ratio of data to NLO calculations is 5.1. However, there the NLO cross section is a factor 0.65 smaller than the prediction of the CASCADE Monte Carlo generator.

γp			cross section [pb^{-1}]	data/theory
Charm				
$\sigma_{vis}^{c,all}$	$\mu^- \leftarrow \bar{c}c \rightarrow D^{*+}$	data	$337 \pm 58 \pm 54$	
		PYTHIA direct	142	2.4
		PYTHIA	242	1.4
		CASCADE	310	1.1
		NLO	269 ± 118	1.3
$\sigma_{vis}^{c,cor\ 4}$	$\mu^- \leftarrow \bar{c}c \rightarrow D^{*+}$ $\Delta\phi^* > 90^\circ$ $Q(\mu) \neq Q(D^*)$	data	$318 \pm 52 \pm 51$	
		PYTHIA direct	141	2.3
		PYTHIA	228	1.4
		CASCADE	271	1.2
		NLO	242 ± 92	1.3
Beauty				
$\sigma_{vis}^{b,all}$	all possibilities	data	$147 \pm 46 \pm 28$	
		PYTHIA direct	55	2.7
		PYTHIA	72	2.0
		CASCADE	100	1.5
		NLO	47 ± 18	3.1
$\sigma_{vis}^{b,cor\ 3}$	$b \rightarrow D^{*+}\mu^-$ $\Delta\phi^* < 90^\circ$ $Q(\mu) \neq Q(D^*)$	data	$73 \pm 23 \pm 14$	
		PYTHIA direct	26	2.8
		PYTHIA	36	2.0
		CASCADE	53	1.4
		NLO	19 ± 7	4.2

Table 7.9: Comparison of the total visible $D^*\mu$ -cross section for charm and beauty production in **photoproduction** with LO + parton shower predictions and with NLO calculations. The PYTHIA Monte Carlo generator (direct component alone or both components, the direct and resolved excitation component) and the Monte Carlo generator CASCADE are used for this comparison. For the NLO calculations only the direct component is used, since the normal resolved component is negligible. For the data the statistical error (first indicated error) and the systematic error (second error) are given separately.

The difference to the recent $b \rightarrow \mu$ measurements might be explained by the different visible range used in this analysis. The visible range of the two $D^*\mu$ -analyses is much closer to the production threshold than for the $b \rightarrow \mu$ analysis, since the required muon momentum is considerably smaller than in the $b \rightarrow \mu$ analysis and since the requirement on the transverse momentum of the D^* meson is also not hard.

The fragmentation as implemented in the code of the NLO program FMNR is performed without any parton showers. For the transition of a b hadron into a D^* -meson only a simplified model (Peterson function) is used. The uncertainty of the predicted NLO cross section due to these effects is unknown but it can depend on the visible range and on the considered particles (muons or D^*) in addition.

$\gamma p + \text{DIS}$			cross section [pb^{-1}]	data/theory
Charm				
$\sigma_{vis}^{c,all}$	$\mu^- \leftarrow \bar{c}c \rightarrow D^{*+}$	data	$357 \pm 58 \pm 57$	
		PYTHIA direct	155	2.3
		PYTHIA	255	1.4
		CASCADE	339	1.1
$\sigma_{vis}^{c,cor 4}$	$\mu^- \leftarrow \bar{c}c \rightarrow D^{*+}$ $\Delta\phi^* > 90^\circ$ $Q(\mu) \neq Q(D^*)$	data	$331 \pm 53 \pm 53$	
		PYTHIA direct	153	2.2
		PYTHIA	240	1.4
		CASCADE	296	1.1
Beauty				
$\sigma_{vis}^{b,all}$	all possibilities	data	$166 \pm 49 \pm 32$	
		PYTHIA direct	61	2.7
		PYTHIA	77	2.2
		CASCADE	109	1.5
$\sigma_{vis}^{b,cor 3}$	$b \rightarrow D^{*+}\mu^-$ $\Delta\phi^* < 90^\circ$ $Q(\mu) \neq Q(D^*)$	data	$86 \pm 24 \pm 16$	
		PYTHIA direct	29	3.0
		PYTHIA	39	2.2
		CASCADE	57	1.5

Table 7.10: Comparison of the total visible $D^*\mu$ -cross section for charm and beauty production in **photoproduction + DIS** with LO + parton shower predictions. The PYTHIA Monte Carlo generator (direct component alone or both components, the direct and resolved excitation component) is used for photoproduction and the direct RAPGAP Monte Carlo generator for DIS. As an alternative Monte Carlo generator CASCADE is used for photoproduction and DIS. The Monte Carlo generator combination of PYTHIA and RAPGAP is indicated in the table as PYTHIA. For the data the statistical error (first indicated error) and the systematic error (second error) are given separately.

Chapter 8

Differential Cross Sections

In this chapter normalised differential cross sections (sum of charm and beauty production) for the photoproduction domain and differential charm and beauty cross sections for the overall data set are determined in the visible range and are compared with theoretical predictions. Differential distributions for quantities which characterise the $D^*\mu$ -system, are presented: the transverse momentum $p_T^*(D^*\mu)$, the rapidity $\hat{y}(D^*\mu)$ and the invariant mass $M(D^*\mu)$ of the $D^*\mu$ -pair. Furthermore, the azimuthal angular difference $\Delta\Phi^*$ between the D^* and the muon is considered. $p_T^*(D^*\mu)$ and $\Delta\Phi^*$ are defined in the photon proton rest frame and are sensitive to higher order contributions, to a possible non-zero initial transverse momentum k_T of one of the initial partons, taking part in the hard interaction, and to fragmentation effects. $M(D^*\mu)$ is directly correlated to $\sqrt{\hat{s}}$, the centre-of-mass energy of the two heavy quarks (LO picture). $\hat{y}(D^*\mu)$ contains information about the direction of the $D^*\mu$ -pair. Furthermore $M(D^*\mu)$ and $\hat{y}(D^*\mu)$ are used for the calculation of the quantities, on which the unintegrated gluon density depends. A detailed description of these $D^*\mu$ -quantities can be found in section 2.1.5.

8.1 Differential Distributions

For both samples, the photoproduction and the total data sample¹, the number of $D^*\mu$ -events of all correlation regions are used for the differential distributions.

For the photoproduction domain no separation of charm and beauty is performed in each bin of the $D^*\mu$ -variables. In order to obtain the number of $D^*\mu$ -events a simultaneous ΔM -fit to the right and wrong charge data sets is used in each bin of the considered variable. To illustrate the quality of the fits, figure 8.1 shows the ΔM -distributions in bins of $p_T^*(D^*\mu)$ for the right (data points) and wrong (histogram) charge combination together with the fit.

The number of $D^*\mu$ -events obtained in this way still contains muon background. In order to correct for the muon background from charm and beauty events, binwise correction factors $f_{cor}(i)$ are applied. These factors are determined using the Monte Carlo simulation: The muon background correction factor $f_{cor}^Q(i)$ (with $Q = c, b$) in the i -th bin of the

¹The total data sample contains photoproduction and DIS (about 20%) events.

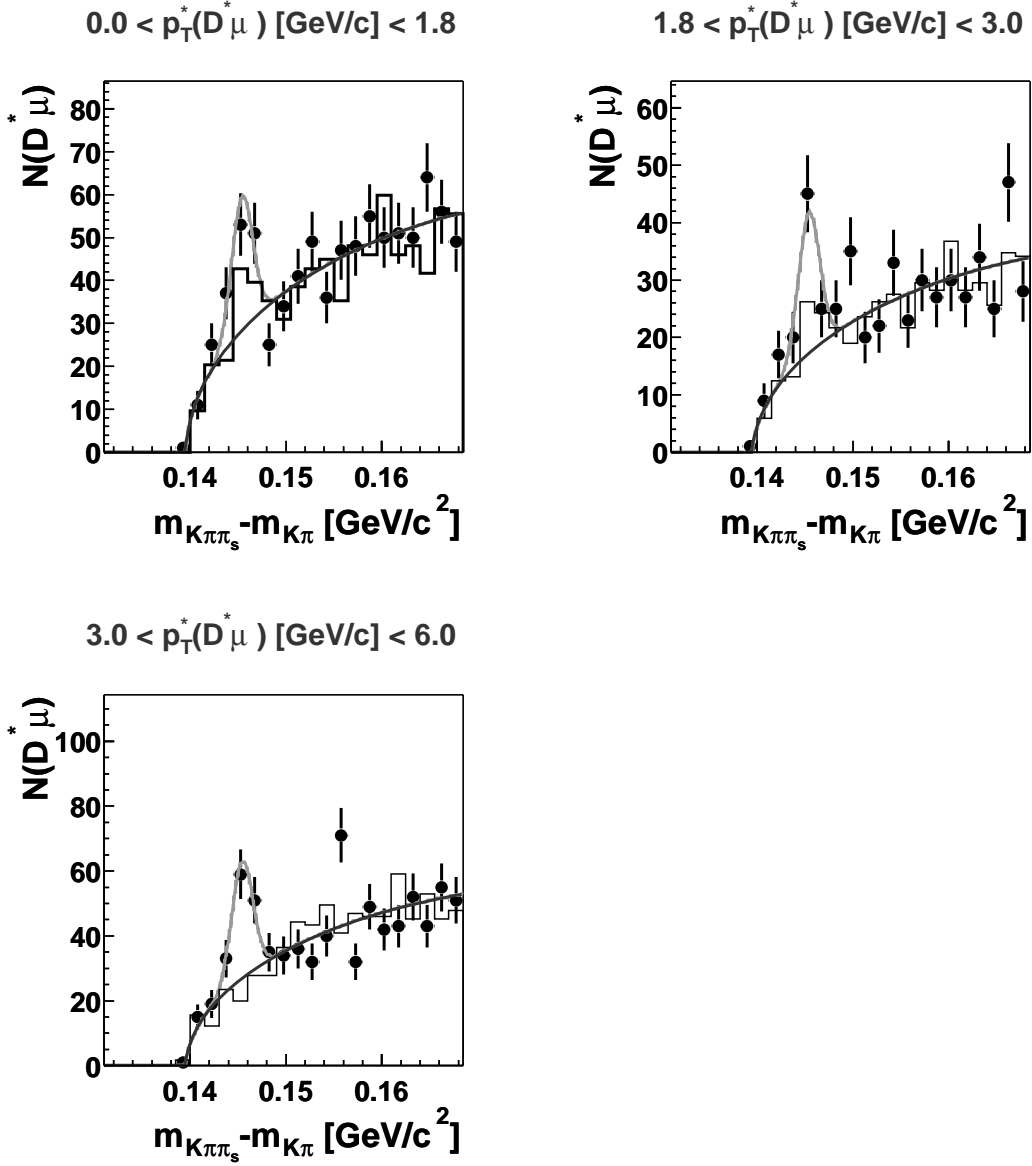


Figure 8.1: ΔM distribution in bins of $p_T^*(D^*\mu)$ for the photoproduction data. The right charge (dots) and wrong charge combination (histogram) data are shown together with the fit.

considered variable is defined as the ratio of real $D^*\mu$ events $N_{gen}^Q(i)$ from charm or beauty production respectively and the number of reconstructed $D^*\mu$ -events $N_{rec}^Q(i)$, containing in addition also muon background events:

$$f_{cor}^Q(i) = N_{gen}^Q(i)/N_{rec}^Q(i) \quad (8.1)$$

The combined correction factor $f_{cor}(i)$ is then given by:

$$f_{cor}(i) = (1 - f_b^{rec}(i)) \cdot f_{cor}^c(i) + f_b^{rec}(i) \cdot f_{cor}^b(i) \quad (8.2)$$

$f_b^{rec}(i)$ is the beauty fraction in the i -th bin of the reconstructed $D^*\mu$ -events. It is calcu-

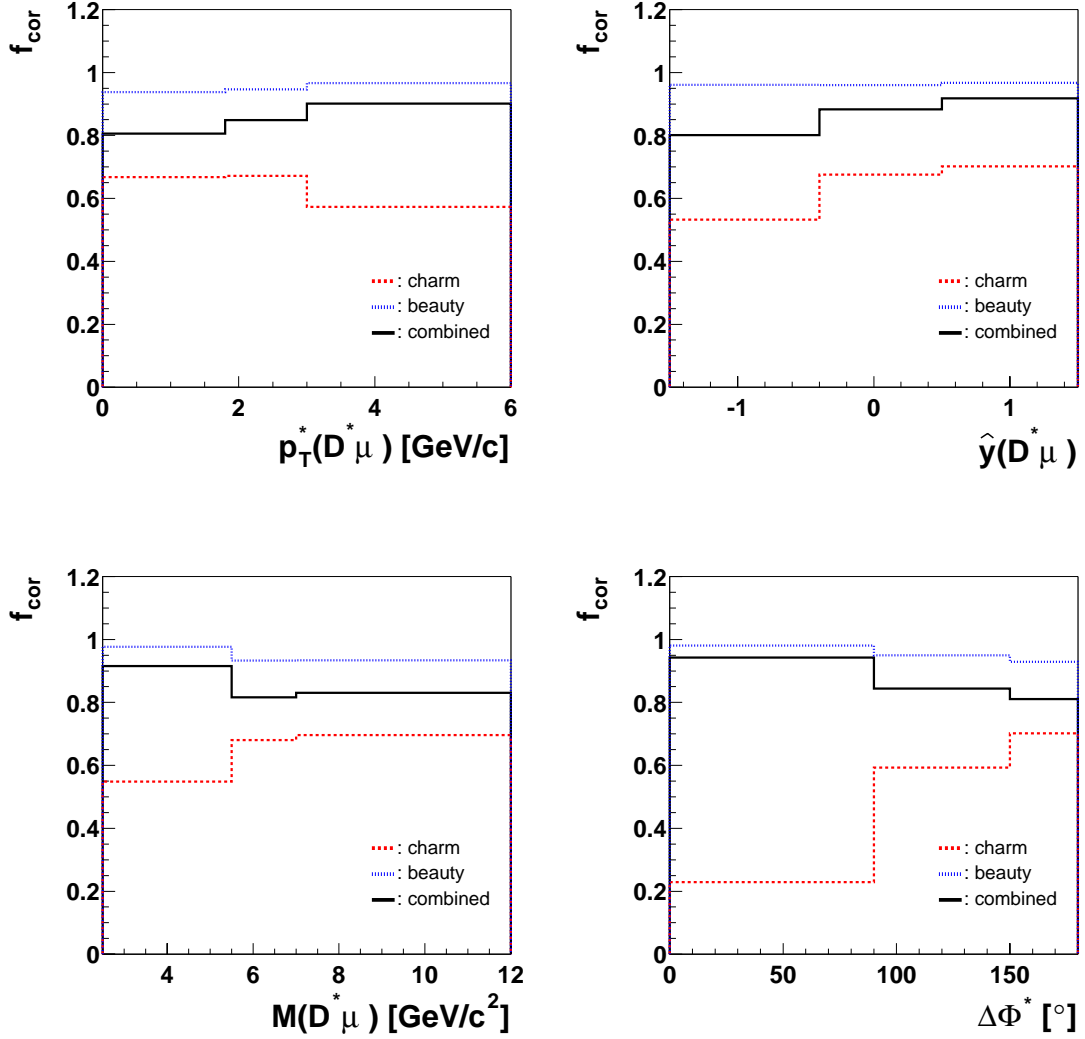


Figure 8.2: Muon background correction factors for the $D^*\mu$ -variables in photoproduction: the transverse momentum $p_T^*(D^*\mu)$, the rapidity $\hat{y}(D^*\mu)$, the invariant mass $M(D^*\mu)$ and the azimuthal angle difference $\Delta\Phi^*$ of the $D^*\mu$ -pair. The combined correction factor ($c+b$) and the correction factor for charm and beauty production are shown separately.

lated using the overall beauty fraction f_b (before muon background correction):

$$f_b^{rec}(i) = \frac{f_b \cdot N_{rec}^b(i)/N_{rec}^b}{f_b \cdot N_{rec}^b(i)/N_{rec}^b + (1 - f_b) \cdot N_{rec}^c(i)/N_{rec}^c} \quad (8.3)$$

In figure 8.2 the combined correction factor as well as the charm and beauty correction factors determined using the PYTHIA Monte Carlo simulation are shown: $p_T^*(D^*\mu)$, $\hat{y}(D^*\mu)$, $M(D^*\mu)$ and $\Delta\Phi^*$.

The differential distributions of the $D^*\mu$ variables after applying the muon background correction factors $f_{cor}(i)$ are shown in figure 8.3. Due to the larger muon background correction for charm events the beauty fraction is larger in the photoproduction $D^*\mu$ -sample after this correction, $f_b = 40\%$. The data (points) in figure 8.3 are compared to

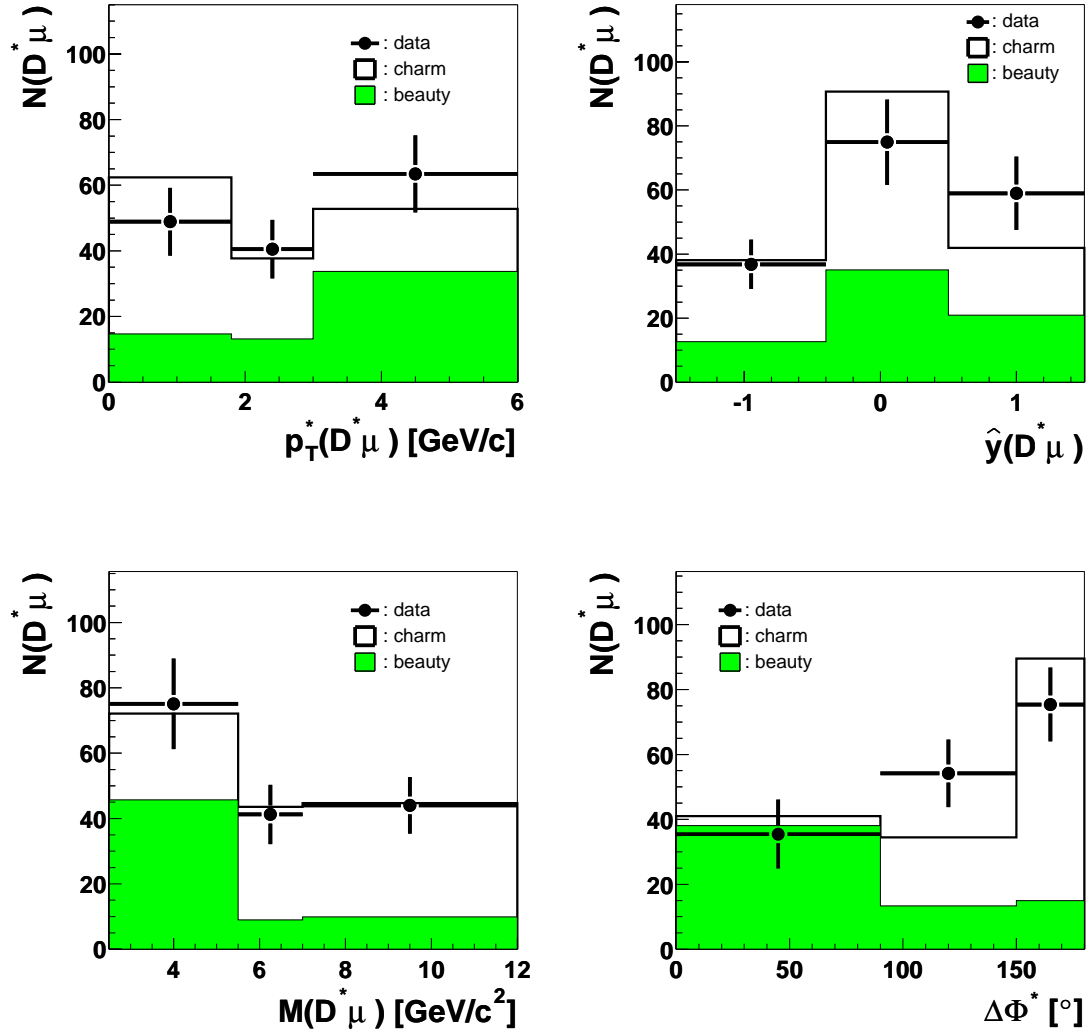


Figure 8.3: *Differential distributions of the $D^*\mu$ -variables in photoproduction after muon background correction. Shown are the transverse momentum $p_T^*(D^*\mu)$, the rapidity $\hat{y}(D^*\mu)$, the invariant mass $M(D^*\mu)$ and the azimuthal angle difference $\Delta\Phi^*$ of the $D^*\mu$ -pair. The data (dots) are shown together with the Monte Carlo distributions, normalised to the data. The beauty fraction of the total photoproduction $D^*\mu$ sample is $f_b = 40\%$. Only statistical errors are shown.*

the sum of the charm and beauty Monte Carlo predictions. The Monte Carlo simulation is normalised to the data and $f_b = 40\%$ is used as beauty fraction. In all variables reasonable agreement between the data and the PYTHIA Monte Carlo prediction is obtained.

The differential distributions have been compared to Monte Carlo predictions of the sum of charm and beauty production which take the overall beauty fraction from the result of the two dimensional fit. Only the normalisation of these two fractions is thus determined from the fit, while the individual shapes of the two contributions are given by the Monte Carlo simulation. In order to get the shape of the different $D^*\mu$ variables separately for charm

variable	bin 1		bin 2		sum	
	f_b^{MC} [%]	f_b^{fit} [%]	f_b^{MC} [%]	f_b^{fit} [%]	N_c	N_b
$M(D^*\mu)$	54 ± 8	51 ± 7	21 ± 4	50 ± 9	78 ± 14	79 ± 17
$\hat{y}(D^*\mu)$	35 ± 5	54 ± 7	46 ± 7	31 ± 10	93 ± 14	65 ± 17
$p_T^*(D^*\mu)$	25 ± 4	89 ± 7	62^{+9}_{-3}	43 ± 10	47 ± 13	132 ± 20
total fit	$f_b = (41 \pm 6)\%$				92 ± 15	65 ± 19

Table 8.1: *Fit result of the differential $D^*\mu$ variables. In the last column the sum of charm and beauty events (after muon background correction) is compared to the number of charm and beauty events obtained from the fit to the total data sample. In addition beauty fractions f_b (after muon background correction) obtained for the differential $D^*\mu$ variables in comparison to the beauty fraction predicted by the Monte Carlo simulation PYTHIA using an overall beauty fraction $f_b = (41 \pm 6)\%$. The values are given for the invariant mass $M(D^*\mu)$, the rapidity $\hat{y}(D^*\mu)$ and the transverse momentum $p_T^*(D^*\mu)$ of the $D^*\mu$ -pair.*

and beauty a two dimensional fit in each bin of the distributions has to be performed.

Since the total data sample contains some more events than the photoproduction sample, this sample is used to try such a separation of charm and beauty production in bins of the $D^*\mu$ variables. Since for the two dimensional fit a larger amount of data is needed than for the normal ΔM -fit, the number of bins is reduced to two. In figure 8.4 the results of the two dimensional fit in two bins of $M(D^*\mu)$, $\hat{y}(D^*\mu)$ and $p_T^*(D^*\mu)$ are shown together with the result of a one dimensional ΔM -fit, which is fitted simultaneously to the right and wrong charge data, in the four correlation regions. Good overall agreement between the two dimensional and the one dimensional fit is obtained for both bins of the three $D^*\mu$ variables except in the second correlation region. The discrepancy in the second correlation region is presumably caused by a statistical fluctuation. The population of the correlation regions changes strongly with the measured invariant mass $M(D^*\mu)$ and the measured transverse momentum of the $D^*\mu$ -pair. At small $p_T^*(D^*\mu)$ or large $M(D^*\mu)$ the dominant contribution comes from events, which have a back-to-back topology (therefore mainly charm), while at large $p_T^*(D^*\mu)$ or small $M(D^*\mu)$ the dominant contribution is given by beauty events, where the D^* -meson and the muon come mainly from the same quark (usually the decay of a B^0 , $m_{B^0} = 5.28 \text{ GeV}/c^2$).

As a cross check the number of charm and beauty events (after muon background correction) is compared to the number of charm and beauty events obtained from the fit to the total data sample (see last column of table 8.1). A large discrepancy is observed for $p_T^*(D^*\mu)$. For the other two variables the agreement is better, for $\hat{y}(D^*\mu)$ excellent agreement is observed. Furthermore the beauty fractions (after muon background correction) in each bin of the three $D^*\mu$ variables from the two dimensional fit are compared in table 8.1 to the beauty fractions predicted by the Monte Carlo simulation PYTHIA, if an overall beauty fraction of $f_b = (41 \pm 6)\%$ is used. A large discrepancy between the beauty fractions is observed in the first bin of $p_T^*(D^*\mu)$. For the other two variables the agreement is somewhat better. The two dimensional fit is very sensitive to statistical fluctuations in particular in bins where only two correlation regions are populated. For this reason, the determination of differential charm and beauty cross sections will be attempted only as a function of $M(D^*\mu)$ and $\hat{y}(D^*\mu)$.

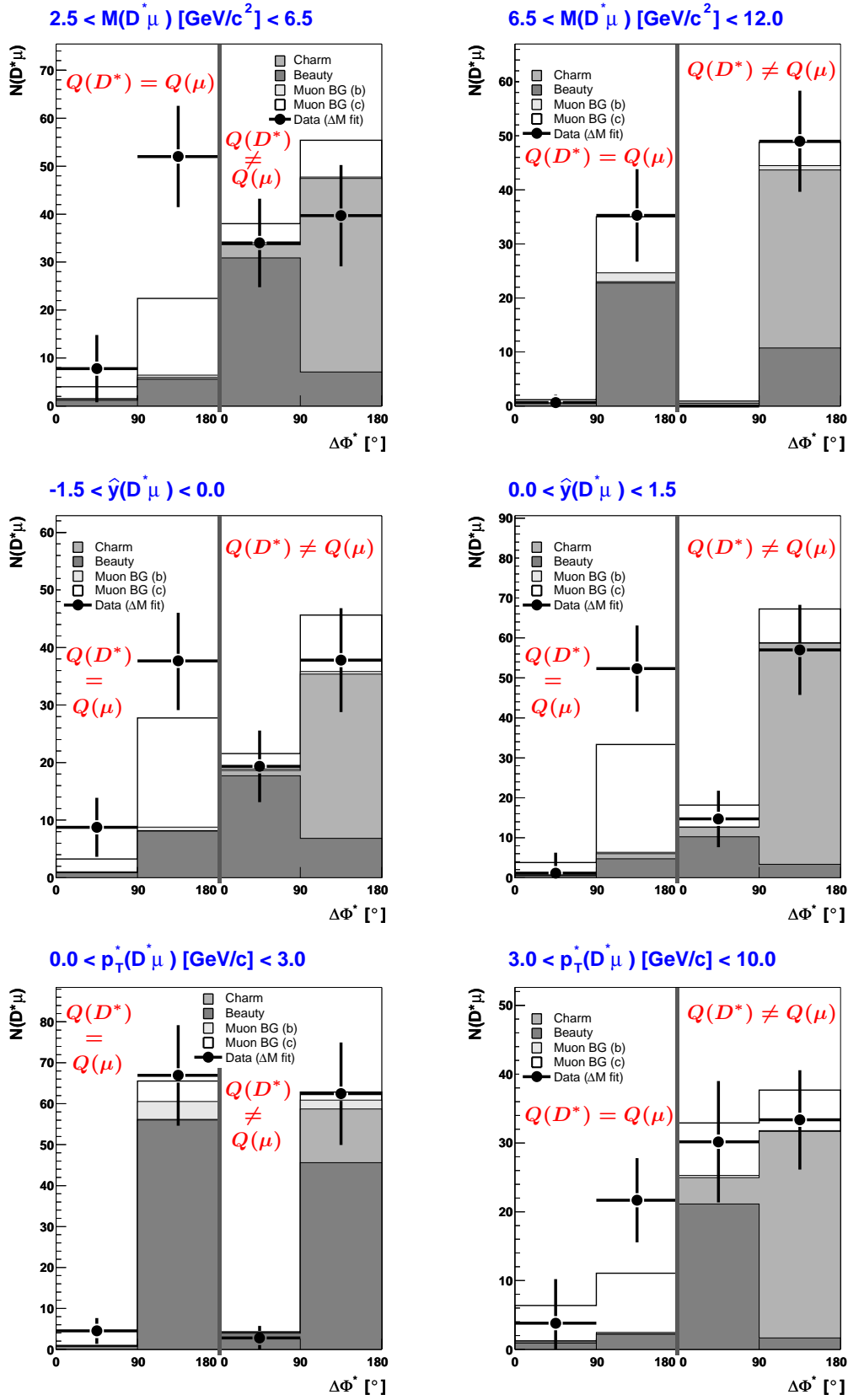


Figure 8.4: Result of the two dimensional fit for the two bins of $M(D^*\mu)$, $\hat{y}(D^*\mu)$ and $p_T^*(D^*\mu)$ using the **total sample**. The charm, beauty and muon background contributions are drawn separately. The black dots are the result of a one dimensional ΔM -fit in bins of the correlation regions.

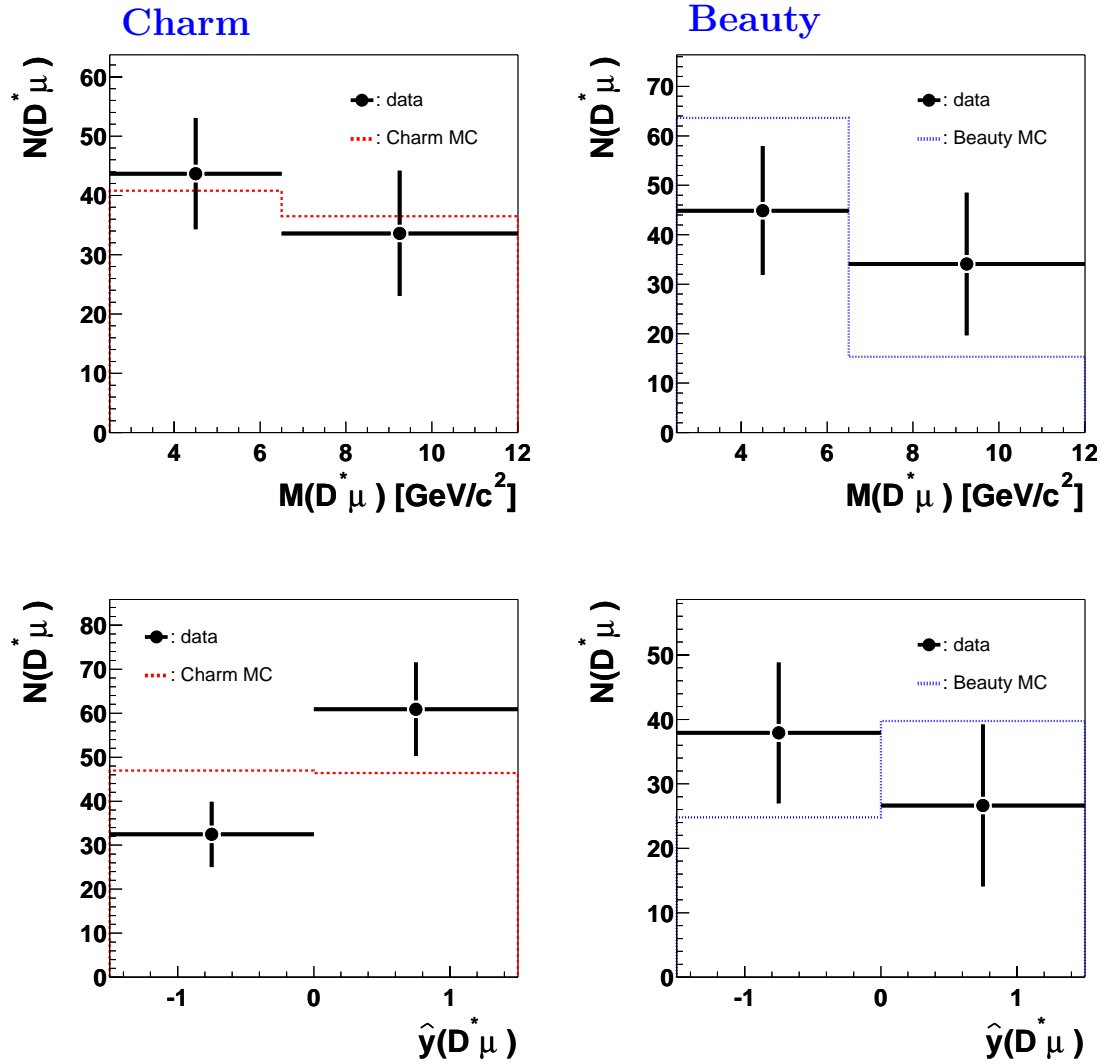


Figure 8.5: *Differential $D^*\mu$ -distributions for charm (left) and beauty production (right) for the total data set. Shown are the invariant mass and the rapidity (measured in the laboratory frame) of the $D^*\mu$ -pair. The data (black dots) are compared to the Monte Carlo prediction from PYTHIA, which is normalised to the data.*

In figure 8.5 the number of $D^*\mu$ -events from charm and beauty production, as obtained from the two dimensional fit and after muon background correction, are presented as a function of the invariant mass and the rapidity of the $D^*\mu$ -pair. The shapes of both distributions are described by the PYTHIA Monte Carlo simulation.

The differential cross sections $d\sigma/dx$ as a function of a variable x are calculated in a similar way as the total cross sections. The number of $D^*\mu$ -events in a bin of a quantity x , for example $p_T^*(D^*\mu)$, and the efficiencies have to be known. Since for the photoproduction sample no separation of charm and beauty events is performed, the differential beauty fraction has to be considered in the total efficiency. For the differential cross section

$d\sigma_{vis}/dx$ in the photoproduction visible range the following formula holds:

$$\begin{aligned} \frac{d\sigma_{vis}}{dx} &= \frac{d\sigma_{vis,c}(ep \rightarrow e'D^*\mu X)}{dx} + \frac{d\sigma_{vis,b}(ep \rightarrow e'D^*\mu X)}{dx} \\ &= \frac{\frac{dN(D^*\mu)}{dx}}{\mathcal{L} \cdot \mathcal{BR}(D^* \rightarrow K\pi\pi_s) \cdot \underbrace{\epsilon_{trig}(x) \cdot \epsilon_{rec}(x) \cdot \epsilon_{L4}(x)}_{\epsilon_{total}(x)}}} \end{aligned} \quad (8.4)$$

The total efficiency $\epsilon_{total}(x)$ in a bin of x is given by:

$$\epsilon_{total}(x) = \frac{\epsilon_{total}^c(x) \cdot \epsilon_{total}^b(x)}{f^b(x)\epsilon_{total}^c(x) + (1 - f^b(x))\epsilon_{total}^b(x)} \quad (8.5)$$

$f^b(x)$ denotes the beauty fraction in the corresponding bin. This is calculated using the overall beauty fraction f_b and the normalised charm and beauty distributions (all after muon background correction) according to:

$$f^b(x) = \frac{f_b \cdot N^b(i)/N^b}{f_b \cdot N^b(i)/N^b + (1 - f_b) \cdot N^c(i)/N^c} \quad (8.6)$$

For the total data sample a separation of charm and beauty events is possible and the cross section formula reduces to:

$$\frac{d\sigma_{vis}^Q}{dx} = \frac{\frac{dN^Q(D^*\mu)}{dx}}{\mathcal{L} \cdot \mathcal{BR}(D^* \rightarrow K\pi\pi_s) \cdot \underbrace{\epsilon_{trig}^Q(x) \cdot \epsilon_{rec}^Q(x) \cdot \epsilon_{L4}^Q(x)}_{\epsilon_{total}^Q(x)}} \quad (8.7)$$

The index Q indicates the type of the heavy quark, charm or beauty respectively. In the next section the differential efficiencies are determined and then the cross sections are calculated.

8.2 Differential Efficiencies

First, similar checks of the trigger, reconstruction and L4-finder efficiencies are performed as already performed for the total cross sections (chapter 7). The only difference is that the trigger element efficiencies, the L4-finder efficiencies and the reconstruction efficiency of the cut on the transverse energy fraction $f_{ET}(D^*\mu)$ of the $D^*\mu$ have been calculated as a function of some chosen variables, for example the transverse momentum $p_T(\mu)$ of the muon.

As an example the L4 muon finder efficiency for $D^*\mu$ -events in photoproduction and for the period 1999 e^+ /2000 together with the efficiency of the cut on the relative fraction of the transverse energy $f_{ET}(D^*\mu)$ of the $D^*\mu$ -pair with respect to the total transverse energy are shown in figure 8.6. The L4 muon finder efficiency is presented as a function of $p_T(\mu)$, while the efficiency of the cut $f_{ET}(D^*\mu)$ is shown as a function of $p_T(D^*)$. Since in the data no separation of charm and beauty is performed, the beauty fraction $f^b(x)$ (determined via equation 8.3), as obtained with the beauty fraction $f_b = 31\%$ for

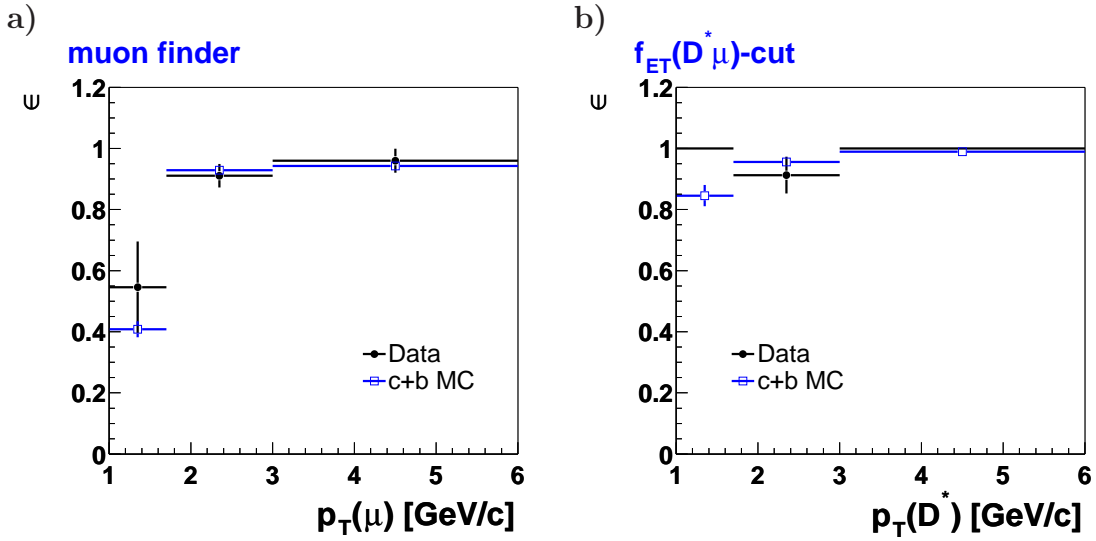


Figure 8.6: Efficiencies of a) the L4 muon finder as a function of $p_T(\mu)$ (period 1999 e^+ /2000 only) and b) of the $f_{ET}(D^*\mu)$ cut as a function of $p_T(D^*)$ for the photoproduction sample. The efficiencies were calculated according to equation 8.5 using a b -fraction of $f_b = 31\%$ (still containing muon background).

the photoproduction sample (still containing muon background), is used, and a combined efficiency is calculated from the simulation. The agreement between data and Monte Carlo simulation is good. The strongest dependence of the finder efficiencies is obtained for the L4 muon finder and for the variable $p_T(\mu)$. This is expected since the muon finder cuts explicitly on this quantity. However the threshold behaviour is well described by the Monte Carlo simulation. The efficiency of the L4 muon finder of the periods 99 e^- and 97 in the simulation has been adjusted to that of the data (see chapter 5). For the trigger elements and the logical OR combination of the L4 D^* and muon finder good agreement between simulation and data was found within errors.

Figure 8.7 shows as an example the reconstruction, trigger and L4 efficiencies as a function of the invariant mass of the $D^*\mu$ -pair separately for charm and beauty production as obtained by the PYTHIA Monte Carlo simulation for the photoproduction sample. Due to the softer momentum spectrum of the muons in charm events the trigger and L4 efficiencies are smaller for charm events than for events from beauty production. For charm production all efficiencies increase strongly with $M(D^*\mu)$, since a small value of $M(D^*\mu)$ is for charm directly related to a small momentum of the two particles. For beauty production a clear rise is only observed for the reconstruction efficiency, while the other two efficiencies show only a slight increase with $M(D^*\mu)$. For other variables like $\hat{y}(D^*\mu)$, $p_T^*(D^*\mu)$ and $\Delta\Phi^*$ weaker dependencies at least for the reconstruction efficiency are observed. The weakest dependence is observed as a function of the transverse momentum of the $D^*\mu$ -pair. In general the dependence of the efficiencies on the selected variables is stronger for charm than for beauty production.

The total efficiency for charm and beauty production as well as the combined total efficiency (c+b) is presented in figure 8.8. For the combined efficiency the beauty fraction $f_b = 40\%$ (photoproduction, after muon background correction) is used.

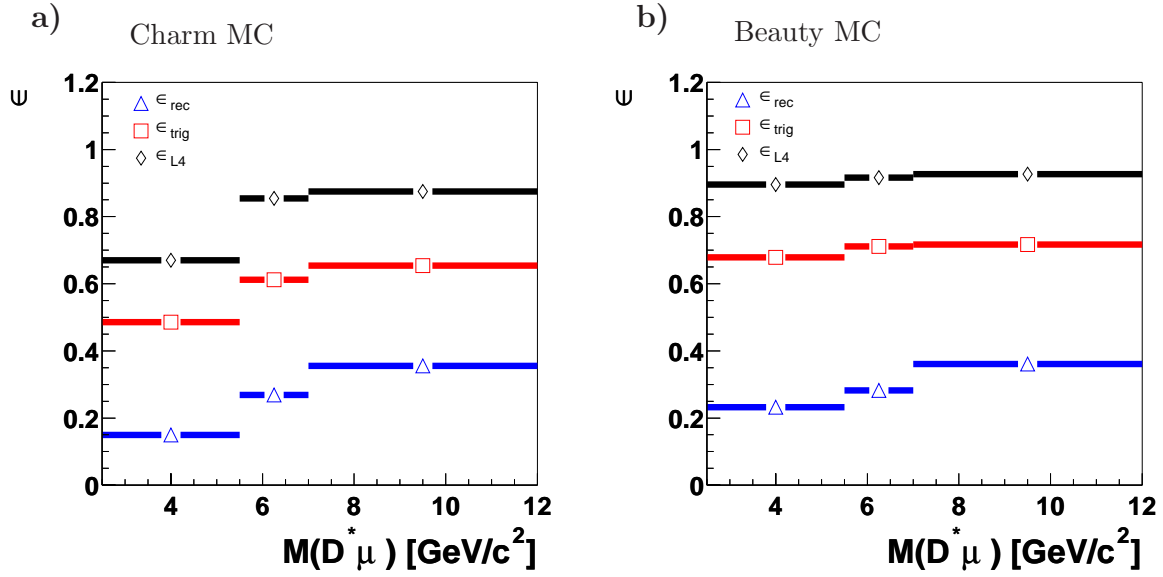


Figure 8.7: Reconstruction, trigger and L4 efficiencies as a function of the invariant mass $M(D^*\mu)$ of the $D^*\mu$ -pair for the photoproduction sample. a) Charm production and b) beauty production.

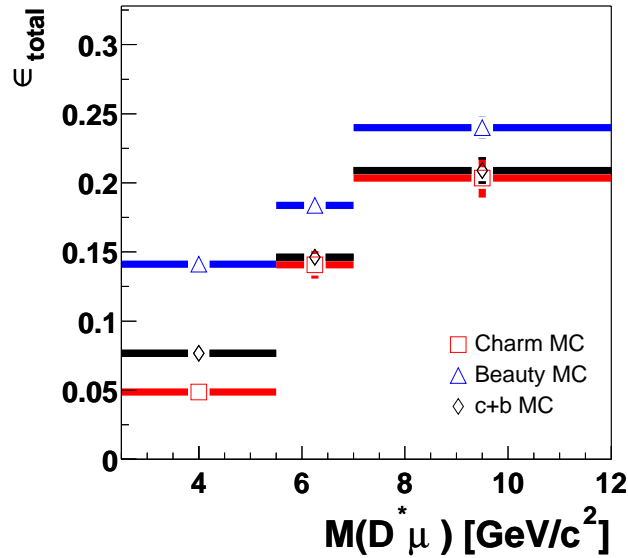


Figure 8.8: Total efficiencies as a function of the invariant mass $M(D^*\mu)$ of the $D^*\mu$ -pair for the photoproduction sample. The total efficiencies for charm and beauty production and the combined efficiency ($f_b = 40\%$) are shown separately.

8.3 Systematic Errors

Many of the systematic uncertainties, as discussed for the total cross section (table 7.8), cancel in the calculation of normalised differential cross sections. The uncertainties which cancel are the uncertainty in the luminosity, in the branching ratio $\mathcal{BR}(D^{*+} \rightarrow K^- \pi^+ \pi_s^+)$, the uncertainty due to reflections, muon identification, track reconstruction for the $D^*\mu$ -pair and the L4 finder efficiencies.

For the combined charm and beauty production cross section, which is determined for the **photoproduction data** set, the uncertainty in the **beauty fraction** affects not only the total number of events, but also the combined efficiency. In the last chapter the systematic uncertainty for the beauty fraction was determined to 10.5%. Taking the statistical error of 20% (all correlation regions) into account this leads to a total error of the beauty fraction of 23%. The systematic uncertainty on the normalised cross sections due to the uncertainty for the beauty fraction and the uncertainty for the **muon background**, is determined by varying simultaneously the beauty fraction by $\pm 23\%$ and the total fraction of the muon fake of charm and beauty by $\pm 20\%$. The systematic uncertainty obtained from the maximum deviation assuming a uniform distribution between two extremes (see section 7.4) is different for the four different $D^*\mu$ -variables. For $p_T^*(D^*\mu)$ and $\hat{y}(D^*\mu)$ the systematic uncertainty is 1%, while for $M(D^*\mu)$ a systematic uncertainty of 6% and for $\Delta\Phi^*$ an uncertainty of 3% is obtained.

The systematic uncertainty due to the **signal extraction** via the one dimensional ΔM -fit is determined by varying the width of the Gaussian by its uncertainty ($\pm 0.2 \text{ MeV}/c^2$). To estimate the effect of a possible change of the width in the different intervals of each variable, which would affect the shape of the distributions, a linear change of the width from the upper value to the lower value is assumed. Assuming a uniform distribution between two extremes (see section 7.4), from the maximum deviations obtained by this method a systematic uncertainty of 3% for each $D^*\mu$ variable is obtained.

Adding the uncertainties, discussed above for the photoproduction sample, in quadrature a systematic uncertainty of 3% for $p_T^*(D^*\mu)$ and $\hat{y}(D^*\mu)$, an uncertainty of 7% for $M(D^*\mu)$ and of 4% for $\Delta\Phi^*$ is obtained. Compared to the statistical errors the systematic uncertainties can be neglected.

For the differential charm and beauty cross section, as determined for the **total data set**, the same investigations as performed for the total cross sections for the uncertainty of the muon background, the signal extraction, the $\Delta\Phi^*$ model dependence and the fragmentation fractions are performed. Here this study is done in each bin of the $D^*\mu$ variables. The systematic uncertainty for each source is estimated from the maximum deviations obtained by the variation of the corresponding parameter and assuming a uniform distribution between these two extreme results (see section 7.4). Here the same uncertainties for the charm and beauty cross sections are used, since the large statistical error restricts the estimation of the systematic uncertainty. The uncertainty in the muon background leads to a systematic uncertainty of 3% in the normalised differential cross sections. For the estimation of the uncertainty in the signal extraction a linear change of the width of the Gaussian used in the fit from the upper value to the lower value along the intervals is assumed. This leads to a systematic uncertainty of 4% in the case of $M(D^*\mu)$ and of 3% for $\hat{y}(D^*\mu)$. The uncertainty due to the $\Delta\Phi^*$ model dependence is estimated to be 4% for all variables. The uncertainty due to the fragmentation fractions is different for each variable. An uncertainty of 3% is obtained for $M(D^*\mu)$, while for $\hat{y}(D^*\mu)$ an uncertainty of 5% is obtained.

Adding the uncertainties, discussed above for the total sample, in quadrature a systematic uncertainty of 7% for $M(D^*\mu)$ and of 8% for $\hat{y}(D^*\mu)$ is obtained. Table 8.2 summarises the systematic errors for the normalised differential cross sections.

$\epsilon_{syst.} [\%]$	γP				$\gamma P + DIS$	
	p_T^*	M	\hat{y}	$\Delta\Phi^*$	M	\hat{y}
μ -BG, f_b	1	6	1	3	-	-
μ -BG			-		3	
signal extraction			3		4	3
$\Delta\Phi^*$ model dependence			-		4	
fragmentation fractions			-		3	5
total syst. error	3	7	3	4	7	8

Table 8.2: *Relative systematic errors of the normalised differential visible cross sections. The uncertainties are shown separately for the photoproduction sample, where combined charm and beauty cross sections are calculated, and for the total data set, where charm and beauty cross sections are computed separately.*

8.4 Normalised Differential Cross Sections

For photoproduction the normalised differential $D^*\mu$ cross sections are shown in figure 8.9 extracted in the visible range for the sum of charm and beauty production using the muon background corrected differential distributions shown in figure 8.3. The differential cross sections are presented as a function of the transverse momentum $p_T^*(D^*\mu)$, the rapidity $\hat{y}(D^*\mu)$, the invariant mass $M(D^*\mu)$ and the azimuthal angle difference $\Delta\Phi^*$ of the $D^*\mu$ -pair. The data (points) are compared to the predictions of the two different Monte Carlo generators PYTHIA and CASCADE and to the NLO prediction obtained using the program FMNR. For the NLO calculation only the direct component is used, since the normal resolved component is very small and can be neglected. The error band assigned to the NLO calculations is obtained in the same way as for the total cross sections (section 7.5). The mass, the renormalisation and factorisation scales are varied and the deviations are added linearly. In the case of the PYTHIA generator the direct as well as the resolved excitation component are contained in the prediction.

The predicted cross sections for charm and beauty production are normalised separately to those of the data and a beauty fraction $f_b = 30\%$, as obtained from the total measured charm and beauty cross sections, is used. In general the shape of the distributions is described reasonably well by all three predictions. The prediction of the NLO calculations or the CASCADE Monte Carlo generator for the shape of the variables $p_T^*(D^*\mu)$ and $\Delta\Phi^*$ are smeared out stronger to larger (smaller for $\Delta\Phi^*$) values than the PYTHIA Monte Carlo generator. The NLO prediction as well as the CASCADE Monte Carlo prediction seem to describe the $p_T^*(D^*\mu)$ and $\Delta\Phi^*$ distribution of the data somewhat better than the PYTHIA Monte Carlo generator. The agreement between NLO calculation and the data is worse for the $\hat{y}(D^*\mu)$ distribution compared to the agreement obtained for the two Monte Carlo generators. Deviations in the forward direction are present between data and predictions. In $M(D^*\mu)$ no large difference between the three theoretical predictions is observed and for all predictions good agreement with the data is obtained. Considering all four distributions the best description of the data is obtained for the CASCADE generator.

The CASCADE Monte Carlo generator is based on the CCFM evolution approach which is related to k_T -factorisation. Therefore the gluon taking part in the hard interaction can

have a non-zero transverse momentum k_T . This leads to a stronger smearing of $p_T^*(D^*\mu)$ and $\Delta\Phi^*$ than predicted by the PYTHIA Monte Carlo generator. NLO behaves in these variables in a very similar way. However since the NLO calculations are based on the DGLAP evolution approach, the $\hat{y}(D^*\mu)$ distribution is different.

With the data used for this analysis it is unfortunately not possible to make a clear statement, whether the photoproduction data prefer the NLO prediction, the CASCADE Monte Carlo prediction or the PYTHIA Monte Carlo prediction. All three predictions are able to describe the shape of the data, even though it seems that the best description is obtained by the CASCADE Monte Carlo generator. Nevertheless clear differences between these three models do occur and with more statistics it should be possible to make a clearer statement on this topic.

Figure 8.10 shows the normalised differential $D^*\mu$ charm or beauty cross sections respectively for the total data set. The data are compared to the predictions of the Monte Carlo generator PYTHIA/RAPGAP as well as to the Monte Carlo generator CASCADE. In view of the large errors no firm conclusion is possible. Both distributions - $M(D^*\mu)$ and $\hat{y}(D^*\mu)$ - are described reasonably by the two different Monte Carlo simulations.

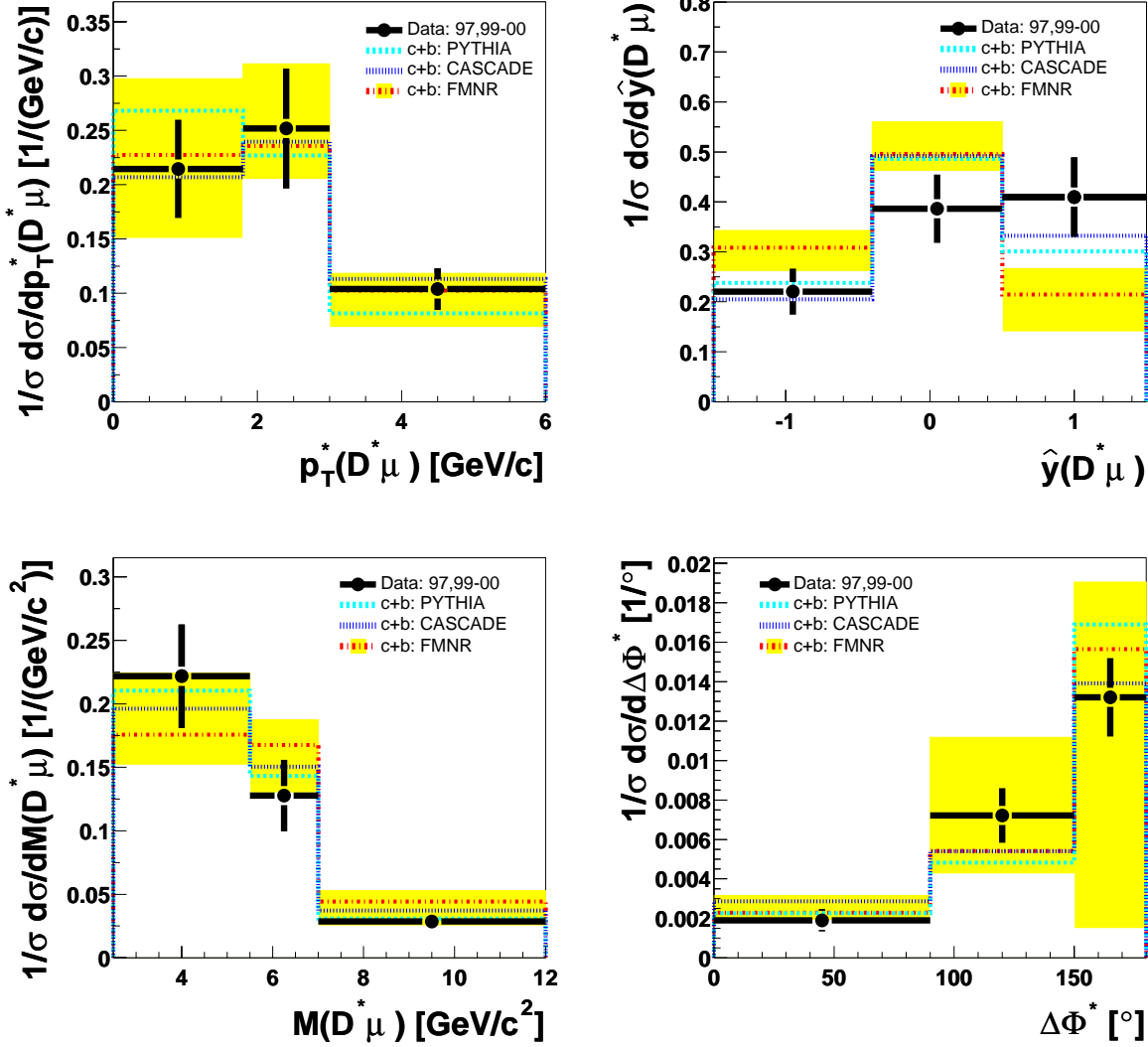


Figure 8.9: Normalised differential visible $D^*\mu$ cross sections ($c+b$) for **photoproduction**. The distributions of the transverse momentum $p_T^*(D^*\mu)$, the rapidity $\hat{y}^*(D^*\mu)$, the invariant mass $M(D^*\mu)$ and the azimuthal angle difference $\Delta\Phi^*$ of the $D^*\mu$ -pair are shown. The data (dots) are compared to the prediction of the Monte Carlo generators PYTHIA and CASCADE as well as to the NLO calculation. In the PYTHIA generator the direct as well as the resolved excitation component are used. For the NLO calculation the direct component alone is used, since the normal resolved component is negligible. The predicted cross sections for charm and beauty production are normalised to those of the data and $f_b = 30\%$ is the used beauty fraction as obtained from the total measured charm and beauty cross sections. The systematic uncertainties are negligible compared to the statistical errors.

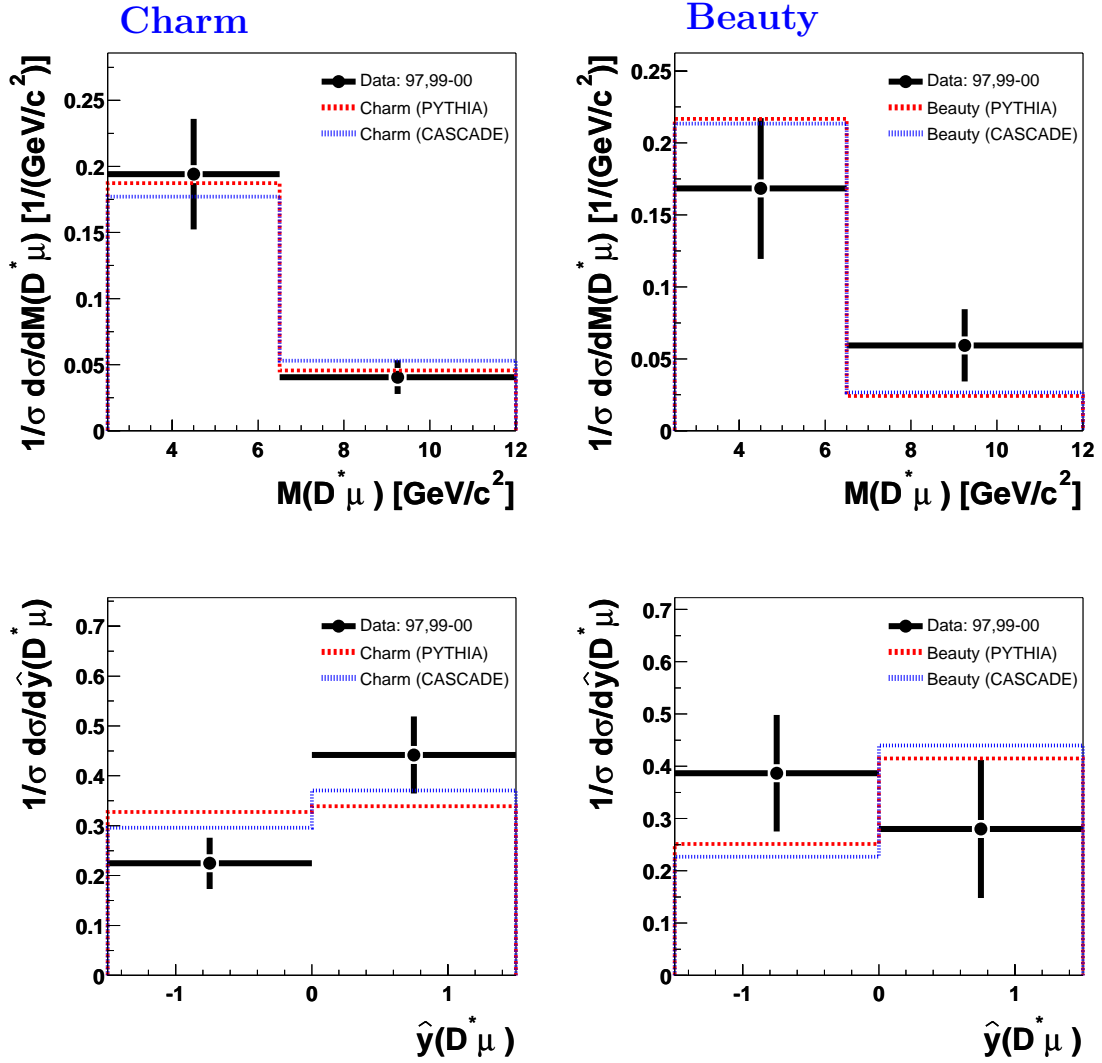


Figure 8.10: Normalised differential visible $D^*\mu$ charm (left) and beauty (right) production cross sections for the **total data set**. The distributions of the invariant mass $M(D^*\mu)$ and the rapidity $\hat{y}(D^*\mu)$ of the $D^*\mu$ -pair are shown. The data (dots) are compared to predictions of the Monte Carlo generators PYTHIA (photoproduction) and RAPGAP (DIS) as well as to the predictions of the Monte Carlo generator CASCADE. The Monte Carlo generator mix of PYTHIA and RAPGAP is indicated in the plots as PYTHIA. The systematic uncertainties are negligible compared to the statistical errors.

Chapter 9

Unintegrated Gluon Density

The aim of this chapter is the determination of the unintegrated gluon density, which depends on the momentum fraction x_g of the gluon with respect to the proton momentum, the transverse momentum k_T of the gluon and the maximum allowed angle \bar{q}'_t . Since the number of $D^*\mu$ -events is limited only the dependence of the gluon density on at most two variables is considered: the gluon density $x_g g(x_g)$ as a function of x_g , inclusively as well as in bins of k_T and \bar{q}'_t . For the extraction of the unintegrated gluon density the Monte Carlo generator CASCADE is used, which is based on the CCFM evolution model. In section 2.5 the quantities x_g, k_T, \bar{q}'_t as well as the procedure for extracting the unintegrated gluon density was described.

This measurement is carried out with the charm dominated sample, using only events from correlation region 4. $x_g(D^*\mu)$ differential distributions are determined inclusive and in bins of $p_T^*(D^*\mu)$ and in bins of $\bar{q}'_t(D^*\mu)$, where $x_g(D^*\mu)$, $p_T^*(D^*\mu)$ and $\bar{q}'_t(D^*\mu)$ are related to the quantities x_g, k_T, \bar{q}'_t based on the quark momenta. The contribution of muon background and also the contribution of beauty events, where a b -hadron decays directly into a $D^*\mu$ -pair, will be corrected for. The latter correction ensures that the D^* -meson and the muon come from different heavy quarks and that thus the D^* -meson and the muon are related to the two quarks. Since the $D^*\mu$ -quantities represent the $Q\bar{Q}$ based quantities only approximately, the $D^*\mu$ -quantities are unfolded in order to obtain distributions depending on the $Q\bar{Q}$ based quantities. The unfolding procedure corrects only for detector effects and fragmentation, and uses the Monte Carlo simulation PYTHIA. The technical details of the unfolding procedure are described in appendix D and in [108, 109].

From the $Q\bar{Q}$ distributions which are the result of the unfolding cross sections are calculated. The inclusive gluon density $x_g g(x_g)$ as well as the gluon densities $x_g g(x_g)$ in bins of k_T and \bar{q}'_t are then obtained by dividing this cross section by the visible $D^*\mu$ -cross section, obtained for a flat gluon density. These cross sections are calculated via the CASCADE Monte Carlo generator, since this Monte Carlo generator contains a k_T -dependent calculation of the cross section of the hard process.

The measured inclusive gluon density $x_g g(x_g)$ and the gluon density in bins of k_T and \bar{q}'_t , are then compared to that used by CASCADE and also to that obtained from the NLO calculations and from the PYTHIA Monte Carlo generator.

9.1 Differential Distributions

In order to get a charm dominated data set only events belonging to *correlation region 4* ($\Delta\Phi^* > 90^\circ$ and $Q(D^*) \neq Q(\mu)$) are selected. This selection ensures a good relation between the two quarks and the $D^*\mu$ -pair. Furthermore only events from photoproduction are taken to make possible a comparison with NLO calculations.

The number of $D^*\mu$ -events obtained from a ΔM -fit are corrected for muon background, $b \rightarrow D^*\mu$ events and events, which are reconstructed within the allowed $0.05 < y_{JB} < 0.75$ range but where the generated y -value is outside the visible range $0.05 < y < 0.75$. For $b \rightarrow D^*\mu$ events it is impossible to get information about the quark pair final state. The same is true for events, where a hadron is misidentified as a muon or where the muon is a decay muon. The y -correction, which is about 10%, is applied to avoid a correction within the unfolding procedure.

The binwise correction for the sum of muon background events, $b \rightarrow D^*\mu$ events and of y migration is performed in a similar way as for the muon background correction alone. A correction factor $f_{cor}^c(i)$ in bin i is calculated for charm as the ratio of generated $D^*\mu$ events within the generated visible y -range $N_{gen}^c(i)$ to the number of reconstructed $D^*\mu$ -events $N_{rec}^c(i)$, containing in addition also muon background events and events with a generated y outside of the visible y -range:

$$f_{cor}^c(i) = N_{gen}^c(i)/N_{rec}^c(i) \quad (9.1)$$

For beauty events the correction factor $f_{cor}^b(i)$ in a bin i is the ratio of $D^*\mu$ -events $N_{gen}^{b,no\ b \rightarrow D^*\mu}(i)$, without the $b \rightarrow D^*\mu$ component, to the number of reconstructed $D^*\mu$ -events $N_{rec}^b(i)$, which contain also muon background events and events with a generated y outside of the visible y -range:

$$f_{cor}^b(i) = N_{gen}^{b,no\ b \rightarrow D^*\mu}(i)/N_{rec}^b(i) \quad (9.2)$$

The combined correction factor f_{cor} is then given by:

$$f_{cor} = (1 - f_b^{rec}(i)) \cdot f_{cor}^c(i) + f_b^{rec}(i) \cdot f_{cor}^b(i) \quad (9.3)$$

Here $f_b^{rec}(i)$ is the beauty fraction in the i -th bin (determined via equation 8.3). Figure 9.1 shows the combined correction factor f_{cor} . In addition to the total combined correction factor above also the combined correction factors for the muon background alone and for the sum of muon background and $b \rightarrow D^*\mu$ events are shown.

Figure 9.2 shows the differential distributions of the observed quantity $\log_{10}(x_g(D^*\mu))$, inclusively as well as in bins of $p_T^*(D^*\mu)$ and $\bar{q}'_t(D^*\mu)$, after the muon background, $b \rightarrow D^*\mu$ and y correction. The range in $\log_{10}(x_g(D^*\mu))$ is adapted to the number of $D^*\mu$ -events. The beauty fraction in the data is now only $f_b = 5.8\%$. The data (black points) are presented together with the PYTHIA Monte Carlo prediction. The Monte Carlo prediction describes the $x_g(D^*\mu)$ -distribution in bins of $\bar{q}'_t(D^*\mu)$ well, while there are some differences in the other two distributions. In the next section these three distributions will be unfolded to get the $Q\bar{Q}$ based quantities.

As explained in the appendix D the number of bins used for a variable has to be twice as large as the desired final number of bins after the unfolding. As can be seen from figure 9.2 this analysis starts with initially six bins and after unfolding three bins in the corresponding $Q\bar{Q}$ based variables will be obtained.

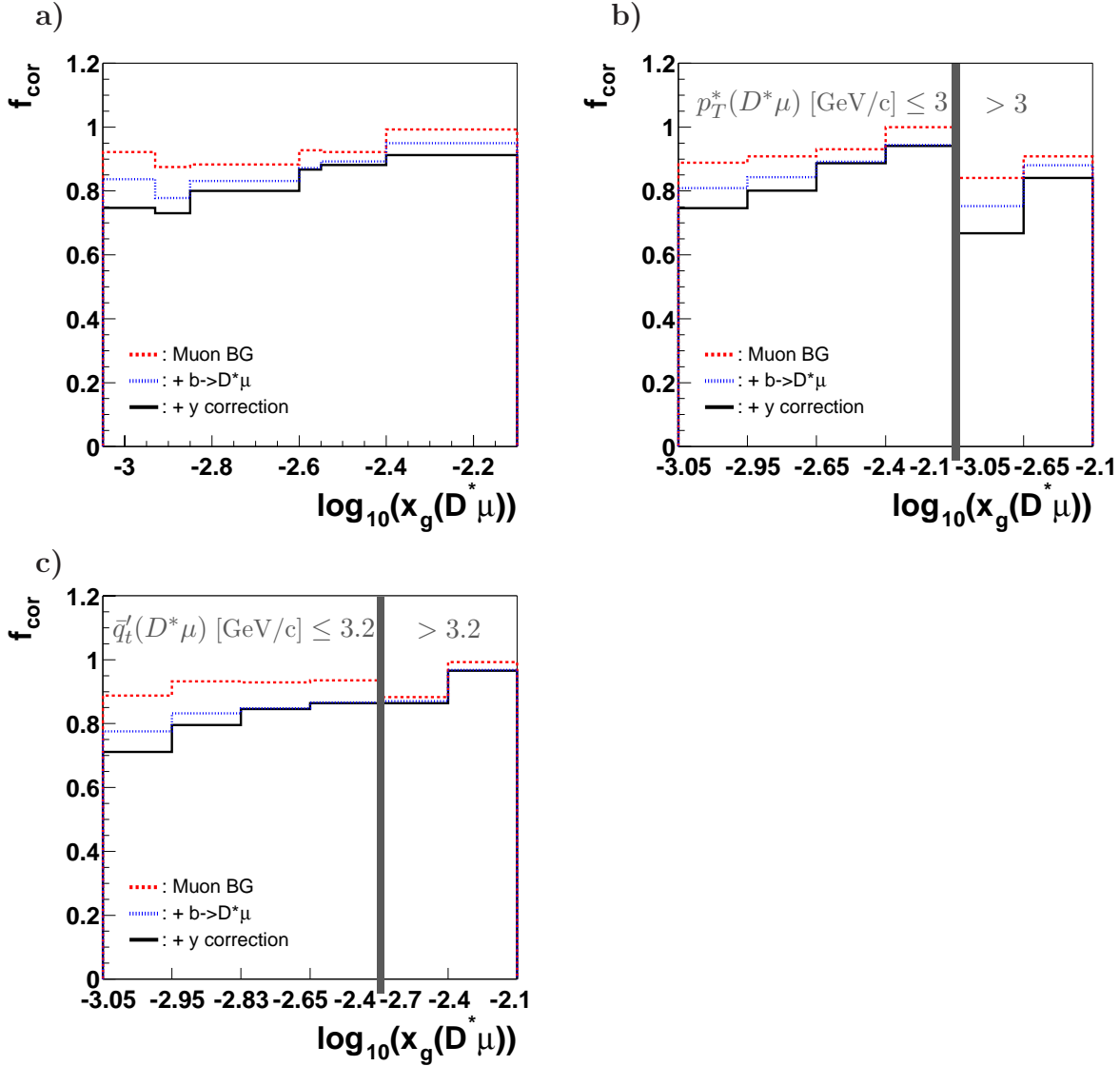


Figure 9.1: Correction factors for the observed quantity $\log_{10}(x_g(D^*\mu))$, inclusive (a) as well as in bins of $p_T^*(D^*\mu)$ (b) and $\bar{q}_t'(D^*\mu)$ (c) in photoproduction as predicted by the PYTHIA Monte Carlo simulation. The full line is the total combined (c + b) correction factor, the dashed line the correction factor for the muon background alone and the dotted line is the correction factor for the sum of muon background and $b \rightarrow D^*\mu$ events. The total correction factor contains in addition also the correction for events with a generated y outside of the allowed y -range (y -correction).

9.2 Unfolding of Gluon Variables

For the unfolding of the measured $D^*\mu$ quantity $x_g(D^*\mu)$, inclusive as well as in bins of $p_T^*(D^*\mu)$ and $\bar{q}_t'(D^*\mu)$, the method explained in detail in appendix D is used (see also [108, 109]).

The reconstructed $D^*\mu$ -quantities are related to the $Q\bar{Q}$ based quantities via a probability matrix. The probability matrix describes the migration effects due to measurement errors

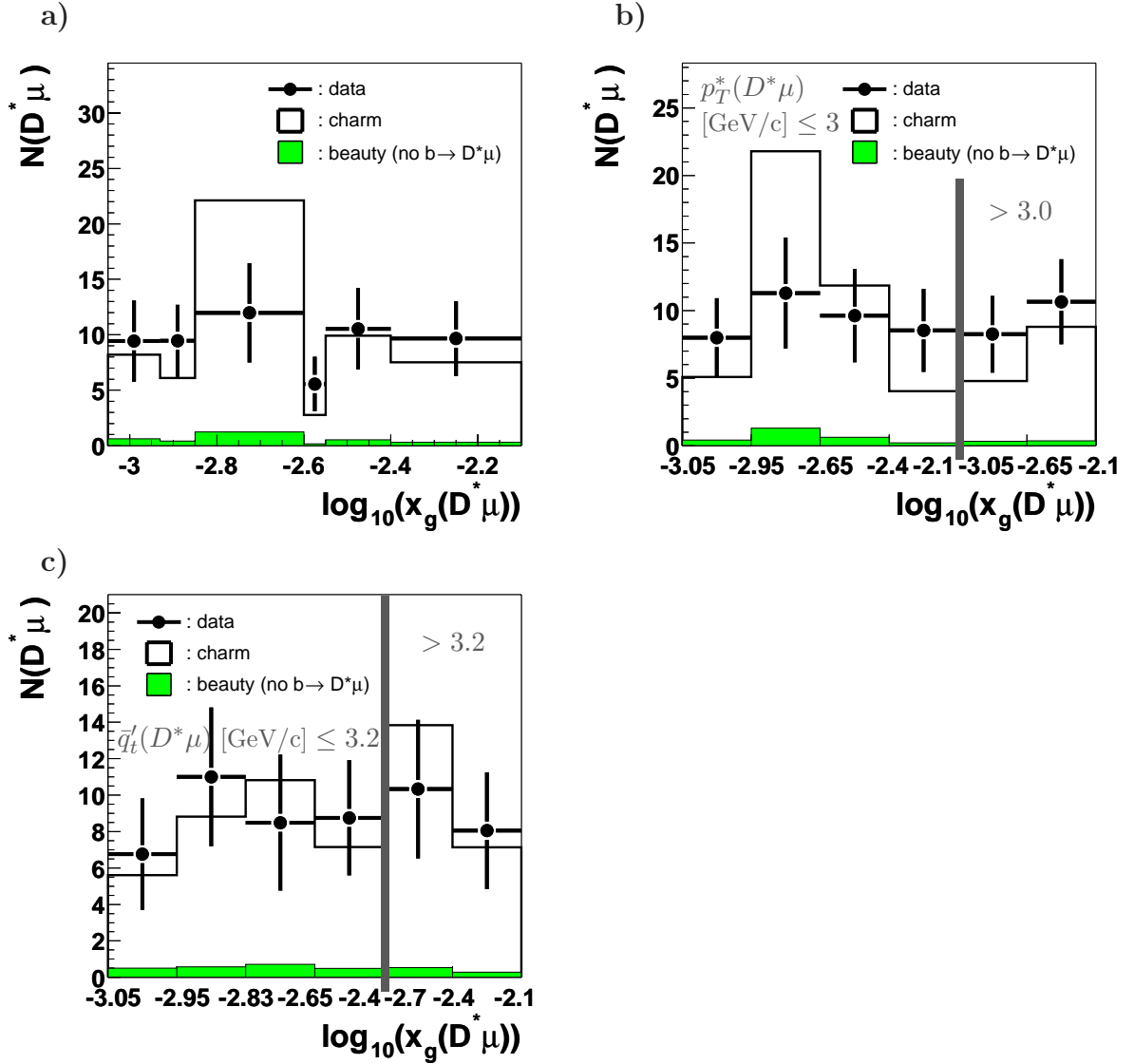


Figure 9.2: Differential distributions of the observed quantity $x_g(D^*\mu)$, inclusive (a) as well as in bins of $p_T^*(D^*\mu)$ (b) and $\vec{q}_t'(D^*\mu)$ (c) in photoproduction. The distributions are corrected for muon background, events from $b \rightarrow D^*\mu$ and for events with y out of the visible range. Shown are the data (black dots) together with the PYTHIA Monte Carlo prediction ($f_b = 5.8\%$), which is split into charm and beauty events.

and fragmentation and is obtained using the Monte Carlo simulation. In order to avoid large fluctuations in the unfolded distributions a procedure based on the significance of coefficients c_i of the rotated solution function is applied. The number of bins of the unfolded distribution is reduced to avoid large correlations between neighbouring bins.

In order to construct the probability matrix some technical details have to be considered. Since the data contain events from charm as well as from beauty production, the beauty fraction of $f_b = 5.8\%$ has to be used for the production of the probability matrix in the Monte Carlo simulation.

In the Monte Carlo simulation still a non-negligible amount of events is reconstructed

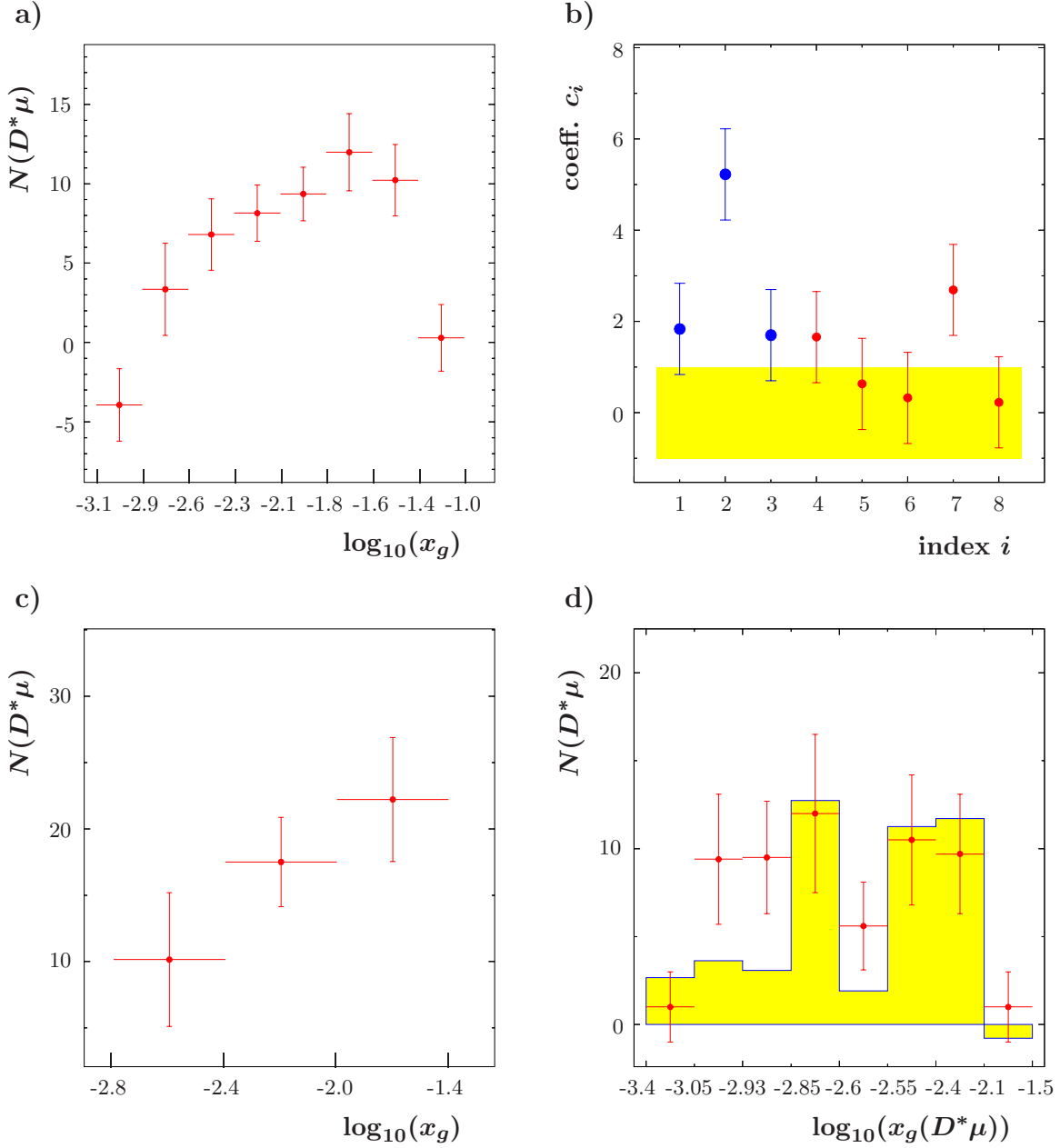


Figure 9.3: *Quality of the unfolding for $x_g(D^*\mu)$. Shown are the $Q\bar{Q}$ based distribution obtained by the unfolding (a), the coefficients c_i (b), the fit result (d) and the final distribution of the $Q\bar{Q}$ based x_g obtained by reducing the number of bins (c). For the unfolding only the first three coefficients c_i are used.*

outside of the $\log_{10}(x_g(D^*\mu))$ range used in the data. In the case of $x_g(D^*\mu)$ an additional bin at the lower and upper edge of $\log_{10}(x_g(D^*\mu))$ and $\log_{10}(x_g)$ is introduced. In data no significant signal is obtained in the lower as well as in the upper additional bin and the value is set to the small value of 1 ± 2 . For the measurement of $\log_{10}(D^*\mu)$ in bins of $p_T^*(D^*\mu)$ and $\bar{q}_t'(D^*\mu)$ only one extra bin is used for the $Q\bar{Q}$ based and the reconstructed quantities. This extra bin contains events, which belong to the lower and upper outside bin for $\log_{10}(x_g(D^*\mu))$, $p_T^*(D^*\mu)$, $\bar{q}_t'(D^*\mu)$ or $\log_{10}(x_g)$, k_T , \bar{q}_t' respectively.

Quantity	correlation coefficients between bins		
	1-2	1-3	2-3
x_g	0.62	-0.24	0.58
x_g in 2 bins of k_T	-0.33	0.61	0.55
x_g in 2 bins of \bar{q}'_t	-0.23	0.71	0.52

Table 9.1: Correlation coefficients between the various bins taking only the first three coefficients c_i .

In $x_g(D^*\mu)$ a clear correlation between the $Q\bar{Q}$ based and measured variables is observed. For the other two quantities this correlation is not as good (see chapter 2). Therefore in these quantities only two intervals are used.

In figure 9.3 some properties of the unfolding procedure and the quality of the unfolding are presented for $x_g(D^*\mu)$. The unfolded distribution x_g depends on the coefficients c_i shown in figure 9.3 b). Only the first three can be measured well enough, the others are compatible with zero. The first three coefficients however are not very significant. This is due to the lack of $D^*\mu$ events. In order to avoid large statistical fluctuations in the unfolded distribution only three coefficients are used which yields the unfolded distribution shown in figure 9.3 a). The corresponding correlation coefficients for the data points are almost 100%, especially for the neighbouring bins. Taking again only these three coefficients and reducing the number of bins the distribution of the $Q\bar{Q}$ based x_g shown in figure 9.3 c) is obtained. The corresponding correlation coefficients for the three bins between the data points are presented in table 9.1. Here also the correlation coefficients for the other two distributions are presented. The correlations are strongly reduced compared to the case, where six bins are used. The figure 9.3 d) shows the fit result using only the first three coefficients compared to the initial data. Reasonable agreement is obtained. The quality of the fit might be improved with more events.

9.3 Differential Cross Sections

In order to calculate the differential cross sections from the $Q\bar{Q}$ based differential distributions obtained in the last section, the efficiencies for the $Q\bar{Q}$ based quantities are needed. These efficiencies are determined from the PYTHIA Monte Carlo simulation in an analogous way as in chapter 8 for the $D^*\mu$ cross sections. Since a correction for events, reconstructed in the allowed y_{JB} -range which originate from outside of the allowed visible range in y , is already applied before unfolding, the efficiencies are always calculated with respect to the number of $D^*\mu$ -events in the visible y range. As an example, the combined total efficiency is shown as a function of x_g in figure 9.4. The beauty fraction used for the calculation of the combined efficiencies is $f_b = 5.8\%$, which is the beauty fraction in correlation region 4 as obtained by the two dimensional fit after correcting for muon background, $b \rightarrow D^*\mu$ and y -migration. An increase of the efficiency towards large $\log_{10}(x_g)$ is observed. A large x_g is related to a large invariant mass of the heavy quark pair and this leads to larger momenta of the single quarks and thereby the D^* -meson and the muon. Especially for large muon momenta the reconstruction, trigger and L4-finder efficiencies are relatively large and thus the total combined efficiency is large here too.

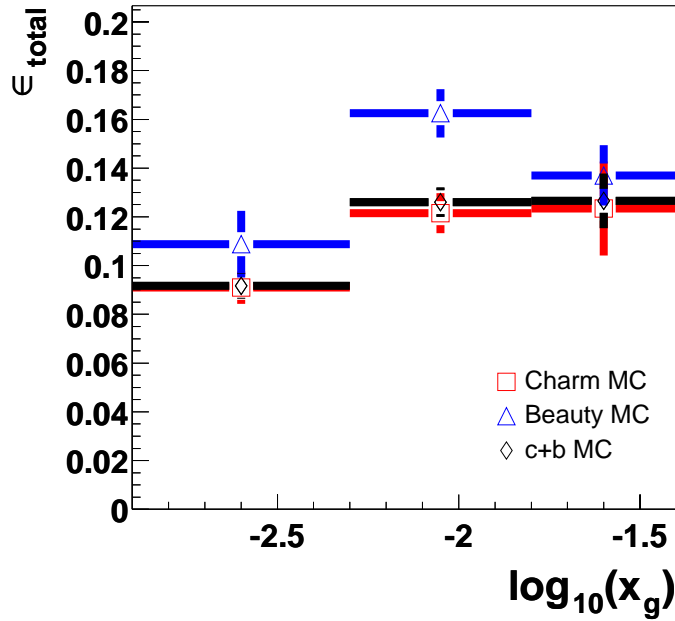


Figure 9.4: Combined efficiency for x_g .

The differential cross sections are presented as a function of the three gluon variables in figure 9.5. They are compared to the PYTHIA and CASCADE predictions as well as to NLO calculations. The Monte Carlo predictions as well as the NLO prediction are normalised to the data. For the beauty fraction the value obtained from the total cross section (correlation region 4 without $b \rightarrow D^* \mu$) is used, $f_b = 4\%$, for all three predictions. The error band of the NLO calculations indicated in all figures presented in this chapter is obtained by varying the heavy quark mass, the factorisation scale and the renormalisation scale and summing up the variations obtained linearly (see section 7.5). The agreement of data and theoretical predictions is reasonable within statistics although the data are somewhat more concentrated at larger $\log_{10}(x_g)$ than predicted by the theories. The prediction of x_g in the two bins of k_T is closest to the data for the Monte Carlo generator CASCADE.

Most of the systematic uncertainties, as discussed for the total cross section (table 7.8), also apply to the cross sections discussed here and the gluon density in the next section. The systematic uncertainties due to the luminosity, the branching ratio $\mathcal{BR}(D^{*+} \rightarrow K^- \pi^+ \pi_s^+)$, the uncertainty due to reflections, the muon identification, the track reconstruction for the $D^* \mu$ -pair and the L4 finder efficiencies add up to a total systematic uncertainty of 15%.

The uncertainty in the muon background and the beauty fraction enters the cross section calculation at the same places as for the differential cross sections ($c + b$) determined for all correlation regions in photoproduction. In addition also a small uncertainty on the correction of $b \rightarrow D^* \mu$ events has to be taken into account. A possible uncertainty due to the applied correction on events with a generated y outside of the allowed range, is neglected, since the correction is with $\leq 10\%$ small and since the y -distributions of the $D^* \mu$ -samples as well as of the inclusive D^* -samples are well described by the Monte Carlo simulation PYTHIA. In chapter 7 the systematic uncertainty of the beauty fraction was

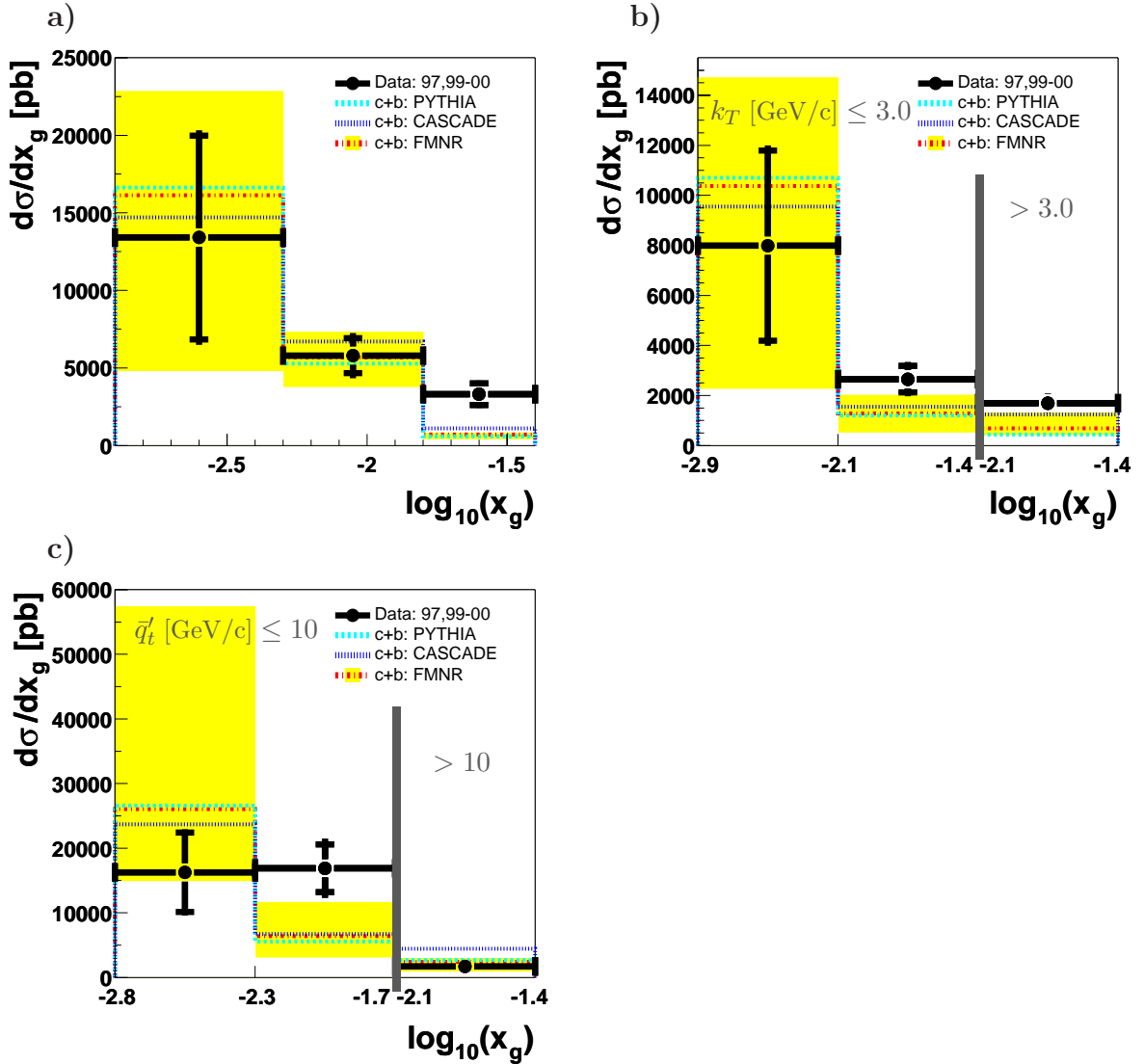


Figure 9.5: Differential cross sections for the gluon variables. Shown is $\log_{10}(x_g)$, inclusive (a) as well as in bins of k_T (b) and \bar{q}'_t (c). The measured data (dots) are compared to the PYTHIA, CASCADE and NLO predictions. A beauty fraction of $f_b = 4\%$ (obtained from the total cross section) is used and the theory predictions are normalised to the data. Statistical (inner error bars) as well as systematic uncertainties (outer error bars) are shown in case of the data.

determined to be 10.5%. Taking the statistical error of 25% (correlation region 4) into account this leads to a total error for the beauty fraction of 27%. Varying simultaneously the beauty fraction f_b by this uncertainty, the muon background correction factor by $\pm 20\%$ and the correction factor on $b \rightarrow D^* \mu$ by the uncertainty of the corresponding fragmentation fraction ($\pm 7\%$) the largest deviations in the number of events is found for the variations, where the variation of the three effects is either all positive or all negative. For these two combinations the unfolding as well as the efficiency calculation was repeated. The maximum deviation in the cross section leads to an uncertainty of 2.5%, assuming a uniform distribution between two extremes (see section 7.4).

The systematic uncertainty due to the signal extraction via the one dimensional ΔM -fit is determined by varying the width of the Gaussian by its uncertainty ($\pm 0.2 \text{ MeV}/c^2$). A systematic uncertainty of 3.5% is obtained.

Altogether a systematic uncertainty for the cross sections of the gluon quantities of 16% is obtained. This value is later also assigned to the extracted gluon densities.

9.4 Extraction of the Unintegrated Gluon Density

In order to extract the gluon density $x_g g(x_g)$ in the context of the CCFM evolution model the differential cross sections shown in the last section (figure 9.5) are used. The measured cross section $d\sigma/dx_g$ is divided by $d\sigma^{g=1}/dx_g$, obtained in the considered $\log_{10}(x_g)$ interval (see chapter 2):

$$x_g g(x_g) = \frac{d\sigma}{dx_g} / \frac{d\sigma^{g=1}}{dx_g} \quad (9.4)$$

The “g=1” indicates that the corresponding cross section is obtained by a constant gluon density, where the hard cross section used holds general for k_T -factorisation. This cross section is calculated in this analysis with the CASCADE Monte Carlo generator using a flat gluon density. In case of the gluon density $x_g g(x_g)$ in bins of k_T and \bar{q}'_t this is done for each interval of k_T or \bar{q}'_t respectively.

The cross section $d\sigma^{g=1}/dx_g$ is based on the photon flux and on the hard scattering cross section (within k_T -factorisation), which are both known very well. The remaining uncertainties are due to the uncertainty of the heavy quark mass as well as due to the uncertainty of the scales. These uncertainties contribute to the theoretical uncertainty in the extraction of the gluon density.

The gluon density $x_g g(x_g)$ is shown as a function of $\log_{10}(x_g)$ inclusively and separately for two bins in k_T and for two bins in \bar{q}'_t in figure 9.6. The prediction from the CASCADE generator, the PYTHIA generator as well as the NLO calculation for the gluon density are compared with the data. The gluon densities are calculated for all three predictions via equation 9.4 using the cross sections shown in figure 9.5. The same conclusion as for the cross sections holds. The differences however between the shapes of the data and the theory predictions are more pronounced. In case of the gluon density in bins of k_T CASCADE describes the data reasonably well and is closer to the data than the other predictions.

The gluon density as a function of k_T is very sensitive to the different evolution models or NLO effects. For example in the high k_T bin deviations of about a factor 3 between the CASCADE and PYTHIA Monte Carlo prediction are obtained, while the NLO calculation lies between them. The other distributions are also sensitive to the different theoretical predictions. In the last bins (large $\log_{10}(x_g)$, k_T or \bar{q}'_t) of these distributions a maximal difference of a factor 2 between the different predictions is obtained.

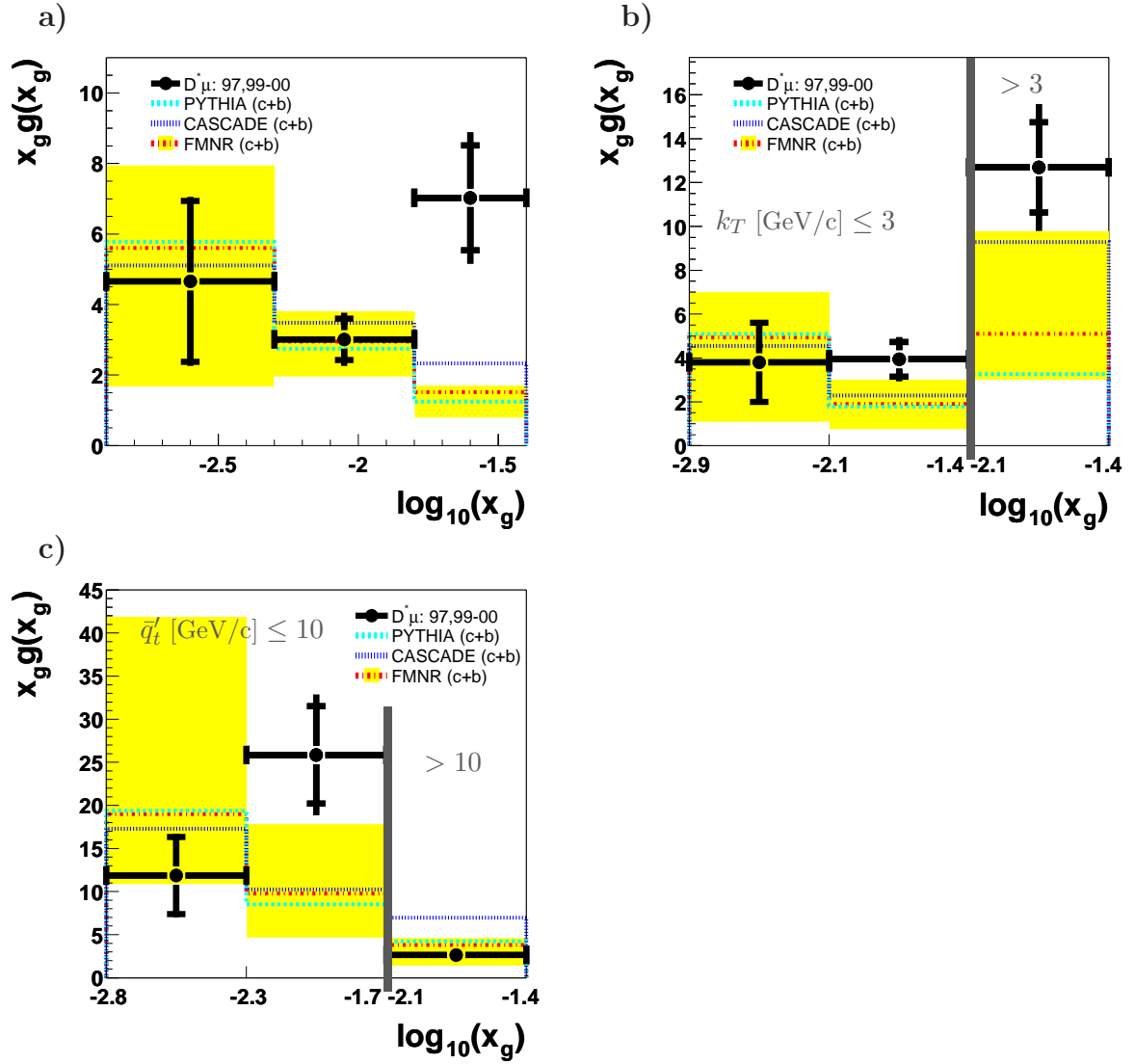


Figure 9.6: The gluon density $x_g g(x_g)$ as a function of $\log_{10}(x_g)$ inclusive a) and separately for two bins in k_T b) and for two bins in \bar{q}_t c). The prediction from the CASCADE generator, the PYTHIA generator as well as the NLO calculation for the gluon density are compared with the data (dots). Statistical (inner error bars) as well as systematic uncertainties (outer error bars) are shown in case of the data.

Chapter 10

Summary and Outlook

In this analysis the production of charm and beauty quarks in ep -scattering at HERA has been investigated. At HERA charm and beauty quarks are produced predominantly via boson gluon fusion as quark antiquark pairs.

In this thesis both heavy quarks were tagged (double tagging) via $D^*\mu$ -pairs. In general several possibilities for double tagging exist experimentally: DD , $D\mu$, $\mu\mu$, ee , etc.. Using the D^* for the reconstruction of a heavy quark, a clean heavy quark sample was obtained and a good approximation of the kinematic quantities of the corresponding quark was ensured. The muon and heavy quark momenta, however, are not so closely correlated and the purity of muon samples is lower. Since the branching ratios for D^* decay chains, which lead to D^* identification, are about an order of magnitude smaller than the branching ratio for the semileptonic decay of heavy quarks (about 10%), the requirement of a D^* and a muon in this analysis is a compromise between statistics and purity. An advantage of the requirement of at least one D^* -meson is the absence of background from light quarks u , d and s (after fitting a mass spectrum obtained from the reconstructed D^* candidates). If only the lepton signature is used, the uds -background would have to be considered in addition.

In the case of charm production both heavy quarks are tagged either by the D^* -meson or by the muon (double tagging). Therefore the kinematics of the heavy quark pair could be approximated by that of the $D^*\mu$ -pair. For beauty there is also the possibility that the $D^*\mu$ -pair originates from the same quark. This contribution however is useful for the separation of charm and beauty production.

The D^* -meson was reconstructed via the decay $D^* \rightarrow D^0\pi_s \rightarrow K\pi\pi_s$ and the muon was identified in the central muon detector. This reduced the contribution of hadrons, which are mis-identified as muons, to an acceptable level compared to the case, where the muons are identified only in the calorimeter. For charm the muon background contribution was about 35% and for beauty only about 4%. The requirement that muons are reconstructed in the muon system automatically leads to muon momenta above 2 GeV/c. This requirement together with the requirement of D^* -mesons and muons identified in the central detector led to a strong enrichment of events from beauty production.

The number of $D^*\mu$ -events was obtained from a fit of the $\Delta M = m_{K\pi\pi_s} - m_{K\pi}$ distribution of the D^* candidates. Afterwards a correction for the muon background was applied.

Two kinematic regimes are distinguished at HERA: the photoproduction regime, where the photon emitted by the incoming electron has almost zero virtuality Q^2 , and the DIS regime, which was selected in this analysis via $Q^2 > 2 \text{ GeV}^2$. Since the inclusive cross section is proportional to $1/Q^4$, photoproduction is dominant. In this thesis $D^*\mu$ events at $Q^2 < 1 \text{ GeV}^2$ (photoproduction sample) and at $Q^2 < 100 \text{ GeV}^2$ (total sample) are analysed. The photoproduction sample is a subset of the total data set. The total sample is used to perform measurements which require more statistics. The photoproduction sample contains $184 \pm 26 D^*\mu$ events and the total sample contains 229 ± 30 events.

For both data sets the data were divided into charge and angle correlation regions. Here it was distinguished, whether the charges of the D^* -meson and the muon were the same or opposite and whether the azimuthal angular difference $\Delta\Phi^*$ between the D^* and the muon, measured in the photon-proton rest frame, was above or below 90° :

1. $\Delta\Phi^* < 90^\circ$ and $Q(D^*) = Q(\mu)$.
2. $\Delta\Phi^* \geq 90^\circ$ and $Q(D^*) = Q(\mu)$.
3. $\Delta\Phi^* < 90^\circ$ and $Q(D^*) = -Q(\mu)$.
4. $\Delta\Phi^* \geq 90^\circ$ and $Q(D^*) = -Q(\mu)$.

According to the Monte Carlo simulation the $D^*\mu$ -pairs from charm production contributed mainly in the fourth correlation region. For beauty production, the contributions to the second, third and fourth correlation regions were all of the same order of magnitude. In correlation region 2 the process $b \rightarrow D^{*+}, \bar{b} \rightarrow \mu^+$ (and charge conjugated process) gave the largest fraction, and in correlation region 3 the process $b \rightarrow D^*\mu$. The latter process contributed also in correlation region 4 and was observed to be larger than the naively expected from the process $b \rightarrow D^{*+}, \bar{b} \rightarrow \bar{c} \rightarrow \mu^-$ (and charge conjugated process).

The charge and angle correlations were then exploited to separate $D^*\mu$ -events from charm and beauty production. A two dimensional Log Likelihood fit in $\Delta M = m_{K\pi\pi_s} - m_{K\pi}$ and the correlation regions was used. For the fit function the normalised population of the correlation regions as predicted by the Monte Carlo simulation PYTHIA was used. The predicted muon background fraction was adopted from PYTHIA as well. The muon background was checked with real data using the kaon and the pion from the D^0 decay. No discrepancy to the Monte Carlo simulation was found.

For both data sets, the beauty fraction obtained by the fit was about 30%. After correcting for muon background this fraction increased to about 40%. In the charm dominated correlation region 4 the beauty fraction was found to be only about 10%. Correcting there for the $b \rightarrow D^*\mu$ contribution in addition, led to an even smaller beauty fraction ($\approx 6\%$). The $b \rightarrow D^*\mu$ correction was applied for the extraction of the unintegrated gluon density (see below), because only for events $b \rightarrow D^*, \bar{b} \rightarrow \mu$ and $b \rightarrow D^*, \bar{b} \rightarrow \bar{c} \rightarrow \mu$ the kinematics of the $Q\bar{Q}$ -pair can be deduced.

From the number of $D^*\mu$ -events from charm and beauty production corrected for muon background, total cross sections in the visible range $p_T(D^*) > 1.5 \text{ GeV}/c$, $|\eta(D^*)| < 1.5$, $p(\mu) > 2.0 \text{ GeV}/c$, $|\eta(\mu)| < 1.735$ and $0.05 < y < 0.75$ were determined for photoproduction, $Q^2 < 1 \text{ GeV}^2$, and for the total data set, $Q^2 < 100 \text{ GeV}^2$. The data of the years 1997

and 1999-2000 were used, corresponding to an integrated luminosity of $\mathcal{L} = 85.4 \text{ pb}^{-1}$. The charm cross sections were found to be in good agreement with the Monte Carlo prediction of the generator PYTHIA (direct and resolved excitation component) as well as of the generator CASCADE and they are also in good agreement with the prediction of the NLO calculation. The ratio between the measured b -cross section and the cross section predicted by NLO was found to be 3.1 ± 1.2 . This result is in good agreement with the $D^*\mu$ -measurement from ZEUS [101] and it is still compatible with the recent $b \rightarrow \mu$ measurements at HERA [7, 8].

For the photoproduction data set differential $D^*\mu$ cross sections for the sum of charm and beauty production have been determined in the visible region as a function of the transverse momentum $p_T^*(D^*\mu)$, the azimuthal angle difference $\Delta\Phi^*$, the invariant mass $M(D^*\mu)$ and the rapidity $\hat{y}(D^*\mu)$ of the $D^*\mu$ -pair. The corresponding $Q\bar{Q}$ quantities of the two first variables are strongly sensitive to NLO effects and to a possible non-zero initial transverse momentum k_T of one of the initial partons. The invariant mass $M(Q\bar{Q})$ corresponds to the centre-of-mass energy of the initial partons, at least in LO, and the rapidity $\hat{y}(Q\bar{Q})$ is related to the direction of the quark pair. The shape of the data is described by the PYTHIA and CASCADE Monte Carlo predictions as well as by the NLO prediction. The distributions predicted by the CASCADE Monte Carlo generator however are closest to the data.

In the total data set ($Q^2 < 100 \text{ GeV}^2$) a separation of charm and beauty was performed in each bin of the differential distributions of $M(D^*\mu)$ and $\hat{y}(D^*\mu)$. Again reasonable agreement between the measured normalised cross sections and the PYTHIA/RAPGAP (PYTHIA for photoproduction, RAPGAP for DIS) and the CASCADE Monte Carlo predictions was found. Here no comparison to NLO calculations was possible, since no NLO program for DIS exists, in which $Q\bar{Q}$ cross sections can be calculated.

The data of correlation region 4 of the photoproduction data set were used for an extraction of the unintegrated gluon density. This more general gluon density does not only depend on the momentum fraction of the gluon with respect to the proton momentum, as is the case for the normal gluon density used in the DGLAP evolution scheme. It depends in addition on the transverse momentum k_T of the gluon and on the maximum possible angle \hat{q}'_t of the produced quark pair. All three variables can be expressed in terms of $Q\bar{Q}$ variables. The latter are obtained from the measured $D^*\mu$ -quantities by an unfolding procedure, which corrects for detector and fragmentation effects. In contrast to single tag analyses no theoretical assumption about the second quark is needed in this analysis. The gluon density is then extracted as a function of x_g , inclusively and also in bins of k_T and in bins of \hat{q}'_t . This procedure is applied to the data and to the theoretical predictions from NLO calculations as well as from the PYTHIA or the CASCADE Monte Carlo generator. The agreement of data and theoretical predictions is reasonable within statistics although the data are somewhat more concentrated at higher x_g . The prediction of the gluon density in two bins of k_T is closest to the data for the Monte Carlo generator CASCADE.

The analysis presented here was limited by the small number of $D^*\mu$ -events available. At the end of the HERA II data taking period, the expected integrated luminosity is of the order of 500 pb^{-1} , which is about a factor five more than used for this analysis. Due to the improved forward tracking device and the new forward silicon detector of the H1 experiment, an extension of the reconstruction of $D^*\mu$ -events to the forward region should become possible. Especially in case of charm production an increased number of

$D^*\mu$ events is expected. Using muons with a smaller minimum momentum would also increase the number of events, especially for charm. However this requires a more efficient triggering, and better muon identification at small momenta.

With more $D^*\mu$ -events, a separation of charm and beauty production could be performed in each bin of the $D^*\mu$ -variables. In the case of charm all events could be used, while for beauty production one could restrict the final sample to correlation region 2, where the kinematic variables of the $Q\bar{Q}$ -pair and those of the $D^*\mu$ -pair are well correlated. More precise measurements of the $D^*\mu$ -variables and of the gluon density should become possible as well as detailed determinations of the photon structure.

Another approach is to use other particles for the double tagging. A double tagging analysis with two leptons is already in progress and this kind of analysis can also profit from the larger integrated luminosity expected at the end of HERA II. For double tagging using D^*e the triggering of D^* events and the reconstruction of electrons, which is currently being studied, has to improved considerably. For the double tagging of DD (D indicating all charmed mesons, e.g. D^* , D^0 , D^+) the triggering of events in the photoproduction regime $0.01 < Q^2 [\text{GeV}^2] < 1.0$ has to be developed, using the Fast Track Trigger (FTT) in combination with trigger information of other detector components. The data of the photoproduction regime would be needed to get a reasonable number of events. Such a sample would be ideal concerning the relation between the quark-pair and the tagged particle pair.

Figure 10.1 shows for an event sample with two selected D^* -candidates (D^*D^* double tagging), the correlation between the mass difference ΔM of the D^* - and D^0 -candidates. Here both D^* candidates are reconstructed via the “golden decay channel” $D^* \rightarrow D^0\pi_s \rightarrow K\pi\pi_s$. An indication of a signal is already observed with the 1997, 1999-2000 data.

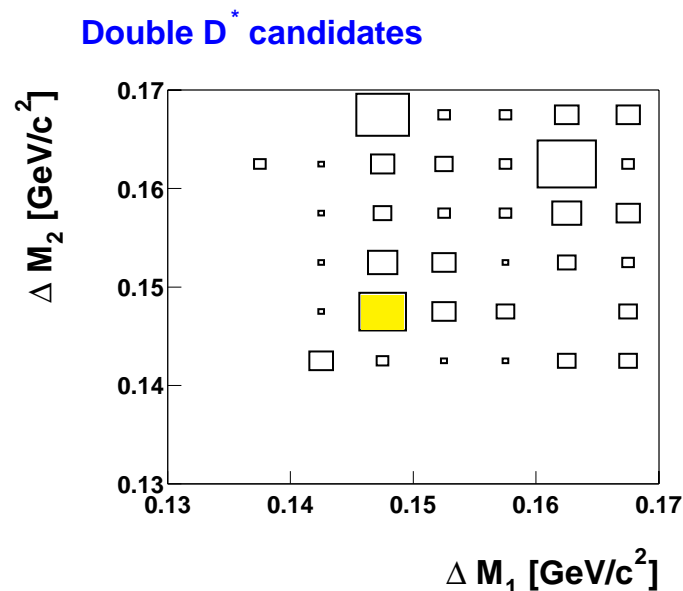


Figure 10.1: D^*D^* double tagging. Shown is the correlation of the mass difference $\Delta M = m(K\pi\pi_s) - m(K\pi)$ of two D^* -candidates in the same event (1997, 1999-2000 data). Double D^* events contribute to the marked bin. From a two dimensional fit to the ΔM distributions of the two D^* -candidates 7 ± 4 events are obtained.

Appendix A

Track Trigger for HERA II

The rate of some physics processes are so small that the luminosity of the accelerator has to be large enough to be able to observe the desired physics process. This is true for heavy quark production, especially for beauty production. For heavy quark double tagging analyses such as presented here the rate is very small.

The aim of the HERA upgrade was to increase the luminosity by about a factor 5. For the instant luminosity the following relation holds [110]:

$$\mathcal{L} \sim \frac{I_e \cdot I_p}{\sigma_x \sigma_y} \quad (\text{A.1})$$

Here I_e and I_p indicate the current of the electron or proton beam, respectively. σ_x , σ_y are the transverse size of the particle bunches at the interaction region. During the HERA upgrade two focusing magnets were installed in the detector to reduce the transverse size of the beam profiles σ_x and σ_y in such a way that a factor 3-4 in luminosity is gained. Further the proton and electron currents should be increased slightly compared to the HERA I data taking period. More detailed information on the operation parameters planned for HERA II can be found in [111, 112].

With increasing luminosity not only the physics rates but also the background rates will increase and the triggering has to become more powerful. Otherwise high rate triggers would have to be prescaled and no gain of the luminosity increase is obtained. For a detailed analysis of the final state already on trigger level the Fast-Track-Trigger (FTT) and the new jet trigger are built. With the FTT a third trigger level (L3) gets active, which will perform a further reduction of the rate.

Below studies on the triggering of charm production events with the FTT for HERA II are presented. Especially the third trigger level is considered, which allows the selection of D^* -events. Investigations of the FTT resolution, the efficiency and the background reduction are presented. First the principle of the FTT is explained.

A.1 The Principle of the FTT

The Fast-Track-Trigger (FTT) consists of three trigger levels and the aim is to provide on each trigger level the best possible track information within the given decision time. The FTT covers the central polar angular range of $25^\circ \leq \theta \leq 155^\circ$.

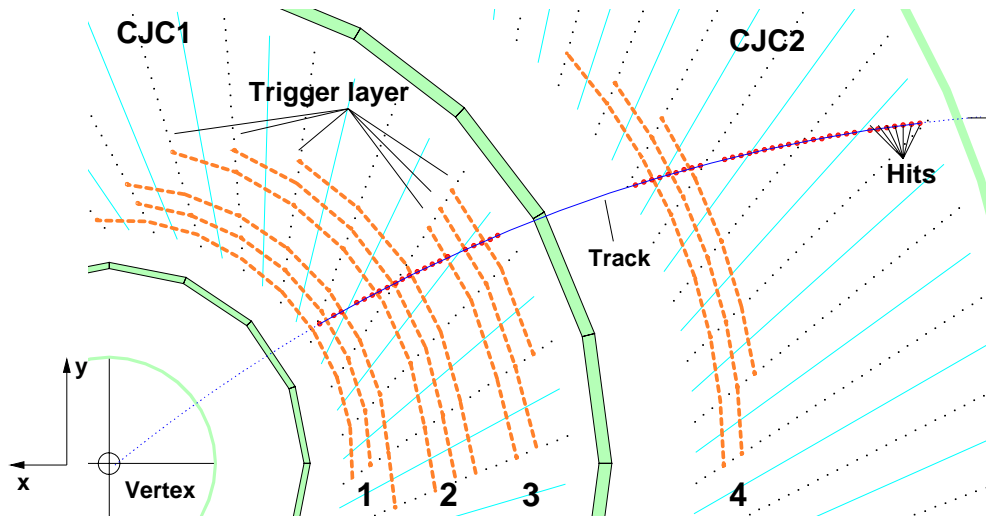


Figure A.1: Wire layers in the CJC used by the FTT. Four trigger layers consisting of three wire layers each exist. Three of them are located in the CJC1 and one in the CJC2.

Trigger layer	Chamber	Wire layer	mean radius	number of cells
1	CJC1	3,5,7	25.1 cm	30
2	CJC1	10,12,14	31.3 cm	30
3	CJC1	18,20,22	38.7 cm	30
4	CJC2	4,6,8	58.7 cm	60

Table A.1: Wire layers used by the FTT.

The input data of the FTT originates from chosen wire layers of the central drift chambers CJC1 and CJC2. Four trigger layers, consisting of three wire layers, are used. Three of the trigger layers are located in the inner chamber CJC1 and one in the outer chamber CJC2. Figure A.1 shows a $r\phi$ view of the CJC, whereby the trigger layers are marked. The starting configuration is given in table A.1. A so called trigger group consists of three sense wires in a drift cell and two sense wires out of the neighbour cells. Hence a trigger group contains five sense wires. This is illustrated in figure A.2. More detailed information about the FTT can be found in [113, 114, 115, 112].

Below a short overview of each FTT level is given:

- **FTT L1:** On the first trigger level hits in selected wire layers of the CJC are searched and the obtained drift time spectra are compared with those from genuine vertex constrained tracks. Track segments can be built, which are then roughly linked together. On L1 it will be possible to define several thresholds based on the number of tracks with a given transverse momentum. Further the charge of the tracks and simple topologies like back-to-back topology or jet topology can also be exploited on L1.
- **FTT L2:** On L2 the track segments found already by trigger level 1 are linked again together with an improved technique and the three dimensional track parameters

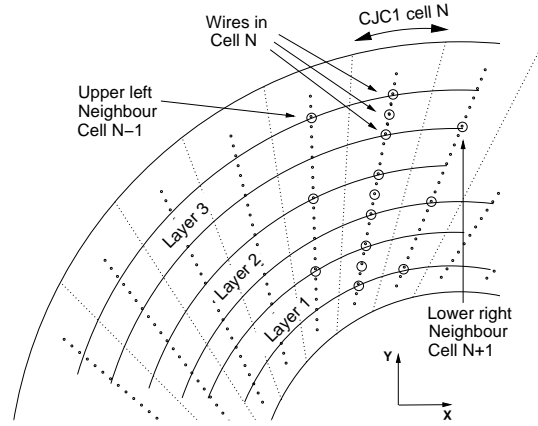


Figure A.2: Illustration of three trigger groups as used for the FTT.

are optimised with a fit algorithm. The r - ϕ resolution of the tracks, reconstructed in this way, is only slightly worse than the resolution of the complete offline CJC reconstruction. On L2 it is possible to use the improved transverse momentum of a track, the number of tracks, the charges of the tracks and again simple topologies. Furthermore it will be possible to look in events with low track multiplicity for vector mesons like J/Ψ or Υ already on the second trigger level.

- **FTT L3:** The tracks reconstructed on L2 are the starting point of the third level (PowerPC farm) and are used to search for particle decays. In the case of a D^* -meson the most suitable decay channel $D^* \rightarrow D^0 \pi_s \rightarrow K \pi \pi_s$ will be used for the D^* -meson reconstruction. First the invariant mass of the D^0 -candidate built up of a kaon and a pion has to be calculated. If the invariant mass of the kaon and pion pair candidate is consistent with the nominal D^0 -mass the invariant mass of the three particle combination with an additional pion π_s (s indicates the slow momentum of this pion) has to be calculated and then the mass difference of the D^* and D^0 candidate ΔM has to be compared to the nominal value of $\Delta M = 0.1454 \text{ GeV}/c^2$. Hence it is possible on L3 to require for example a D^* candidate with a specific cut on the transverse momentum of the D^* -meson and on the decay particles. For this task up to $100 \mu\text{s}$ can be used.

The simulation of the tracks obtained by the FTT reconstruction is performed by the programm FTTEMU (version 3) [112]. For this study the package is used in such a mode, that offline reconstructed tracks (only CJC information) were simulated. Then FTT hits are calculated from the measured track parameters using calibration constants, drift velocity and information on the chamber geometry. This method was checked by comparing FTT hits to hits determined with the standard readout. A good performance of this method was observed [112]. The noise in the chambers is considered by generating randomly additional hits and also the small single hit inefficiency is taken into account. Then almost the same procedure as used for the online FTT reconstruction is applied and the obtained track parameters are stored in the same way as the offline reconstructed data.

Subtrigger	L1 trigger rate [Hz]		L1 PF (2000)
	HERA I (2000)	HERA II	
61	6	30	1.2
83	12	60	1.2
84	25	125	4.5
108	12	60	1.3

Table A.2: Unprescaled L1 trigger rates of the main triggers for open charm analyses in the year 2000 and the expected rates after the luminosity upgrade. The averaged prescale factors (PF) for the subtriggers in the year 2000 are indicated in the last column.

A.2 Triggering Charm with D^* -Mesons

In the data taking period HERA I the main triggers for open charm analyses are subtrigger 61 and subtrigger 83. Subtrigger 61 requires an energy deposition of a scattered electron candidate in the SpaCal, thus selecting DIS events (in analyses using subtrigger 61 usually $2 \leq Q^2 \leq 100 \text{ GeV}^2$ is applied). Subtrigger 83 demands a scattered electron in the electron tagger ET33, selecting low Q^2 , $Q^2 \lesssim 0.01 \text{ GeV}^2$. In table A.2 the unprescaled trigger rates for some chosen subtriggers are shown for the year 2000 together with the expected rates after the luminosity upgrade. The subtrigger 84 and 108 are also ET triggers, but subtrigger 84 uses the ET at $z = -44 \text{ m}$ and s108 the ET at $z = -8 \text{ m}$. All triggers contain in addition to the above explained conditions also requirements on the tracks, like transverse momentum and charge cuts, and on the z -position of the event vertex. No L2 (and L3) requirement was applied for these subtriggers and the output rates on L1 correspond directly to the L4 input rate. The output rate of L4 of the subtriggers has to be of the order of 1 Hz. After the luminosity upgrade the rate will be significantly too high for all subtriggers. Without further trigger requirements the subtriggers would need at least a factor five larger prescale factor and no gain of the increased luminosity would be obtained. Furthermore the ET33 was removed due to the new focussing magnets near the H1 detector and the electron taggers ET44 and ET8 were moved to 40 m and 6 m respectively.

The FTT hit resolution in $r\phi$ is not much worse than the offline reconstruction and thus also the resolution of the transverse momentum p_T and the azimuthal angle ϕ . But the resolution in the polar angle θ is about a factor 10 worse compared to the resolution of the offline reconstruction, since the intrinsic z -resolution of the CJC is in case of the FTT not improved by the Z -chambers. Figure A.3 shows the resolution of the transverse momentum $p_T(D^*)$, the polar angle $\theta(D^*)$ and the azimuthal angle $\phi(D^*)$ of the D^* -candidate obtained with the FTT. This is compared to the resolution of the offline reconstruction. To ensure that in the FTT and offline reconstruction the same D^* -mesons are considered the following cuts on the D^* candidates are applied:

$$\begin{aligned}
 |p_T(K, \pi)_{FTT} - p_T(K, \pi)_{\text{offline}}| &< 75 \text{ MeV}/c \\
 |p_T(\pi_s)_{FTT} - p_T(\pi_s)_{\text{offline}}| &< 40 \text{ MeV}/c \\
 |\phi(K, \pi, \pi_s)_{FTT} - \phi(K, \pi, \pi_s)_{\text{offline}}| &< 15^\circ
 \end{aligned}$$

The resolution of $p_T(D^*)$, reconstructed by the FTT, is only slightly worse than the offline resolution. This holds also for transverse momentum the decay particles of the D^* -meson. The relative resolution for the π_s is somewhat worse compared to the other

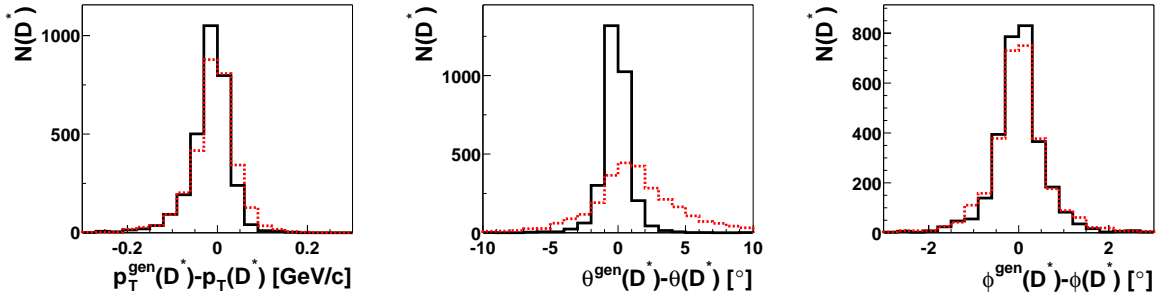


Figure A.3: D^* momentum and angular resolution. The full line indicates the offline reconstruction and the dashed line the FTT reconstruction. The direct LO Monte Carlo simulation AROMA for the year 2000 is used for these plots.

two decay particles, due to the small momentum of the pion, which is already in the regime where multiple scattering becomes important. As expected the resolution of $\phi(D^*)$, reconstructed by the FTT, is almost as good as the offline resolution. But the resolution of $\theta(D^*)$, measured by the FTT, is much worse than the offline resolution. The worse $\theta(D^*)$ resolution has direct impact on the resolution of the invariant mass $m_{K\pi}$ of the D^0 -candidate, shown in figure A.4. Again the FTT resolution is compared with the offline resolution. Also in $m_{K\pi}$ the FTT resolution is significantly worse than the resolution of the offline reconstruction. The maximal shift obtained by the FTT reconstruction is about $200 \text{ MeV}/c^2$. But in most of the cases the discrepancies between the generated values and the values reconstructed by the FTT are smaller than $100 \text{ MeV}/c^2$. On the right side of figure A.4 the invariant mass distribution of the D^0 candidate is shown for D^* -candidates, which are in a range of $\pm 3 \text{ MeV}/c^2$ around the nominal mass difference of the D^* and the D^0 candidate of $\Delta M = m_{K\pi\pi_s} - m_{K\pi} = 0.1454 \text{ GeV}/c^2$ (called signal region SR). This distribution is obtained from offline reconstructed data. The bright inner lines give the $\pm 100 \text{ MeV}/c^2$ deviation from the nominal D^0 -mass and the outer grey lines correspond to a deviation of $\pm 200 \text{ MeV}/c^2$. In order to be able to study the D^0 -sidebands in a D^* analysis, one should not cut too hard on the invariant mass of the D^0 -candidate with the FTT. A cut around the D^0 -mass of $200 \text{ MeV}/c^2$ is at the limit.

In figure A.5 the ΔM resolution obtained with the FTT reconstruction is shown together with that obtained by the offline reconstruction. The maximal shift towards larger values is with about $5 \text{ MeV}/c^2$ smaller than the maximal shift towards smaller values of about $9 \text{ MeV}/c^2$. To obtain in an analysis the number of D^* events a parameterisation containing the D^* -signal and the combinatorial background is fitted to the ΔM distribution of the data (see figure A.5b). For this, a large sideband on the right side of the signal is needed to get a good handle on the background distribution. In most of the D^* analyses the ΔM cut lies between 0.165 and $0.17 \text{ GeV}/c^2$. On trigger level this cut has to be slightly looser.

Several L3-FTT cut scenarios were tested, always with respect to usual analysis cuts in a given kinematic regime. The FTT cut scenarios and the corresponding analyses cut scenarios are presented in table A.3. On analysis level for all scenarios the same additional cut on the radial track length of the decay particles of $R > 15 \text{ cm}$ was applied. Since the background situation is much better in DIS events than in photoproduction harder cuts on the transverse momentum of the D^* -candidate and its decay particles are applied in case

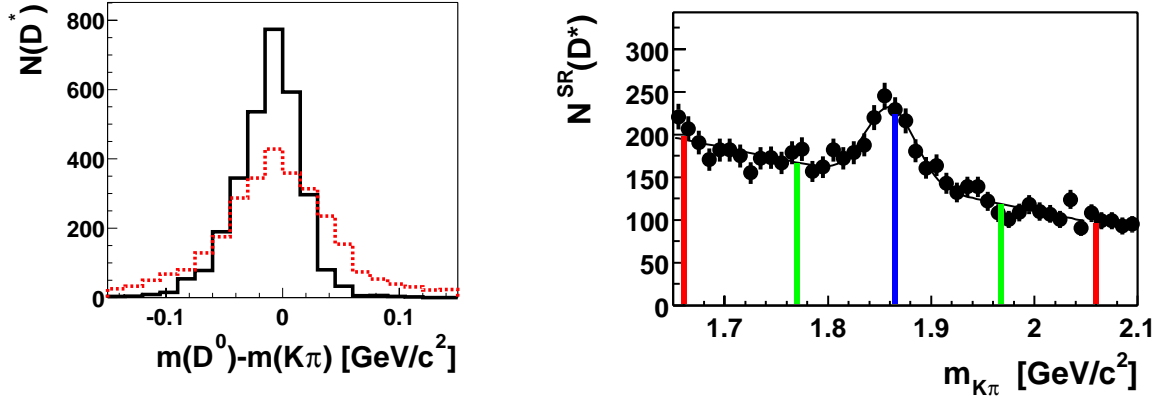


Figure A.4: Left: Resolution of the invariant mass of the D^0 -candidate of the FTT reconstruction (dashed line) compared with that of the offline reconstruction (full line). The LO direct Monte Carlo simulation AROMA with the simulation and reconstruction of the year 2000 is used. Right: Invariant mass distribution of the kaon-pion pair forming a D^0 -candidate (analysis level).

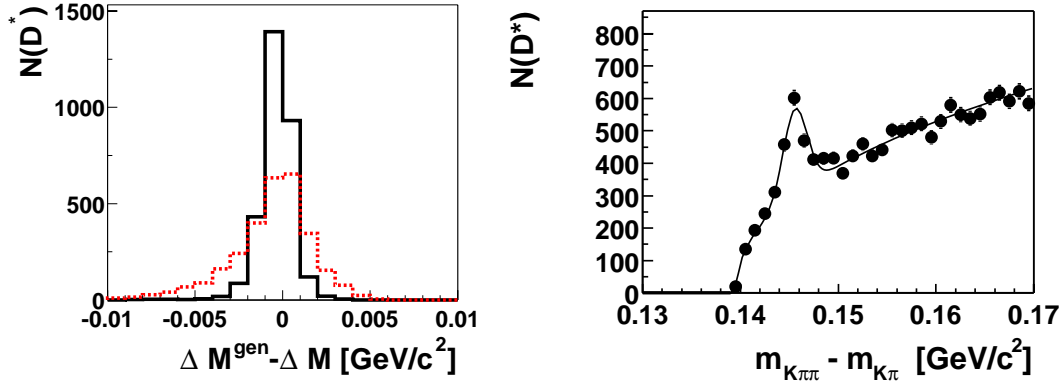


Figure A.5: Left: Resolution of the mass difference of the D^* and D^0 -candidate of the FTT reconstruction (dashed line) compared with that of the offline reconstruction (full line). The LO direct Monte Carlo simulation AROMA with the simulation and reconstruction of the year 1997 is used. Right: Mass difference $\Delta M = m_{K\pi\pi_s} - m_{K\pi}$ of the D^* and D^0 candidate (analysis level).

of photoproduction, also on analysis level. For all investigated main open charm triggers the L3-FTT achieves a good efficiency of above 80%. Hereby the L3-FTT efficiency is defined as:

$$\epsilon_{FTT(i)} = \frac{N^{FTT(i)+\text{Analysis } i}(D^*)}{N^{\text{Analysis } i}(D^*)} \quad (\text{A.2})$$

In figure A.6 the efficiencies determined for the different data samples in DIS (s61) and in photoproduction (s83, s84) as well as the corresponding efficiencies obtained with the Monte Carlo generator AROMA are shown. As an example the ΔM distribution obtained with the analysis cut set 1 is shown in figure A.7a) and with an additional FTT(1) cut

scenario	$p_T(D^*)$ [GeV/c]	$p_T(K, \pi)$ [GeV/c]	$p_T(\pi_s)$ [GeV/c]	$ m(D^0) - m(K\pi) $ [GeV/c ²]	ΔM [GeV/c ²]
FTT(1)	> 1.2	> 0.25	> 0.1	< 0.25	< 0.18
Analysis 1	> 1.5	> 0.3	> 0.12	< 0.06	< 0.17
FTT(2)	> 1.8	> 0.3	> 0.1	< 0.2	< 0.18
Analysis 2	> 2.0	> 0.5	> 0.12	< 0.06	< 0.17
FTT(3)	> 2.2	> 0.4	> 0.13	< 0.2	< 0.17
Analysis 3	> 2.5	> 0.5	> 0.15	< 0.06	< 0.17
FTT(4)	> 4.5	> 0.5	> 0.15	< 0.2	< 0.17
Analysis 4	> 5.0	> 0.6	> 0.17	< 0.06	< 0.17

Table A.3: Different cut scenarios for the D^* selection on the FTT and the corresponding analysis cut scenarios. On analysis level a cut on the radial track length of the decay particles of $R > 15$ cm was applied for all scenarios.

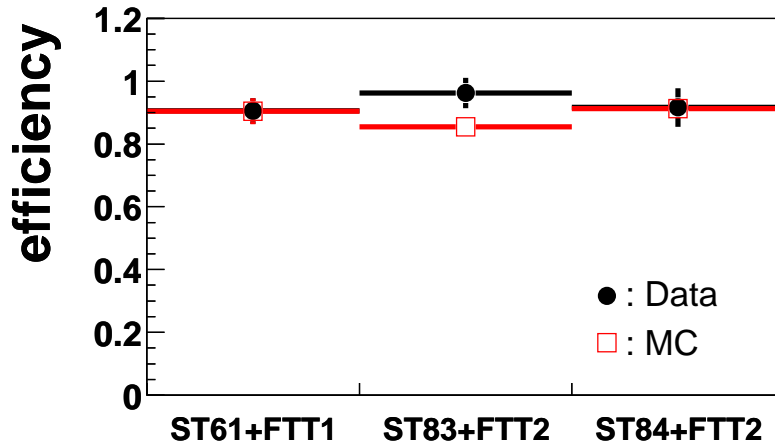


Figure A.6: Selection efficiency of the third FTT level for different subtrigger and cut scenarios. The dots indicate the data and the rectangles the Monte Carlo simulation. This study was done with offline preselected D^* data of the year 2000.

scenario in figure A.7b) for the DIS subtrigger s61. The corresponding D^0 -candidate mass distribution for the D^* signal region is presented in figure A.8a) and b). Both distribution look very well also after applying the FTT(1) scenario. In photoproduction a nice ΔM distribution is obtained if the FTT(2) scenario is applied (see figure A.7c) and d)), but the $m(D^0)$ distribution looks much worse, as can be seen from figures A.8c) and d). However it will not be possible to remove the $m(D^0)$ -cut for the FTT cut scenarios, since the rate would increase strongly.

The expected rate of the main open charm triggers depending on the different FTT cut scenarios is obtained from the unrescaled L1 subtrigger rate and the reduction factor obtained with a FTT cut scenario. Only L4 transparent runs were used for this study. L4 transparent means, that the L4 trigger is operational but does not reject any events. The rates obtained in such a way are illustrated in figure A.9. With the FTT(1) cut scenario the L1 trigger rate is reduced by a factor of more than 10. Since the quoted rates are for the year 2000 all values have to be scaled by a factor 5 to get the expected HERA II rates.

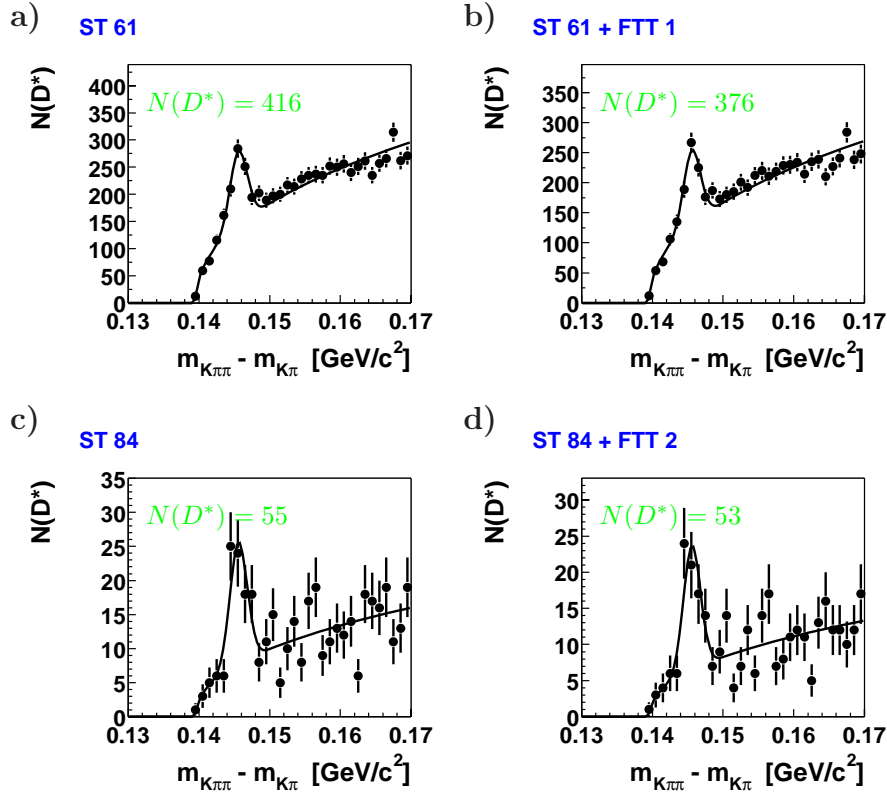


Figure A.7: ΔM distribution (analysis level) obtained for analysis cut 1 and s61 (a,b) and for analysis cut 2 and s84 (c,d) without and with corresponding FTT cut scenario.

All rates of the proposed FTT scenarios, FTT(1) for DIS (s61) and FTT(2) for tagged photoproduction (s83, s84, s108), are acceptable. Thus no prescaling should be needed in HERA II for these triggers if the FTT is used in addition.

Up to now, it is only possible to trigger at H1 D^* photoproduction events via tagged photoproduction events, where the scattered electron is identified in one of the electron taggers. These events have all very small photon virtualities, for example $Q^2 < 0.01 \text{ GeV}^2$ for the ET33. But the photoproduction regime is usually defined by $Q^2 < 1 \text{ GeV}^2$. Due to the limited Q^2 -range and the restricted y -acceptance of the electron taggers only a small fraction of all photoproduction events can be selected with the electron taggers. The trigger rate of an untagged photoproduction trigger is huge. Below some rate studies are presented concerning an untagged D^* photoproduction trigger using the FTT.

The starting point is the subtrigger s32, which requires only a certain number of tracks above a p_T threshold. Further a requirement on the z -position of the event vertex is applied. The L1 trigger rate of 500 Hz of s32 is very high and in HERA I it was strongly prescaled (averaged prescale factor of about 1600). Figure A.10a) shows the rate of the subtrigger s32 depending on the FTT cut scenarios, which are applied in addition. With the FTT(2) cut scenario the rate is reduced by more than a factor 25. And with the very hard FTT cut scenario FTT(4) the estimated rate is smaller than 1 Hz. All the indicated rates are obtained for the year 1997 and they have to be scaled with about a factor 5 (the

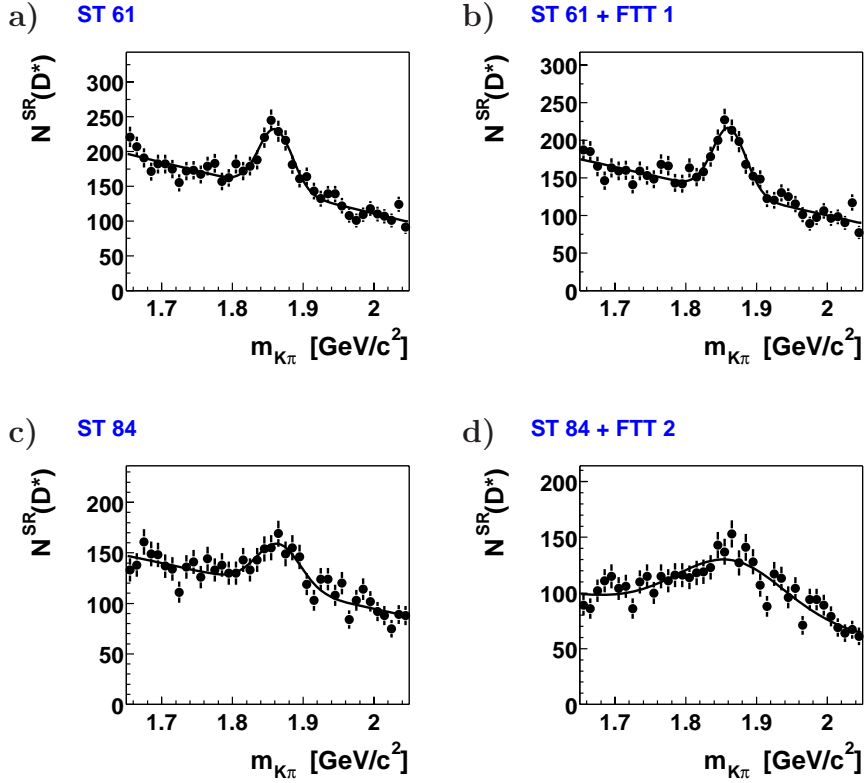


Figure A.8: $M(D^0)$ distribution (analysis level) obtained for analysis cut 1 and s61 (a,b) and for analysis cut 2 and s84 (c,d) without and with corresponding FTT cut scenario. For these plots no cut on the $m(D^0)$ was applied and only D^* events within the signal region (SR) were considered.

factor should be for 1997 slightly larger than for 2000 due to the smaller centr-of-mass energy in 1997) to get the expected HERA II rates. For this study the data of the year 1997 are used, since for this year more L4 transparent runs exist. From figure A.10b) it is clear that with the FTT(4) cut scenario only a very small fraction of the D^* events can be selected. A cut on the track topology of the event in addition to FTT(3), like at least one track with $\theta > 110^\circ$ (indicated as bwTr in the figure A.10a) can reduce the rate slightly without rejecting a huge D^* fraction, since most of the D^* -events are located centrally in the detector.

The triggering of D^* events in DIS and tagged photoproduction should be possible in HERA II without a prescaling if the FTT is used in addition. An untagged D^* photoproduction trigger should be possible without any prescale if the very hard cut scenario FTT4 is used. But to develop a D^* trigger in untagged photoproduction with a more relaxed FTT cut scenario further information from other detector components like the LAr are needed to reduce the rate further. Nevertheless, the strong rate reduction by using the FTT allows to consider the development of such a trigger.

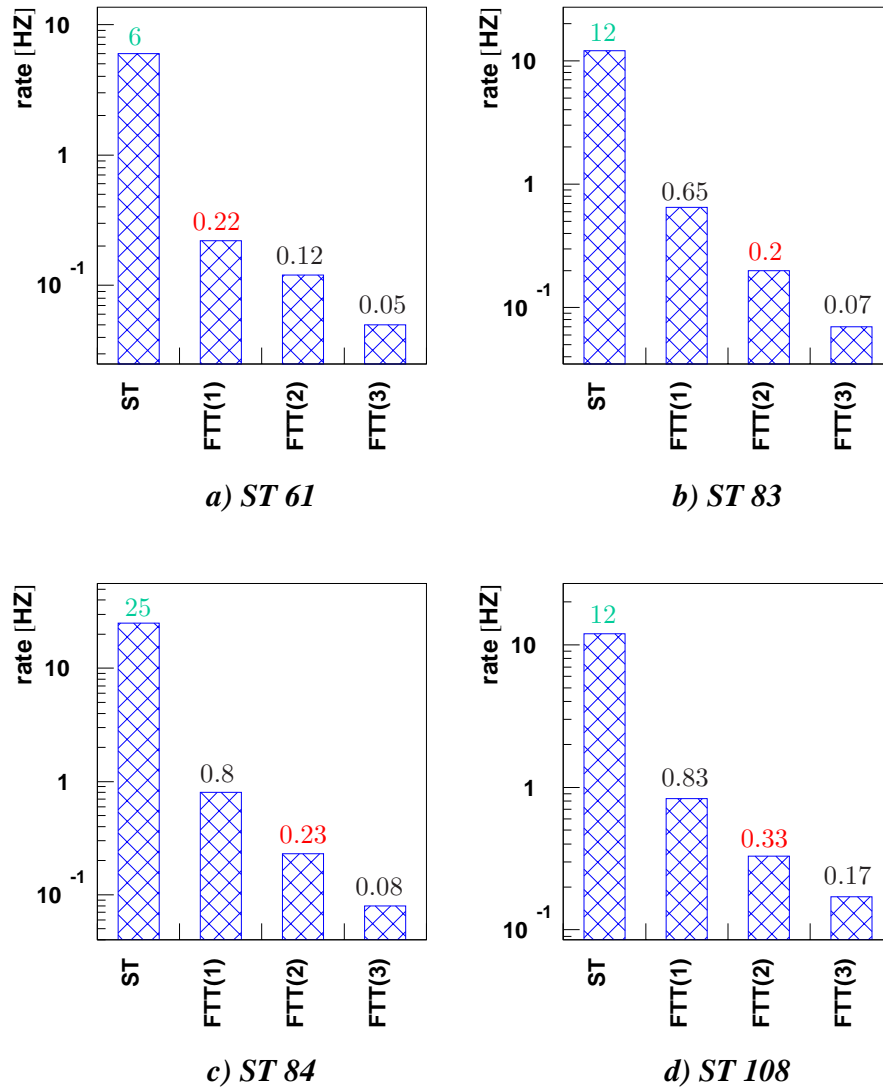


Figure A.9: Trigger rates determined without and with FTT cut scenarios for the subtriggers 61, 83, 84 and 108. Since the trigger rates are indicated for the year 2000 all rates have to be scaled with a factor 5 to get the expected HERA II rates.

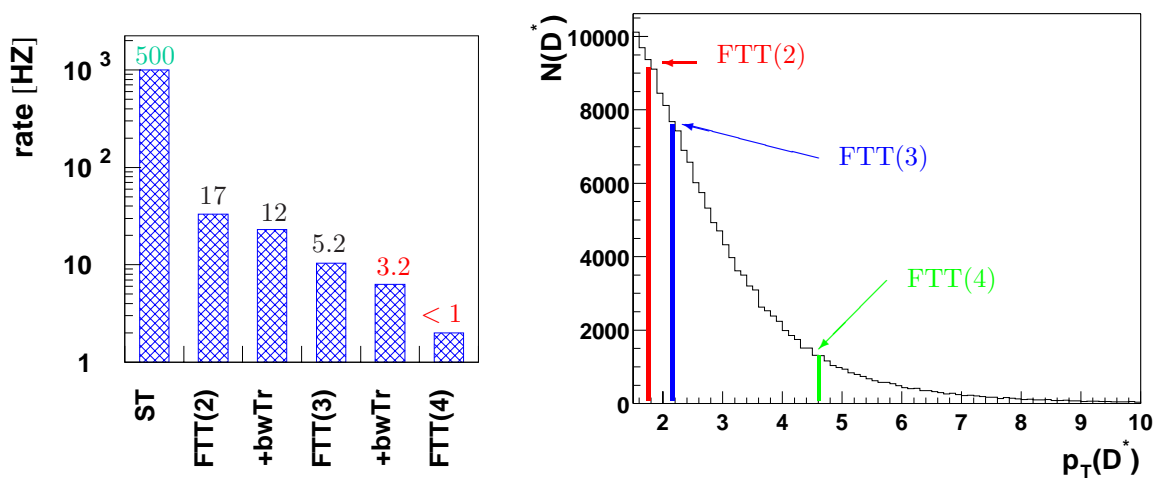


Figure A.10: *Left: Untagged D^* trigger rates depending on several FTT cut scenarios. bwTr indicates the additional requirement of at least one track with $\theta > 110^\circ$. The rates are given for the year 97, and to obtain the expected HERA II rates all values have to be scaled with about a factor 5. Right: Generated transverse momentum distribution of D^* -mesons, as obtained by the AROMA Monte Carlo simulation.*

Appendix B

Track and Muon Selection

B.1 Track Selection

Tracks matching the criteria listed in table B.1 are used in this analysis as basic selection for muon candidates.

central tracks	
Transverse momentum of the track	$p_T > 0.1 \text{ GeV}/c$
Polar angle of the track	$20^\circ < \theta < 160^\circ$
Minimal distance of the track with respect to the primary vertex	$ d'_{ca} < 2.0 \text{ cm}$
Radial distance of the first hit with respect to the origin	$R_{Start} < 50 \text{ cm}$
Radial track length	$R > 10 \text{ cm}$ for $\theta \leq 150^\circ$ $R > 5 \text{ cm}$ for $\theta > 150^\circ$

Table B.1: *Cuts of the track selection*

B.2 Muon Selection

Muon candidates matching the criteria listed in table B.2 are used in this analysis.

Forward endcap		Backward endcap	
ρ_x	< 100 cm	ρ_x	< 100 cm
ρ_y	< 100 cm	ρ_y	< 100 cm
N_{Layer}	≥ 6	N_{Layer}	≥ 3
$i_{first\ layer}$	≤ 5	$i_{first\ layer}$	≤ 8
$i_{last\ layer}$	≥ 6	$i_{last\ layer}$	≥ 3
Barrel		Calorimeter muons	
ρ	< 100 cm	μ -quality	≥ 2
z_0	< 100 cm	Separation angle	$> 12^\circ$
N_{Layer}	≥ 2		
$i_{first\ layer}$	≤ 5		
$i_{last\ layer}$	≥ 2		

Table B.2: *Cuts of the muon selection*

The meaning of the abbreviations is:

- ρ, ρ_x, ρ_y : Radial distance of the extrapolated iron track with respect to the event vertex as well as its x- and y-component
- z_0 : z-coordinate at the starting point of the iron track
- $i_{first\ layer}, i_{last\ layer}$: Number of the first or last hit layer in the muon chambers in the instrumented iron
- N_{Layer} : Number of hit layers in the muon chambers in the instrumented iron

Appendix C

Maximum Likelihood Method

For the two dimensional fit used in this analysis for the separation of charm and beauty events a negative log-likelihood function F has to be minimised. Here the formula of F will be derived.

The measured number of events in an interval of a differential distribution has a Poisson distribution, which is given by:

$$P_{\mu}(r) = \frac{\mu^r e^{-\mu}}{r!} \quad (\text{C.1})$$

The Poisson distribution gives the probability, that a certain event appears exactly r -times, if μ is the mean value. The variance $V = \sigma^2$ is equal to μ .

In general the data can depend on several variables. Below the special case of two variables i and j is considered. In this analysis i corresponds to the mass difference ΔM of the D^* and D^0 -candidate and j stands for a separation variable. The probability, that $r(i, j)$ events in an interval (i, j) are measured, is given by the Poisson distribution $P_{\mu(i, j)}(r(i, j))$ with the mean value $\mu(i, j)$. The overall probability, that in all intervals the corresponding event numbers $r(i, j)$ are obtained in a measurement, is then given by the product:

$$L = P_{\mu(1,1)}(r(1,1)) \cdot P_{\mu(1,2)}(r(1,2)) \cdot \dots \cdot P_{\mu(n,m)}(r(n,m)), \quad (\text{C.2})$$

Here n is the number of bins in the variable i and m the number of intervals of the quantity j .

If a function should be fitted to the data, the function L has to be maximised. For this purpose the mean value μ has to be described by a suitable function with free parameters \vec{a} , in this case $\vec{a} = (N_c, N_b, U(1), \dots, U(m))$. Here N_c or N_b is the number of D^* - μ -events from charm- or beauty-production respectively. $U(1), \dots, U(m)$ are parameters for the background. To emphasize, that the mean value μ depends on the free parameters, the mean values is indicated as $\mu^{\vec{a}}$ below. Usually the minimum of $-2 \ln(L(\vec{a}))$ is determined instead of $L(\vec{a})$. This is justified, since the logarithm is a monotonically increasing function.

$$F(\vec{a}) := -2 \cdot \ln(L(\vec{a})) = -2 \cdot \sum_{i,j} \ln \left(P_{\mu^{\vec{a}}(i,j)}(r(i,j)) \right) \quad (\text{C.3})$$

Each term of the sum is transformed as follows:

$$-2 \cdot \ln(P_{\mu^{\vec{a}}}(r)) = 2 \cdot \left(\mu^{\vec{a}} - r \cdot \ln(\mu^{\vec{a}}) + \ln(r!) \right) \quad (\text{C.4})$$

The term $\ln(r!)$ is constant and can be omitted, since the minimum is not affected.

$$-2 \cdot \ln(P_{\mu^{\vec{a}}}(r)) = 2 \cdot \left(\mu^{\vec{a}} + r \cdot \ln\left(\frac{1}{\mu^{\vec{a}}}\right) \right) \quad (\text{C.5})$$

The second term in equation C.5 is zero, if $r = 0$. To obtain a function, which behaves asymptotically like a χ^2 function, the equation above is modified by constant contributions. The minimum is not affected by this and the following equation is obtained:

$$-2 \cdot \ln(P_{\mu^{\vec{a}}}(r)) = 2 \cdot \underbrace{\left[(\mu^{\vec{a}} - r) + r \ln\left(\frac{r}{\mu^{\vec{a}}}\right) \right]}_{:= F(\vec{a})} \quad (\text{C.6})$$

The total function $F(\vec{a})$, which has to be minimised, then is:

$$F(\vec{a}) = \sum_{i,j} F(i, j) \quad \text{with} \\ F(i, j) = 2 \cdot \left[(\mu - r) + r \ln\left(\frac{r}{\mu}\right) \right]. \quad (\text{C.7})$$

For $r = 0$ the second term is set to zero.

Appendix D

Unfolding Method

The unfolding method used in this analysis, is described in this section in more detail. Further information can be found in [108, 109].

The n measured histogram bin contents, given by the vector $\mathbf{y} = (y_1, ..y_n)$, are related to the true values, expressed by the vector $\mathbf{x} = (x_1, .., x_m)$, by the resolution matrix \mathbf{A} ($n \times m$):

$$\mathbf{Ax} = \mathbf{y} \tag{D.1}$$

The j -th row is the response on the j -th component of \mathbf{x} and can lead to a contribution in each component of \mathbf{y} . The matrix \mathbf{A} can be interpreted as a probability matrix. The sum of all elements within a row of the matrix \mathbf{A} is 1, which means “no loss of events”. Each element is the probability to yield an element in \mathbf{y} .

In practice the resolution matrix \mathbf{A} is obtained by the Monte Carlo simulation. Bins in the observed quantity and in the true quantity are defined. This gives the index-pair for the matrix \mathbf{A} and fills a two dimensional histogram. Each row is then normalised to one and the probability matrix \mathbf{A} is obtained.

Due to measurement errors σ_i , equation D.1 in general does not hold precisely. Residuals, indicated by the vector $\mathbf{r} = (r_1, ..r_i, .., r_n)$, different from zero are obtained. Equation D.1 is modified to:

$$\mathbf{r} = \mathbf{Ax} - \mathbf{y} \tag{D.2}$$

In this analysis the components of \mathbf{y} are the numbers of $D^*\mu$ -events, which are obtained from a D^* -fit. The assigned errors σ_i to the data y_i are obtained by the fit and thus not equal to the square root of the measured number of $D^*\mu$ -events. Therefore the best estimation for \mathbf{x} is obtained by applying the least square fit method. The sum of the squared error weighted residua $F(\mathbf{x}) = \sum(r_i^2/\sigma_i^2)$ has thus to be minimised. The sum $F(\mathbf{x})$ can be written via matrices as:

$$F(\mathbf{x}) = \mathbf{r}^T \mathbf{W} \mathbf{r} = (\mathbf{Ax} - \mathbf{y})^T \mathbf{W} (\mathbf{Ax} - \mathbf{y}) \tag{D.3}$$

\mathbf{W} is the weighting matrix and since the data are uncorrelated it is of the form:

$$\mathbf{W} = \begin{pmatrix} \frac{1}{\sigma_1^2} & 0 & \dots & 0 \\ 0 & \frac{1}{\sigma_2^2} & & 0 \\ \vdots & & \ddots & \vdots \\ 0 & \dots & & \frac{1}{\sigma_n^2} \end{pmatrix} \quad (\text{D.4})$$

The minimisation requirement of $F(\mathbf{x})$ can be mathematically formulated as:

$$\frac{\partial F}{\partial \mathbf{x}} = 0 \quad (\text{D.5})$$

Thus the minimisation of $F(\mathbf{x})$ leads to the solution of the linear equation system $\mathbf{C}\mathbf{x} = \mathbf{b}$:

$$\underbrace{(\mathbf{A}^T \mathbf{W} \mathbf{A})}_{\mathbf{C}} \mathbf{x} = \underbrace{\mathbf{A}^T \mathbf{W} \mathbf{y}}_{\mathbf{b}} \quad (\text{D.6})$$

$$\mathbf{C} \mathbf{x} = \mathbf{b} \quad (\text{D.7})$$

In the last step a new $m \times m$ -matrix $\mathbf{C} = \mathbf{A}^T \mathbf{W} \mathbf{A}$ and a new vector $\mathbf{b} = \mathbf{A}^T \mathbf{W} \mathbf{y}$ is defined. The formal solution $\mathbf{x} = \mathbf{C}^{-1} \mathbf{b}$ often shows large fluctuations.

An improved solution is based on the orthogonal decomposition $\mathbf{C} = \mathbf{U} \mathbf{D} \mathbf{U}^T$ ($\mathbf{U}^T \mathbf{U} = \mathbf{1}$) of the matrix \mathbf{C} . The rows of the matrix \mathbf{U} are the eigenvectors of the matrix \mathbf{C} and the elements of the diagonal matrix \mathbf{D} are the eigenvalues λ_i of the matrix \mathbf{C} . The eigenvalues in \mathbf{D} are sorted in order of decreasing value in the procedure used in this analysis. Multiplying equation D.7 from left with \mathbf{U}^T leads to:

$$\begin{aligned} \mathbf{C} \mathbf{x} &= \mathbf{b} \\ \Leftrightarrow \mathbf{U} \mathbf{D} \mathbf{U}^T \mathbf{x} &= \mathbf{b} && | \cdot \mathbf{U}^T \text{ from left} \\ \Rightarrow \mathbf{D} \underbrace{(\mathbf{U}^T \mathbf{x})}_{\mathbf{z}} &= \underbrace{(\mathbf{U}^T \mathbf{b})}_{\mathbf{c}} \end{aligned} \quad (\text{D.8})$$

$$\mathbf{D} \mathbf{z} = \mathbf{c} \quad (\text{D.9})$$

\mathbf{U} can be interpreted as a rotation matrix. The vectors $\mathbf{c} = \mathbf{U}^T \mathbf{b}$ and $\mathbf{z} = \mathbf{U}^T \mathbf{x}$ are the rotated vector \mathbf{b} and the rotated solution vector \mathbf{x} . The coefficients c_i are the scalar product of the i -th eigenvector \mathbf{u}_i and the vector \mathbf{b} : $c_i = \mathbf{u}_i \mathbf{b}$.

Due to the diagonal matrix in equation D.9 each coefficient z_i of the transformed solution vector \mathbf{x} is directly connected to the i -th coefficient c_i of vector \mathbf{c} :

$$z_i = \frac{c_i}{\lambda_i} \quad i = 1..m \quad (\text{D.10})$$

Since the eigenvalues are in these equations in the denominator, the values of z_i can become very large for small eigenvalues and with that the statistical fluctuation of the coefficient c_i is magnified. Eventually, for very small eigenvalues (corresponding to large i), the final result $\mathbf{x} = \mathbf{U} \mathbf{z}$ will be dominated by one or a few of the coefficients z_i with small eigenvalues and large statistical errors, and the complete result is unsatisfactory.

The solution of this problem is to omit the small λ_i . This is equivalent to setting z_i to zero for large i . This is possible, since the eigenvalues are sorted by the order of decreasing values. The last "true" z_i are in general small and can be neglected. All coefficients z_i , for which the one standard deviation error of c_i is larger or equal to the value, can not be measured and should be set to zero. This leads to the transformed solution vector $\mathbf{z} = (z_1, z_2, \dots, z_k, 0, \dots, 0)$. \mathbf{x} is then obtained via:

$$\mathbf{x} = \mathbf{U}\mathbf{z} \quad (\text{D.11})$$

The error matrix of the solution vector \mathbf{x} of a linear transformation $\mathbf{A}\mathbf{x} = \mathbf{y}$ is always [100]:

$$\mathbf{V}(\mathbf{x}) = (\mathbf{A}^T \mathbf{W} \mathbf{A})^{-1} = \mathbf{C}^{-1} \quad (\text{D.12})$$

In the rotated system the error matrix of the transformed solution vector \mathbf{z} is given by the inverse of diagonal matrix, in which the diagonal elements from V_{ii} are set to zero for $k < i \leq m$:

$$\mathbf{V}(\mathbf{z}) = \mathbf{D}^{-1} = \begin{pmatrix} \frac{1}{\lambda_1} & 0 & \dots & 0 \\ & \cdot & & \\ \vdots & \frac{1}{\lambda_k} & & \vdots \\ & & 0 & \\ 0 & \dots & & 0 \end{pmatrix} \quad (\text{D.13})$$

The rank of the matrix $\mathbf{V}(\mathbf{z})$ is k and thus smaller than m . The error matrix of \mathbf{x} is then obtained by backtransformation of \mathbf{D}^{-1} :

$$\mathbf{V}(\mathbf{x}) = \mathbf{U}\mathbf{D}^{-1}\mathbf{U}^T \quad (\text{D.14})$$

The rank of $\mathbf{V}(\mathbf{x})$ is again equal to k and therefore smaller than m . This leads to large positive correlations between adjacent coefficients x_i .

These large positive correlations can be avoided, if the final transformation uses not all initially made bins n in the data, but a number of bins, which corresponds to the degrees of freedom k . Thus only a limited number of bins can be obtained in a measurement with large migration effects. The standard deviations of the data points are almost unchanged due to the positive correlations. But the error matrix is of full-rank and has only small correlations. Practically the reduction of bins is achieved by averaging each two neighbour bins: $1/2(x_1 + x_2)$, $1/2(x_3 + x_4)$,

It is clear that some resolution is lost due to the necessary bin reduction. Thus the number of used bins n should be twice the number of desired bins k in the unfolded distribution.

List of Figures

1.1	<i>ep</i> scattering Feynman diagrams	4
1.2	Examples for loops in QCD	7
1.3	Principle of factorisation	8
1.4	p structure at different scales	9
1.5	Gluon splitting	10
1.6	General gluon ladder	10
1.7	Summation of all considered gluon ladders	11
1.8	Angular ordering of emitted gluon in the CCFM evolution model	12
1.9	CCFM: angular ordering	12
1.10	CCFM gluon ladder	13
1.11	Contributions of the non-Sudakov form factor	16
1.12	Comparison of evolution paths in the DGLAP and CCFM approach	17
1.13	Different states of a quasi real photon	18
1.14	Illustration of the factorisation for heavy quark production in case of photoproduction	19
1.15	Different regimes of heavy flavour production	21
1.16	LO BGF Feynman diagrams	21
1.17	LO BGF cross section	23
1.18	Feynman diagrams for the resolved process	23
1.19	Virtual corrections considered in NLO calculations	24
1.20	Gluon radiation corrections considered in NLO calculations	24
1.21	Feynman diagrams in the massive scheme	26
1.22	Feynman diagrams in the massless scheme	26
1.23	Illustration of the NLO accuracy	27

1.24	Comparison between collinear and k_T factorisation	27
1.25	k_T dependence of the heavy quark cross section within the k_T -factorisation	28
1.26	Illustration of independent fragmentation and Peterson function	29
1.27	Illustration of the Lund string fragmentation	31
2.1	Principle of double tagging	33
2.2	Possible charge and angle correlation for charm events in the γg rest frame	37
2.3	Possible charge and angle correlations for beauty events in the γg rest frame	38
2.4	$\Delta\Phi(D\bar{D})$ - and $p_T^2(D\bar{D})$ -distribution for charm production in γN -collisions obtained by E687	40
2.5	Elements of an ep event generator	41
2.6	Muon momentum spectrum in the rest frame of a charm hadron as obtained from the Monte Carlo	44
2.7	Muon momentum spectra in the rest frame of a beauty hadron as obtained from the Monte Carlo	45
2.8	Correlations of the angles and the momenta of the $D^*\mu$ -pair from a b hadron decay	46
2.9	Correlation between the transverse momentum of the D^* and the momen- tum of the muon	49
2.10	Correlation between the pseudorapidities of the D^* and the muon	49
2.11	Differential distributions of the D^* -meson and the muon in photoproduction for charm events	51
2.12	Differential distributions of the D^* -meson and the muon in photoproduction for beauty events	52
2.13	Contributions to the heavy quark cross section up to NLO	54
2.14	Correlation of x_g , k_T and \bar{q}'_t reconstructed via the quark and via the $D^*\mu$ quantities	56
3.1	The HERA collider and its pre-accelerators	58
3.2	Construction of the H1 detector	60
3.3	Cross section view of the CJC	63
3.4	Construction of the central silicon tracker CST	64
3.5	Cross section view of the spaghetti type calorimeter SpaCal	65
3.6	Layout of the modules of the instrumented iron	66
3.7	Cross section of the central muon detector	67

3.8	Cross section view of the basic chamber unit	67
3.9	Overview of the trigger system	68
4.1	Z-vertex trigger	73
4.2	Invariant mass of the D^0 candidates	79
4.3	Mass difference for D^* candidates	81
4.4	Muon quality for $D^*\mu$ events in photoproduction	84
4.5	Illustration of a $D^*\mu$ candidate belonging to the third correlation region . .	87
4.6	Illustration of a $D^*\mu$ candidate belonging to the second correlation region .	87
4.7	Mass difference ΔM for $D^*\mu$ candidates ($D^* \rightarrow D^0\pi_s \rightarrow K\pi\pi_s$)	88
4.8	Mass difference ΔM for $D^*\mu$ candidates ($D^* \rightarrow D^0\pi_s \rightarrow K^0\pi\pi\pi_s$)	89
5.1	Number of $D^*\mu$ events depending on the trigger combinations of the photoproduction sample	92
5.2	Muon quality of $D^*\mu$ events	94
5.3	Link probability of the muons in $D^*\mu$ events	94
5.4	Reweighting of photoproduction $D^*\mu$ samples in the Monte Carlo simulation	95
5.5	Description of the photoproduction variables in the inclusive D^* sample . .	96
5.6	Description of the photoproduction variables in the final $D^*\mu$ sample	97
5.7	Description of the DIS variables in the inclusive D^* sample	98
5.8	Description of the DIS variables in the $D^*\mu$ sample	99
5.9	Event variables of the photoproduction $D^*\mu$ sample	100
5.10	Description of the kaon variables in the inclusive D^* photoproduction sample	101
5.11	Description of the kaon variables in the $D^*\mu$ photoproduction sample	102
5.12	Description of the D^* variables in the inclusive D^* and $D^*\mu$ photoproduction sample	104
5.13	Description of the muon variables in the $D^*\mu$ photoproduction sample . . .	105
5.14	Description of the combined $D^*\mu$ variables in the $D^*\mu$ photoproduction sample	106
5.15	Muon mis-identification probabilities in D^* -events	109
6.1	Population of the four correlation regions in the photoproduction sample . .	111
6.2	The four correlation regions for direct and excitation charm photoproduction	112

6.3	Correlation between reconstructed and generated $\Delta\Phi$	113
6.4	Correlation between reconstructed $\Delta\Phi$ and $\Delta\Phi^*$	113
6.5	Population of the four correlation regions in the photoproduction + DIS-sample	114
6.6	ΔM distribution of the photoproduction data together with the function obtained from the two dimensional fit	117
6.7	ΔM distribution of the total data set together with the function obtained from the two dimensional fit	118
6.8	Population of the correlation regions in the photoproduction data set	119
6.9	Population of the correlation regions in the photoproduction + DIS data set	120
6.10	Control distributions of the photoproduction data	122
6.11	Control distributions of the total data set	123
6.12	Check of the excitation resolved contribution in the photoproduction data. .	124
6.13	Decay length $r(D^0)$ (in the $r\phi$ -plane) in an event with b hadron	125
6.14	Lifetime of the D^0 -meson obtained for the photoproduction data, separately for correlation region 2+3 and 4	126
6.15	Result of the two dimensional fit using the lifetime of the D^0 -meson	127
6.16	Result of a two dimensional fit using ΔR as separation variable (photoproduction data)	128
7.1	Comparison of the measured b -cross section with other HERA results	140
8.1	ΔM distribution in bins of $p_T^*(D^*\mu)$ for the photoproduction data	144
8.2	Muon background correction factors for the $D^*\mu$ -variables in photoproduction	145
8.3	Differential distributions of the $D^*\mu$ -variables in photoproduction after muon background correction	146
8.4	Result of the two dimensional fit for the two bins of $M(D^*\mu)$, $\hat{y}(D^*\mu)$ and $p_T^*(D^*\mu)$	148
8.5	Differential $D^*\mu$ -distributions for charm and beauty production for the total data set	149
8.6	Efficiencies of the L4 muon finder and of the $f_{ET}(D^*\mu)$ cut for the photoproduction sample	151
8.7	Reconstruction, trigger and L4 efficiencies as a function of $M(D^*\mu)$ for the photoproduction sample	152
8.8	Total efficiencies as a function of $M(D^*\mu)$ for the photoproduction sample .	152

8.9	Normalised differential visible $D^*\mu$ cross sections (c+b) for photoproduction	156
8.10	Normalised differential visible $D^*\mu$ charm and beauty production cross sections	157
9.1	Correction factors for the observed quantity $\log_{10}(x_g(D^*\mu))$, inclusive as well as in bins of $p_T^*(D^*\mu)$ and $\vec{q}_t'(D^*\mu)$	160
9.2	Differential distributions of the observed quantity $\log_{10}(x_g(D^*\mu))$, inclusive as well as in bins of $p_T^*(D^*\mu)$ and $\vec{q}_t'(D^*\mu)$	161
9.3	Quality of the unfolding for $x_g(D^*\mu)$	162
9.4	Combined efficiency for x_g	164
9.5	Differential cross sections for the gluon variables	165
9.6	Extracted gluon density	167
10.1	D^*D^* double tagging	171
A.1	Illustration of the wire layers in the CJC used for the FTT	173
A.2	Illustration of three trigger groups as used for the FTT	174
A.3	D^* momentum and angular resolution obtained with the FTT	176
A.4	Resolution of the invariant mass of the D^0 -candidate obtained with the FTT	177
A.5	Resolution of the mass difference of the D^* and D^0 -candidate obtained with the FTT	177
A.6	Selection efficiency of the L3-FTT for different subtriggers and cut scenarios	178
A.7	ΔM distribution obtained with and without FTT cut scenario	179
A.8	$M(D^0)$ distribution obtained with and without FTT cut scenario	180
A.9	Trigger rates determined without and with FTT cut scenarios	181
A.10	Untagged D^* trigger rates depending on the FTT cut scenarios	182

List of Tables

1.1	Peterson parameter for D^* meson	30
2.1	Decay channels and branching ratios of D^{*+} -mesons	34
2.2	Decay channels and branching ratios of D^0 -mesons	34
2.3	Important branching ratios used in the Monte Carlo simulation	43
2.4	Fractions of the different beauty scenarios used in the Monte Carlo simulation	43
2.5	Predicted cross sections for inclusive charm and beauty production from the PYTHIA Monte Carlo generator	48
2.6	Contributions of the three different beauty decay scenarios depending on the correlation regions	50
2.7	Contributions of the three different beauty decay scenarios in each correla- tion region	53
3.1	Overview of trigger levels L4 and L5 in 1997 to 2000	70
4.1	Data samples used in this analysis	71
4.2	Integrated luminosity before and after applied corrections	72
4.3	Integrated luminosity	72
4.4	Definition and mean prescale factors of the relevant subtriggers	73
4.5	Trigger elements of the subtriggers used in this analysis	74
4.6	Overview of L4-finders used in this analysis	77
4.7	Selection of the inclusive D^* data sets	80
4.8	Purity and efficiency depending on the muon qualities for $D^*\mu$ events . . .	85
4.9	Selection of the final $D^*\mu$ data sets	86
4.10	Fit parameters of the ΔM distribution for both $D^*\mu$ data sets	88
5.1	Weights of the Monte Carlo simulation for the two finder preconditions . . .	93

6.1	Different contributions of the two $D^*\mu$ samples	112
6.2	Population and muon background of the correlation regions	114
6.3	Number of $D^*\mu$ events from charm and beauty production as well as the beauty fraction in the selected two data samples	121
6.4	Comparison of different fit methods	129
7.1	Visible range of the total $D^*\mu$ cross sections	130
7.2	Definition of total cross sections	131
7.3	Efficiencies of the trigger elements used in this analysis	133
7.4	Efficiencies of the used L4-finders	134
7.5	Efficiencies of the cut on the relative transverse energy of the $D^*\mu$ -pair . . .	135
7.6	Total visible $D^*\mu$ cross sections in photoproduction	135
7.7	Total visible $D^*\mu$ cross sections in $\gamma p + \text{DIS}$	136
7.8	Relative systematic errors of the total visible charm and beauty cross sections	138
7.9	Total visible $D^*\mu$ -cross section for c and b production in γp in comparison with Monte Carlo predictions and NLO calculations	141
7.10	Total visible $D^*\mu$ -cross section for c and b production in $\gamma p + \text{DIS}$ in comparison with Monte Carlo predictions	142
8.1	Fit result of the differential $D^*\mu$ variables	147
8.2	Relative systematic errors of the normalised differential visible cross sections	154
9.1	Correlation coefficients between the various bins	163
A.1	Wire layers used by the FTT	173
A.2	L1 trigger rates of the main triggers for open charm analyses	175
A.3	Different D^* cut scenarios for the FTT	178
B.1	Cuts of the track selection	183
B.2	Cuts of the muon selection	184

Bibliography

- [1] F. Abe *et al.* (CDF Collaboration), *Inclusive J/ψ , $\psi(2S)$ and b Quark Production in $p\bar{p}$ Collisions at $\sqrt{s} = 1.8$ TeV*, Phys. Rev. Lett. **69** (1992) 3704–3708.
- [2] F. Abe *et al.* (CDF Collaboration), *J/ψ and $\psi(2S)$ Production in $p\bar{p}$ Collisions at $\sqrt{s} = 1.8$ TeV*, Phys. Rev. Lett. **79** (1997) 572–577.
- [3] S. Abachi *et al.* (D0 Collaboration), *Inclusive μ and b Quark Production Cross-Sections in $p\bar{p}$ Collisions at $\sqrt{s} = 1.8$ TeV*, Phys. Rev. Lett. **74** (1995) 3548–3552.
- [4] S. Abachi *et al.* (D0 Collaboration), *J/Ψ Production in $p\bar{p}$ Collisions at $\sqrt{s} = 1.8$ TeV*, Phys. Lett. **B370** (1996) 239–248.
- [5] J. Breitweg *et al.* (ZEUS Collaboration), *Measurement of Open Beauty Production in Photoproduction at HERA*, Eur. Phys. J. **C18** (2001) 625–637, [hep-ex/0011081](#).
- [6] C. Adloff *et al.* (H1 Collaboration), *Measurement of Open Beauty Production at HERA*, Phys. Lett. **B467** (1999) 156–164, [hep-ex/9909029](#).
- [7] H1 Collaboration, *Measurement of Beauty production at HERA using semi-muonic decays*, July 2003.
- [8] S. Chekanov *et al.* (ZEUS Collaboration), *Beauty photoproduction measured using decays into muons in dijet events in ep collisions at $\sqrt{s} = 318$ GeV*, 2003, [hep-ex/0312057](#).
- [9] M. Acciarri *et al.* (L3 Collaboration), *Measurements of the Cross Sections for Open Charm and Beauty Production in $\gamma\gamma$ Collisions at $\sqrt{s} = 189 - 202$ GeV*, Phys. Lett. **B503** (2001) 10–20, [hep-ex/0011070](#).
- [10] A. Csilling (OPAL Collaboration), *Charm and Bottom Production in Two-Photon Collisions with OPAL*, 2000, [hep-ex/0010060](#).
- [11] H1 Collaboration, *Beauty Production in Deep Inelastic ep Scattering*, July 2001.
- [12] ZEUS Collaboration, *Measurement of beauty production in deep inelastic scattering at HERA*, July 2002.
- [13] I. Abt *et al.* (HERA-B Collaboration), *Measurement of the b anti- b production cross section in 920-GeV fixed-target proton nucleus collisions*, Eur. Phys. J. **C26** (2003) 345–355, [hep-ex/0205106](#).

- [14] H1 Collaboration, *Inclusive D^* Meson and Associated Dijet Production in Deep Inelastic Scattering*, April 2003.
- [15] S. Chekanov *et al.* (ZEUS Collaboration), *Dijet angular distributions in photoproduction of charm at HERA*, Phys. Lett. **B565** (2003) 87–101, hep-ex/0302025.
- [16] P. L. Frabetti *et al.* (E687 Collaboration), *Studies of D anti- D correlations in high-energy photoproduction*, Phys. Lett. **B308** (1993) 193–199.
- [17] S. Frixione, M. L. Mangano, P. Nason and G. Ridolfi, *Heavy-Quark production*, Adv. Ser. Direct. High Energy Phys. **15** (1998) 609–706, hep-ph/9702287.
- [18] J. M. Link *et al.* (FOCUS Collaboration), *Studies of correlations between D and anti- D mesons in high energy photoproduction*, Phys. Lett. **B566** (2003) 51–60, hep-ex/0305018.
- [19] G. Altarelli and G. Parisi, *Asymptotic Freedom in Parton Language*, Nucl. Phys. **B126** (1977) 298–318.
- [20] M. Ciafaloni, *Coherence Effects in Initial Jets at Small Q^2/s* , Nucl. Phys. **B296** (1988) 49.
- [21] S. Catani, F. Fiorani and G. Marchesini, *QCD Coherence in Initial State Radiation*, Phys. Lett. **B234** (1990) 339.
- [22] C. Adloff *et al.* (H1 Collaboration), *Forward Jet and Particle Production at HERA*, Nucl. Phys. **B538** (1999) 3–22, hep-ex/9809028.
- [23] B. Heinemann, *Measurement of Charged Current Cross Sections in Positron-Proton Collisions at $\sqrt{s} \simeq 300$ GeV*, Dissertation, Univers. Hamburg, December 1999.
- [24] P. Schmüser, *Feynman-Graphen und Eichtheorien für Experimentalphysiker*, Springer, Berlin/Heidelberg/New York, 2. edition, 1995.
- [25] S. Bethke, *Jet physics at LEP and world summary of $\alpha(s)$* , 1998, hep-ex/9812026.
- [26] E. A. Kuraev, L. N. Lipatov and V. S. Fadin, *The Pomeron Singularity in Nonabelian Gauge Theories*, Sov. Phys. JETP **45** (1977) 199–204.
- [27] I. I. Balitsky and L. N. Lipatov, *The Pomeron Singularity in Quantum Chromodynamics*, Sov. J. Nucl. Phys. **28** (1978) 822–829.
- [28] M. Kuhlen, *The Hadronic Final State in Deep Inelastic Scattering*, Springer, Berlin/Heidelberg/New York, 1999.
- [29] D. S. F. Lenz, H. Gießhammer, *Lectures on QCD - Applications*, Springer, Berlin/Heidelberg/New York, 1997.
- [30] H1 Collaboration, *Photoproduction of D^* Mesons at HERA*, April 2003.
- [31] ZEUS Collaboration, *Measurement of D^* photoproduction at HERA*, July 2002.
- [32] G. Marchesini and B. R. Webber, *Final states in heavy quark leptonproduction at small x* , Nucl. Phys. **B386** (1992) 215–235.

- [33] M. A. Kimber, J. Kwiecinski, A. D. Martin and A. M. Stasto, *The unintegrated gluon distribution from the CCFM equation*, Phys. Rev. **D62** (2000) 094006, hep-ph/0006184.
- [34] H. Jung, *What is CCFM? Why k_T -factorisation? Why and how all that?*, Talk in the ZEUS Student seminar, Winter Semester 2001/2002, URL <http://sesam.desy.de/seminar/jung.ps.gz>.
- [35] T. Greenshaw, *Forward jet and hadron production at low x and Q^2* Prepared for Ringberg Workshop: New Trends in HERA Physics 1999, Ringberg Castle, Tegernsee, Germany, 30 May - 4 Jun 1999.
- [36] G. Marchesini, *QCD coherence in the structure function and associated distributions at small x* , Nucl. Phys. **B445** (1995) 49–80, hep-ph/9412327.
- [37] H. Jung, *$k(t)$ -factorization and CCFM: The solution for describing the hadronic final states - everywhere?*, Mod. Phys. Lett. **A19** (2004) 1–18, hep-ph/0311249.
- [38] H. Jung and G. P. Salam, *Hadronic final state predictions from CCFM: The hadron-level Monte Carlo generator CASCADE*, Eur. Phys. J. **C19** (2001) 351–360, hep-ph/0012143.
- [39] M. Hansson and H. Jung, *Status of CCFM: Unintegrated gluon densities*, Mod. Phys. Lett. **A19**, hep-ph/0309009.
- [40] S. Frixione, M. L. Mangano, P. Nason and G. Ridolfi, *Improving the Weizsäcker-Williams approximation in electron - proton collisions*, Phys. Lett. **B319** (1993) 339–345, hep-ph/9310350.
- [41] M. Erdmann, *The Partonic Structure of the Photon*, volume 138 of *Springer Tracts in Modern Physics*, Springer, Berlin/Heidelberg/New York, 1997.
- [42] L. Stodolsky, *Hadronlike Behavior of γ , ν -Nuclear Cross Sections*, Phys. Rev. Lett. **18** (1967) 135–137.
- [43] B. W. Harris and J. Smith, *Heavy quark correlations in deep inelastic electroproduction*, Nucl. Phys. **B452** (1995) 109–160, hep-ph/9503484.
- [44] E. Laenen, S. Riemersma, J. Smith and W. L. van Neerven, *Complete $O(\alpha_s)$ corrections to heavy flavor structure functions in electroproduction*, Nucl. Phys. **B392** (1993) 162–228.
- [45] J. Smith and W. K. Tung, *Heavy flavor production*, NIKHEF-H-93-20.
- [46] R. K. Ellis, *Heavy Quark Production in QCD*, Invited talk given at Advanced Research Workshop on QCD Hard Hadronic Processes, St. Croix, Virgin Isl., October 8-13, 1987.
- [47] R. Brock *et al.* (CTEQ Collaboration), *Handbook of perturbative QCD, Version 1.1*, September 19994, FERMILAB-PUB-94-316.
- [48] J. Smith and W. L. van Neerven, *QCD corrections to heavy flavor photoproduction and electroproduction*, Nucl. Phys. **B374** (1992) 36–82.

- [49] S. Frixione, M. L. Mangano, P. Nason and G. Ridolfi, *Total cross-sections for heavy flavor production at HERA*, Phys. Lett. **B348** (1995) 633–645, hep-ph/9412348.
- [50] W.-K. Tung, S. Kretzer and C. Schmidt, *Open heavy flavor production in QCD: Conceptual framework and implementation issues*, J. Phys. **G28** (2002) 983–996, hep-ph/0110247.
- [51] S. Frixione, *Heavy quark photoproduction*, Nucl. Phys. Proc. Suppl. **79** (1999) 399–402, hep-ph/9905545.
- [52] S. P. Baranov *et al.*, *A phenomenological interpretation of open charm production at HERA in terms of the semi-hard approach*, Eur. Phys. J. **C24** (2002) 425–437, hep-ph/0203025.
- [53] ZEUS Collaboration, *Measurement of charm fragmentation function in D^* photoproduction at HERA*, July 2002.
- [54] LEP Heavy Flavour Working Group, *Input Parameters for the LEP/SLD Electroweak Heavy Flavour Results for Summer 1998 Conferences*, LEP note, January 1998, LEPHF/98-01, URL <http://lepewwg.web.cern.ch/LEPEWWG/heavy/lephf9801.ps.gz>.
- [55] ALEPH Collaboration, *Combining heavy flavour electroweak measurements at LEP*, Nucl. Instrum. Meth. **A378** (1996) 101–115.
- [56] C. Peterson, D. Schlatter, I. Schmitt and P. Zerwas, *Scaling Violations in Inclusive e^+e^- Annihilation Spectra*, Phys. Rev. **D27** (1983) 105.
- [57] P. Nason and C. Oleari, *A phenomenological study of heavy-quark fragmentation functions in e^+e^- annihilation*, Nucl. Phys. **B565** (2000) 245–266, hep-ph/9903541.
- [58] B. Andersson, G. Gustafson, G. Ingelman and T. Sjöstrand, *Parton Fragmentation and String Dynamics*, Phys. Rept. **97** (1983) 31.
- [59] D. E. Groom *et al.* (Particle Data Group), *Review of particle Physics*, Eur. Phys. J. **C15** (2000) 1–878.
- [60] L. Gladilin, *Charm Hadron Production Fractions*, 1999, hep-ex/9912064.
- [61] K. Ackerstaff *et al.* (OPAL Collaboration), *Measurement of $f(c \rightarrow D^{*+}X)$, $f(b \rightarrow D^{*+}X)$ and $\Gamma_{c\bar{c}}/\Gamma_{had}$ Using $D^{*\pm}$ -Mesons*, Eur. Phys. J. **C1** (1998) 439–459, hep-ex/9708021.
- [62] K. Hagiwara *et al.* (Particle Data Group), *Review of particle physics*, Phys. Rev. **D66** (2002).
- [63] T. Sjöstrand, *PYTHIA 5.7 and JETSET 7.4: Physics and manual*, 1995, hep-ph/9508391.
- [64] H. Jung, *Hard diffractive scattering in high-energy ep collisions and the Monte Carlo generator RAPGAP*, Comp. Phys. Commun. **86** (1995) 147–161.

- [65] A. Kwiatkowski, H. Spiessberger and H. J. Mohring, *HERACLES: An event Generator for ep Interactions at HERA Energies including radiative Processes: Version 1.0*, Comp. Phys. Commun. **69** (1992) 155–172.
- [66] H. Jung, *The CCFM Monte Carlo generator CASCADE*, Comput. Phys. Commun. **143** (2002) 100–111, hep-ph/0109102.
- [67] T. Sjöstrand, *High-Energy Physics Event Generation with PYTHIA 5.7 and JETSET 7.4*, Comput. Phys. Commun. **82** (1994) 74–90.
- [68] H. L. Lai *et al.* (CTEQ Collaboration), *Global QCD Analysis of Parton Structure of the Nucleon: CTEQ5 Parton Distributions*, Eur. Phys. J. **C12** (2000) 375–392, hep-ph/9903282.
- [69] M. Gluck, E. Reya and A. Vogt, *Photonic parton distributions*, Phys. Rev. **D46** (1992) 1973–1979.
- [70] B. W. Harris and J. Smith, *Charm Quark and $D^{*\pm}$ Cross Sections in Deeply Inelastic Scattering at HERA*, Phys. Rev. **D57** (1998) 2806–2812, hep-ph/9706334.
- [71] S. Frixione, P. Nason and G. Ridolfi, *Differential distributions for heavy flavor production at HERA*, Nucl. Phys. **B454** (1995) 3–24, hep-ph/9506226.
- [72] S. Frixione, M. L. Mangano, P. Nason and G. Ridolfi, *Heavy quark correlations in photon - hadron collisions*, Nucl. Phys. **B412** (1994) 225–259, hep-ph/9306337.
- [73] S. Frixione, M. L. Mangano, P. Nason and G. Ridolfi, *On the Determination of the Gluon Density of the Proton from Heavy Flavor Production at HERA*, Phys. Lett. **B308** (1993) 137–146, hep-ph/9304289.
- [74] H. Niggli, *Direct Gluon Density Determination in Tagged Charm-Photoproduction at HERA*, Dissertation, ETH Zürich, March 1998.
- [75] H1 Collaboration, *Silicon Tracker Home Page*, URL <http://www-h1.desy.de/h1det/tracker/sitracker/poster.html>.
- [76] H1 Collaboration, *H1 Track Detectors*, URL <http://www-h1.desy.de/h1/www/h1det/tracker/>.
- [77] H1 Collaboration, *Liquid Argon Calorimeter Homepage*, URL <http://www-h1.desy.de/h1/www/h1det/calor/lar/lar.html>.
- [78] H1 Collaboration, *SpaCal Homepage*, URL <http://www-h1.desy.de/h1/www/h1det/calor/spacal/>.
- [79] H1 Collaboration, *The Central Muon Detector of H1*, URL http://www-h1.desy.de/h1/www/h1det/muon/c_muon/digmuhome.html.
- [80] H1 Collaboration, *The H1 Forward Muon Detector*, URL http://www-h1.desy.de/h1/www/h1det/muon/f_muon/index.html.
- [81] I. Abt *et al.* (H1 Collaboration), *The H1 Detector at HERA*, Nucl. Instrum. Meth. **A386** (1997) 310–347.

- [82] I. Abt *et al.* (H1 Collaboration), *The Tracking, Calorimeter and Muon Detectors of the H1 Experiment at HERA*, Nucl. Instrum. Meth. **A386** (1997) 348–396.
- [83] H1 Collaboration, *The H1 detector at HERA*, URL <http://www-h1.desy.de/h1/www/h1det/list.html>.
- [84] D. Pitzl *et al.*, *The H1 Silicon Vertex Detector*, Nucl. Instrum. Meth. **A454** (2000) 334–349, [hep-ex/0002044](https://arxiv.org/abs/hep-ex/0002044).
- [85] R. D. Appuhn *et al.* (H1-SPACAL-Group), *The H1 Lead/Scintillating-Fibre Calorimeter*, Nucl. Instrum. Meth. **A386** (1997) 397–408.
- [86] C. Kleinwort and U.-P. Krueger, *Track Reconstruction in the Iron*, H1 internal software note, August 1992, H1-08/92-35.
- [87] H1 Collaboration, *H1REC: Reconstruction program*, URL <https://www-h1.desy.de/icas/imanuals/h1rec/h1rec9/h1rec.html>.
- [88] S. Egli *et al.*, *Calculating event weights in case of downscaling on trigger levels 1-4*, H1 internal note, April 1997, H1-04/97-517.
- [89] F. Jacquet and A. Blondel, *Detection and Study of the Charged Current Event*, in U. Amaldi (Hg.) *Study of an ep-Facility for Europe*, DESY, August 1979 391–396.
- [90] J. Marks, *HFS*, URL <http://www-h1.desy.de/~marks/hfs/hfs.html>.
- [91] T. Kuhr, *Messung des Wirkungsquerschnittes von b-Quark-Produktion in tief-unelastischer Elektron-Proton-Streuung bei H1*, Dissertation, Univers. Hamburg, September 2002.
- [92] D. Dünkemann, *Wirkungsquerschnitte für Photoproduktion von D*-Mesonen in ep-Wechselwirkungen am H1-Experiment bei HERA*, Diplomarbeit, Univers. Hamburg, June 2001.
- [93] L. West, *How to use the Heavy Flavour Working Group Track, Muon and Electron selection Code*, H1 internal software manual, 2000.
- [94] B. Naroska *et al.*, *Lepton Identification in the H1 Detector at Low Momenta*, H1 internal note, May 1997, H1-05/97-518.
- [95] M. Göttlich, *Messung von Wirkungsquerschnitten fuer die Produktion von D*-Mesonen über den Zerfall $D^{*+} \rightarrow D^0\pi^+ \rightarrow \bar{K}^0\pi^+\pi^-\pi^+$ beim H1 Experiment*, Diplomarbeit, Univers. Hamburg, March 2003.
- [96] J. Abbiendi *et al.* (ZEUS Collaboration), *Measurement of Inclusive $D^{*\pm}$ and Associated Dijet Cross Sections in Photoproduction at HERA*, Eur. Phys. J. **C6** (1999) 67–83, [hep-ex/9807008](https://arxiv.org/abs/hep-ex/9807008).
- [97] P. Fleischmann, *Elastic J/Ψ Production at HERA*, Dissertation, Univers. Hamburg, May 2004.
- [98] U. Langenegger, *A Measurement of the Beauty and Charm Production Cross Sections at the ep Collider HERA*, Dissertation, ETH Zürich, April 1998.

- [99] J. Kroseberg, *A Measurement of the Beauty Production in High-Energy Positron-Proton Scattering*, Dissertation, ETH Zürich, December 2002.
- [100] V. Blobel and E. Lohrmann, *Statistische und numerische Methoden der Datenanalyse*, Teubner, Stuttgart/Leipzig, 1998.
- [101] ZEUS Collaboration, *Measurement of open beauty production at HERA using a D^* +muon tag*, July 2002.
- [102] ZEUS Collaboration, *Measurement of open beauty production at HERA using a D^* +muon tag*, July 2003.
- [103] K. Krüger, *Photoproduction of J/Ψ Mesons at Medium and Low Elasticities at HERA*, Dissertation, Univers. Hamburg, April 2001.
- [104] M. Erdmann, *Untersuchung der Photoproduktion von D^* -Mesonen am ep-Speichering HERA*, Dissertation, ETH Zürich, January 1996.
- [105] S. Hengstmann, *A Measurement of Diffractive Charm Production at HERA*, Dissertation, Universität Zürich, 2000.
- [106] N. Gogitidze *et al.*, *An Offline Luminosity Determination for the 1995 e^+p Data*, H1 internal note, Februar 1996, H1-02/96-471.
- [107] S. Frixione and P. Nason, *Phenomenological study of charm photoproduction at HERA*, JHEP **03** (2002) 053, hep-ph/0201281.
- [108] V. Blobel, *An unfolding method for high energy physics experiments*, Contribution to Conference on Advanced Statistical Techniques in Particle Physics, Durham, September 2002, URL <http://www.desy.de/~blobel/punfold.ps>.
- [109] V. Blobel, *Comments on χ^2 minimisation*, Talk at PHYSTAT, September 2003, URL <http://www.desy.de/~blobel/Tcommchi.pdf>.
- [110] E. Lohrmann, *Hochenergiephysik*, Teubner, Stuttgart, 1992.
- [111] G. Hoffstaetter, Talk in the HERA status seminar, January 2002.
- [112] C. Wissing, *Entwicklung eines Simulationsprogramms und Implementierung schneller Spurfitalgorithmen für den neuen H1-Driftkammertrigger*, Dissertation, Univers. Dortmund, March 2003.
- [113] A. Baird *et al.*, *A fast high resolution track trigger for the H1 experiment*, IEEE Trans. Nucl. Sci. **48** (2001) 1276–1285, hep-ex/0104010.
- [114] S. Baird *et al.*, *A Fast Track Trigger with High Resolution for H1*, H1 internal note, June 1996, H1-06/99-573.
- [115] S. Baird *et al.*, *Addendum to the proposal: A Fast Track Trigger with High Resolution for H1*, H1 internal note, September 1999, H1-09/99-576.

Acknowledgments

I wish to express my gratitude to all who supported me in analysing the data, writing this thesis or in other way. Especially I wish to thank Prof. Dr. Naroska for offering me the opportunity to work as a PhD. student for the H1 experiment and for the support, especially during the last months. PD Dr. Elsen I wish to thank for his rediness to examine this work.

Heartfelt thanks go to my advisor Dr. Ralf Gerhards, who died surprisingly in December last year. I could count always on his advice and continuous support. He shared all off the ups and downs of this work. I much appreciated our discussions on physics topics as well as topics outside of physics.

I am also thankful to Prof. Dr. Blobel for many stimulating discussions concerning topics of this analysis as well as for proof-reading. Dr. Hannes Jung I would like to thank for the support concerning the extraction of the gluon density, many discussions concerning the theoretical framework of this analysis and for proof-reading. Dr. Olaf Behnke I wish to thank for his suggestions on parts of this analysis and for proof-reading. I am thankful to Dr. Duncan Brown for proof-reading, especially for correcting my "german"-english. Furthermore I am thankful to Bengt, Gero, Martin and Svetlana for the common effort of the final reading.

Furthermore I would like to thank all members of the HQ-group for several ideas and the support during the last years. The FTT-group I wish to thank for supporting me during my studies concerning the triggering of charm for HERA II.

I am thankful to all room-mates and ex-room-mates, who helped in making my time at H1 an enjoyable experience. My parents I would like to thank for the support throughout my life. My special thanks go to my boyfriend Thomas, for many motivations and tips concerning this analysis, the patient and continuous support as well as the necessary and often very welcome deflection from physics.